DEVELOPMENT OF A COMBINED ATOMIC FORCE MICROSCOPY AND SIDE-VIEW IMAGING SYSTEM FOR MECHANOTRANSDUCTION RESEARCH

Kellie N. Beicker

A dissertation submitted to the faculty at the University of North Carolina at Chapel Hill in partial fulfillment of the requirements for the degree of Doctor of Philosophy in the Department of Physics.

Chapel Hill
2016

Approved by:

Richard Superfine

Michael R Falvo

Richard Cheney

Sorin Mitran

Gerald Cecil

ABSTRACT

Kellie N. Beicker: Development of a Combined Atomic Force Microscopy and Side-View Imaging System for Mechanotransduction Research
(Under the direction of Richard Superfine)

Key metrics for understanding cell response to mechanical stimuli include rearrangement of the cytoskeletal and nucleoskeletal structure, induced strains and biochemical distributions; however, structural information during applied stress is limited by our ability to image cells under load. In order to study the mechanics of single cells and subcellular components under load, I have developed a unique imaging system that combines an atomic force microscope (AFM) with both vertical light-sheet (VLS) illumination and a new imaging technique called PRISM – Pathway Rotated Imaging for Sideways Microscopy. The combined AFM and PRISM system facilitates the imaging of cell deformation in the direction of applied force with accompanying pico-Newton resolution force measurements. The additional inclusion of light-sheet microscopy improves the signal-to-noise ratio achieved by illumination of only a thin layer of the cell. This system is capable of pico-newton resolution force measurements with simultaneous side-view high frame rate imaging for single-molecule and single-cell force studies. Longer-term goals for this instrument are to investigate how external mechanical stimuli, specifically single-molecule interactions, alter gene expression, motility, and differentiation.

The overall goal of my dissertation work is to design a tool useful for mechanobiology studies of single cells. This requires the design and implementation of PRISM and VLS systems that can be coupled to the standard Asylum AFM on inverted optical microscope. I also examine the strategy and implementation of experimental procedures and data analysis pipelines for single-cell and single-molecule force spectroscopy. These goals can be broken down as follows:

- Performed single-molecule force spectroscopy experiments.
- Performed single-cell force spectroscopy experiments.
- Constructed and characterized the side-view microscopy system.
- Applied combined AFM and side-vew microscopy system.

ACKNOWLEDGEMENTS

This work would not have been possible without the help and support of many dedicated individuals. My advisors, Professor Rich Superfine and Professor Michael Falvo, were critical to my growth as a scientist and researcher. I am deeply grateful to Professor Richard Superfine for pushing me outside of my comfort zone and into the world of optics; he has an energy and love for science which I endeavor to match. I am grateful to Professor Michael Falvo for his patience and guidance on all things, from single-molecule mechanics to whole-cells to "real world" advice. Mike always has his door open for mechanics discussions, general science enthusiasm, and a well-deserved high-five. I would also like to thank the remaining members of my committee: Richard Cheney, Sorin Mitran, and Gerald Cecil. Their valuable time spent into providing feedback on my research project was much appreciated.

My colleagues in CISMM, both past and present, have been invaluable to my graduate career. The collaborative atmosphere, cultivated in large part by Professor Superfine, has made the laboratory a great place to work. I am indebted to Professor E. Timothy O'Brien for his endless patience for every ignorant biology question, the countless sample preparations, and invaluable insight throughout my research. Professor Sean Washburn has helped me grow by asking tough questions and being available for discussions about work and life. I am grateful for Professor Russ Taylor's insights on all things computer related (including camera synchronization, existing data analysis methods, and the deception of the rainbow color map). Importantly, a big thank you to my labmates who have fielded every question and brainstormed every obstacle with genuine enthusiasm: Joe Hsiao, Robert Judith, Lukas Osborne, Bethany Lanham, Suzy Lynch, Jerome Carpenter, Nathan Hudson, Jay Fisher, Adam Turner, and Pranav Haravu. I am especially thankful to Jeremy Cribb for always being there for any science or MATLAB questions; moreover, I am so grateful to both Jeremy Cribb and Juan Arango for opening their home and hearts to me – you are amazing friends. Lastly, thank you to Evan for continuing PRISM – this project was so much fun and there are so many great questions yet to answer.

During my graduate career at the University of North Carolina, I have had the privilege of working with a large group of talented individuals outside of our laboratory. I would particularly like to thank Laurel Averett who gave me my first introduction to the AFM and the importance of a good set of controls. I am grateful for my collaboration with Nathan Hudson, Professor Oleg Gorkun, Professor Susan Lord, and Professor Mark Schoenfish during my work on fibrin; my research would not have been the same without

their aid. I am thankful for my cell mechanics collaborators, including Professor Richard Cheney, David Graham, Whasil Lee, Holly Leddy, and Sreeja Asokan for their insight and driving questions. I'd also like to thank Dr. Ryan Fuierer and the other members of Asylum Research who answered every technical question and were always willing to help. I am very appreciative to the faculty and staff in the UNC Department of Physics and Astronomy for fostering a delightful environment to work and learn. I am indebted to my fellow physics graduate students, especially those who entered graduate school with me, for their enthusiasm, support, and camaraderie.

I would like to thank the Physics Department at Texas State University for helping me discover a love for physics and for giving me a push toward graduate school. I am especially grateful to Professor Donald Olson for giving me my first taste of research – it was addictive. I have applied many of Professor Olson's early lessons my graduate research projects.

I would like to thank my parents, Gus and Vicki Beicker, for their guidance and encouragement that has enabled me to reach this point in my academic career. I am truly lucky for such amazing role models. I would also like to thank my sister, Tracey Grier, for being my eternal cheerleader and offering unfiltered opinions – both essential for me to make it to where I am today. I am grateful to Lauren Trammell for her frequent visits and phone calls to keep me sane – you are proof that true friendship spans distance and time. Finally, I want to thank my fiancé T.J. Corona for his constant love, support, and encouragement, which carried me through. I love you so very much.

TABLE OF CONTENTS

LIST OF TABLES

LIST OF FIGURES

LIST OF ABBREVIATIONS AND SYMBOLS

AA	Amino Acid
AHTM	Array High-Throughput Microscope
AFM	Atomic Force Microscope or Atomic Force Microscopy
BASS	Biomedical Analysis and Simulation Supercomputer
CA	C-α main chain atoms
CB	C-β side chain atoms
Δx	Distance to Transition State
DMD	Discrete Molecular Dynamics
DMSO	Dimethylsulfoxide
DOF	Depth of focus.
ECM	Extracellular Matrix
EDC	1-Ethyl-3-(3-dimethylaminopropyl) carbodiimide
FOV	Field-of-view
FWHM	Full Width at Half Maximum
GFP	Green Fluorescent Protein
GOF	Gain of Function
GUI	Graphical User Interface
HMDS	Hexamethyldisilazane
HPDE	human pancreatic ductal epithelial cells
HPNE	h-TERT transformed HPDE cells
H2B	Histone H2B (one of the 5 main histone proteins)
H2B-GFP	Fusion Protein of the Human Histone H2B Gene and the Gene Encoding GFP
ibw	IGOR Binary Wave
IGROV-H2B or IH2B	Ovarian Cancer Cell Transfected with H2B-GFP
k_0	Unfolding Rate
LINC	Linker of Nucleoskeleton and Cytoskeleton
LSFM	Light Sheet Fluorescence Microscopy

MFP3D	Molecular Force Probe 3D (Asylum Research - Atomic Force Microscope)
MSD	Mean Squared Displacement
NA	Nucleic Acid
NEA	Normalized Ensemble Average
NHS	N-Hydroxysuccinimide ($C_4H_5NO_3$)
PBS	Phosphate Buffered Saline
PRISM	Pathway Rotated Imaging for Sideways Microscopy
PSF	Point Spread Function
ROI	Region-of-Interest
RPMI	Roswell Park Memorial Institute
SAM	Self Assembled Monolayer
SEM	Scanning Electron Microscope
SLD	Superluminescent Diode
SKOV-H2B or SH2B	SKOV Ovarian Cancer Cell Transfected with H2B-GFP
SMFS	Single-Molecule Force Spectroscopy
SPIM	Single Plane Illumination Microscopy
STICS	Spatio Temporal Image Correlation Spectroscopy
sulfo-SANPAH	Sulfosuccinimidyl 6-(4'-azido-2'-nitrophenylamino)hexanoate
UNC	University of North Carolina
VLS	Vertical Light Sheet

CHAPTER 1: Introduction to forces in biology

Mechanical forces have been identified as instrumental in regulating many physiologic and pathologic processes; as such, the analysis of mechanotransduction is a rapidly advancing area of current research. Mechanical forces affect a broad range of biological scales from single-molecule interactions and domain unfolding to viscoelastic properties and remodeling of single-cells. Mechanotransduction is the process by which mechanical stimuli are converted into biochemical and functional responses from the single-molecule to the single-cell levels. The atomic force microscope (AFM) offers unprecedented opportunity to probe the functional properties of cell surface molecular mechanics (piconewtons) and entire-cell mechanical properties (nanonewtons). Additionally, the AFM can be coupled with optical microscopy to observe the effects of nanoscale mechanics on the remodeling and on changes to cells' functional states.

This chapter is comprised of several key sections:

1.1 Mechanobiology

1.2 Fundamentals of Atomic Force Microscopy

1.3 Significance and Goals

Section 1.1: Mechanobiology

Mechanical forces play a crucial role in the growth and shape of virtually every tissue and organ in our bodies. The skeleton provides structural support against the force of gravity; in the absence of skeletal loading, humans suffer from muscle atrophy and bone resorption.(26) Our skin must stretch to accommodate motion and interaction with our environment.(27) Circulation requires the generation of forces to pump blood around the body and the ability of blood vessels to withstand the shear forces associated with blood flow.(28) As fundamental biological components, living cells must possess the ability to sense, withstand and respond to external mechanical forces from their environment. These properties are essential to the physical integrity and biological function of the cell. However, understanding the mechanisms by which individual cells sense their mechanical environment and convert these mechanical cues into a biological response, a process known as mechanotransduction, is an active field of research with much left to be understood.

Cells sense their environment through a diverse group of mechanosensory proteins and cellular structures (Figure 1.1).(29) At the most fundamental level, mechanotransduction results from single-molecule

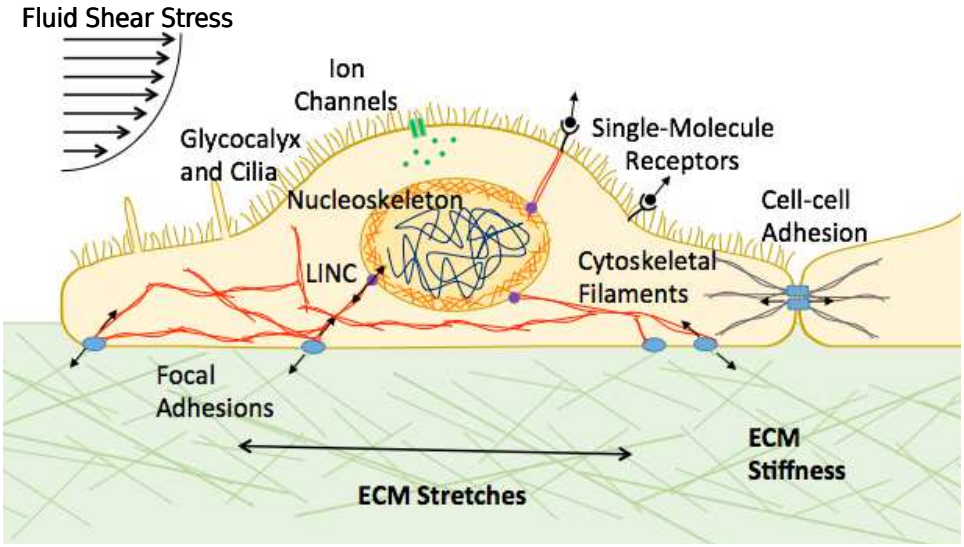

Figure 1.1: Cells exist in a complex mechanical environment, in which there are a variety of mechanosensors and force transducers with overlapping signaling pathways. Mechanotransduction pathways include, but are not limited to, the following: glycocalyx and cilia sense fluid shear, ion channels are stretch activated, cell-cell adhesion complexes and gap junctions allow cell communication, focal adhesions to ECM allow the cell to sense changes in stiffness or stretching, and signaling molecules can bind to cell-surface receptors to create a chemical signal cascade or direct force propagation to DNA through cytoskeletal filaments, LINC complexes and the nucleoskeleton. Mechanical signaling pathways are specific to cell type.

interactions at the cell surface. These interactions induce conformational changes in proteins, which become biochemical events that produce downstream signals (Figure 1.2).(30) Mechanotransduction pathways include proteins in focal adhesions, which can sense a stretch or change in stiffness of the extracellular matrix (ECM); surface structures like the glycocalyx and cilia, which are exposed to changes in fluid shear; ion channels, which are activated by cell membrane stretching; and cell-cell adhesion complexes and gap junctions that allow cells to transmit mechanical response. At the single-molecule level, force can induce unfolding or conformational changes in proteins to expose mechanical domains. For example, forces applied to stretch talin induce conformational changes to facilitate vinculin (a membrane-cytoskeletal protein in focal adhesion plaques) binding.(31) These triggers can lead to cytoskeletal reorganization and modulations in cellular and nuclear shape, as well as gene expression. A few of these mechanotransduction pathways are listed below:

1. Forces can cause protein unfolding or unraveling to expose previously inaccessible (hidden) domains.

2. Forces can structurally expose protein-binding domains or reorient proteins for signaling other proteins.

3. Forces (e.g., pressure, rigidity) can modulate mechanosensitive ion channels by altering tension over a membrane.

4. Force can influence the assembly, stability and turnover of subcellular structures and proteins.

5. Forces can physically bring molecules closer together to increase their local concentration and probability of interaction.

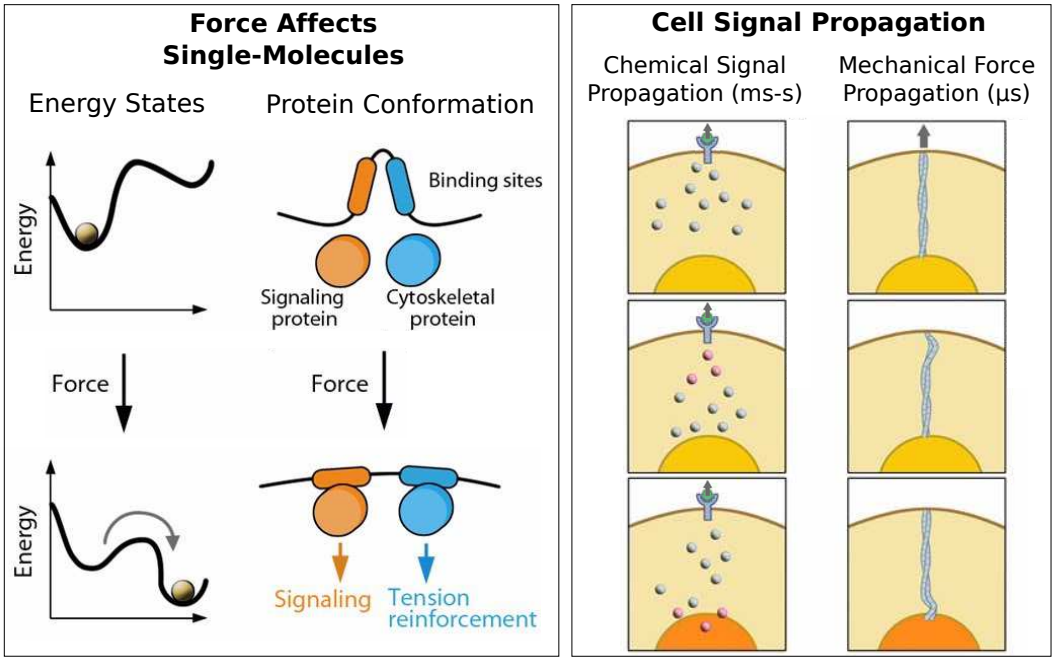

Figure 1.2: Mechanotransduction has effects at many length scales, from single-molecule to whole-cell. (Left) Force affects single-molecule interactions and conformation. Force applied to an interaction decreases bond lifetime and induces conformational changes in a molecule by tilting the energy landscape. Adapted from Thomas et al.(2) (Right) Signal propagation in a cell can be either mechanical or chemical. Chemical signal propagation occurs when an interaction of the membrane causes a biochemical signal cascade that takes tens of seconds to reach the nucleus. Mechanical signal propagation is facilitated by direct mechanical linkage from the cell membrane, through the cytoskeleton and LINC complexes, to the nucleus; this propagation occurs over the course of microseconds. Adapted from Wang et al.(3)

Signal propagation from the initial mechanical event can be either chemical or mechanical in nature (Figure 1.2). A mechanical force that induces a chemical signal cascade within the cell propagates its signal to the nucleus within a few seconds.(3) The recent discovery and study of specialized nuclear anchoring structures for cytoskeletal filaments, known as the LINC (linker of nucleoskeleton and cytoskeleton) complex, has revealed a method of direct mechanical signal propagation to the nucleus. A force that is applied to cytoskeleton-linked integrins propagates to the nucleus in just a few microseconds.(3) Recent findings indicate that the nucleus may bypass mechanosignaling through the cytoplasm altogether to directly modulate the expression of mechanically exposed genes.(3; 32) The molecular mechanisms responsible for a cell's mechanical response are of interest due to the downstream effects of force on gene expression, differentiation and motility.(33; 34)

In addition to the large disparity in timescales for signaling, mechanically relevant processes can span a wide range of biologically relevant time, force, and length scales (Figure 1.3).(4; 5) Mechanical response behaviors include both passive material response and active biological responses. The material response of a cell or subcellular structure can run the gamut from microseconds for a purely elastic response to several minutes for viscous response. Active biological responses to mechanical stimuli occur over disparate timescales, as seen in the activation of signaling; changes in contraction behavior; focal adhesion strengthening, phosphorylation, and growth; transcriptional regulation; and differentiation and proliferation (reviewed by Ricca et al.).(4) Force and length scales of relevance to cell and molecular biomechanics span several orders of magnitude, range from piconewtons for protein-protein interactions to micronewtons for cell contraction and from nanometers for proteins to hundreds of microns for cells.

Mechanobiology can be described as an amalgam of contributions from individual cellular components; however, it is important to understand that these components do not act in isolation but instead contribute to a complex network of signaling pathways. These mechanical responses may encourage the cell to test its environment again, thereby producing a feedback loop of amplifying force response. Therefore, each seemingly discrete event or individual component exerts an influence on others and allows the system to continuously adjust to changes in its environment in order to maintain integrity by eliciting appropriate responses.

As discussed, cells experience a multitude of external forces, from single-molecule receptor interactions to large deformations due to fluid shear or extracellular matrix stretching. These forces are then transmitted from the outer surface of the cell via the cytoskeleton to inner cellular organelles like the nucleus. Moreover, cells themselves also generate force and change their mechanical properties in response to applied forces. A variety of methods, including complaint substrates, micropillar arrays, micropipette aspiration, and magnetic tweezers, have been used to measure the mechanical properties of single molecules or single cells; however, few are able to span a significant portion of the force parameter space to measure both single-molecule and single-cell mechanics (Figure 1.4).

Section 1.2: Fundamentals of Atomic Force Microscopy

The AFM is capable of applying and sensing forces from several piconewtons well into the nanonewton range, which makes it the tool of choice for a broad range of biomechanics studies. Though originally invented as a high-resolution imaging tool, the force spectroscopy application of the AFM has rapidly become a popular method for studying both single-molecule and single-cell mechanics. The AFM has been used to investigate levels of cellular mechanics ranging from the strength of individual cadherin-cadherin bonds(35; 36; 37; 38)

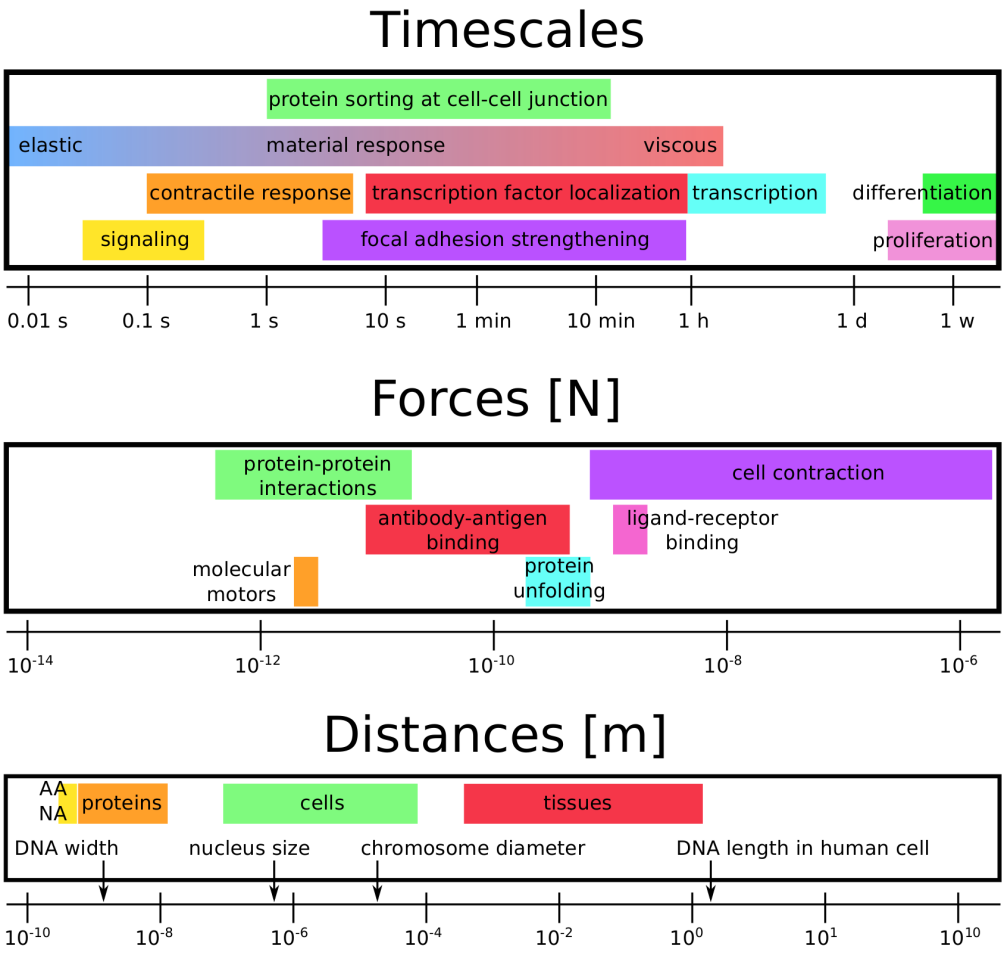

Figure 1.3: Mechanical response behaviors span a wide range of biologically relevant time (top), force (middle), and length (bottom) scales. Both passive material response and active biological responses scan many timescales from elastic response to differentiation and proliferation. Forces range from sub-piconewton protein-protein interactions to micronewton cell contractions, and relevant length scales range from nucleic acids up to full tissues. Adapted from Ricca et al(4) and Suresh.(5)

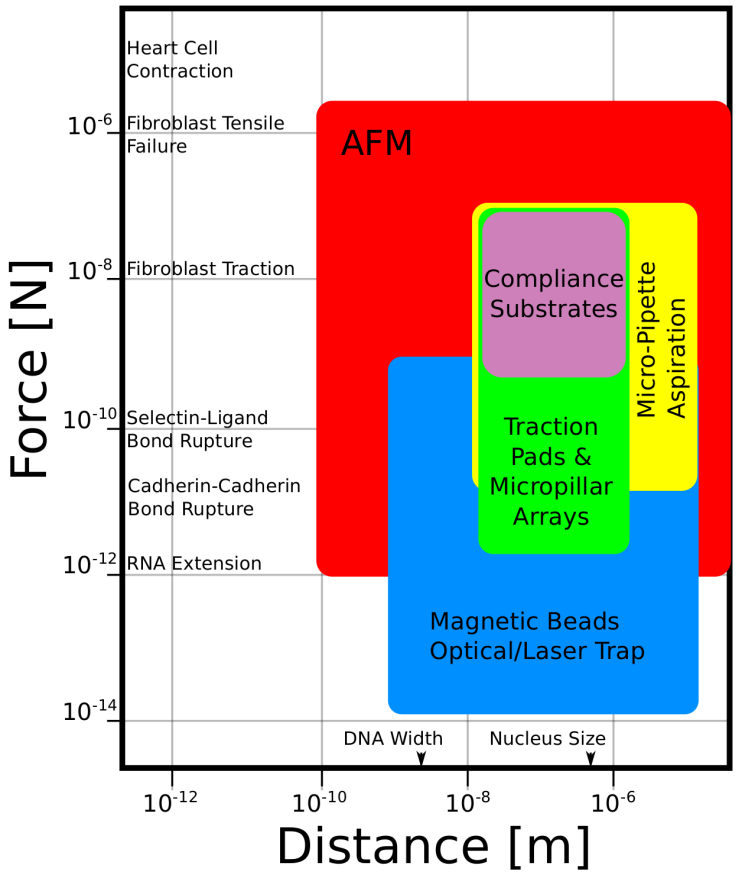

Figure 1.4: Comparison of force and length scales for cell mechanics techniques. Note that the ranges reported are not necessarily attainable using the same device setup (e.g. different stiffness substrates or pillar arrays, and different AFM cantilevers). Adapted from Loh et al.(6)

to global viscoelastic properties of the cell.(39; 40; 41) Additionally, the AFM can be combined with various forms of optical microscopy (e.g., fluorescence microscopy) for simultaneous imaging of the cell.(29) Despite the complexity of data gathered, the AFM requires only basic principles to describe, as shown in Figure 1.5.

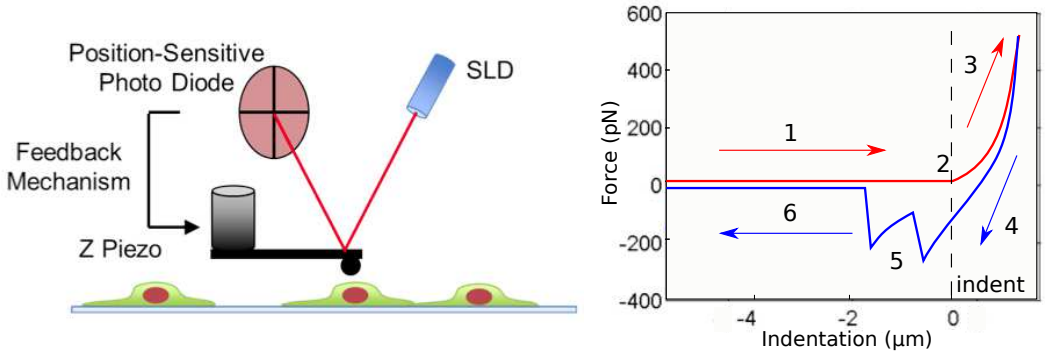

Figure 1.5: Schematic of the AFM and force-indentation data. (A) AFM cantilever motion is measured by the SLD signal collected on a position-sensitive detector. (B) Sample force-indentation determined from raw z-piezo and deflection data. The cantilever (1) approaches, (2) contacts, and (3) indents the sample up to some predefined trigger force. Then the cantilever is (4) retracted from the surface. If there is adhesion between the tip and sample, then (5) force-rupture peaks corresponding to the rupture of adhesions are produced with the final rupture event peak causing complete detachment of tip from surface and (6) the cantilever continues to retract without any deflection (i.e., zero-force).

The AFM cantilever with a tip on its end is moved toward and away from the substrate with sub-nanometer precision via a piezo. This piezo is referred to as the z-piezo because it moves the AFM cantilever in the z-direction relative to the sample stage (which provides x and y motion to the sample). The z-piezo can be used to move the cantilever at a constant speed, allowing the cantilever to bend as it interacts with the surface, or it can vary the cantilever position in order to maintain a constant deflection. These two spectroscopy modes are respectively described as 'force-ramp' and 'force-clamp', and are discussed in more detail in relation to single-molecule experiments in Chapter 2. The default operation for AFM force spectroscopy is the constant-velocity, force-ramp mode.

The cantilever's deflections are detected with a superluminescent diode (SLD) reflected off the back of the cantilever and onto a quadrant position-sensitive photodetector. The measured deflections are converted into applied force using a Hooke's law approximation for the cantilever (i.e., $F = -k \cdot x$, where F is force, x is the deflection, and k is the empirically determined spring constant).(42; 43)

Parameters such as tip geometry, cantilever stiffness and surface functionalization are varied to probe the mechanical properties of interest. For single-molecule experiments (Chapter 2), a flexible cantilever and a protein-coated silicon nitride pyramid probe are selected to measure piconewton forces associated with unfolding and to reduce surface area, thus decreasing the probability of multiple interacting molecules.

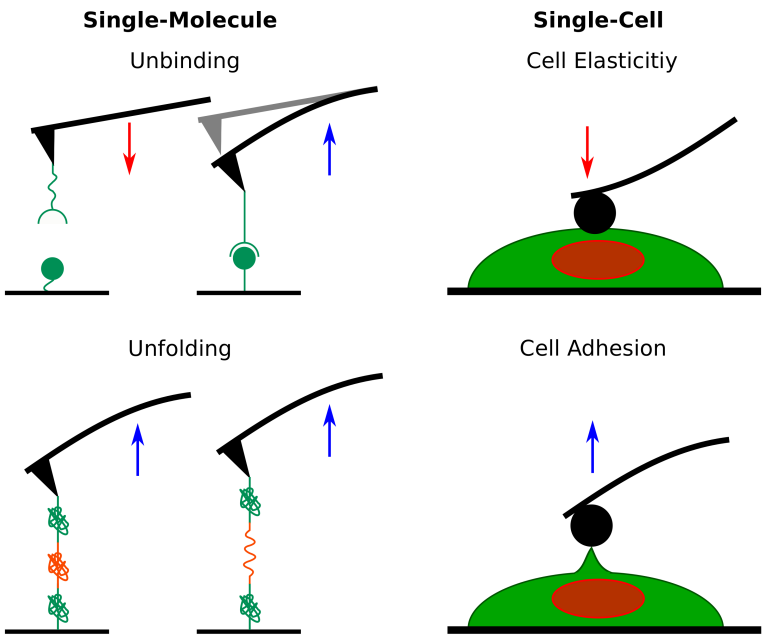

Figure 1.6: Schematic of the different single-molecule and single-cell force spectroscopy experiments. Adhesion events in the retract portion of a force curve are informative in (top-left) single-molecule unbinding and (bottom-left) unfolding experiments. (Top-right) Cell elasticity and (bottom-right) adhesion can be measured from the approach and retract portions of single-cell force curves.

For single-cell mechanics measurements, a 5 μm polystyrene bead is attached in-house as described in Appendix I). Beaded tips are more suitable for single-cell measurements (Chapters 3 and 5) in order to avoid puncturing the cell during measurement; the bead reduces the indentation depth and localized pressure, increases contact area over inhomogeneous surfaces for elasticity measurements and increases interactions for adhesion measurements. Experiments have also been performed that measure cell-cell adhesions where the tip is replaced by a living cell,(44); this technique was not used in our studies.

A typical force spectroscopy experiment begins with the cantilever away from the sample (Figure 1.5). The cantilever approaches the substrate and, as the probe encounters the sample, the cantilever is bent upward until a predetermined trigger force (or deflection) is reached. The cantilever is then retracted from the sample at a constant velocity. If interactions occur between the tip and sample, the cantilever is bent downward until the restoring force of the cantilever exceeds the strength of the tip-sample interaction. After the tip-sample interaction is broken, the cantilever continues to retract without any deflection (i.e., zero-force).

The data collected in a force spectroscopy experiment are traces of force versus separation, or 'force curves'. Depending on the type of experiment performed (Figure 1.6), different information can be extracted from these force curves. In single-molecule experiments (Chapter 2), the height and separation of rupture

events in the retract curve can be used to extract information about bond strength and unfolding domains. Varying the protein type on the tip and substrate, forces or solution conditions can provide information on physiologically relevant force-dependent behavior. For single-cell experiments, the Young's modulus (i.e., stiffness) of a cell can be determined by fitting a contacts mechanics model (i.e., Hertz in the case of a spherical indenter) to the indentation portion of approach curve (Chapter 3). From the retract portion of the curve, information related to the number and strengths of adhesions was acquired.

When coupled with optical microscopy, the AFM can provide simultaneous force and structural data on a cell's response to mechanical stimuli. The Asylum MFP-3D-BIO AFM, used for all experiments described herein, is a commercial, fully-capable AFM integrated with an inverted optical microscope, and it has been used for single-molecule and cell mechanics studies.

Section 1.3: Significance and Goals

One of the overall goals of my dissertation work has been to design a tool that is useful for mechanobiology studies of single cells. In order to study this broad range of mechanosensing components (from single-molecules to subcellular structures such as the nucleus) of biological elements as they occur in realtime in the cell, an instrument and analysis pipeline is needed that will allow the user to probe a broad range of force and to perform high-speed and high-resolution imaging in the direction of applied load. To study the mechanics of single cells and subcellular components such as the nucleus under load, I have integrated a new imaging technique called PRISM (pathway rotated imaging for sideways microscopy) with atomic force microscopy and light sheet illumination. This system is sensitive enough to measure single-molecule unfolding, while maintaining the breadth to measure single-cell mechanical properties and structural changes.

A large portion of my work is associated with the design and implementation of the this new technique, which required the design, construction, characterization, and implementation of the PRISM system (Chapter 4 and Chapter 5) and the implementation of experimental procedures and data analysis pipelines for single-molecule (Chapter 2) and single-cell spectroscopy (Chapter 3). The work described in Chapter 2 was part of a larger research project within our group on the mechanical properties of fibrin that was distinct from the more recent research effort focused on mechanobiology (which is the biophysical problem motivating Chapters 3, 4, and 5). However, the single-molecule mechanical work described in Chapter 2, including the AFM protocols and single-molecule force spectroscopy analysis, are directly applicable to the larger cell mechanobiology goal outlined in the later chapters. Chapters 3, 4, and 5 are of a piece and describe the co-evolution of cell mechanics work and instrument development.

This document is organized into AFM measurements of different types – single-molecule force spec-

troscopy, single-cell mechanics measurements, and the combined AFM-PRISM-VLS system.

1. The goal of Chapter 1 has been to provide a brief overview of mechanobiology and the AFM instrument.

2. In Chapter 2, I applied the AFM to single-molecule force spectroscopy experiments on fibrin. Here, I used applied constant-velocity, constant-force and force-quench experimental techniques in conjunction with Monte Carlo methods and molecular dynamics simulations to understand the origins of fibrin's dynamic properties. These are the first investigations into fibrin unfolding under constant-force and the reversibility of single-molecule fibrin unfolding. As such, they reveal previously unobserved unfolding and refolding behavior in the fibrin molecule. All protocols for unfolding event recognition and kinetic analysis can be used to study single-molecule interactions in the single-cell environment.

3. In Chapter 3, I applied AFM single-cell force spectroscopy techniques to ovarian cancer, pancreatic cancer, and de-nucleated cells. These studies provided unique mechanical measurements of the cells investigated and insight into the contribution of the nucleus to a cell's mechanical properties. However, these experiments lacked the imaging capabilities necessary to acquire structural information in the direction of applied force.

4. In Chapter 4, I described the design and characterization of the system necessitated by experiments performed in Chapter 3. The combined AFM and PRISM system simultaneously delivers imaging of cell deformation in the direction of applied force and piconewton resolution force measurements with the additional inclusion of light-sheet microscopy to improve image quality. With this new system, I was able to acquire previously unattainable ~ 300 nm xz-plane image resolution and millisecond time resolution in the direction of applied force.

5. In Chapter 5, I demonstrated the utility of the combined AFM-PRISM-VLS system for identifying the structural components of the cell responsible for changes in depth-dependent mechanical properties during deformation and identifying direct mechanical linkages between the cell membrane and the nucleus during adhesion. Through a detailed analysis, I illustrate the utility of the integrated force measurement and synchronized high frame rate, side-view imaging system for the study of intracellular (and intranuclear) motion due to force applied at the cell surface. These data are some of the first continuous side-view imaging of nuclear deformation with corresponding AFM force measurements.

6. Finally, I present a discussion of the conclusions and future directions of this work in Chapter 6.

CHAPTER 2: Single-Molecule Force Spectroscopy Studies of the Fibrin 'A-a' Interaction and γ Module Unfolding

Fibrin networks, the structural mesh upon which blood clots form, must elastically withstand the shear forces of blood flow and provide mechanical stability to the clot. The mechanics of these networks are determined by the mechanical properties of individual fibrin monomers and the interactions between them. A critical interaction in the polymerization of fibrin fibers is the 'A-a' knob-hole interaction. In order to investigate the mechanical response and unfolding dynamics of the protein when pulled from the knob-hole interaction, I (1) built on previous work by Laurel Averett to investigate the effect of environmental conditions on the knob-hole forced rupture pattern, (2) designed single-molecule force-clamp experiments to apply constant force specifically to the 'A-a' knob-hole location, and (3) performed preliminary force-quench experiments to understand reversibility of 'A-a' forced unfolding. This represents the first application of the force-clamp and force-quench techniques to single-molecule fibrin studies. The resultant information about the reversible nature of single-molecule fibrin unfolding may be helpful in creating a course-grained model for fibrin clot behavior. Additionally, all protocols for unfolding event recognition and kinetic analysis can be used for understanding single-molecule interactions in the single-cell environment.

This chapter is broken down into several key sections:

Section 2.1: Background on Fibrin and Single-Molecule Force Spectroscopy

Cells can sense and convert mechanical factors in their environment into a biological response that ultimately regulates cellular processes, including adhesion, proliferation, differentiation, and apoptosis.(45) Researchers are only beginning to learn how cells convert mechanical forces into biochemically relevant information through a processes referred to as mechanotransduction. At the most fundamental level, mechanotransduction results from single-molecule interactions at the cell surface inducing conformational changes in proteins, which become biochemical events that produce down stream signals involving complex signaling

pathways that intersect and modify each other to produce reliable cell responses.(30) Understanding the molecules involved and molecular mechanisms by which mechanical cues are converted into biological signals requires measurements of the mechanical properties of individual biomolecules, protein unfolding pathways, and characterization of the change in functional states of proteins under load.(30) Single-molecule studies have uncovered diverse force sensing arrangements, including force-regulated conformational changes and intermediate states in unfolding pathways which provide access to previously unaccessible regions of the protein for binding, phosphorylation, or transcription. Combining single-molecule force-spectroscopy (SMFS) with cell biology provides a powerful method for exploring how forces applied to the cell-surface differentially regulate cell signaling pathways.

To study the effect of single-molecule interactions on cell signaling pathways, the force measurement system must accomplish force measurement and application from the piconewton to nanonewton scale under physiological conditions. The AFM has become a powerful tool in molecular and cell biology for single-molecule and cell mechanics studies due to (1) high vertical and lateral resolution for precise force application and topographic information, (2) precise application and measurement of piconewton forces, (3) variety of probe devices and tip functionalization methodologies, and (4) the ability to probe a variety of sample geometries in natural conditions, such as buffer. AFM force spectroscopy has facilitated piconewton force measurements of single-molecule interactions to provide insights into cell adhesion,(46; 47) molecular recognition,(48; 49; 50) protein folding and unfolding,(51; 52) and DNA mechanics.(53)

To collect SMFS on fibrin monomers, methodologies for single-molecule tip functionalization, various methods of force application, and methods for analysis of single-molecule forced protein unfolding and unbinding were developed. Here in, I use AFM SMFS methods to measure the single-molecule unfolding properties of fibrin. Fibrin has been implicated in cell mechanosensing;(54; 55; 56) however the original motivation for fibrin mechanics was a separate research thrust from the cell mechanics project but fibrin unfolding serves well as a trial mechanical protein.

Fibrin, the structural mesh upon which blood clots form, is an inherently mechanical protein with various domains implicated in physiologically relevant single-molecule unfolding.(57; 58) Experiments designed to probe the unfolding pathways of fibrin through forces applied to a critical clot formation interaction have revealed a complex but incomplete picture of single-molecule fibrin force response.(57) Here in, I use AFM SMFS methods to measure the single-molecule unfolding properties of fibrin. This will inform our understanding of the mechanical properties of fibrin as they relate to blood clot formation and also provide an ideal single-molecule system for developing force application and analysis pipelines.

2.1.1: Fibrinogen and Fibrin

Fibrinogen, the precursor of fibrin monomer, is a 340 kDa glycoprotein made up of three pairs of polypeptide chains Aα, Bβ, and γ, held together by 29 disulfide bonds.(59) The amino termini of all six chains are held together by disulfide bonds in the central E region, while the C termini of the Bβ and the γ chains form the β and the γ modules that constitute the distal D regions. The structural regions are connected by helical coiled-coils of all three polypeptide chains that maintain a symmetrical D-E-D linear conformation of fibrinogen.(60; 61)

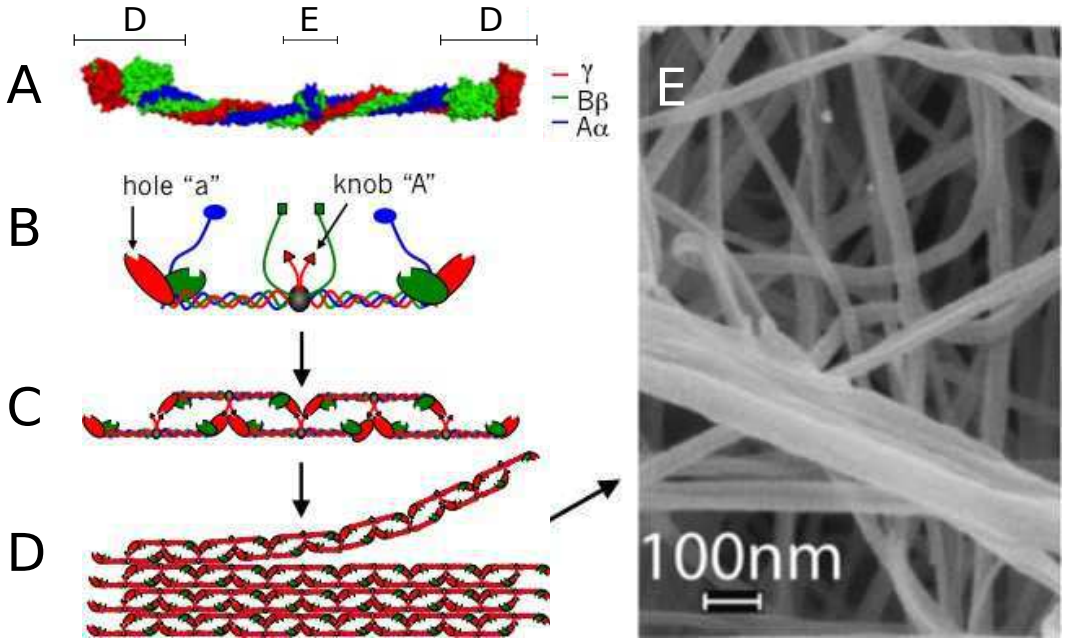

Figure 2.1: Schematic of fibrin polymerization. (A) Space-filled rendering of fibrin structure colored by chain. In the crystal structure, created using Protein Data Bank entry 3GHG, neither the αC domains nor the N-termini of the Aα and Bβ chains are resolved and are therefore not shown. (B) Cartoon illustration of the same fibrin monomer with exposed 'A' knobs. (B) Interaction between holes 'a' and knobs 'A' form double stranded, half-staggered protofibrils. (C) Protofibrils grow and aggregate laterally to form fibers. Fibers grow, branch and merge to form a complex fibrin network. (D) Scanning electron microscope image of fibrin network. Images adapted from Averett thesis.(1)

Upon injury to a blood vessel, the coagulation cascade generates thrombin, which converts soluble fibrinogen into insoluble fibrin. Thrombin cleaves the fibrinopetides from the N termini of fibrinogen's Aα and Bβ chains, exposing polymerization sites called knobs 'A' and 'B'.(62) The knobs 'A' of one molecule noncovalently interacts with complementary binding sites, holes 'a', located in the γC modules of the D region of another molecule.(63; 64) The 'A-a' knob-hole interaction forms half-staggered protofibrils and laterally aggregate to form fibers.(60; 65) Fibrin fibers branch and undergo cross-linking to form stable, three-dimensional fibrin networks critical to blood clotting. In addition to 'A-a' interactions, other specific

interactions play a critical role in the assembly of fibrin clots include 'B-b' knob-hole , D-D interface, γ module and β module lateral, and αC-αC interactions.(64; 66; 67) Because elimination of knob-hole interactions impair fibrin formation and dissolve formed clots,(68; 69) the knob-hole interactions are viewed as the principle promotors of fibrin clot assembly and contributors to clot integrity.

2.1.2: Mechanical Studies of Fibrin

As the structural scaffold of blood clots, fibrin must stop hemorrhaging at the site of vessel injury. In order to be successful, fibrin possesses seemingly contradicting mechanical characteristics. In hemostasis, the clot must withstand the shear forces associated with blood flow to stop hemorrhaging. However, fibrin cannot impede the flow of blood when a clot is not necessary. Inappropriate mechanical properties of fibrin clots may cause bleeding and clotting disorders such as hemophilia (insufficient clotting and excessive bleeding), thrombosis (excessive clotting leading to vessel blockage), and thromboemoblism (dislodged clots that can block vessels away from the site of injury). The biological roles and physical properties of fibrin have made it an attractive molecule for mechanical studies.

Despite such critical importance, the structural basis of clot mechanics is not well understood.(58) The rising attention to this dilemma has resulted in an abundance of papers describing mechanical properties on multiple levels, including the strength of the whole-clot network, the elasticity of individual fibers, and changes to monomeric structure under force. Whole-clot viscoelastic and rheology studies have focused on the correlation between clot structure (i.e., thickness of fibers and porosity) and mechanics.(70) Individual fibers, manipulated in the context of a whole clot or gel, are characterized as semi-flexible biopolymers and exhibit strain-stiffening behavior.(71; 72) Single fibers suspended over micro-channels were mechanically extended resulting in the discovery that fibrin fibers are among the most extensible biopolymers. Furthermore, much of the observed fiber extensibility is reversible.(73; 74; 75; 76; 77; 78)

The exceptional extensibility of fibrin fibers is generally considered an important mechanism helping to accommodate strain, but there is no agreement on the particular structures of the fibrin molecule responsible. The following molecular origins have been suggested: (1) unfolding of the globular γ module,(57; 79) (2) unfolding of the coiled-coil region,(65; 80) (3) straightening and unfolding of the αC domain,(71; 81; 75; 82; 83) and (4) some combination of these regions.(76; 84; 74; 85; 86)

In previous thesis work by previous UNC physics graduate student Laurel Averett, the AFM was used to perform SMFS experiments on the monomeric restructuring of fibrin's γ module and the effects of force on the 'A-a' molecular bond.(1) Force applied to the 'A-a' interaction resulted in a reproducible, well-defined forced rupture pattern consisting of two to four peaks in the force-extension curve associated with stepwise

unfolding of the γ module of fibrinogen, where the final peak is rupture of the 'A-a' interaction. The distribution of rupture forces measured during a typical force map did not produce a single mode or most probable rupture force. Instead, the force distribution was characterized by two distinct force populations (Figure 2.2B), which lead to a thorough examination of the individual events in the force curves. The largest population of curves was characterized by a doublet of high force rupture events ($\sim$ 225 pN) separated by $\sim$ 8 nm, which was often preceded and/or followed by an event of lower force. A sample force-extension curve is shown in Figure 2.2A with all four rupture peaks labeled. Peaks 2 and 3 contributed the higher force rupture mode ($\sim$ 225 pN), and peaks 1 and 4 contributed to the lower force rupture mode ($\sim$ 100 pN). Through a rigorous battery of controls, these interactions were found to be highly specific to unfolding of the γ module due to force applied to the 'A-a' interaction, as none of the other known fibrin interactions contributed to the characteristic pattern.

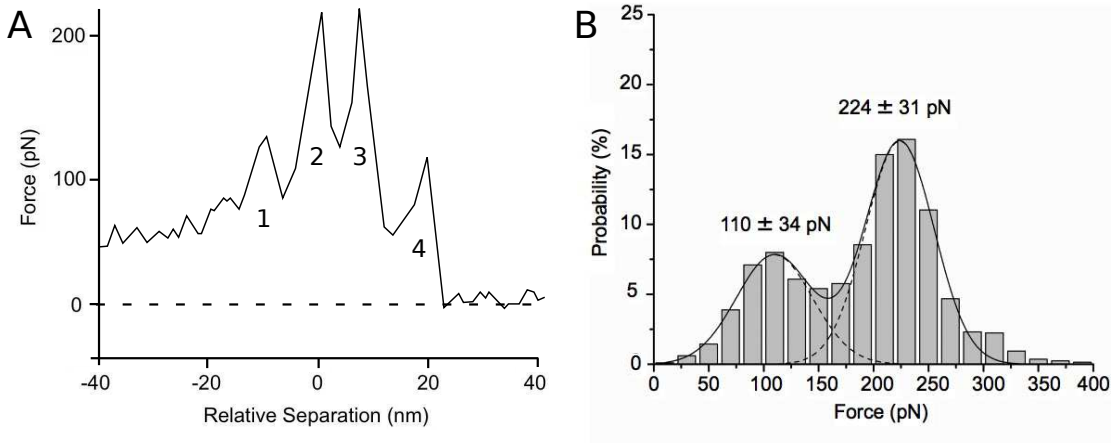

Figure 2.2: Constant-velocity SMFS of fibrin 'A-a' interaction. (A) Representative four-event characteristic rupture pattern observed in constant-velocity AFM SMFS experiments aligned relative to the second event. Characteristic 'A-a' forced unfolding of fibrin occur in one of four phenotypes consisting of a doublet of higher force events (events 2 and 3) and optional proceeding or following lower force events (events 1 and 4). (B) The distribution of force rupture events observed through the 'A-a' interaction is bimodal with most probable rupture forces of 110 $\pm$ 34 and 224 $\pm$ 31 pN . The uncertainties represent half-widths at half-maximum of the Gaussian fits and bins size is 20 pN. Figure modified from Laurel Averett's Thesis.(1)

2.1.3: Significance and Goals

The exceptional extensibility of fibrin fibers is an important mechanism for the accommodation of physiological strain, but there is no agreement on the particular structures of the fibrin molecule responsible. Fibrin unfolding through 'A-a' knob-hole interactions are the focus of the work presented in this chapter because they are critical intermolecular interaction involved in the assembly and structural stability of fibrin polymer. I attempt to gain a molecular-level understanding of forced γ module unfolding and dissociation of the 'A-a'

interaction through the application of SMFS techniques. Specifically, two aspects of fibrin single-molecule unfolding are investigated in this chapter – (2.3) the effect of solution conditions on 'A-a' interaction and (2.4) γ module unfolding due to a constant-force.

Fibrin polymerization is a complex, multistep process that is influenced by solution conditions, including sodium chloride (NaCl) concentration, pH and temperature. Each of these parameters has notable effects on the kinetics of fibrin polymerization, as well as the structural and mechanical properties of the final clot. However, the effect each of these parameters on fibrin polymerization at the molecular level is poorly understood. Therefore, I sought to evaluate the influence of environmental parameters (i.e., NaCl concentration, pH, and temperature) on the mechanical behavior of the 'A-a' knob-hole interaction in Section 2.3.

In the case of constant-velocity force spectroscopy, the force applied to the interaction varies dramatically and inconsistently, as the protein is unfolded. Mechanical unfolding of a protein is known to be dependent on applied force,(87) therefore it would be beneficial to directly measure protein unfolding as a function of applied force. In Section 2.4, I develop a force-clamp spectroscopy technique and analysis pipeline to allow probing unfolding behavior under constant force. This technique enables the probing of unfolding behavior at lower force to measure conformational diversity inaccessible with constant-velocity experiments and a direct method of extracting unfolding kinetics without assumptions associated with current models. The force-clamp methodology is also an ideal system for understanding the reversible nature of γ module unfolding due to force applied at the 'A-a' interaction in a variant technique often referred to as force-quenching.

Identification of the molecular mechanism responsible for fibrin extensibility would allow identification and possible treatment of fibrin related clotting disorders. In the more general field of protein unfolding, lower force unfolding events remain an uncommon observation but they may contribute the unfolding kinetics observed in experiments. Understanding the contribution of multiple subdomains to protein mechanics provides a different perspective on sources of non-Markovian behavior in protein unfolding. In the broader view of cell mechanosensing and mechanotransduction, the detailed mapping of force unfolding behavior of single-molecule fibrin can provide insight into the different mechanisms by which mechanical proteins in the cell transmit forces. Because both (un)binding and protein unfolding could be measured in single-molecule force-spectroscopy experiments on living cells targeted by the new combined force-imaging technique, single-molecule fibrin measurements are useful for developing a pipeline of analysis for these measurements.

Section 2.2: Single-Molecule Force Spectroscopy Experimental Methods

2.2.1: Materials, Tip Functionalization, and Sample Preparation

All reagents were of analytical grade and purchased from Sigma (St. Louis, MO) unless noted otherwise. N-hydroxysuccinimide (NHS) and 1-ethyl-3-(3dimethylaminopropyl) carbodiimide (EDC) were purchased from Pierce Scientific (Roxford, IL).

For all experiments, aliquots of the protein solutions synthesized and purified in the laboratory of Professor Susan Lord were acquired from Professor Oleg Gorkun. A detailed description of procedures required to generate, purify, or aliquot any of the fibrinogen can be found elsewhere. Specifically, interested readers are directed to other sources for protocols to obtain the wild-type recombinant fibrin(88) and the desAB-NDSK fragment, which represents the central region of fibrinogen and contains polymerization knobs 'A' and 'B'.(89) After purification, the fibrinogen and desAB-NDSK were dialyzed against HEPES-buffered saline (HBS) (20mM HEPES and 150mM NaCl, pH 7.4) buffer and stored at -80°C.

2.2.2: AFM Experiments

All surfaces for AFM experiments were prepared as described in detail elsewhere.(57) Briefly, clean glass microscope slides and silicon nitride TR400PSA cantilevers (Olympus) were coated with gold. Then carboxylic-acid-terminated self-assembled monolayers were used to randomly, covalently attach the proteins to the surfaces. The protein arrangement was such that holes 'a' were on the substrate and knobs 'A' were on the tip as shown in Figure 2.3. It was previously shown that reversing the protein arrangement, such that knobs were on the substrate and holes were on the tip, did not affect the force-extension pattern.(57) Importantly, the concentration of proteins on tip and substrate were such that less than 15% of all contacts with the substrate resulted in a measurable interaction. Both tip and substrate remained in buffer solution (20mM HEPES, 150mM NaCl, 2mg/mL BSA, 3 mM $CaCl_2$, and 0.01% Triton X-100, pH 7.4) for AFM experiments.

Differing from previous research,(57) the gold-coated substrates were adhered to glass slides with buffer wells using vacuum grease rather than epoxy. The benefit to using vacuum grease is that substrates can be removed from the glass slide and the slide can be cleaned then reused for another experiment. Preserving the same slide and buffer well results in similar volumes of buffer solution used in the experiments. The capillary forces are sufficient for vacuum grease to give the same force-extension pattern as experiments performed with epoxy.

AFM experiments were conducted using a Molecular Force Probe 3D (MFP3D) instrument (Asylum

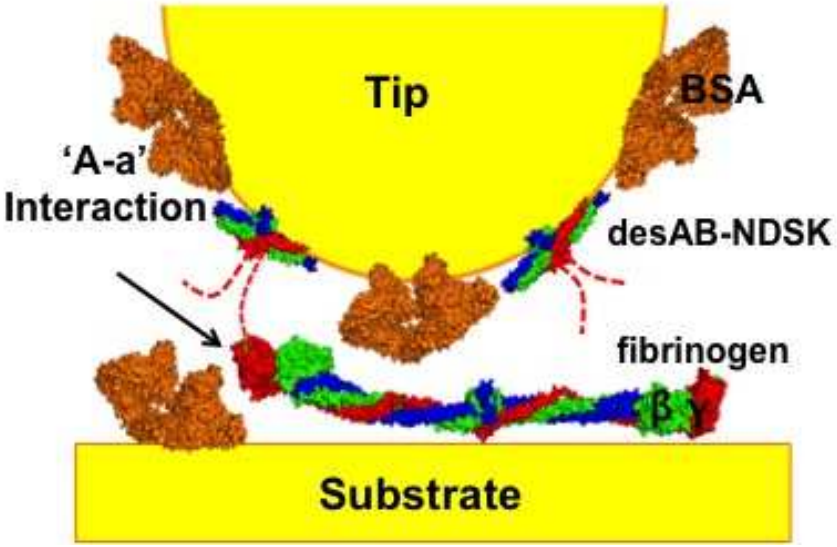

Figure 2.3: Schematic of single-molecule AFM experimental configuration. Fibrin fragments desAB-NDSK and fibrinogen were immobilized covalently onto a gold-coated AFM probe and substrate with a carboxylic acid terminated SAM through NHS/EDC chemistry. All experiments were performed in a buffer, which contained both surfactant and BSA. Space filling models of desAB-NDSK and fibrinogen colored by chanis: α (blue), β (green), and γ (red). The formation of an 'A-a' knob-hole interaction is shown. The N-termini of the α chains do not appear in crystal structures; therefore, the knobs 'A' are approximated (dashed lines). N-termini of β chains and αC domains are not shown.

Research, Santa Barbara, CA). Protein-coated cantilever and substrate were allowed to equilibrate at room temperature in buffer until the deflection signal stabilized (∼1 h). The spring constant of the TR400PSA cantilever (∼20 pN/nm) was determined for each scan area before force curves were collected using the built-in thermal calibration method.(90; 91; 92) The average value of all spring constants found for that cantilever was used in subsequent analysis. From this starting point either constant-velocity or constant-force SMFS experiments were performed to probe the 'A-a' knob-hole interaction. Because the experimental and data analysis protocols differ for each force spectroscopy technique, they are discussed in detail in the appropriate sections.

Section 2.3: Effect of Solution Conditions on Constant-Velocity Fibrin Unfolding

2.3.1: Introduction

Polymerization of fibrin clots has been extensively studied. Variations in environmental conditions lead to the formation of clots with variable polymerization kinetics and structural properties. Each solution condition investigated herein (i.e., NaCl concentration,(93; 94; 95) pH,(96; 94; 97; 98; 99; 100) temperature(94; 99; 101)) has known effects on protein stability and structure, and fibrin polymerization. Clot turbidity, a measure of fibrin fiber thickness, is inversely related to the NaCl concentration.(93; 97; 99; 102; 103; 104; 96) Acidic solution conditions slow the kinetics of fibrin polymerization and both acidic and basic conditions lead to formation of clots with lower final turbidity.(100) Polymerization experiments have only been performed for physiological and lower temperatures.(99; 101) These polymerization experiments determined fibrin networks formed thinner fibers at higher temperatures.(99) This occurs through a complex process in which temperature affects enzymatic cleavage and polymerization interactions.

Although much is known about the effect of environmental conditions on fibrin polymerization and final clot structure, there has been no investigation into the effects of solution conditions on the single-molecule mechanics of fibrin. Because the 'A-a' interaction is integral to the polymerization of fibrin clots, SMFS of fibrin with the 'A-a' interaction as the location of force application provides insights into the molecular mechanisms that give rise to polymerization results. I use a protocol developed by Averett et al. that enables the measurement of single-molecule fibrin unfolding and rupture of the 'A-a' interaction.(57)

Laurel Averett found that force applied to the 'A-a' interaction resulted in a reproducible, well-defined forced rupture pattern consisting of two to four peaks in the force extension curve associated with stepwise unfolding of the fibrin γ module (Figure 2.4 A-D). For brevity, these curves are referred to as 'characteristic'. All characteristic curves possess a doublet of force peaks that may be preceded or followed by a lower force peak. The final peak in the curve is associated with rupture of the 'A-a' knob-hole interaction. In two of

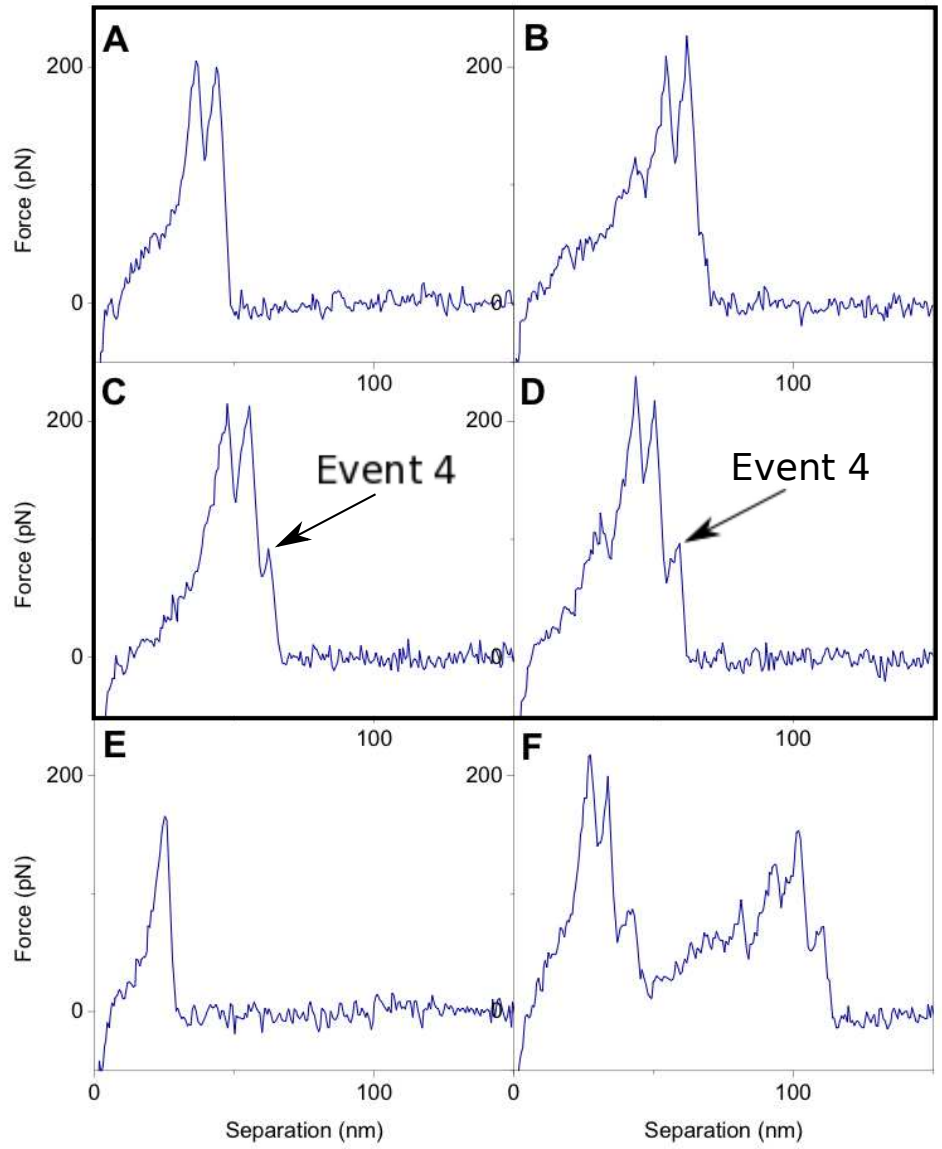

Figure 2.4: Representative force curves showing prevalent patterns of rupture of interactions between desAB-NDSK (tip) and fibrinogen (substrate). Curves A-D are characteristic of an 'A-a' interaction, defined as containing a doublet of rupture events of ∼200 pN. Of the four types of characteristic force curves, two (C and D) contain an additional rupture event (event 4) following the doublet. (E) Single event and (F) multiple event force curves occur with significantly less probability at standard solution conditions (0.15 M NaCl, 27°C, pH 7.4).

the force curve types, an additional lower force peak follows the doublet characteristic of 'A-a' knob-hole interaction (Figure 2.4 C-D). This lower force peak is referred to as 'event 4'. This additional extension due to the lower force peak has been attributed to the stability of hole 'a' during forced unfolding.(105)

Herein, experiments investigating the effects of NaCl concentration, pH, and temperature on the 'A-a' knob-hole interaction are examined. Specifically, two metrics related to the stability of the 'A-a' interaction are used to study the influence of environmental conditions: (1) the probability that an interaction results in the characteristic doublet of forced unfolding through the 'A-a' interaction and (2) the probability that a characteristic force curve contains lower force event 4.

2.3.2: Methods

Each sample (i.e., substrate and tip) was prepared and AFM experiments were performed as described in Section 2.2 with the following solution condition variations. Because it is known that calcium effects structure and stability of fibrinogen, additional experiments were done with additional 3 mM $CaCl_2$ in AFM buffer for each of the following experimental conditions.

AFM Experiments at various NaCl Concentrations

The fibrin '$A-a'$ interaction was examined at four concentrations of sodium chloride (NaCl): 0.02 M, 0.15 M, 0.5 M, and 2 M. Concentrations of NaCl higher than 2 M were not investigated because the buffer solution opacity, due to precipitation of buffer components, interfered with ability of AFM to measure deflection. For each NaCl concentration, the solution was buffered with 20 mM HEPES, the pH adjusted to 7.4, and 2 mg/mL BSA and 0.01% Triton X-100 were added. For each NaCl concentration, at least three force volumes were collected. Between experiments, the tip and substrate were rinse with buffer and refilled with new NaCl concentration buffer. The exposure of tip and substrate to air was minimized during this process. The 0.15 M NaCl data point represents the standard operating conditions, in order to assess variations in unfolding and rupture probabilities.

AFM Experiments at various pHs

The fibrin 'A-a' interaction was examined at seven different pH values: 4.5, 5.5, 6.5, 7.4, 8.5, 9.5, 10.5. For each pH, the solution was buffered with 20 mM HEPES and 0.15 M NaCl, and 2 mg/mL BSA and 0.1% Triton X-100 were added. For each experiment, at least three force volumes were collected in each of the buffers in the order of increasing pH (7.4 to 10.5) or decreasing pH (7.4 to 4.5). Increasing and decreasing pH experiments were performed on separate days with fresh substrates and probes. Between experiments, the

tip and substrate were rinse with buffer and refilled with new pH buffer. The exposure of tip and substrate to air was minimized during this process. The pH 7.4 data point represents the standard operating conditions.

AFM Experiments at various Temperatures

The temperature-controlled flow-cell accessory for the AFM (Asylum Research, Santa Barbara, CA) was used to vary the temperature of the buffer (20mM HEPES, 150mM NaCl, 2 mg/mL BSA, and 0.01% Triton X-100, pH 7.4). The temperature controller was used to achieve and maintain temperatures of 27, 32, 37, 42, and 47°C. The system was allowed to equilibrate for at least 20 minutes after each temperature adjustment. Because the increase in temperature caused significant drift in the tip deflection even after equilibration, force volume collection was occasionally paused to re-adjust the deflection.

Fibrin Polymerization Experiments

Plasma fibrinogen, purified using a GPRPAA affinity column in a manner similar to that previously reported for the fibrinogen D fragment,(106) was diluted in AFM buffer to a final concentration of 0.51 mg/mL. Thrombin and batroxobin were diluted to 2 U/mL in HBS, stored on ice, and used within 1 h of preparation. A 0.63 mL volume of the fibrinogen solution was placed into a quartz cuvette and incubated for 5 min in a thermostatically-controlled cuvette holder (Multi Temp III recirculating thermostat, Amersham Bioscience) in a spectrophotometer (Biospec 1601, Shimadzu). Fibrin polymerization was initiated by adding of 0.07 mL of the thrombin or batroxobin solution to the cuvette. The turbidity change at 350 nm was monitored for 30 min. All reactions were performed twice, and the curves presented represent their averages. The lag time was determined as the time between enzyme addition and increase in A_{350} to >0.01. The v_{max} was determined as the maximum slope of the turbidity curve. The final turbidity was the average A_{350} during the last third of the analysis (i.e., 20-30 min).

AFM Data Analysis

Custom MATLAB analysis code described in Section 2.2 was used for data analysis. Then multiple filters were used to identify force curves containing the pattern characteristic of the fibrin 'A-a' bond forced rupture ("characteristic force curve" for brevity).(57) Briefly, 1.) the curve had to consist of two sequential events less than 75 pN different in force magnitude, 2.) the curve could include an event prior to the doublet of events, and 3.) the curve could include an event after the doublet, but this event would need to be greater than 50 pN less than the first event in the doublet. The four force curves considered characteristics of an 'A-a' interaction are thus a curve with just the doublet (events 2 and 3), a curve with the doublet and a preceding event (events 1-3), curve with the doublet and a following event (events 2-4), and curve

with the doublet both preceded and followed by an event (events 1-4). The probabilities that an interaction was characteristic and that a characteristic interaction included event 4 (an event following the doublet) represent the mean and standard deviation of the probabilities for several force volumes. When shown as normalized probability, the probability was calculated so that the area under the histogram equaled one. The numbers generated from each analysis method were averaged over all curve types, weighted by their respective errors.(107) Statistical significance (p-value <0.05) was evaluated with the Student's t-test (two-tailed, type three) against experiments performed in 'standard' conditions (i.e., pH 7.4, 150 mM NaCl, 27°C, with or without 3 mM $CaCl_2$). I also examine the histograms of all forces in a characteristic forced rupture of the 'A-a' bond and the histograms of single rupture event force curves for each of the solutions conditions with and without additional calcium present in the buffer.

2.3.3: Results

Forced unfolding of fibrinogen through the 'A-a' knob-hole interaction has a well-characterized force profile. This pattern was used to detect changes in molecular behavior under force due to changes in environmental conditions. The validity and reproducibility of this method has been documented in detail elsewhere.(57) By performing experiments with a low probability of tip-substrate interactions ($< 15\%$), the likelihood of multiple-molecule interactions is dramatically reduced. Previously performed control experiments verify that the 'A-a' knob-hole interaction is singularly, specifically responsible for the complex rupture patterns observed in Figure 2.4. Stochastic unfolding of fibrinogen molecule and random orientation of surface bound proteins result in the differences in force extension curves.(108) Because it is known that calcium effects structure and stability of fibrinogen,(105) additional experiments were done with additional 3 mM $CaCl_2$ in AFM buffer. Thus, probabilities comparing buffers both with and without calcium, reflect the relative stability of the fibrinogen molecule.

There are two types of interactions that can occur under the constraints of this experiment – characteristic (Figure 2.4 A-D) and non-characteristic interactions (Figure 2.4 E-F). Because competitive inhibition of the 'A-a' interaction, using GPRP, a synthetic knob 'A', eliminated all interactions producing force rupture events in Figure 2.4, all force-extension curves are associated with the 'A-a' interaction.

Among force versus separation curves that resulted in rupture events, multiple rupture event force curves shown in Figure 2.4 A-D characterized the greatest population. Based on their regularity and abundance, this group was classified as the 'characteristic' interaction between desAB-NDSK and fibrinogen. A notable feature of characteristic curves was a doublet of forces $\sim$200 pN in magnitude, separated by $\sim$8 nm. Because the 'A-a' knob-hole interaction was the sole tether connecting the tip and the substrate, the last event in

each force curve is attributed to rupture of this interaction. Preceding force events are the result of step-wise unfolding of the fibrinogen γ module. The unfolding of fibrinogen is signified by an increase in extension and decrease in applied force in the force-extension plots. AFM force-extension curves measure extension of the fibrin molecule due to force applied to the 'A-a' interaction.

Because the unfolding of fibrinogen is a stochastic process, there are a variety of unfolding patterns that could result from force exerted through the 'A-a' knob-hole interaction. The last peak in a force-extension curve always coincides with rupture of the 'A-a' knob-hole interaction. When fibrinogen unfolds in such a way that the 'A-a' interaction maintains through characteristic doublet unfolding, an extra extension event is observed prior to rupture of the 'A-a' interaction. In two of the four characteristic force curves (Figure 2.4 C-D), there exists a lower force peak following the doublet resultant from this additional extension. Because a characteristic force curve may have up to four peaks and this lower force peak is the final event in the force curve, this peak is referred to as event 4.

In addition to characteristic curves, single-event curves (a case that comprises 20±6% of force curves with rupture events at standard solution conditions) can result from the 'A-a' knob-hole interaction. Single rupture events represent instances in which the 'A-a' interaction breaks prior to the unfolding of the γ module of the fibrinogen molecule. Single-event curves provide insight into the strength of the 'A-a' interaction in the fully folded molecule.

Effect of NaCl concentration. To examine the effect of sodium chloride on the forced rupture of the 'A-a' knob-hole interaction, SMFS experiments were performed in buffers with concentrations of NaCl ranging from 0.02-2 M. Figure 2.5 shows the probability that an interaction is characteristic and the probability that a characteristic interaction contains event 4. The probability that an interaction was characteristic of was not significantly varied over the range of NaCl concentration investigated (Figure 2.5 A). On the other hand, the probability that a characteristic interaction included event 4 was inversely proportional to the concentration of NaCl for experiments performed in standard AFM buffer (Figure 2.5 B). However, experiments performed in AFM buffer with additional 3 mM $CaCl_2$ resulted in no significant variation in the probability of event 4 in the characteristic pattern over the range of NaCl concentrations (Figure 2.5 B). There was no consistent trend between the concentration of NaCl in the buffer solution and the probability of an interaction (Figure 2.6). There was no change in the relationship between NaCl concentration and the rupture force data (i.e., the force and relative separation) for characteristic (Figure 2.7) or single event curves.

Effect of pH: To investigate the role of pH on fibrin polymerization at the single-molecule level, the forced rupture of the 'A-a' knob-hole interaction was examined for the pH range of 4-10. Figure 2.5 shows the probability that an interaction is characteristic, and the probability that a characteristic interaction contains event 4 as a function of pH. For experiments performed in standard AFM buffer, the probability that an

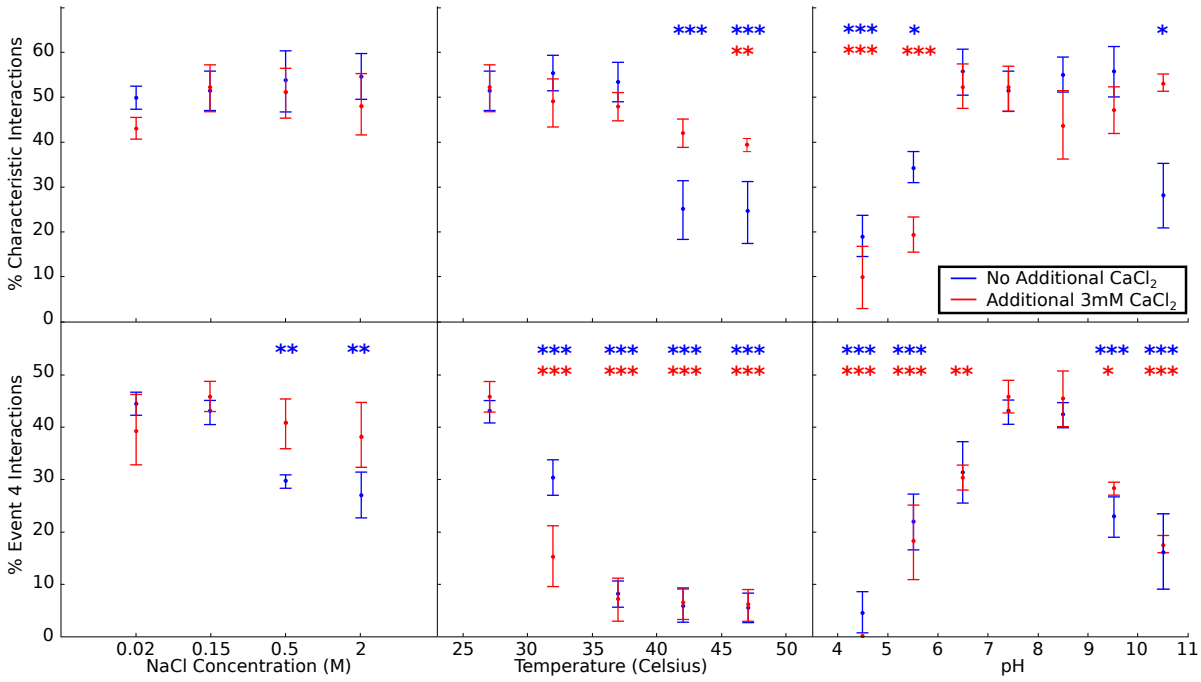

Figure 2.5: Probability that an interaction is characteristic (top row) and a characteristic interaction includes event 4 (bottom row) as a function of NaCl concentration, temperature, and pH. Standard operating conditions are NaCl concentration of 0.15 M, temperature 27°C, and pH 7.4. Asterisks (*,**, ***) represent significance values of p< 0.05, 0.01, 0.001 as determined by the t-test. The asterisk color indicates standard $CaCl_2$ concentration (blue) or the addition of additional 3 mM $CaCl_2$ (red).

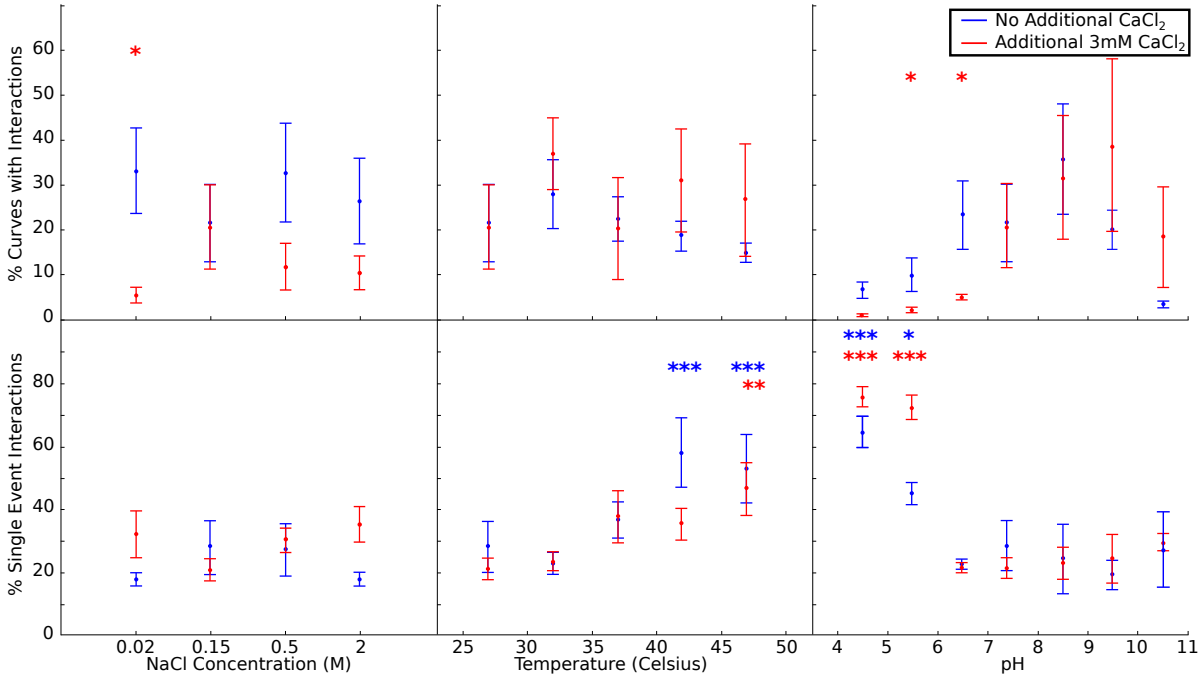

Figure 2.6: Probability that a force curve produces an interaction (top row) and the probability that a force curve produces a single event interaction (bottom row) as a function of NaCl concentration, temperature, and pH. Standard operating conditions are NaCl concentration of 0.15M, temperature 27°C, and pH 7.4. Asterisks (*,**, ***) represent significance values of p< 0.05, 0.01, 0.001 as determined by the t-test. The asterisk color indicates standard $CaCl_2$ concentration (blue) or the addition of additional 3 mM $CaCl_2$ (red).

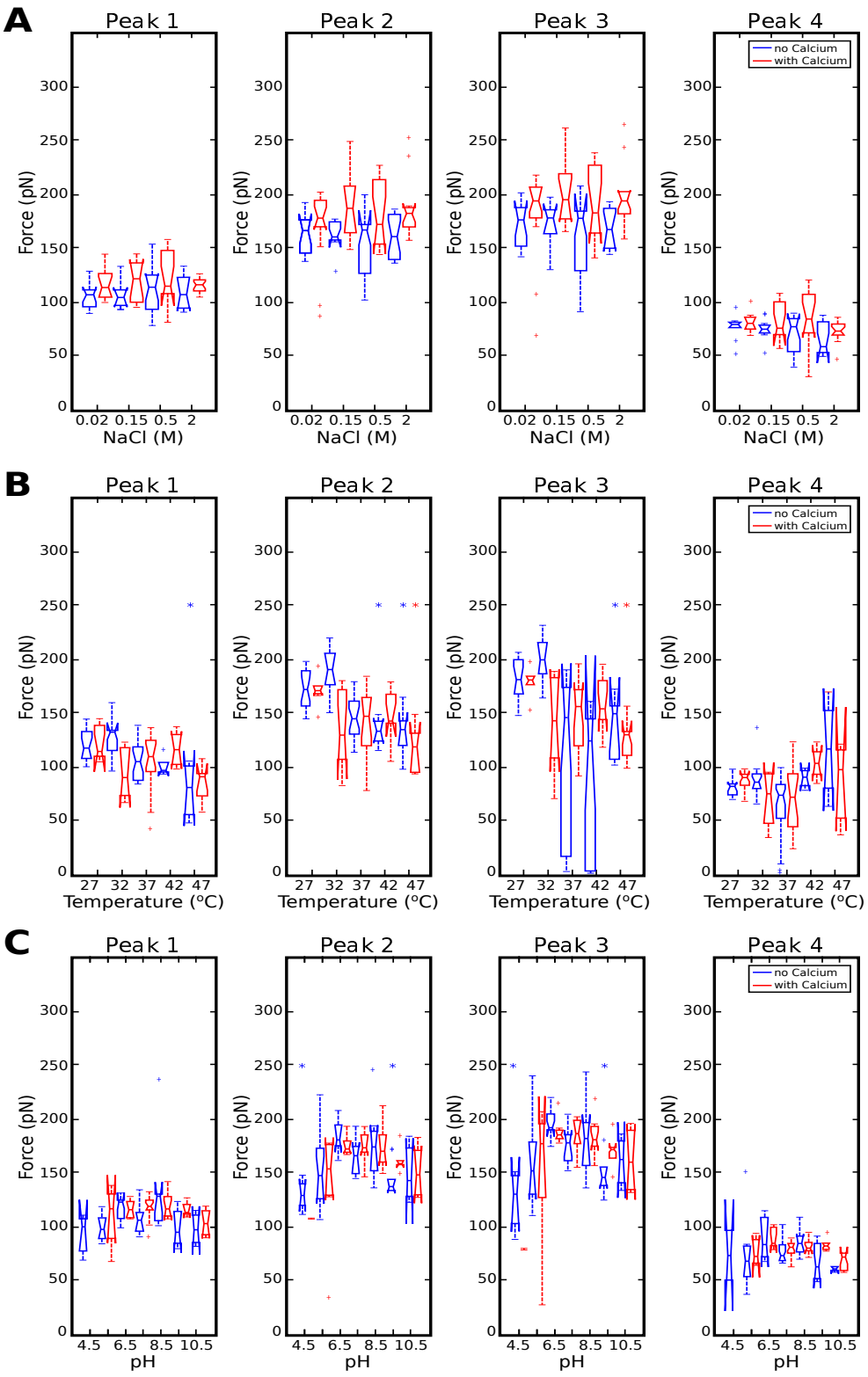

Figure 2.7: Forces for events in characteristic force rupture curves as a function of solution conditions - (A) NaCl concentration, (B) temperature, and (C) pH. Standard operating conditions are NaCl concentration of 0.15M, temperature 27°C, and pH 7.4. Asterisks indicate statistical significance with p-value$<$ 0.05 as determined by the t-test. The asterisk color indicates standard $CaCl_2$ concentration (blue) or the addition of additional 3 mM $CaCl_2$ (red).

interaction is characteristic was constant except for low pH of 5.5 and 4.4, at which time the probability significantly decreased. Of note, experiments performed in 3 mM $CaCl_2$ AFM buffer had a greater decrease in the probability of an interaction being characteristic between standard solution conditions and pH 5.5. The probability that a characteristic interaction contained event 4 significantly decreased as the solutions became more acidic or basic. For experiments performed in AFM buffer with additional 3 mM $CaCl_2$, the rate of decrease was more rapid in the acidic pH range. Comparing experiments performed in the two buffer solutions for high pH, the additional calcium resulted in a less dramatic decrease in the probability of the presence of event 4 in the characteristic curve for pH increasing above 8.5. For all experiments, the number of interactions decreased for any deviation in pH from 7.4 (except pH 8.5 without calcium which remained similar). This decrease in the number of interactions was most dramatic for pH 4.5, 5.5, and 10.5. Here the probability of an interaction was increased by the addition of calcium, still less than 5% of force curves had an interaction. There was no change in the relationship between pH and rupture force data (i.e., the force and relative separation of rupture events) for force rupture events in characteristic force curves (Figure 2.7). The dramatic decrease in the number of interaction, makes it difficult to distinguish a trend for low (4.5) and high (10.5) pH.

Effect of temperature. To explore the influence of temperature on the forced unfolding of the 'A-a' knob-hole interaction, single-molecule experiments were performed in buffer held at temperatures between 27-47°C. The probability that an interaction was characteristic and the probability that a characteristic interaction contains event 4, as a function of temperature, are shown in Figure 2.5. The probability that an interaction was characteristic in AFM buffer with 3 mM $CaCl_2$ did not significantly change over the temperature range; however, in AFM buffer without additional calcium present, the probability significantly decrease for high temperatures (42, 47°C). The probability that a characteristic interaction contained event 4 was inversely related to temperature. In both buffers, the probability a characteristic force curve contained event 4 was significantly lower for temperatures above 27°C. The number of interactions varied little over the temperature range, but noticeable decrease in rupture forces associated with increasing temperature was observed (Figure 2.7).

Because fibrin polymerization had not previously been reported for temperatures above 37°C, turbidity as a indicator of fibrin polymerization induced by either batroxobin or thrombin was investigated by Laurel Averett at three temperatures: 27, 37, and 47°C. The lag time, ν_{max}, and A_{350} for both thrombin- and batroxobin-catalyzed fibrin polymerization at 27, 37, and 47°C are shown in Table 2.1. For thrombin-catalyzed clots, the relationship between temperature and fibrin polymerization was complex (Figure 2.8A). The final turbidity of the clot was greatest when fibrin was polymerized at 47°C but not different between 27 and 37°C. Like turbidity, the ν_{max} was similar between 27 and 37°C, but was slower at 47°C. The lag

time was directly related to the temperature of polymerization. The batroxobin-catalyzed polymerization results were more straightforward (Figure 2.8B). The lag time and final turbidity were both inversely related to temperature. However, the ν_{max} increased when increasing the temperature from 27 to 37°C but was the same for both 37 and 47°C.

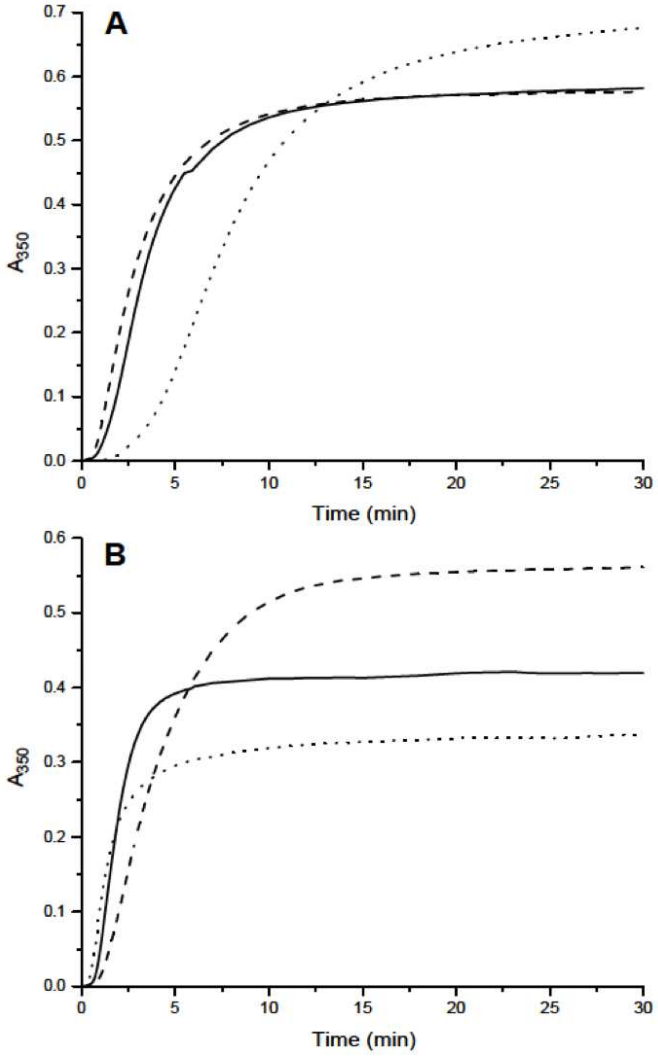

Figure 2.8: Absorbance at 350 nm as a function of time and temperature for fibrin polymerization. Figure polymerization was catalyzed by (A) thrombin and (B) batroxobin. The polymerization was investigated at three temperatures: 27°C (dashed line), 37°C (solid line), and 47°C (dotted line). Figure from Laurel Averett's thesis used with consent. (1)

2.3.4: Discussion

Each of the solution conditions investigated (i.e., NaCl, pH, temperature) has known effects on protein stability and structure, and fibrin polymerization. By examining the effect of these parameters on the

	Temperature (°C)	**Lag time (min)**	ν_{max}**(min**$^{-1}$**)**	$\mathbf{A}_{350}$
Thrombin	27	0.5	0.2	0.57
	37	0.7	0.2	0.57
	47	0.9	0.1	0.66
Batroxobin	27	0.9	0.1	0.56
	37	0.6	0.2	0.42
	47	0.4	0.2	0.33

Table 2.1: Parameters of fibrin polymerization as a function of temperature and enzyme. Table from Laurel Averett's thesis used with consent.(1)

forced rupture of the 'A-a' interaction, I draw connections between the structural stability of the fibrinogen molecule and the 'A-a' interaction, and the 'A-a' interaction and fibrin polymerization. The rupture pattern characteristic of the forced dissociation of the 'A-a' interaction serves as a tool for understanding the effects of solution conditions on the structure and function of the area surrounding hole 'a'. If the manner in which the knob-hole interaction reacts to force is altered, the probability that the interaction is characteristic (i.e., contains a doublet of events) will be reduced. If the hole is destabilized but not structurally changed, as in the case with the effects of calcium on the 'A-a' bond,(105) the probability that a characteristic interaction contains event 4 will decrease. Additionally, if the 'A-a' knob-hole interaction is weakened, then the rupture event curves will show a decrease in rupture force. The nature of changes to the structure and function of the 'A-a' interaction can thus be deducted from the observation of two parameters: 1) the probability that an interaction is characteristic and 2) the probability that a characteristic interaction contains event 4. To a lesser extent, insight can be gleaned from trends in the force rupture event parameters.

The manner in which the knob-hole interaction reacts to changes in solution conditions can be monitored by the probability that an interaction is characteristic of the 'A-a' knob-hole interaction. The step wise extension of fibrinogen by force applied to fibrinogen's hole 'a' through bound knob 'A' indicates that the 'A-a' interaction is sufficiently stable under tension to allow unfolding of γ module. Of the parameters investigated, only low pH (i.e., pH $\leq$ 5.5) and high temperature (i.e., temperature $>$ 42°C) resulted in a decreased probability that an interaction was characteristic of 'A-a' knob-hole interaction. Less efficient 'A-a' binding may be the result of changes to the structure of the γ module near hole 'a' due to these solution conditions.

Low pH likely affects the effectiveness of 'A-a' binding by protonation of histidine residues in the γ module of fibrinogen. Histidine (pKa of 6) is the only amino acid with a pKa in the range of pH examined and one of the critical residues in hole 'a' involved in hydrogen-bonding with the knob, γH340 (Figure 2.9B). Polar contacts are lost at low pH due to protonation of histidine which disrupts hydrogen-bonding interactions with knob 'A'. Additionally, there are three histidine residues in the core of the γ module near hole 'a'

(Figure 2.9A). At lower pH, protonation of histidine groups effectively increases the net charge density. The collection of positively charged groups may create repulsive electrostatic forces, destabilizing the structure of hole 'a' or preventing the knob from entering the pocket. Fibrinogen is known to have an additional high affinity calcium-binding site at high pH (i.e., pH > 7.4).(109) The force stabilizing role of this calcium binding site on hole 'a' is evidenced by the higher occurrence of characteristic interactions in additional calcium buffer for high pH (i.e., pH of 9.5, 10.5) solution environments (Figure 2.5).

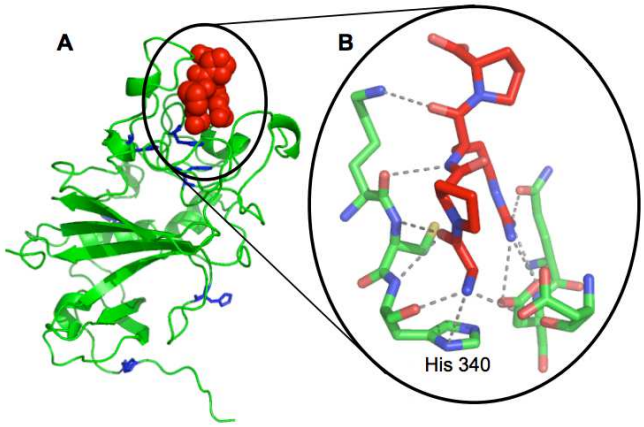

Figure 2.9: (A) Structure of γ module (ribbon) with bound GPRP peptide (spheres), with histidine residues are shown in blue. (B) Region of interest shows magnification of hole 'a' with GPRP peptide, where all components are displayed as sticks and polar contacts are dashed lines. Figure created from PDB-ID 1LTJ using Pymol and modified from Averett thesis.(1)

The effectiveness of 'A-a' binding is reflected in not only the decrease in the characteristic interactions for high temperature experiments. The melting temperature of the fibrinogen D region containing the γ module and hole 'a' is between 45-55°C when destabilized by altered pH (e.g., pH 3.5 or 8.5).(110). Therefore, it is reasonable for high temperatures (i.e., 42, 47°C) that the γ module is partially denatured. Partial denaturation near hole 'a' would result in an inefficiently bound knob 'A'. Small amounts of calcium have been shown to provide protection of fibrinogen against moderate denaturation by heat.(111) Therefore additional calcium present in buffer solution, results in stabilization of the γ module against denaturation and 'A-a' interaction rupture for high temperatures. Additionally, the effectiveness of 'A-a' binding is reflected in the number of interactions for high temperature experiments. The percentage of interactions obtained during a force map is dependent on the number of molecules in region sampled, as well as the number molecules with the stability to produce interactions above threshold filtering parameters.

The interaction strength of the 'A-a' interaction as a function of solution conditions can be monitored with the rupture force of the characteristic double unfolding events. Because this doublet of events represents instances in which the maximum force is exerted on the knob-hole interaction prior to rupture, this can be

used to detect changes in the interaction strength of the 'A-a' interaction. Though there is a significant decrease in the probability of characteristic interactions, the rupture forces of the characteristic doublet events decrease for both low pH (i.e., pH $\leq$ 5.5) and high temperature (i.e., temperature $>$ 42°C). Future work should be done to investigate the change in rupture force of single rupture event force curves to supplement characteristic force rupture data as this could be a direct measure of the interaction of the 'A-a' interaction. Because single rupture events represent instances in which the knob-hole interaction ruptured prior to unfolding of the structure of the fibrinogen molecule, single event curves can be used to detect changes in the interaction strength of the 'A-a' interaction. However, this measurement value can also be populated by nonspecific interactions in which knob 'A' may not have associated with hole 'a', possibly providing further insight into structural stability of the hole region.

Solution conditions that resulted in a decreased probability that an interaction was characteristics are also solution conditions that have an effect on fibrin polymerization and final clot stability. Unligated fibrin clots have been reported to dissolve at both low pH (i.e., pH $\leq$ 3.5) and high temperature (i.e., >42°C at pH 5).(112; 113; 114) Additionally, viscosity measurements and ultracentrifugal experiments show no clot formation when fibrinogen incubated with thrombin at pH 5.(113) It is known that the 'A-a' interaction is critical to the stability to fibrin clots because addition of GPRP (the peptide that competes with knob 'A' for the fibrin hole 'a') to an unligated clot can lead to dissolution. The central role of the 'A-a' knob-hole interaction in fibrin polymerization and stability suggests that conditions that inhibit clot formation and dissolve clots do so by affecting the knob-hole interaction. That this disruption is detectible by a mechanical technique suggests that the mechanical properties of the 'A-a' interaction (i.e., the ability of the knob-hole interaction to withstand extensions of the fibrin monomer) are critical to fibrin clot formation.

The stability of hole 'a' as a function of solution conditions can be monitored by the probability that a characteristic interaction will contain event 4. The final event of characteristic 'A-a' unfolding can occur either at the final event in the doublet or at event 4. The degree of extension of the γ module prior to the rupture of the 'A-a' interaction is greater when rupture occurs at event 4, thus a decrease in the probability of event 4 is reflective of a destabilization but not structurally changed hole. As shown in Figure 2.5, the probability that a characteristic interaction ruptures in event 4 is affected by every solution conditioned examined including pH, temperature, and NaCl. This indicates that perturbations to the solution environment decrease the ability of hole 'a' to maintain its structural integrity under tension. The probability of event 4 occurring is highest at concentrations of NaCl and temperatures below the physiological range (i.e., 0.02 M NaCl and 27°C). Additional calcium present in the AFM buffer only produced a significant variation in the probability of event 4 for high NaCl concentrations (Figure 2.5). Calcium has been shown to provide protection of fibrinogen against moderate denaturation by alkali.(111) The presence of additional

calcium in the buffer and thus in these binding sites could contribute to the increased probability of event 4 in the characteristic pattern compared to experiments run in standard AFM buffer.

Because limited data exists regarding fibrin polymerization at elevated temperatures, we sought to fill this gap by examining both thrombin- and batroxobin-catalyzed fibrin polymerization over the temperature range of 27-47°C. Thrombin cleaves both fibrinopeptide A and fibrinopeptide B, where as batroxobin cleaves only fibrinopeptide A. Therefore, thrombin-catalyzed polymerization is more complex than batroxobin as both knob 'A' and knob 'B' are exposed, and more of the αC domains are liberated from their association with the fibrin E region. In contrast, batroxobin-catalyzed polymerization is more dependent on the 'A-a' knob-hole interactions. The effect of temperature on fibrin polymerization was different for each of the enzymes. For thrombin, the effects of temperature on the ν_{max}, and lag time indicates that temperature slows protofibril formation. In addition, the final turbidity was not different between 27 and 37°C, but was higher at 47°C, suggesting that temperatures above physiological parameters enhance lateral aggregation, leading to thicker fibers. Enhanced lateral aggregation may be attributed to either greater efficiency in the interactions normally responsible for lateral aggregation, or partial denaturation of fibrin monomers, causing nonspecific adhesion between protofibrils and fibers. These results agree with previous work that reported the mass-to-length ratio of fibrin fibers was unchanged from 24-37°C.(99) When batroxobin was used to catalyze fibrin polymerization, protofibril formation was enhanced and lateral aggregation suppressed by temperature. The source of the discrepancy between these results is not immediately clear, and is likely attributable to several factors including the presence of fibrinopeptide B, availability of αC domain, temperature dependence of enzymatic efficiency, and/or bond formation kinetics. The activity of each enzyme is indeed temperature-dependent. As such, it is impossible to deconvolute the temperature-dependencies of the enzyme and the 'A-a' interaction. Examining clot formation via turbidity made the distinction between both polymerization steps (i.e., fibrinopeptide cleavage, protofibril formation, and lateral aggregation) and clot morphology (i.e., degree of branching, porosity, and fiber thickness) equally difficult.

Solution conditions that caused a decrease in the probability of the characteristic pattern containing event 4, indicative of destabilization of hole 'a', correlated with conditions associated with decreased asymptotic final turbidity.(95; 100) Because turbidity has been related to fiber thickness,(115) conditions suppressing thick fibers also reduce the ability of the γ module to achieve extended lengths associated with event 4 prior to 'A-a' knob-hole rupture. One possible explanation for this correlation is the hypothesis posted by Weisel et al.(116) Because monomers in fibrin fibers are twisted structures in register, the fibrin molecules on the outer portions of a fiber must be longer than those in the center. The possible difference in length of fibrin monomers therefore is a limiting factor in the diameter of fibers. Because the fibrin monomer extends 17 nm between the last event in the doublet and event 4, this added length might contribute to the upper limit of

fibrin fiber diameter. It should be noted that electron microscopy studies of fibrin fibers formed at a variety of conditions suggest that high-turbidity clots have bundled groups of fibers of normal thickness versus large fibers.(116) The role of such fiber bundles is unclear. Furthermore, the thickness of fibers and turbidity are also affected by the amount of fiber branching, a parameter that remains poorly understood.(117; 65; 116)

In conclusion, the relationship between solution environment and the single-molecule mechanics of fibrin interactions was explored. SMFS experiments are sensitive enough to detect changes in behavior under force due to solution conditions and can be used as a metric for understanding protein function. A correlation was established between conditions that suppress the forced dissociation characteristic of the 'A-a' knob-hole interaction and those that have been previously reported to inhibit fibrin polymerization (i.e., high temperatures and acidic pH). This was further supported by changes in knob-hole interaction strength at these solution conditions. In addition, a relationship was found between solution conditions that caused a decrease in the probability of a characteristic 'A-a' interaction contained event 4 and those associated with thin fibers in fibrin clots. Additional calcium ions in buffer effected both metrics of 'A-a' interaction stability, indicating that different calcium binding sites instabilities in the knob-hole interaction.

Section 2.4: Intermediate Unfolding Domains Revealed by Constant-Force Fibrin Unfolding

2.4.1: Introduction

Single-molecule unfolding experiments have provided a wealth of information about the mechanical properties of biomolecules, protein unraveling pathways, and characterization of the change in functional states of proteins under load.(118) Specifically, SMFS fibrin experiments have shown a complex rupture pattern associated with the unfolding of subdomains. These experiments were performed by retracting the AFM tip away from the substrate at a constant velocity creating a complex, sawtoothed force-rupture pattern. During this process the force applied to the tip-protein interaction changes dramatically over 100s of piconewtons, which has the following drawbacks: (1) it creates a complex and indirect relationship between force applied and unfolding kinetics, and (2) due to the timescale of unfolding, low force and low probability unfolding events can be missed.

Mechanical unfolding of proteins, similar to bond rupture, is a force-dependent process;(119; 120) therefore, it is desirable to probe the mechanical unfolding of proteins as a direct function of applied force. This is accomplished using a more recent SMFS technique, 'force-clamp' spectroscopy. In force-clamp spectroscopy, the AFM tip is retracted from the sample at a rate that varies in order to maintain a constant stretching force applied to the protein. This produces a stepwise extension of the protein, in which the separation-time trace will exhibit a series of plateaus. The length of each plateau is the lifetime of a molecular conformation

and varies between force curves due to the stochastic nature of molecular unfolding. By applying controlled forces to reduce the energy barrier (Figure 2.10), force-clamp facilitates a direct relationship between force and unfolding kinetics.

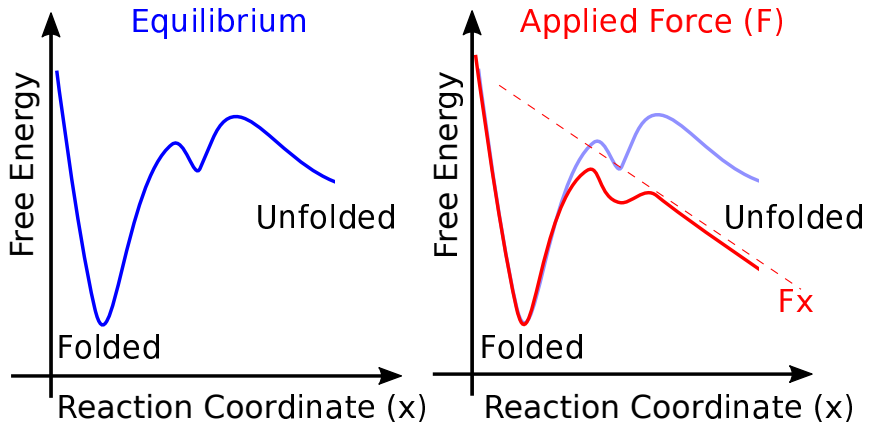

Figure 2.10: Energy landscape along a molecular reaction coordinate under force. The magnitude of the pulling force affects the height of the energy barrier that must be overcome in the transition from folded to unfolded state by tilting the energy landscape by F·x. This exemplifies the convenience of force-clamp mode, where the energy landscape can be controlled experimentally.

An additional benefit of force-clamp is the ability to probe intermediate unfolding events unobservable with the constant-velocity method. A mechanical force of just a few tens of piconewtons is sufficient to trigger the unfolding and extension of a protein;(87) therefore, due to the rapid change in applied force in constant-velocity experiments, lower force and lower probability unfolding events are missed. Force-clamp spectroscopy allows for low forces to be applied for long time periods so the stochastic nature of protein unfolding due to applied force, previously unobserved with other spectroscopy techniques, can be measured.

In this section, I probed 'A-a' forced unfolding through the use of force-clamp spectroscopy. Constant-force unfolding separation-time trace characteristic of γ module unfolding and intermediate unfolding configurations inaccessible by previous constant-velocity experiments were identified. The subdomains involved in experimentally observed unfolding events and the particular residues responsible for mechanical behavior of fibrin were determined with the aid of molecular dynamics simulations. The direct relationship between fibrin unfolding kinetics and applied force were explored with experiment and Monte Carlo simulations. The differences between parameters determined from force-clamp and constant-velocity experiments reveal the complexity in the relationship between the bond free energy profile and force. These experiments are precursors to measuring the refolding of fibrin while under tension in a technique referred to as 'force-quench'. Preliminary force-quench experiments indicate the fibrin γ module may play a role in reversible extensibility observed in fibrin clots.

2.4.2: Methods

Following the methods presented in Section 2.2, proteins were covalently attached to the gold coated AFM cantilever and glass substrate such that the fibrinogen holes 'a' were on the surface and the knobs 'A' were on the AFM tip as shown in Figure 2.3. Concentrations of proteins were sufficiently sparse to ensure measurement of only single-molecule interactions.

Force-clamp experiments are setup to maintain constant deflection of the cantilever, i.e. constant force applied to the single-molecule interaction. In order to accomplish this, the piezoelectric actuator (z-piezo in Figure 1.5) is constantly being adjusted to maintain the deflection of the cantilever, as the molecule is reoriented, stretched or bonds break.

Stretching fibrinogen under force-clamp conditions produced a staircase-like elongation of the protein as shown in Figure 2.11. In a typical experiment, the AFM tip was brought into contact with the substrate to promote a knob-hole interaction. Then the tip was moved away from the surface at a constant speed until a predefined pulling force (also called trigger force) was reached. The first step in a force-clamp curve is associated with lifting and reorienting of fibrinogen. The force is held constant by adjusting the z-piezo length to maintain deflection of the cantilever, until a bond in the protein breaks allowing a portion of the protein to unfold increasing the length of the protein and reducing the amount of force applied to AFM tip. This will trigger a readjustment of the piezoelectric actuator such that the protein is extended to an increased length to keep the pulling force constant. This process is repeated until the final interaction, the 'A-a' knob-hole interaction, holding the tip to the substrate is ruptured at which point the cantilever retracts from the surface and the cantilever returns to a relaxed position (zero force). The external feedback maintains a force set point throughout the experiment ($\sim$30 s) and position resolution was less than 0.5 nm.

Intermediate Steps Data Analysis

The length of each step is the lifetime of a given configuration of fibrinogen. The height of each step, following the first, corresponds to the increase in length marked by unfolding of a portion of fibrin's γ module.

In order to efficiently collect enough data on fibrin unfolding at different forces, I created an analysis pipeline to take force-clamp data and determine the start and end of steps in the separation-time curve. This analysis package is discussed in detail in Appendix A; briefly, the code reads in IGOR binary wave (ibw) files output by software used to acquire AFM data into MATLAB and uses a trapezoidal filter to identify inflection points in the separation-time curve corresponding to the start or end of an extension step. From these data points, relevant parameters such as step height, total extension, and lifetime can be calculated and compared for different clamping forces.

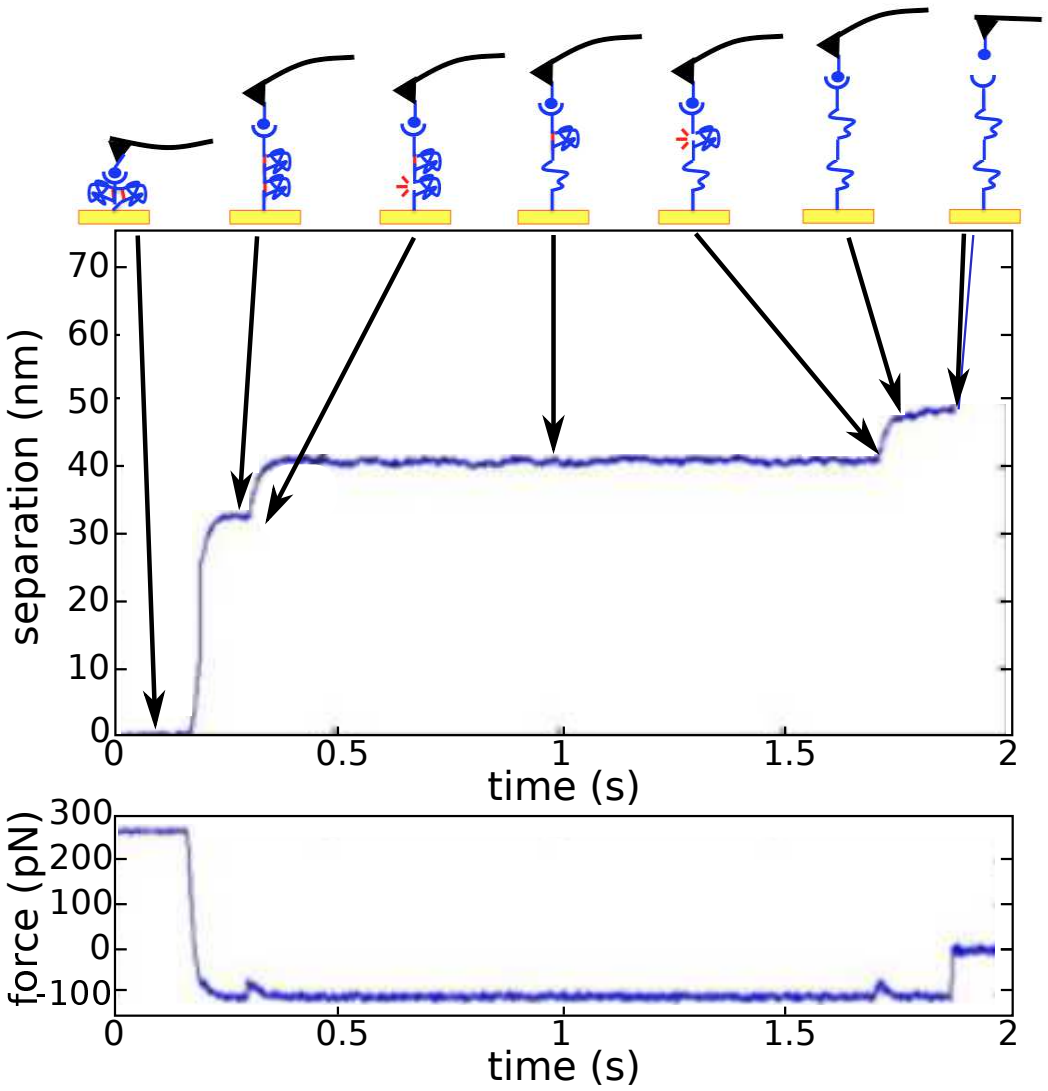

Figure 2.11: Interpreting force-clamp experiment results. A typical separation versus time recording (top trace) obtained by stretching fibrinogen through the 'A-a' knob-hole interaction at a constant force of 100 pN. The force applied to the AFM tip during this force-clamp pull is represented as force versus time (bottom trace). A cartoon illustrating the extension of a protein in a typical force-clamp experiment is shown above the data, where the final event is full rupture of the knob hole interaction.

Additional criteria to qualify force curves for further analysis include (1) extension step(s) following the first must occur in order to measure unfolding, (2) step height must be greater than 1nm to identify step above baseline noise, and (3) extension steps must occur 10nm from substrate to exclude activity associated with nonspecific near-surface events. A typical force-clamp data set consists of 300-500 force curves.

Analysis of Unfolding Kinetics

Although all fibrinogen molecules experienced the same external force, the time evolution of unfolding varied for each case due to the stochastic nature of protein unfolding. Because all force-clamp experiments were unfolding the same region of fibrinogen and the ergodic theorem states, given a sufficient time a single-molecule in equilibrium will visit conformations in the same proportion as a molecular ensemble in any given moment of time, the extension-time plot for each protein can be treated as a percentage of unfolding curve for the given molecule.(121) So the probability of a fibrin γ module unfolding at a given force was obtained by first normalizing each extension-time trace. For all curves, the tip-substrate separation is characterized by two key data points: (1) the point at which the trigger force is first experienced, where the fibrin molecule is fully lifted from the surface and still folded, and (2) the final tip-substrate separation prior to knob-hole rupture and loss of force application. These separations are assigned percentage of unfolding values of 0 and 1, respectively, and all separations between these two data points receive corresponding percentages between 0 and 1. At times following the knob-hole rupture, the percentage of unfolding for that molecule was assigned the value of 1 because all unfolding that could be measured had already occurred. Only force curves with an overabundance of events (>6) were removed from the average. Then all normalized separation-time traces are averaged to produce the probability of unfolding for the ensemble of fibrin molecules sampled. This result is often referred to as the normalized ensemble average (NEA).(121) Over 100 separation-time curves were averaged to produce the NEA at each force.

Additionally, these results were compared to simple Monte Carlo models for different unfolding patterns. This is discussed in detail in Appendix C.

2.4.3: Results and Discussion

Fingerprint of 'A-a' Forced Unfolding of Fibrin

In previously performed constant-velocity SMFS experiments,(57; 79) fibrin γ module unfolding was characterized by a precise 2-4 peak force-extension rupture pattern (Figure 2.2A). The two higher force rupture peaks are the defining feature present in all variations of the 'A-a' forced rupture pattern.

In force-clamp experiments, the characteristic two peak rupture exhibits as a series of plateaus. The

average rupture forces of events in constant-velocity experiments were used to inform the identification of constant-force fibrin unfolding events. Application of a constant pulling force of 150 pN, a force larger than constant-velocity peaks 1 and 4 but lower than characteristic peaks 2 and 3, to the knob-hole interaction yields force-clamp steps corresponding to the high force doublet events (Figure 2.12). Typical force data of fibrin unfolding in response to a constant force is shown in Figure 2.13. The upper trace shows the stepwise increase protein length as fibrin's γ module unfolds. The lower trace shows the time course of force applied to the AFM tip, which is constant at either 150 pN or 0 pN punctuated by transient deviations due to the finite response time of the system feedback to extension and force drop of each unfolding event.

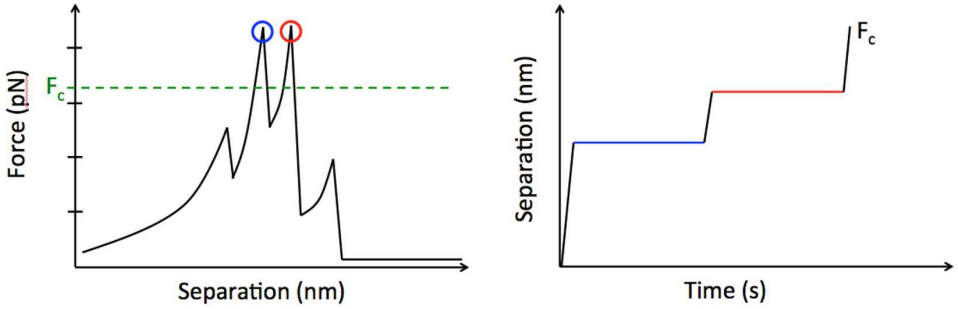

Figure 2.12: Constant pulling force selected from constant-velocity SMFS results. Illustration of characteristic 'A-a' fibrin unfolding produced by (left) constant-velocity experiment displayed as force versus separation trace and (right) force-clamp experiment displayed separation versus time trace. The hypothetical clamping force (F_C) for used to produce the force-clamp trace is shown in the force-separation trace as a dashed green line. Each plateau represents a mechanically stable conformation associated with an event in the characteristic pattern (as indicated by color), and the rise between the plateaus represents the increase in molecular length between the mechanically stable conformations.

A collection of several force-clamp fibrin-unfolding traces is shown in Figure 2.14. Although the knob-hole interaction was subjected to the same 150 pN constant pulling force, the initial step height varies dramatically between curves. This variation was likely due to the random attachment of proteins to the tip and substrate, and was on the order of the combined length of fibrinogen and the desAB-NDSK fragment ($\sim$45 nm and $\sim$10 nm in crystal structures, respectively). This dimension suggests that the fibrinogen was immobilized such that most of the molecule was available to extend in attempts exhibiting the characteristic step pattern. Similar variation in the tip-substrate separation was seen in previous constant-velocity rupture patterns.(57) Because the first step in a separation-time curve gives no insight into extension/unfolding of fibrinogen, all further extensions plots will be shown relative to the first plateau unless otherwise stated.

Due to the sparse amount of protein attached to the substrates' surfaces, the overwhelming majority of extension curves acquired at 150 pN clamping force did not reach the trigger force because a knob-hole interaction did not occur. Of those curves that did reach the trigger force, approximately half did not have

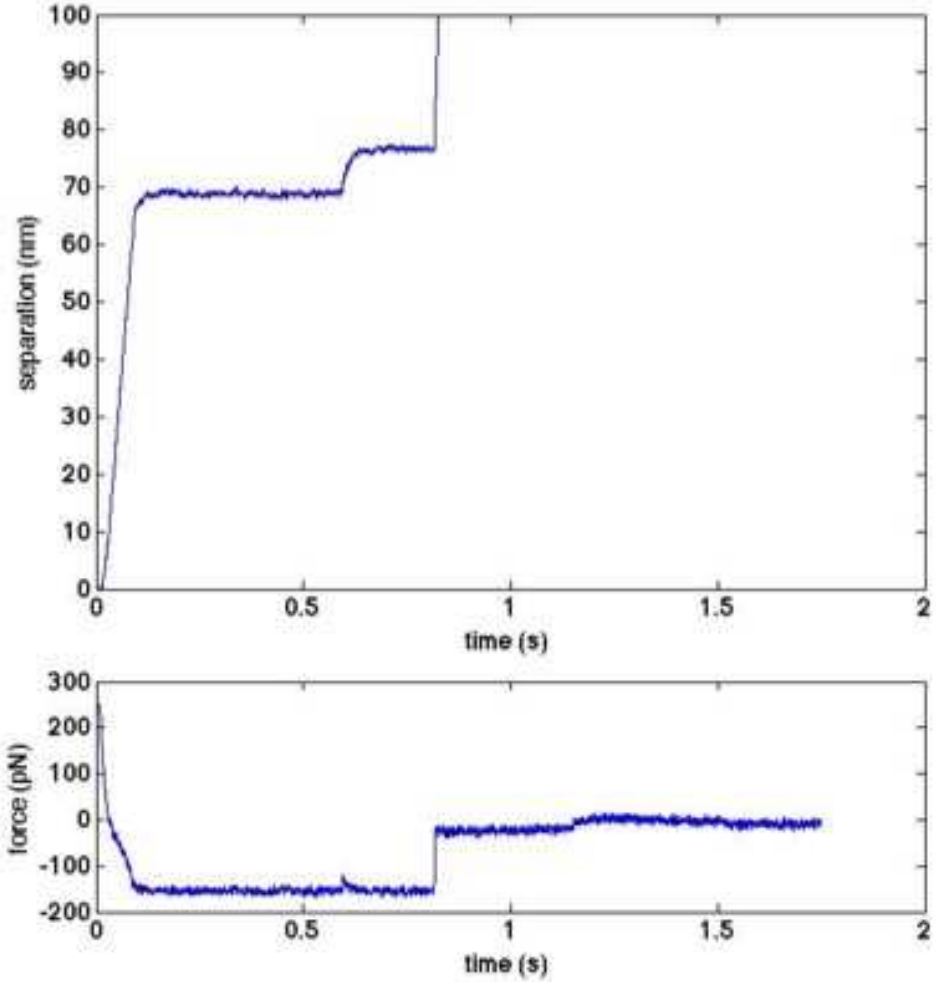

Figure 2.13: Fingerprint of 150 pN constant-force 'A-a' unfolding of fibrin. (Top) Separation versus time and (bottom) force versus time for a typical 150 pN force-clamp recording of fibrinogen unfolding. The step noise level in the separation-time plot above is 0.49 and 1.01 nm for the standard deviation and range, respectively. The force applied to fibrin during these steps is 154.49 ± 4.79 pN. Each step had over 100 data points and reported average and standard deviation are calculated from 1280 data points equivalent to 0.64 s.

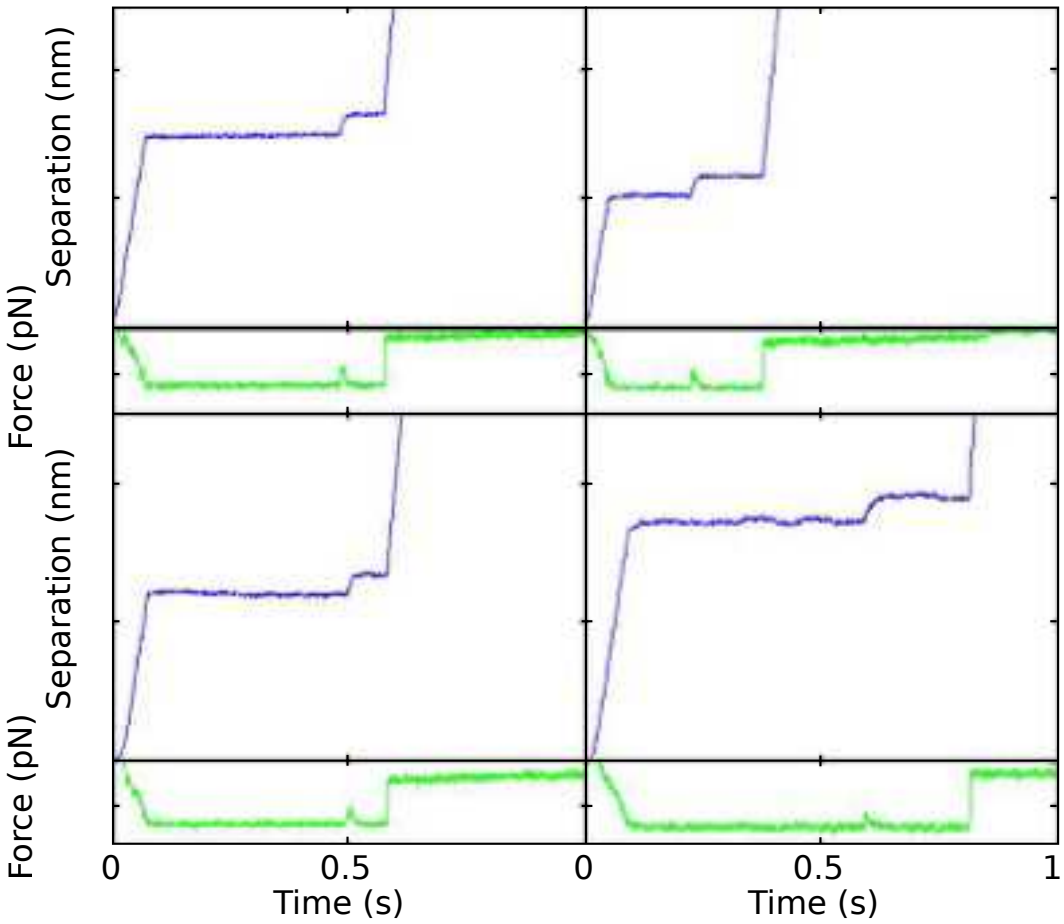

Figure 2.14: Variations in characteristic 150 pN constant-force 'A-a' unfolding of fibrin. Multiple sample force-clamp curves for different fibrinogen molecules taken with a 150 pN pulling force. The blue curves show separation versus time and the green curves show the corresponding force versus time plots for characteristic fibrinogen unfolding through the 'A-a' knob-hole interaction.

extension steps. Single plateau events are likely due to nonspecific or suboptimal binding of knob 'A' into hole 'a'. Curves lacking an extension step provide no insight into the unfolding of fibrinogen; therefore, only force-clamp curves with extension steps will be considered in all further analysis.

Force-clamp data acquired at 150 pN plotted relative to the first step in the separation-time curve exhibit a clear, repeatable single step height (Figure 2.15). The most probable step height was determined by fitting a Guassian model to a histogram of step heights where the uncertainty reported represents the half-widths of the Gaussian fit. This is an acceptable first approximation to describe a real-valued random variable that clusters around a single mean. The step height of this extension step, as found from a Gaussian fit to 122 curves that exhibit a single extension step, was 6.6 $\pm$ 1.1 nm (Figure 2.16). Another basic observation on the unfolding of fibrin under constant force, is that each unfolding plateau lifetime varies curve-to-curve as expected for stochastic unfolding.

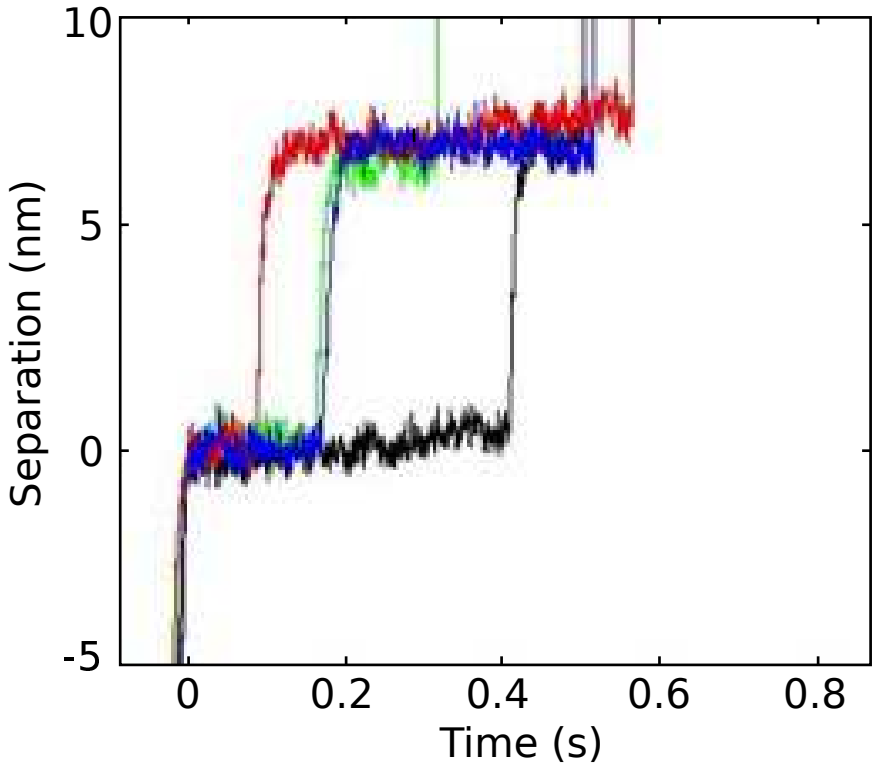

Figure 2.15: Repeatable 6.6 nm extension step characteristic of 150 pN constant-force fibrin 'A-a' unfolding. Plots of several separation-time curves at a constant pulling force of 150 pN. All force curves exhibit an ~6.6 nm extension step; however, they each have different lifetimes for each step. The curves have been modified such that the first steps all have the same value in order to emphasize the reproducibility of the extension step.

The method of immobilizing proteins to the tip and substrate in this experiment allowed force to be applied to a single-molecule 'A-a' knob-hole interaction. A series of control experiments for this protein

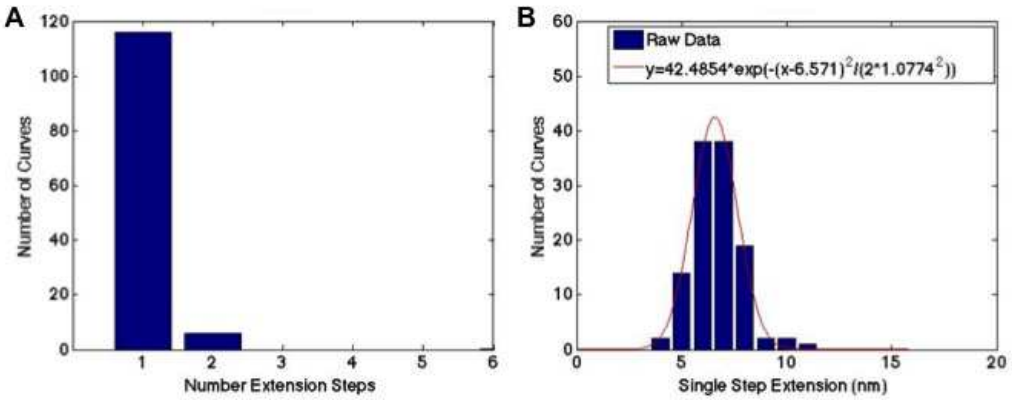

Figure 2.16: Constant-force fibrin unfolding at 150 pN is characterized by a single extension step of ∼6.6 nm. For a data set of force-clamp curves (n=363) acquired at a constant pulling force of 150 pN, the curves with extension steps are dominated by single-step curves as shown in (A) the plot of number of curves with a certain number of extension steps. (B) A histogram of the step height of each single extension step curve shows a clear peak at 6.57 ± 1.08 nm when fit by a Gaussian.

attachment method has been conducted with constant-velocity force spectroscopy to show that the force applied to the 'A-a' interaction does in fact unfold the γ module of fibrinogen.(57) If desired to further prove the reliability of the force-clamp technique and identification of the 'A-a' unfolding fingerprint, several control experiments could be performed.

1. The first control experiment should confirm 'A-a' interactions are responsible for the ∼7 nm extension step. This is accomplished by adding the GPRP peptide, a synthetic knob 'A', to the buffer that binds to the fibrin hole 'a'. After a few minute incubation to allow GPRP to bind to the active holes 'a' of fibrinogen on the substrate, the interactions between desAB-NDSK on the AFM tip and fibrinogen on the surface should be reduced by a significant percentage if the observed extensions are specifically due to the 'A-a' interaction.

2. Another control experiment would be to show that the extension is indeed due to γ module unfolding and not unfolding of another portion of the fibrinogen molecule. This can be accomplished by attaching the D fragment of fibrinogen, which contains only the γ module and a very small portion of the coiled-coil region, to the substrate and performing the same experiment. This controls should produce force-clamp curves with the same extension step as the original fibrinogen experiments.

3. Further verification that this interaction is indeed fibrinogen γ module unfolding can be obtained by performing experiments with BSA attached to the substrate and desAB-NDSK on the AFM tip or conversely, BSA on the tip and fibrinogen on the substrate to produce nonspecific interactions.

These experiments were not performed due to their redundancy with previous constant-velocity single-

molecule fibrin experiments.(57) Building on work performed by Averett et al., I was confident that all interactions measured between the tip and substrate seen in force-clamp data were the result of 'A-a' knob-hole interactions between fibrinogen and desAB-NDSK. Additionally, any steps following the first in separation-time traces were associated with extension of the γ module. Therefore, I concluded that the single 6.6 nm extension step observed in force-clamp spectroscopy experiments at 150 pN was due to unfolding of fibrinogen's γ module through force applied to the 'A-a' knob-hole interaction.

Comparison to Constant-Velocity Unfolding Experiments

Constant-velocity fibrin unfolding produced a distinctive force-extension curve of 2-4 rupture events as shown in Figure 2.2. This was compared to the measurement of constant-force fibrin unfolding in the single-molecule force-clamp experiments. By applying a constant force of 150 pN, a force that is between the high and low force constant-velocity rupture events, to the knob-hole interaction, force-clamp steps corresponding to the high force doublet event resulted. The correlation between these two methods was demonstrated with the overlap in force and separation results for constant-force (blue) and constant-velocity (red) experiments showne in Figure 2.17A.

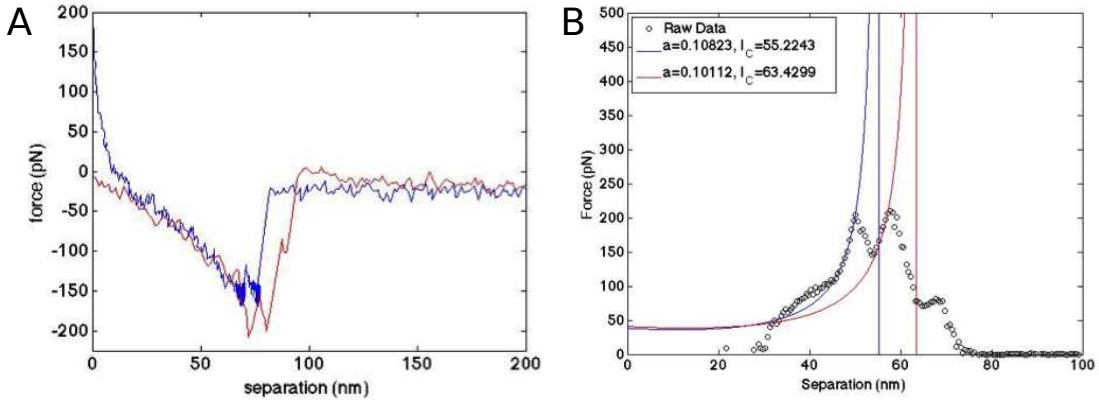

Figure 2.17: Force-clamp and constant-velocity results agree for 150 pN clamping force. (A) Force-separation data data for a force-clamp experiment at 150 pN (blue) and a constant-velocity experiment (red). This shows the direct correlation between beaks in the two methods. (B) Force-separation data for 157 constant-velocity force experiments were averaged to obtain the scatter plot data below. All force curves exhibiting characteristic peaks 2 and 3 were averaged and the averaged peaks were fit with a freely-jointed chain model. The Kuhn length (a) and contour length (l_C) in nm for the fit to each peak are shown in the legend.

For the measurement of unfolding structures in constant-velocity SMFS measurements, a force-extension curve was fit with models describing an ideal polymer chain. The average of 157 constant-velocity force-extension curves was modeled as a freely jointed chain (FJC) to extract the Kuhn length and contour length of the region of the protein lengthened by external force. The extension under force of a polymer

approximated by the FJC model is described by

$$F(x) = \frac{k_B T}{a} L^*(R) \tag{2.1}$$

where a is the Kuhn length, $k_B T$ is the thermal energy, R is the extension ratio (current end-to-end distance divided by the contour length, l_C), and $L^*(R)$ is the inverse Langevin function. The end-to-end distance was considered to be the measured tip-substrate separation (x). Thus the approximate closed-form function for the inverse Langevin used in this analysis is

$$L^*\left(\frac{x}{l_C}\right) = \frac{1}{1-\frac{x}{l_C}} + \left(1 - \frac{x}{l_C}\right)^2 \tag{2.2}$$

The average force-extension curve was fit using a nonlinear regression allowing the Kuhn length, contour length and extension at rupture to vary. Data analysis focused on peaks 2 and 3 because they should be directly related to the steps observed in constant force unfolding at 150 pN. The resulting Kuhn length (a) and contour length (l_C) values for events two and three are shown in Figure 2.17B. The separation between the two fits at 150 pN is 6.6 nm. This separation agrees very well with the extension step height seen in constant-force separation time data (Figure 2.16).

The FJC fitting performed on this data set differs from previous constant-velocity data and yields slightly different results.(1) The Kuhn length values measured here were smaller (nearly half that of previous results) and the change in contour lengths between the two fits was larger (8.2nm compared to previous 6±2nm). The reason for these differences could be the size of our data sets and choices in curves to be averaged prior to fitting. However, using previous calculations for FJC fits to force-extension data, the separation at 150 pN is 5.8 nm, still within uncertainty of the steps seen in force-clamp experiments.

Therefore, I can conclude that the single 6.6 nm extension step observed in force-clamp spectroscopy experiments at 150 pN directly corresponds to the characteristic rupture pattern seen in similar constant-velocity force spectroscopy experiments. Both of these rupture events are due to unfolding of fibrinogen's γ module through force applied to the 'A-a' knob-hole interaction.

Intermediate γ Module Unfolding Events

In the simplest case, single-molecule forced unfolding of a protein can be viewed as a two-state process where a protein rapidly goes from a folded to unfolded state due to applied force. This is consistent with the unfolding pattern observed at 150 pN. However, it has become increasingly clear that a more complex unfolding energy landscape, indicated by deviations of kinetics from a simple exponential model and the presence of intermediate unfolding states, may be necessary to fully understand protein unfolding (Figure

2.18).(7) Intermediate unfolding states have been observed in SMFS experiments for a variety of proteins including fibronectin type III,(122) Maltose-binding proteins,(123) surface layer protein SbsB,(124) titin,(125; 126) and ubiquitin.(87)

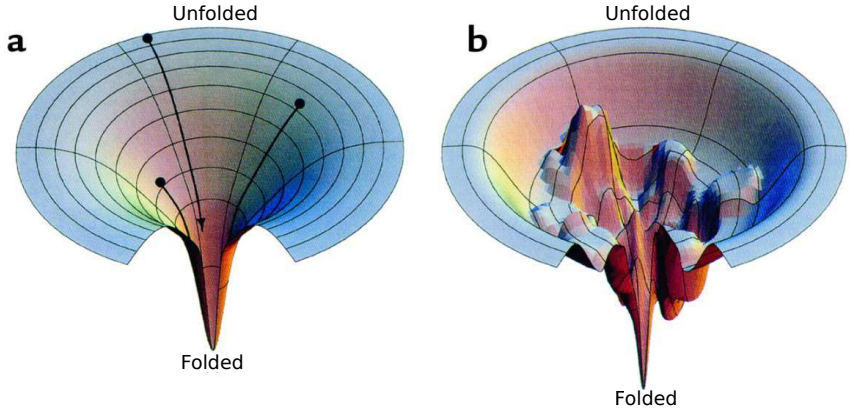

Figure 2.18: Interpretations of the protein folding energy landscapes. In this representation, the vertical axis represents the free energy and the horizontal represents conformational degrees of freedom. (A) An idealized funnel energy landscape for protein folding describes two-state folding kinetics with no significant kinetic traps. (B) A rugged energy landscape for protein folding describes a multi-state system. Modified from *Nature Structural Biology*.(7)

As previously shown by Averett et al., fibrin also exhibits a complex unfolding pattern when forces are applied to the 'A-a' knob-hole interaction.(57) However, in constant-velocity SMFS experiments, the force applied to the 'A-a' interaction varied dramatically and inconsistently, as the protein was unfolded. Additional intermediate states may be missed due to their short lifetime at high pulling forces. In force-clamp experiments, a constant force is applied to the knob-hole interaction over a range of constant pulling force to probe all possible intermediate-unfolding states.

The investigation of fibrin unfolding through the knob-hole interaction over a range of constant pulling forces reveals a more complex unfolding landscape. Constant-force fibrin unfolding was investigated over forces ranging from 50-200 pN. A custom MATLAB analysis package developed to efficiently determine the start and end of steps in separation time curves is discussed in detail in Appendix A.

Due to the specific protein interaction in this experiment, any steps following the first in separation-time traces are the result of extension of fibrin's γ module. The entire γ module is much longer than the extension events observed. Therefore, individual steps correspond to the unfolding of subdomains within the γ module. There are two parameters of particular importance for determining the presence of intermediate unfolding states in this region of fibrinogen – total extension and step height (Figure 2.19). Total extension refers to the tip-sample separation that occurs between the first and the last step in a separation-time trace. This corresponds to the unfolded length of the protein prior to knob-hole rupture at a given clamping force. Step

height is the separation between sequential steps in a separation-time curve. This reflects the length of protein extended by unfolding specific domains within fibrinogen's γ module.

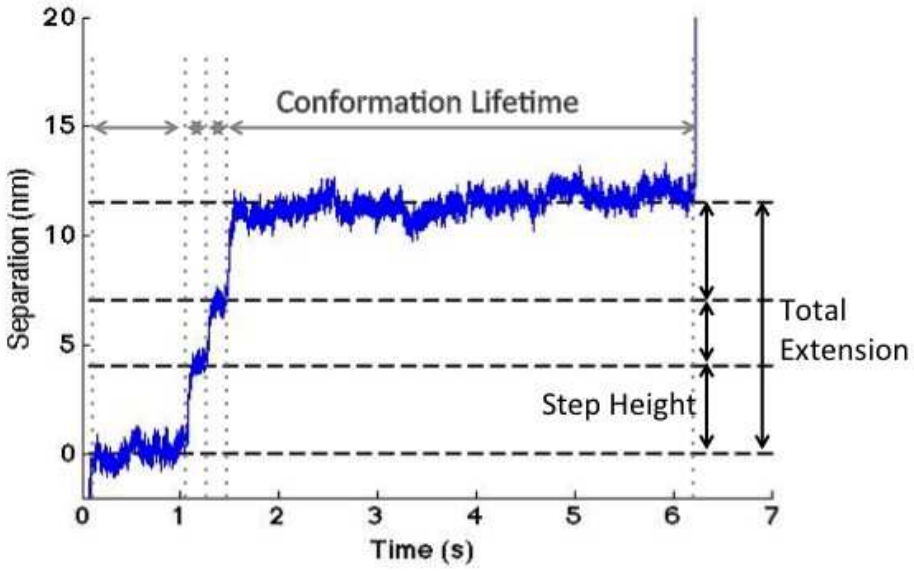

Figure 2.19: Definition of force-clamp terms. Separation-time curve produced by force-clamp experiment at 75 pN, separation is normalized so that first step is zero. Step height is the separation between sequential steps in a separation-time curve. Total extension is the separation between the first and last steps in a separation-time curve. Associated with each step is a lifetime for the conformation state; the end of the final conformation lifetime is rupture of the 'A-a' knob-hole interaction.

Constant-velocity experiments determined that high force rupture events in force-extension curves occur at 224±31 pN.(57) Therefore, at greater than 200 pN, the probability of observing characteristic γ module unfolding was low because a significant number of knob-hole interactions rupture prior to reaching the constant trigger force. Even if the constant pulling force was reached, the unfolding events happened too rapidly to reliably determine the conformation life time (i.e., the points corresponding to the start and end of unfolding steps). Characteristic fibrin 'A-a' unfolding was verified by examining the untriggered force-clamp curves to see constant-velocity rupture pattern; however, no information could be gathered as to lifetime of the intermediate unfolded state because the trigger force was not reached.

At the other extreme, when the clamping force is too low, fibrinogen is unable to unfold on the time scales of this experiment. A constant force of 50 pN applied to the knob-hole interaction for greater than 30 s did not cause unfolding of the γ module and allowed the monitor of tip-substrate separation over time to measure the drift in the system. The drift in the system was cantilever dependent, but in general was less than 1nm over 30 s. To avoid the interference of system drift in the separation-time measurements, all force-clamp experiments were performed on time scales less than 10 seconds. This time scale was sufficient

for investigating fibrinogen unfolding for forces ranging from 65 pN to 200 pN.

The first parameter compared was the number of steps measured in force-clamp traces for different forces (left column in Figure 2.20). High clamping force (125-200 pN) traces were primarily single-step force curves. These curves conformed to the previously described and characterized fibrin 'A-a' forced unfolding fingerprint with a single extension step of approximately 6.6 nm. For these curves, the total extension and step height (Figure 2.21A,B) represent the same extension of 6.6 nm because the majority of curves are single extension step curves. The total number of 200 pN force-clamp curves containing measurable extension steps was lower not because fewer pulling experiments were performed but rather because unfolding occurred prior to the 200 pN trigger force being reached.

At low clamping forces (100-65 pN), the majority of force-clamp pulls produced multi-step separation-time traces (left column in Figure 2.20). The average total extension was not significantly different for any of the pulling forces, except 65 pN (Figure 2.21A). This indicated the fibrinogen γ module unfolding was still dominated by the 6.6 nm extension described above and corresponding to the doublet in constant-velocity experiments. However, there was a decrease in the individual step height of steps in force-clamp traces for low clamping force (Figure 2.21B). Therefore, at lower forces, multiple smaller steps produced the same extension observed in a single step at higher forces. The same variability in initial (reorientation/lift up) step height and step lifetime can be seen in high force (125 pN, Figure 2.22) and low force (75 pN, Figure 2.23) traces.

To examine the more complex unfolding behavior of fibrinogen at low forces in more detail, the total extension and step height of separation-time traces were binned according to the number of steps observed (i.e., single step, two steps, three steps, etc.) (middle and right columns Figure 2.20, Figure 2.21). The total extension of single- and two-step curves was the same for all clamping forces except 65 pN. This is best illustrated in the 100 pN total extension plot of Figure 2.21. On the other hand, the individual extension steps measured were smaller for the two-step force curves compared to the single-step curves. This is best illustrated in the 100 pN individual step extension plot of Figure 2.21. These data suggested the two small steps compose the larger single step described as the fingerprint of 'A-a' fibrinogen unfolding (Figure 2.24, Figure 2.25). These intermediate unfolding steps indicate the presence of a previously unknown (unmeasured) intermediate unfolding domain in fibrinogen γ module unfolding.

At lower forces (100 pN and less), force-clamp traces produced three- and four-step separation-time curves. These traces produced a total extension greater than 6.6 nm and individual extension step height of 3.3 nm (Figure 2.21C,D). Consequently, in addition to the characteristic 6.6 nm extension for fibrinogen unfolding, there were additional unfolding domains prior to or following the 6.6 nm extension. With this data it was not possible to determine if these additional unfolding events occurred prior to or following the

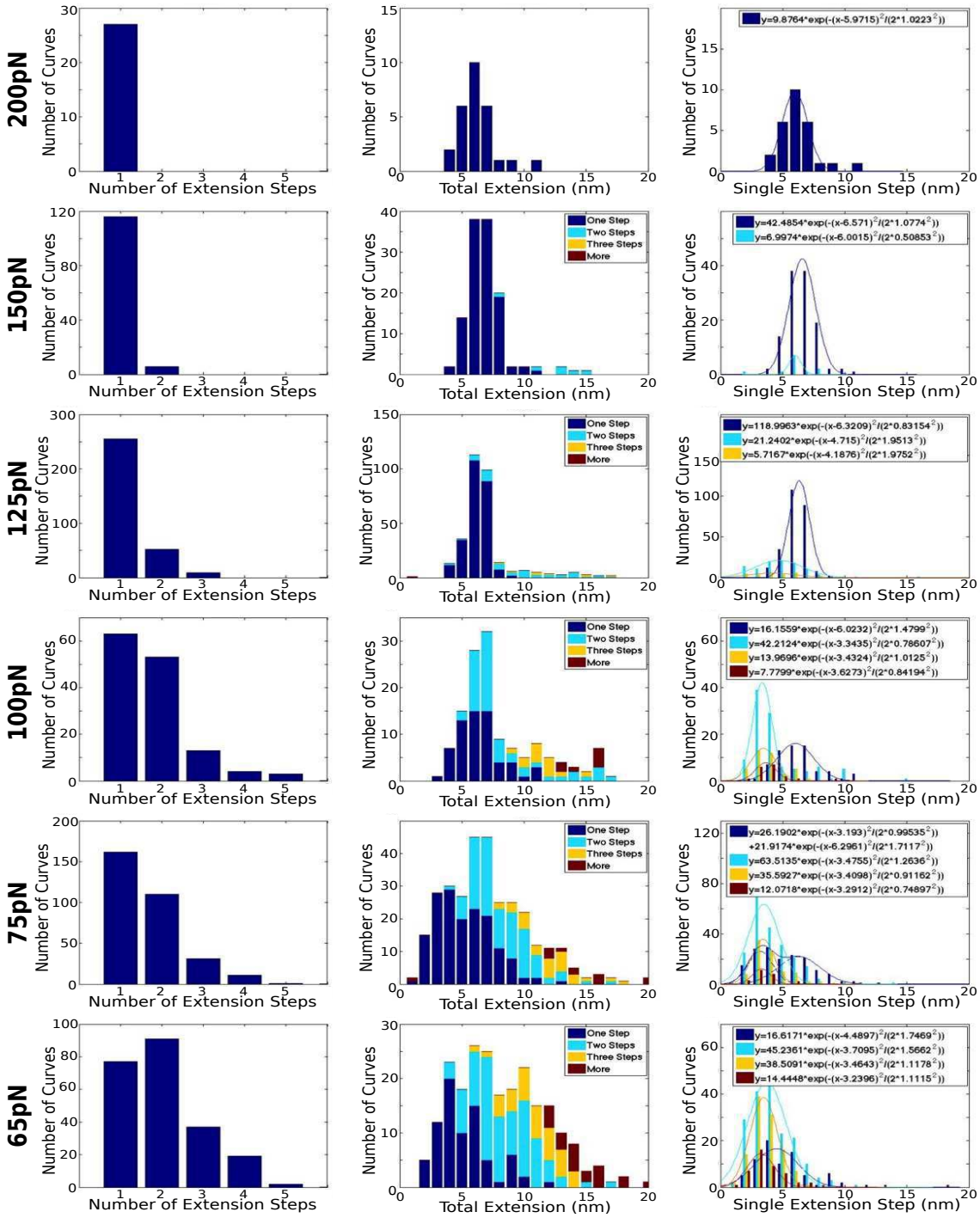

Figure 2.20: Comparison of extension steps for different clamping forces. Fibrin γ module unfolding behavior over a range of clamping forces. Each row corresponds to a different constant pulling force from 200 pN to 65 pN. The first plot (left) gives the number of separation time curves with a given number of unfolding steps. The second plot (middle) is a histogram of the total unfolded extension of the γ module prior to knob-hole rupture where each color represents the number of unfolding steps in the separation time curve. The data is represented as a stacked bar graph. The final plot (right) is a histogram of the height of extension steps, grouped by number of steps in the curve, fit with a Gaussian distribution (or double Gaussian, as necessary).

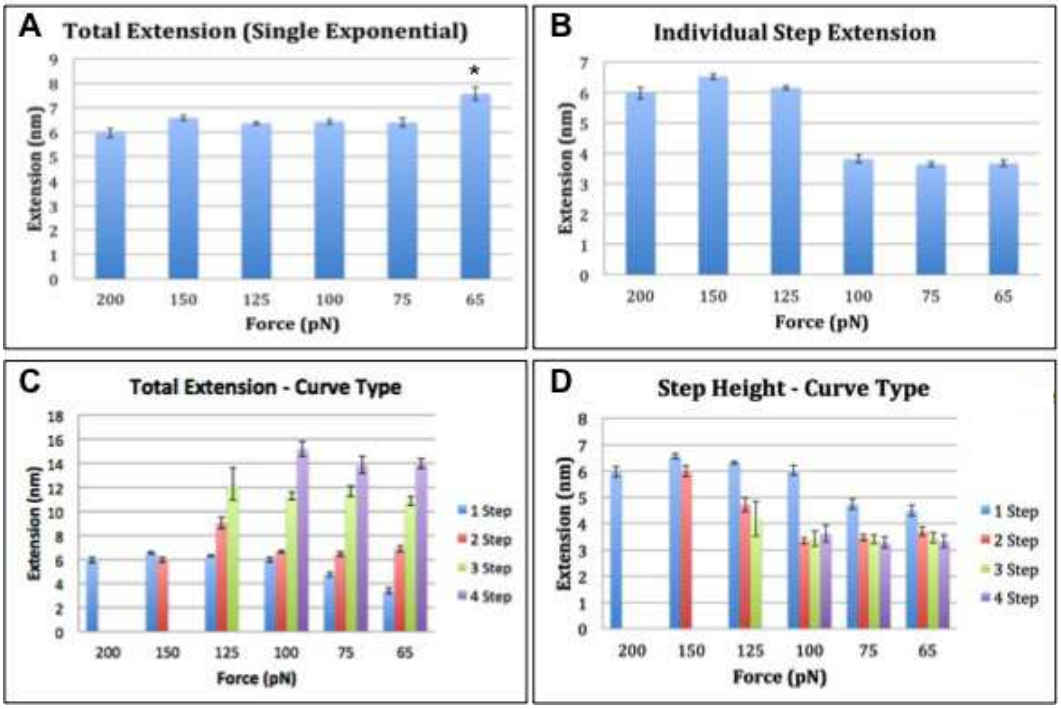

Figure 2.21: The average extension increased and step size decreased for lower clamping forces. Average and deviation values extracted from Gaussian fits to histograms of the total extensions and individual step heights of all force-clamp curves (top two plots) and force-clamp curves with a specific number of steps (bottom two plots). Bar graphs exhibiting the center and standard deviation for (A) the total extension, exposing the average extension of fibrinogen due to unfolding, (B) the individual extension step height, exposing the average extension of individual unfolding domains, (C) the total extension grouped by the number of extension steps in the force curve, and (D) the individual step heights grouped by the number of extension steps in the force curve taken at each constant pulling force. Asterisk indicates significance ($p<0.05$) as determined with a t-test.

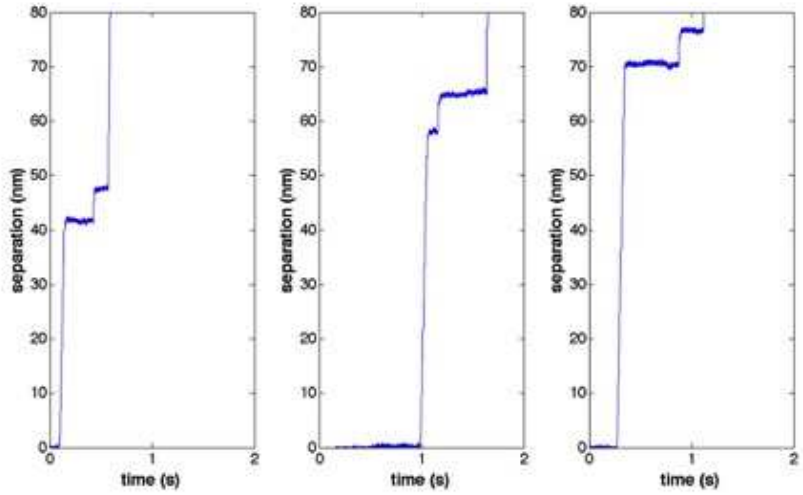

Figure 2.22: Sample 125 pN force-clamp traces. Typical constant force unfolding trajectories as separation versus time plots. All data acquired at 125 pN.

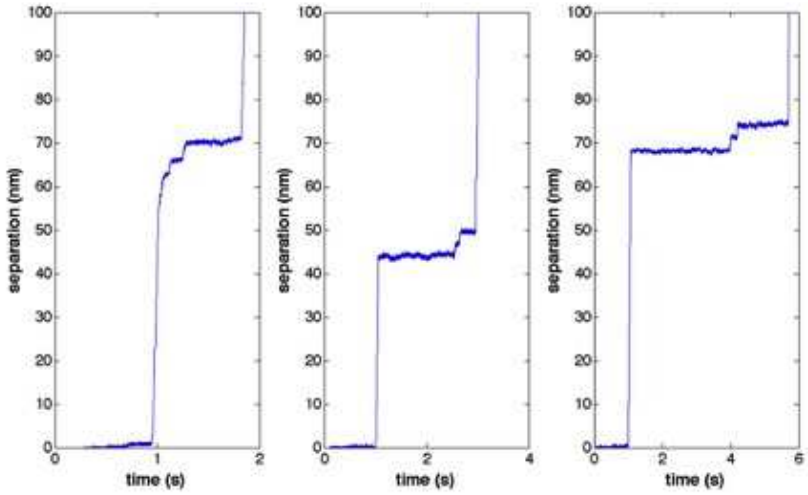

Figure 2.23: Sample 75 pN force-clamp traces. Typical constant force unfolding trajectories as separation versus time plots. All data acquired at 75 pN. Note the time scales are different for each plot.

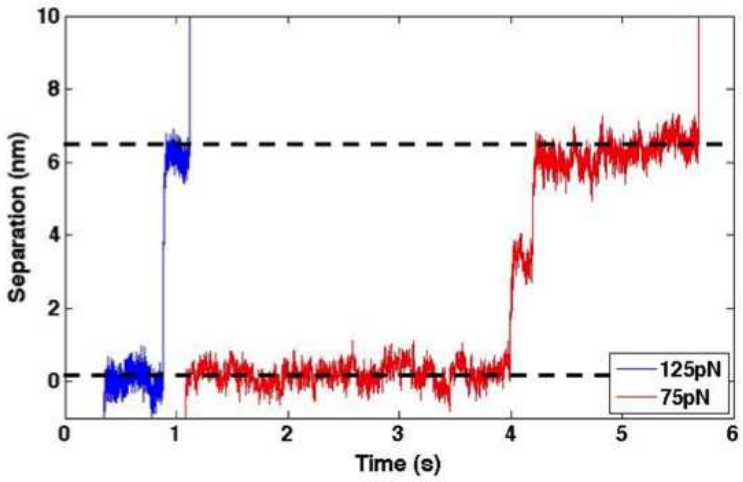

Figure 2.24: Intermediate unfolding state observed at low clamping force. The intermediate unfolding state present at low force fibrinogen unfolding shown here with separation-time plots of fibrinogen unfolding at 125 pN (blue) and 75 pN (red). The plots are artificially offset in time to make visualizing the differences easier.

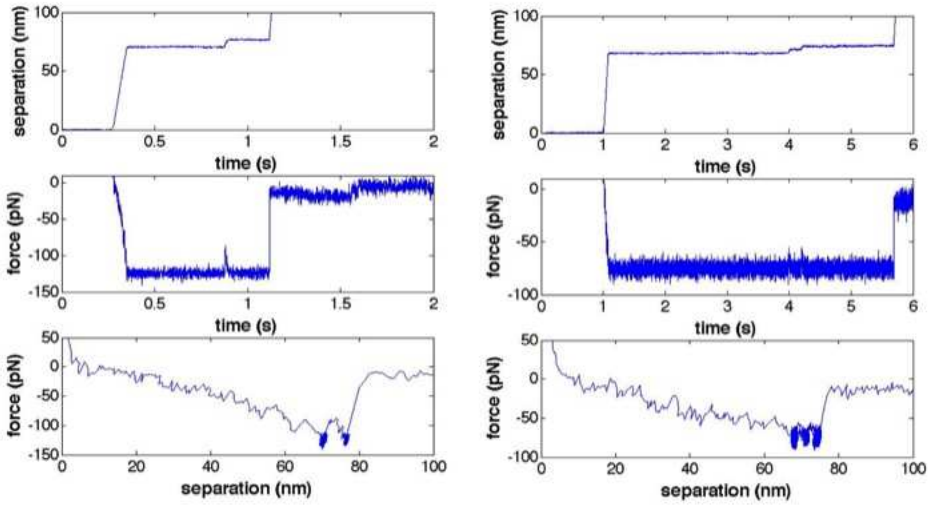

Figure 2.25: Sample force-clamp data collected at 125 pN (left) and 75 pN (right). The data is displayed as (top) separation-time in which extension events are plateaus in extension, (middle) force-time in which extension events are brief changes in constant force application, and (bottom) force-separation in which extension events appear as rupture peaks. Note that the time axis differs between the two forces because it takes longer for unfolding to occur at 75 pN than 125 pN.

6.6 nm extension because the additional extension steps were on the same length scale as the intermediate unfolding events observed in 6.6 nm extension. The presence of lower force unfolding peaks both prior to and following the characteristic high force doublet in constant-velocity experiments may indicate that force-clamp measured the same unfolding events. However, these unfolding events occur much closer to the 6.6 nm 'A-a' fingerprint in force-clamp experiments than the constant-velocity peaks prior to the 225 pN characteristic doublet. This indicates a different unfolding pathway or mechanism for constant-velocity and constant-force application to the 'A-a' knob-hole interaction. Additionally, this could indicate the presence of other intermediate unfolding states that were unmeasurable in constant-velocity experiments due to the limitations of this technique.

At 65 pN, curves with a greater number of total steps produce a larger total extension and all step heights are approximately the same for single-step or multi-step traces. This is likely due to the fact that 'A-a' unbinding is occurring on the same timescales as unfolding of one of the single 3.3 nm domain comprising the total 6.6 nm extension. This could be further verified by collecting a larger number of force-clamp traces at 65 pN, to show that the distribution of total extension heights observed in single-step force curves becomes a bimodal distribution with one dominant peak at 3.3 nm and another peak at 6.6 nm. Some evidence of this can already be seen in the single-step total extension plots at 75 pN and 65 pN.

There are two observations that were made from this analysis:

1. previously unseen intermediate unfolding states in the characteristic 6.6 nm extension,

2. and unfolding events performed and/or following the characteristic 6.6 nm extension seen at high forces.

It is worth noting that the additional extension events did not exhibit the same extension observed in constant-velocity unfolding experiments, so force-clamp could be probing different unfolding domains or sub-domains from constant-velocity experiments. The specific domains responsible for unfolding events are discussed in conjunction with molecular dynamics situations, Section 2.4.3.

Kinetics of Fibrin Unfolding

Protein (un)folding is a stochastic process where each molecule can follow a different microscopic trajectory due to thermal fluctuations. The stochastic behavior of protein unfolding due to an applied force generally has several unproven assumptions: (1) protein unfolding is history independent (i.e., Markovian),(127) and (2) unfolding rates are exponentially dependent on the pulling force (i.e., Bell's Model).(119) The Markovian nature of protein unfolding has proved especially difficult to confirm by constant-velocity experiments because the rate of change of the pulling force and the unfolding probability are history dependent. Force-clamp allows for direct measurement of unfolding kinetics at well-defined force, eliminating the ambiguity of interpreting constant-velocity data.

Bond rupture and protein unfolding under a stretching force has been modeled as two-state Marokovian process showing both unbinding and unfolding rates exponentially dependent on the pulling force.(87; 120; 128) Recent work has shown, with a large statistical pool of force-clamp data at a given force, deviations from the simple two-state, exponential kinetics indicative of alternative unfolding barriers are previous studies in the ensemble measurement.(129; 130) Lower probability unfolding events that deviate from simple two-state kinetics have been observed; however, these events were sufficiently rare in previous studies as not to bias the ensemble averages.(87) This is due in large part to advances in protein engineering to create polyproteins, which allow for a higher pick up ratio than monomers and multiple repeats of the same protein unfolding in a single force-clamp trace. Observed intermediate unfolding events in these experiments were attributed to the conformation of the protein when force was applied.(87)

The experimental setup deviates from previous experiments in that it probed a range of protein conformations, corresponding to a range of pulling directions, and there is the added complexity of the 'A-a' knob-hole rupture. Therefore the experiments relied on large statistics to get representative behavior of fibrin γ module unfolding. Due to the significant number of intermediate steps for low clamping forces, I investigated fibrin's unfolding relative to the simple exponential behavior of the two-state kinetics model.

As described in Section 2.4.2, the unfolding probability versus time behavior of a fibrin γ module un-

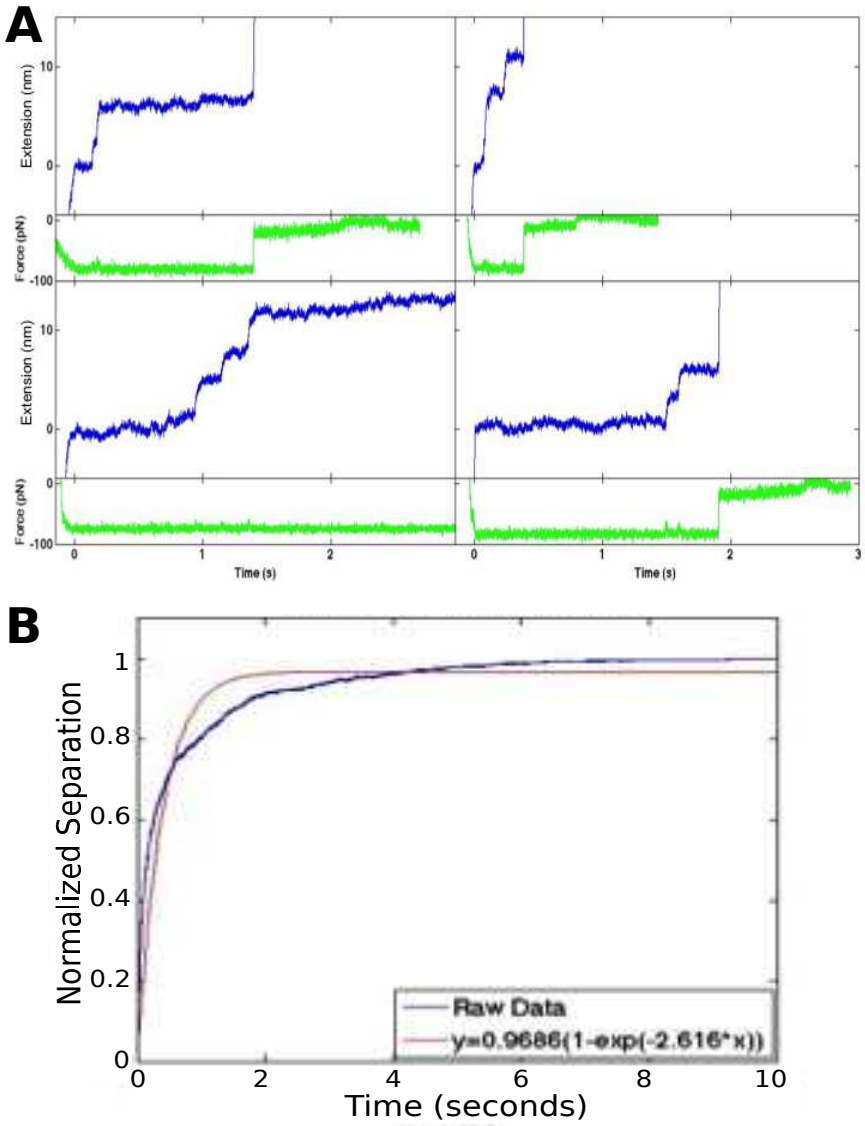

Figure 2.26: Sample NEA for 75 pN force-clamp experiment. (A) Typical separation-time traces (blue) for fibrinogen γ module unfolding through the 'A-a' knob-hole interaction at a constant force of 75 pN (green). Under a constant stretching force, fibrinogen elongates in a series of stair steps with a minimum of 3 nm extension each. (B) The normalized average time course of unfolding obtained by summation and normalization of 315 separation-time traces, including those shown (A). The unfolding of fibrinogen is non-exponential at a constant stretching force and the shown single exponential fit is a poor descriptor for these unfolding traces

folding was obtained by creating an NEA all extension-time traces for a given force. In this representation, separations are ascribed values between 0 (folded protein) and 1 (fully unfolded protein) then averaged to represent the probability that a protein was fully unfolded. Representative force-clamp traces and the resulting NEA for the set can be seen in Figure 2.26. As described in previous Section 2.4.3, a variety of separation-time traces result from constant force application to the knob-hole interaction based on the conformation of the γ module when force is applied and the stochastic unfolding of fibrinogen. The differences in separation-time traces are direct evidence of a complex energy landscape for fibrinogen unfolding, as a variety of unfolding pathways will lead to rupture of the knob-hole interaction. The variety of unfolding pathways are all involved in creating the energy landscape associated with γ module unfolding and therefore, all contribute to understanding the complexity of γ module unfolding kinetics.

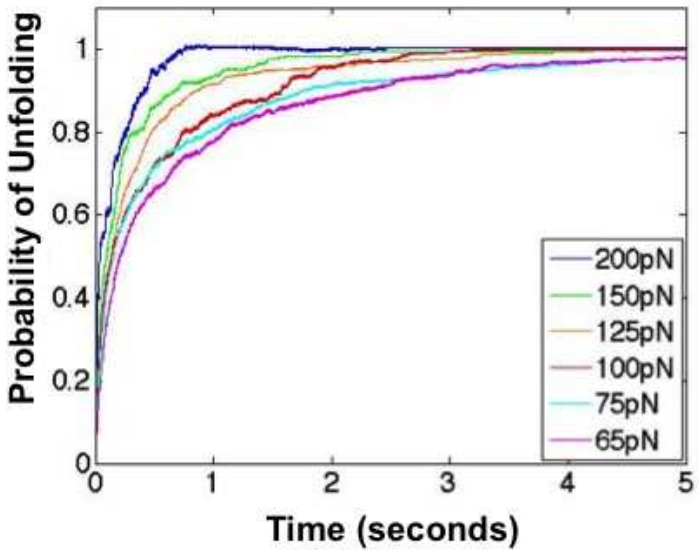

Figure 2.27: Fibrin γ module unfolding is force dependent. NEA of separation-time traces for the range of forces investigated, 65-200 pN, indicates that the probability of unfolding is dependent on the constant pulling force.

An NEA was calculated for force traces acquired at constant forces ranging from 65-200 pN. The unfolding probability versus time for each force determined from the ensemble average is shown in Figure 2.27. The greater the constant applied force, the more rapidly the probability of unfolding reaches 1 or the protein becomes completely unfolded.

Kinetic information about fibrin unfolding was extracted from NEA behavior as a function of applied force, specifically obtaining the intrinsic rate of γ module unfolding along a pulling coordinate. This required (1) determining the force dependent unfolding rate and (2) relating pulling rate to the applied force in order to determine the force-free parameters. I briefly investigated several methods of extracting rate constants

through a single-exponent (two-state unfolding), multiple-exponentials (multiple two-state domains), and a stretched-exponential (rough energy landscape).(129) Then I applied Bell's model to test the exponential relationship between unfolding rate and pulling force.

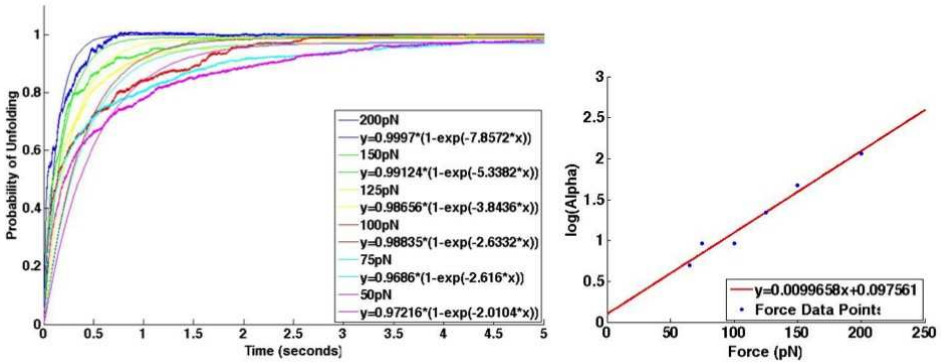

Figure 2.28: Single-exponential fits to NEA. (A) Single-exponential fits to normalized averages of separation-time traces for the range of forces investigated, 65-200 pN, indicate that the probability of unfolding is not a Markovian process. (B) Plot of the exponent (α) of the single-exponential fits versus the constant pulling force. Bell's model was used to determine $\alpha_0 = 1.1\ s^{-1}$ and $\Delta x = 0.04$ nm.

I tested the Markovian nature of protein unfolding by fitting a single exponential to the NEA of fibrin γ module unfolding. An exponential time course is consistent with a memory-free, all-or-none Markovian process where the probability of unfolding at any given time is independent of the previous history (derivation in Appendix B). The NEA calculated from force-clamp experiments for fibrin's γ module cannot be readily described by a single exponential fit (Figure 2.26B and 2.28), indicating a more complex unfolding landscape than approximated with the two-state model. The deviation from a single exponential, the presence of intermediate unfolding states and multiple unfolding pathways in force-clamp separation-time traces, and proposed force protected domains in the γ module(79) all strongly suggest non-markovian behavior. Therefore a more complex method of analysis was required to fully understand the kinetic parameters of this system.

I used Monte Carlo simulations to investigate the stochastic unfolding of proteins with different parameters (e.g., number of domains, various domain lengths and unfolding rates, and force protected domains). A detailed description of simulation methods and results can be found in Appendix C. The results can be summarized as follows:

1. Multi-domain unfolding with domains of different lengths and the same kinetic parameters is described well by the two-state Bell model.

2. Using multiple exponentials to determine the kinetic parameters of different domains from NEA was

highly sensitive to input parameters and only valid if the number of domains was known.

3. The force protected domains postulated by constant-velocity experiments are not the dominant factor contributing to deviations from simple two-state, single-exponential unfolding.

4. A stretched-exponential, often used for describing glassy dynamics behavior, is an effective approximation of one domain for a rugged energy landscape while maintaining the exponential force-dependence of domain unfolding.

The results of single-exponential, two single-exponential and stretched-exponential fits to fibrin NEA data is shown in Figure 2.29. This data showed for all forces, except for the largest, there were significant deviations in unfolding from single-exponential behavior. Both two single-exponential or a stretched-exponential accurately reflect fibrin unfolding data; however, because multiple exponentials presupposes only two domains and is sensitive to input parameters (as shown with Monte Carlo simulations, Appendix C), I used a stretched-exponential to approximate the kinetic parameters associated with fibrin's γ module unfolding. Figure 2.30 shows stretched-exponential fits to NEAs at each unfolding force. By approximating the multi-domain protein as a single 'rough' unfolding domain then the force dependent unfolding rates can be used in Bell's model to approximate the equilibrium kinetic parameters of fibrin's γ module as k_0=1.2 s^{-1} and Δx = 0.4 nm. These values fall within the range of kinetic parameters reported by constant-velocity measurement of fibrin unfolding (k_0 = 0.003-3.5 s^{-1} and Δx = 0.21-0.57 nm)(1) and other proteins.(131; 126)

Future work could be done in Monte Carlo to iteratively calculate and fit to NEAs to determine the kinetic parameters associated with individual unfolding each domain. This however, would require further work to understand the process and theory required to extract relevant parameters from Monte Carlo simulations. Additionally, I have disregarded information about the 'A-a' bond itself which could be extracted from these data sets by analysis of time from initial force application to the knob-hole interaction to dissociation of bond. Previous studies have used dwell-time analysis to understand protein unfolding,(130) this method of data analysis would allow for both extraction of protein unfolding kinetic parameters and bond lifetime for the 'A-a' interaction.

Molecular Dynamics Simulations

As discussed in Section 2.4.3, unfolding of the γ module through force applied to the 'A-a' knob-hole interaction is characterized by a ~6.6 nm extension but can exhibit extensions ranging from ~6 to 12 nm in 2-4 steps of ~3 nm. Due to an elegant series of AFM single-molecule studies performed by Laurel Averett,(1) the extensions measured by force-clamp are attributed to extensions of the γ module; however, the specific regions of the γ module are still unknown. Extension of the entire γ module would produce a 78 nm extension;

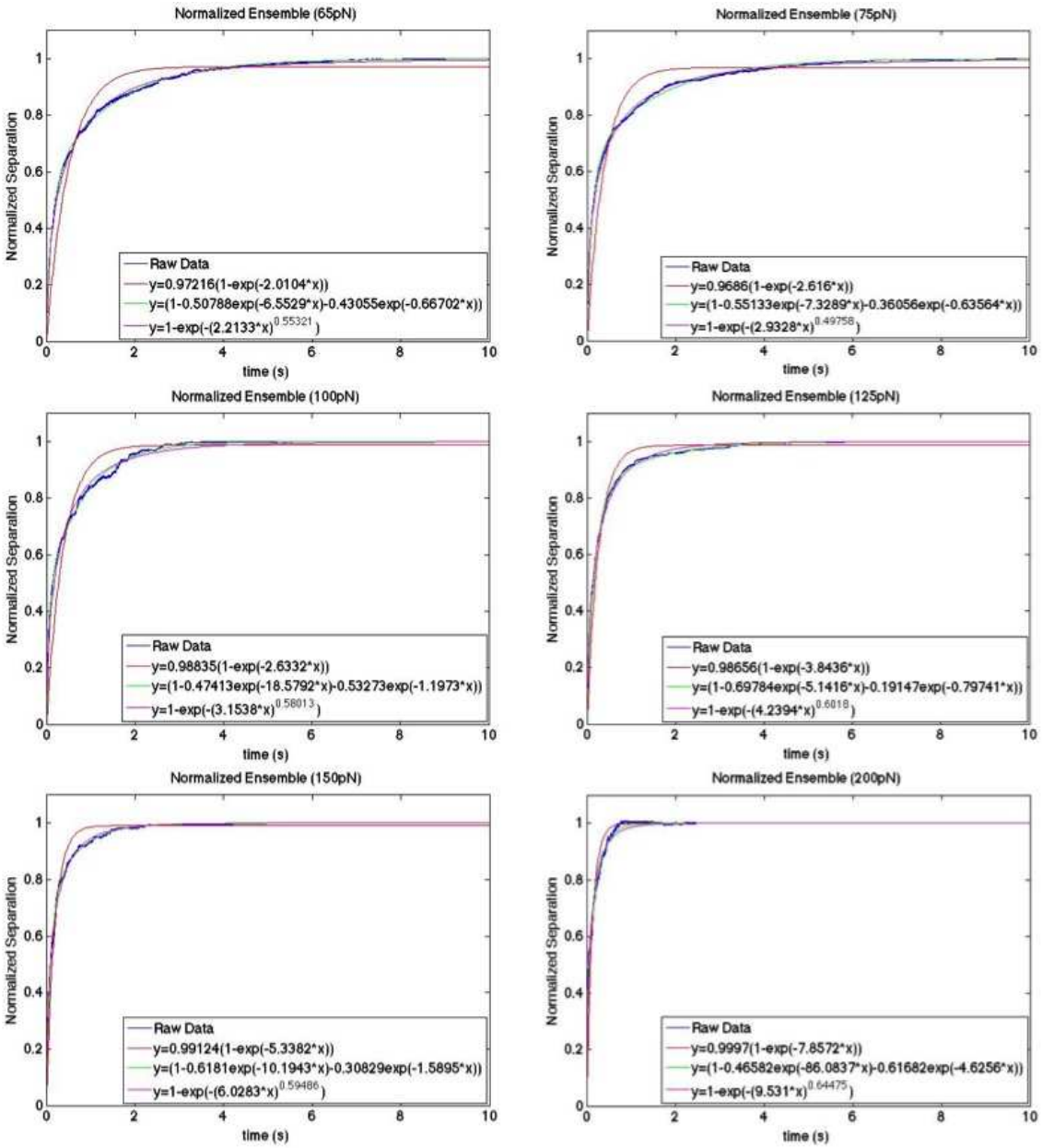

Figure 2.29: Multiple fits to NEAs. NEA traces for each of the constant pulling forces investigated – 65 pN (226 curves), 75 pN (315 curves), 100 pN (136 curves), 125 pN (316 curves), 150 pN (122 curves), and 200 pN (27 curves). At all forces, there is deviation form a single-exponential fit. Additionally, the curves have been fit with a second exponential to account for a second unfolding rate constant and a stretched exponential to investigate glassy dynamics in fibrinogen unfolding.

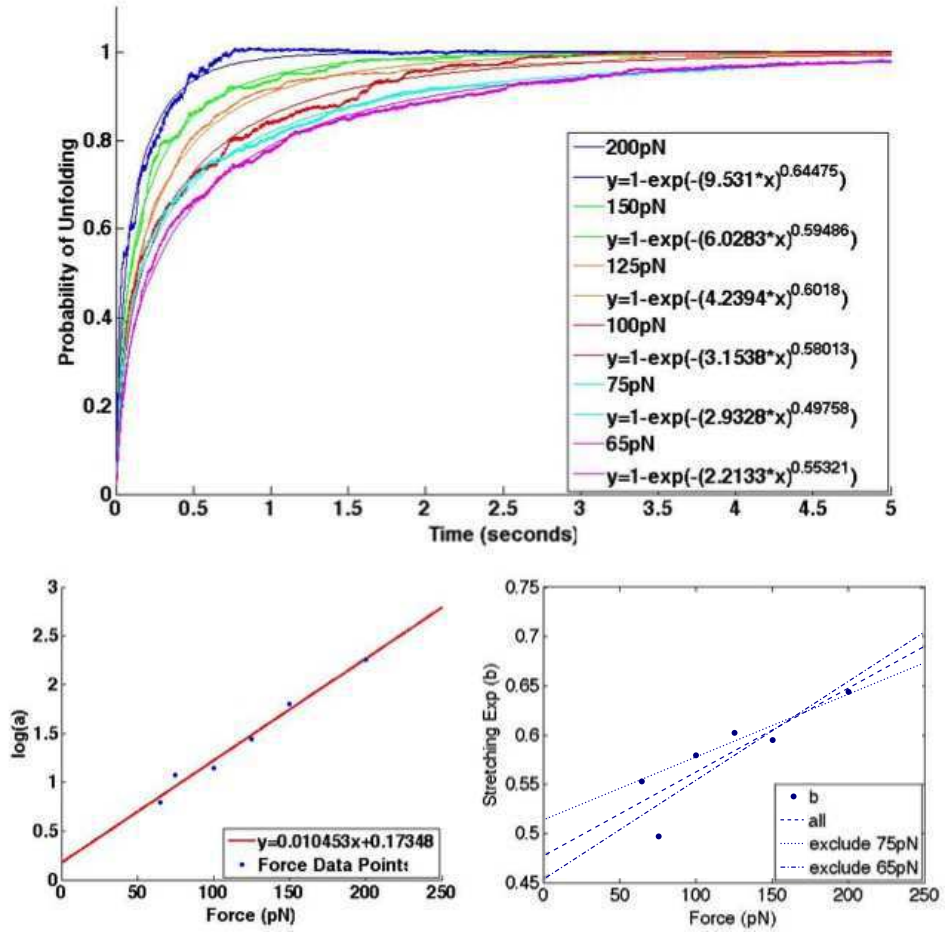

Figure 2.30: Stretched exponential fits to NEA. (A) Stretched-exponential fits $\left(1-e^{-(at)^b}\right)$ to normalized averages of separation-time traces for the range of forces investigated, 65-200 pN, indicate that the probability of unfolding is representative of rough energy landscape where a is the unfolding rate and b is the stretching factor. (B) Plot of the unfolding rate (a) versus the constant pulling force. Bell's model was used to determine $\alpha(t_0) = 1.2\ s^{-1}$ and $\Delta x = 0.4$ nm. (C) Plot of the stretching factor (b) versus the constant pulling force deviates from a simple linear trend.

therefore, sub-domains within the γ module must be responsible for the experimentally observed extension. Calorimetric evidence (132) and subsequent crystal structures (133) revealed that each γ module has three compact domains which may unfold separately (Figure 2.31B). The estimated unfolding lengths are ~7 nm for the N-terminal domain (19 residues, γ143-γ153 and γ182-γ191, Figure 2.31B red), ~40 nm for the central domain (106 residues, γ192-γ286 and γ380-γ392 of the β strand insert, Figure 2.31B yellow), and ~30 nm for the C-terminal domain (79 residues, γ287-γ326 and γ339-γ379, Figure 2.31B orange).(133; 86) The C-terminal domain is unlikely to be responsible for unfolding length because the 'a' binding pocket (Figure 2.31C) must remain intact in order to maintain 'A-a' interaction and observe unfolding. The N-termial or some portion of the central domain of the γ module is responsible for force-clamp observed extensions.

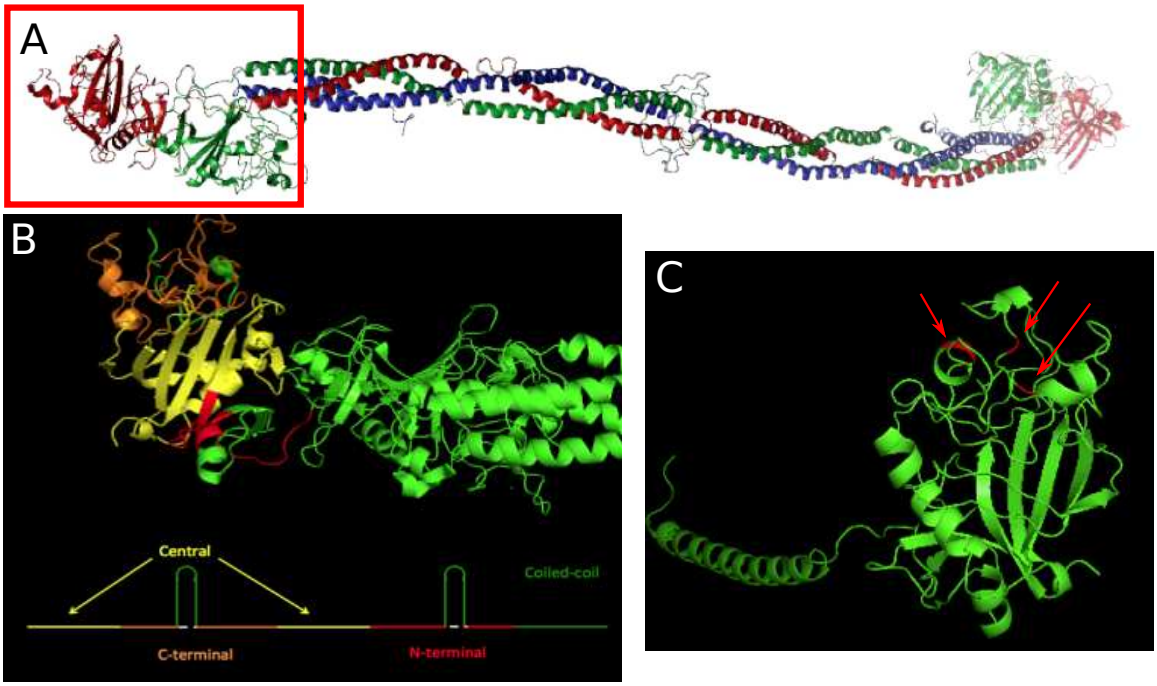

Figure 2.31: Unfolding domains in the γ module. (A) Cartoon ribbon rendering of fibrin structure, created using Protein Data Bank entry 3GHG, colored by chain. Boxed region is enlarged in (B) and (C). (B) The γ module contains compact domains - (red) N-terminal, (yellow) central, and (orange) C-terminal domains. Fully unfolded structure colored below. (C) One coiled-coil strand and γ module as used for simulations with key residues involved in the 'A-a' knob-hole interaction identified in red.

To further inform the current understanding of fibrin γ module unfolding, discrete molecular dynamics (DMD) simulations were carried out on the Biomedical Analysis and Simulation Supercomputer (BASS) at UNC-Chapel Hill by previous labmate, Nathan Hudson, for his dissertation work.(134) In protein folding studies, DMD is a rapid sampling method, in which simplified models of atoms interact over a period of time giving a view of motion and evolution of the system. The all-atom DMD employed in these studies of fibrin was developed in the Dokholyan Lab at UNC to allow detailed analysis of unfolding due to a transferable

force field.(135)

In the simulation results presented here, I investigate the unfolding pattern associated with pulling on the 'A-a' knob-hole interaction. This was accomplished by binding the 'a' pocket of the fibrin crystal structure (2FFD in the protein data base)(136) to A-knob mimic GPRP. To mimic the salt bridge and ensure that the peptides stay bound, the salt bridge was modeled as an infinite square well potential between the NH_2^+ arginine in GPRP and the delta oxygen of the γAsp234. By using an infinite square well, the peptide was forced to remain bound in the pocket to allow visualization of all possible unfolding events. Assuming that having an ion bound to a pocket is better than an empty pocket, calcium binding pockets were simulated with zinc because the all-atom DMD field did not include calcium parameterization.(135) This is particularly important for the fibrin γ module due to evidence by previous work (Section 2.3 and Averett et al.(105)) implicating calcium binding as a force stabilizing mechanism. To speed up the simulation, the beta-C domain was omitted and the atoms in the coiled coil region were fixed in place and not allowed to fluctuate. The simulations were performed in a rectangular box of 300 Å x 300 Å x 1200 Å with periodic boundary conditions and an Anderson thermostat was used to maintain room temperature (300 K). Force was applied to the protein through the GPRP peptide and the coiled-coil region at the base of the γ module. Constant-force pulling was achieved by applying discretized step-function with a constant energy drop at the distance step of 0.1 Å between the coiled-coil attachment point and a fixed end point 200 Å away from there. For a more detailed description of the DMD simulations, please refer to previous work by Nathan Hudson(134) or Dokholyan Lab publications.(135) Ten simulations run at a constant force of 150 pN are analyzed here.

Each of the 10 simulations of a constant 150 pN force applied to the 'A-a' interaction produced slightly different pathways for unfolding; however, there are several unfolding steps that can be observed in all simulations (Figure 2.32). The initial extension of the γ module is characterized by separation of the hole 'a' binding region from the rest of the γ module. Also present in the extension is the reorientation of the γ module and extension of the region at the base of the γ module near the coiled-coil region. These unfolding events produce an extension of $\sim$70 Å that will vary slightly between simulations.

The next extension is due to the bulk of the γ module unfolding into three subdomains (SD1, SD2, SD3). This process occurs through one of two pathways shown in Figure 2.33. In the first pathway, the subdomain closest to the coiled-coil region (SD1) separates from the bulk of the gamma module before formation of the three subdomains. Pathway 1 accounts for the unfolding pathway in 7 of the 10 simulations. The second pathway is characterized by separation of the subdomain closest to the 'a' pocket (SD3) separating from the bulk of the gamma module prior to formation of the three subdomains. Pathway 2 accounts for the unfolding pathway in 3 of the 10 simulations. Regardless of the unfolding pathway, the final result is the gamma module separated into several subdomains. SD1 and SD2 (closest to the coiled-coil) have no

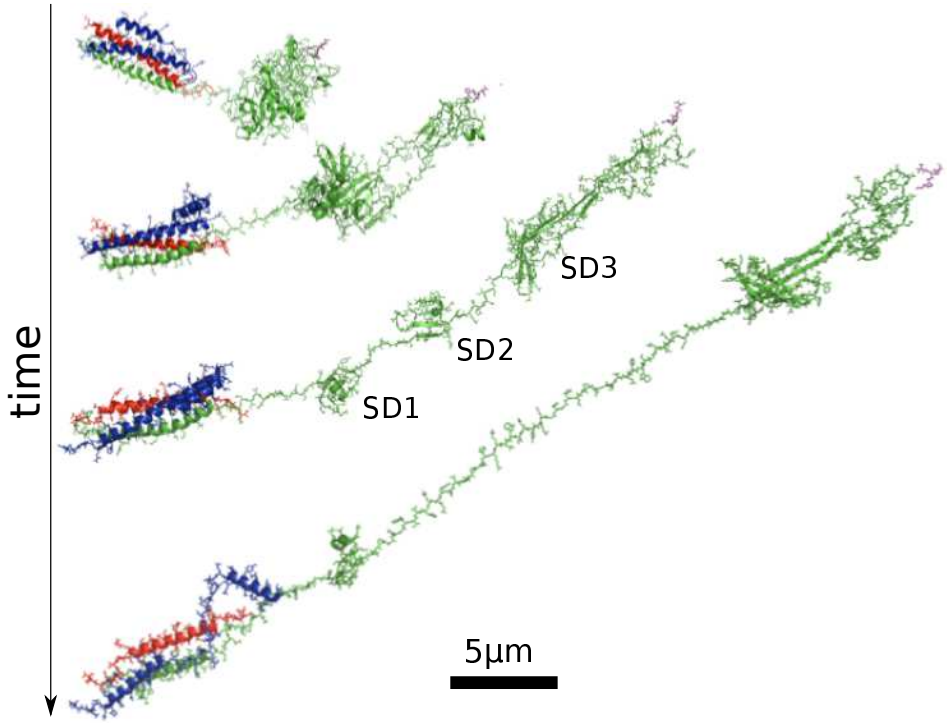

Figure 2.32: Simulated 150 pN γ constant force module unfolding. The times at which these configurations appear will vary depending on the simulation, but they occur in the same order from top to bottom. First, the D fragment prior to unfolding; force is applied up and to the right. First extension is due to the region at the base of the gamma module near the coiled-coils extending and almost simultaneously the 'a' binding region separates from the rest of the gamma module. Then the region of the gamma module closest to the coiled-coil unfolds into 3 different subdomains (SD1, SD2, SD3). Finally the middle domain completely unfolds. Additionally there become two well defined beta strands near the 'a' pocket.

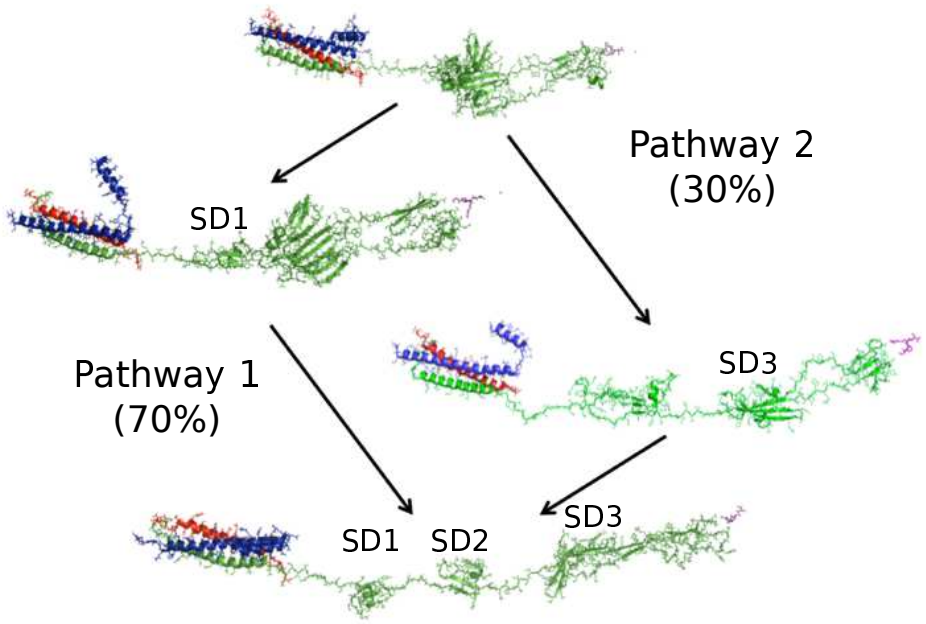

Figure 2.33: Multiple unfolding pathways produce three different subdomains in the γ module. To accomplish the extension between separation of separation of the 'a' pocket from the rest of the γ module and the γ module dividing into three subdomains (labeled as SD1, SD2, SD3 from left to right), the protein unfolds through one of two pathways. Pathway 1 accounts for 7 of the 10 simulations and is characterized by subdomain 1 (SD1) separating from the bulk of the gamma module before the formation of subdomain 2 (SD2) and 3 (SD3). Pathway 2 accounts for 3 of the 10 simulations and is characterized by SD3 separating from the bulk of the gamma module prior to the formation of SD1 and SD2.

interactions with the other subdomains. SD3 and the 'a' pocket region are separate initially but quickly form a double beta strand between the two. Both of these unfolding pathways account for approximately 100 Å of extension in the gamma module.

The final extension consists of complete unfolding of the beta sheet composing SD2. This accounts for the final approximately 120 Å of extension seen in all but two simulations. Had the two anomalous simulations been allowed to run for more iterations, they would have likely reached the same final extension.

It is important to remember some differences between the simulations and AFM experiments. First in simulations, the knob 'A' is permanently attached to the residues in hole 'a' by an infinite potential well. This means that some of the extensions seen in simulation will not be seen in AFM experiments because rupture of the 'A-a' interaction terminates unfolding measurements taken with the AFM prior to these unfolding events. Additionally, in AFM experiments fibrinogen is covalently attached to the substrate using standard NHS/EDC chemistry to link free amines in the protein (i.e., lysine residues) to the carboxyl of the SAM. Therefore, some unfolding events seen in simulation will not be seen in experiment because these regions are protected from force by the attachment of fibrinogen to the surface. For these reasons, analysis to determine critical interactions responsible for extension seen in AFM experiments, particular attention is paid to the initial unfolding steps (before dramatic structural changes are made to the binding pocket) seen in simulations and those interactions located in the gamma module

To compare simulation data with force-clamp extension versus time data, a PyMOL script was used to extract the distance between the γCys153 and GPRP Gly1 α carbons for each state in a simulation. The γCys153 and GPRP Gly1 α carbons were chosen because they are located at the base of the γ module and the tip of the 'A' knob, respectively. This allows for any separation (or change in separation) between these two points to be attributed to the length (or extension) of the γ module. Figure 2.34A shows the results of the PyMol script displayed as extension in angstroms versus iteration for one simulation at 150 pN. The separation-time trace shows periods of time where the length of the γ module remains constant and times where there are dramatic increases in the distance between the two residues, similar to the stair-step pattern observed in force-clamp experiments.

By utilizing and modifying the analysis code writen by Andrey Krokhotin, a postdoc in the Dokholyan lab, I was able to evaluate a variety of parameters in each of the simulated unfolding videos. Andrey's codes allowed for the determination of the number of contacts and the native contacts broken at a specified iteration. This is accomplished by specifying a threshold distance between two C-β (CB) side chain atoms (or C-α (CA) main chain in case of GLY determined contacts). The residues satisfying the contact threshold prior to iterations in the simulation were considered native contacts. The native contacts are considered broken when they exceed this separation in a given time step and do not reappear in the next time frames.

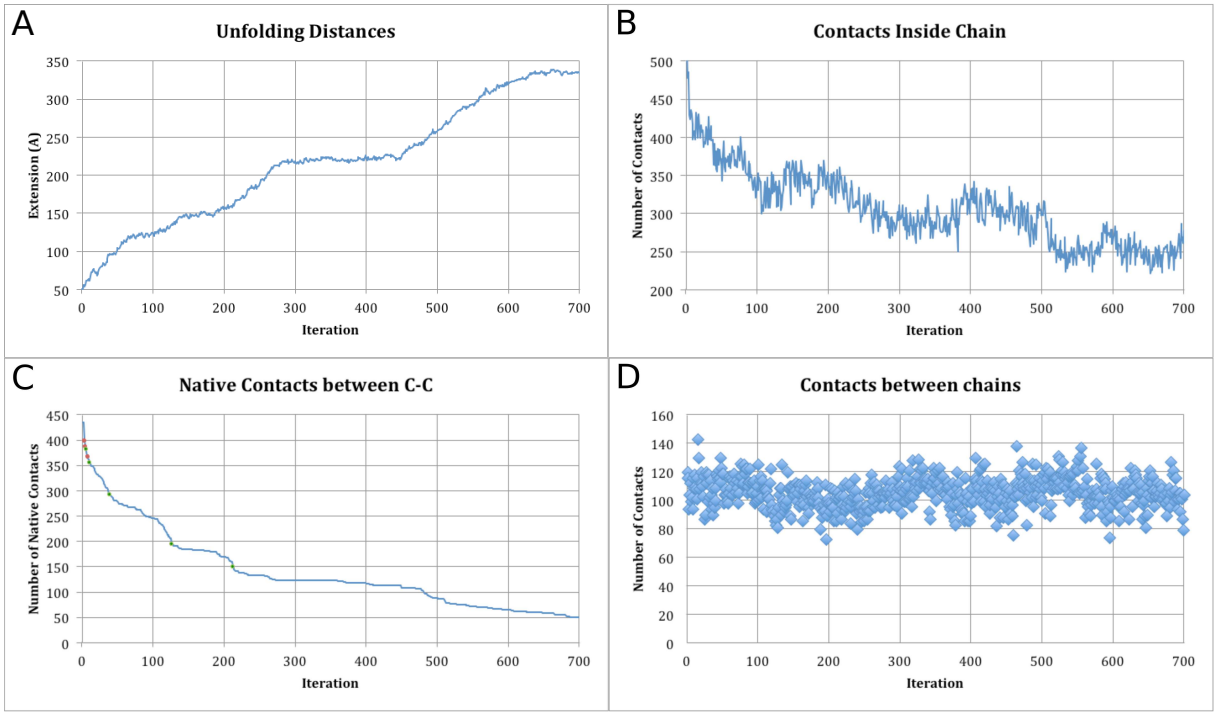

Figure 2.34: Residue separations in 150 pN γ module unfolding. (A) Separation between γCys 153 and GPRP GLy1 αCarbons for each iteration. For the same simulation, the number of residues with CB atoms (or CA in the case of GLY) separated by 7.5 Å where both residues are in the (B) same chain or (D) different chains versus the iteration step. (C) The number of native contacts, where both residues are in the C chain, still remaining in contact at each iteration. The red and green dots identify iterations that have a large decrease in the number of native contacts greater than 10 and 5, respectively. DMD time units ($\sim$1 ns).

All results in this report were calculated for a threshold of 7.5 Å. Minor modifications to these codes were made to see trends in the unfolding simulation by outputting the number of contacts or the number of native contacts broken in each iteration.

The results of this analysis for one simulation at 150 pN are displayed in Figure 2.34. Figure 2.34B displays the number of contacts where both residues are in the same chain as a function of iteration step. The crystal structure is primarily composed of the C chain and the γ module; therefore, the number of contacts inside the same chain reflects a change in the γ module. The noise in this plot makes it difficult to determine precise changes in the number of contacts, but it does exhibit a definite decrease in the number of contacts within the same chain as the γ module unfolds. Figure 2.34D displays the number of contacts where each residue composing the contact is in a different chain as a function of iteration step. This is dominated by contacts between each of the three chains involved in the section of coiled-coil included in the crystal structure. There is no apparent trend to the change in the number of contacts between different chains; this corresponds to a lack of dramatic change in the coiled-coil region of fibrin. Both of the conclusions drawn from Figure 2.34 B and D can be confirmed by watching the simulation (Figure 2.32). Figure 2.34C displays the number of native contacts where both residues are in the C chain as a function of iteration step. There is significantly less noise in this graph than in the number of native contacts (Figure 2.34B). The dramatic decreases in the number of native contacts in the C chain correspond to increases in extension of the γ module (Figure 2.34A). This indicates that extensions in the γ module correspond to restructuring of the native structure of the γ module.

For all 10 simulations of fibrin γ module unfolding due to 150 pN force applied to the 'A-a' knob-hole interaction, the number of contacts inside a single chain decreases over the course of the simulations (Figure 2.35A). Additionally, the number of contacts between residues in different chains remains constant over the course of the simulations (Figure 2.35B). This reaffirms what can be seen by watching changes to fibrin's structure in the simulations, namely that the γ module and not the coiled-coil region unfolds over the course of the simulation. This unfolding produces an increase in distance between the base of the γ module (γCys 153) and the 'A-a' interaction (GPRP Gly1). This is accomplished through a variety of unfolding pathways characterized by holding at different extensions for different time periods depending on the simulation (Figure 2.36). However, a few broad sweeping trends are dwell times at 120 Å and 220 Å extensions in most curves.

These data were used to determine critical contacts, residues associated with unfolding of different regions within the gamma module. This is accomplished by first identifying iterations associated with steps in the separation-time curves and dramatic decreases in the number of native contacts for each simulation. Then specific contacts broken at each of the iterations identified can be compared between all 10 simulations to determine contacts critical to unfolding the γ module. For instance, in Figure 2.34A there is an extension

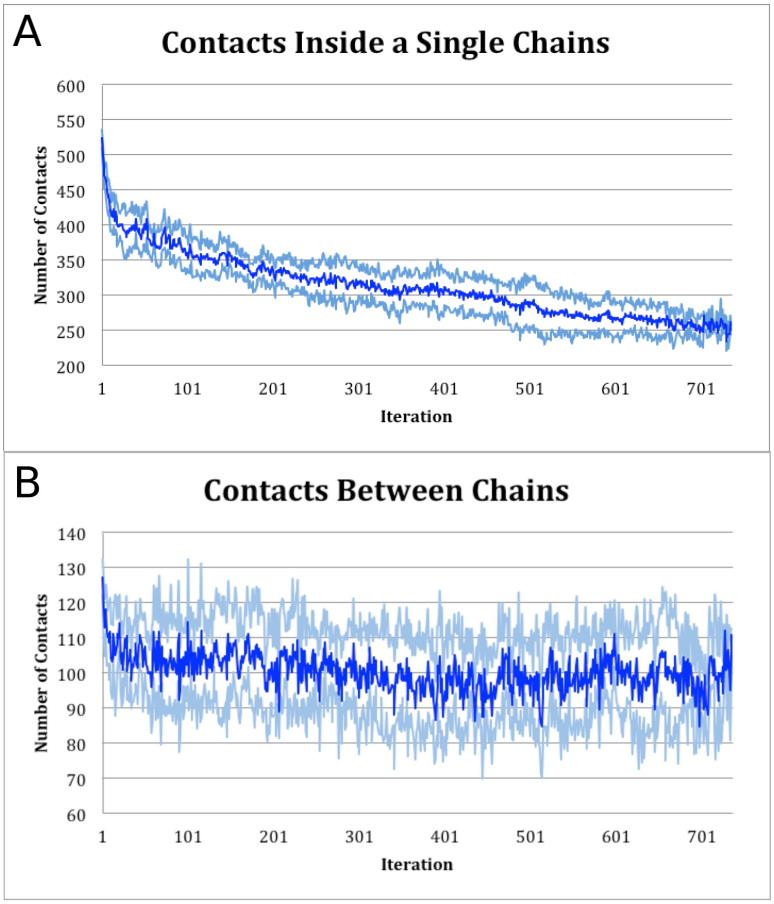

Figure 2.35: Average number of contacts for all 10 simulations where both residues are in the (A) same chain and (B) different chains versus iteration. The dark blue line is the average over 10 simulations and the light blue lines represent the upper and lower bounds to these results determined by the standard deviation of the average.

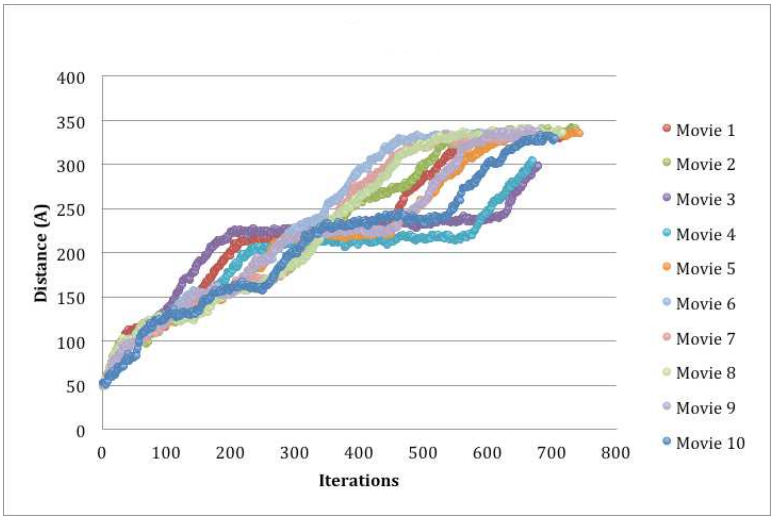

Figure 2.36: Average number of contacts for all 10 simulations where both residues are in the (A) same chain and (B) different chains versus iteration. The dark blue line is the average over 10 simulations and the light blue lines represent the upper and lower bounds to these results determined by the standard deviation of the average.

from 120 Å to 150 Å occurring around iteration 100. All native contacts ruptured within a few iterations of this event are recorded and compared to native contacts ruptured at a similar extension in other simulations. Simulations were grouped and compared based on the unfolding pathway they appeared to follow (Figure 2.33. Ruptures of native contacts frequently occurring in simulations were mapped out in a pseudo contact map and extensions produced by rupture were used to identify 9 native contacts that when broken were likely responsible for the simulated γ module unfolding.

The first 5 interactions all occur before the γ module reaches an extension of 140 Å, so prior to separation of the γ module into 3 different subdomains. Of these 4 sets of native contacts are most likely to be observed in the AFM experiments - γ 285-90:319-24, γ 301-5:382-3, γ 303-8:313-8, and γ 315-8:349-50.

The native contact γ 156-8:178-80 (Figure 2.37) is located at the base of the γ module near the coiled-coil region and gives an extension between $\sim$25 Å, of extension. This extension can occur either before or after the 'a' pocket separation from the rest of the γ module. However, this extension may not be measured in single-molecule AFM experiments due to the method of covalent attachment of fibrinogen a gold substrate by the free amines in the protein.

The rupture of γ 285-90:319-24, γ 301-5:382-3, γ 303-8:313-8, and γ 315-8:349-50 are associated with the separation of the 'a' pocket region from the bulk of the γ module. The break of native contacts γ 301-5:382-3 (Figure 2.37) is one of the initial steps in separation of the 'a' pocket and yields an extension of $\sim$20 Å. In the same region of the γ module, the rupture of γ 315-8:349-50 (Figure 2.37) provides extension of $\sim$25 Å

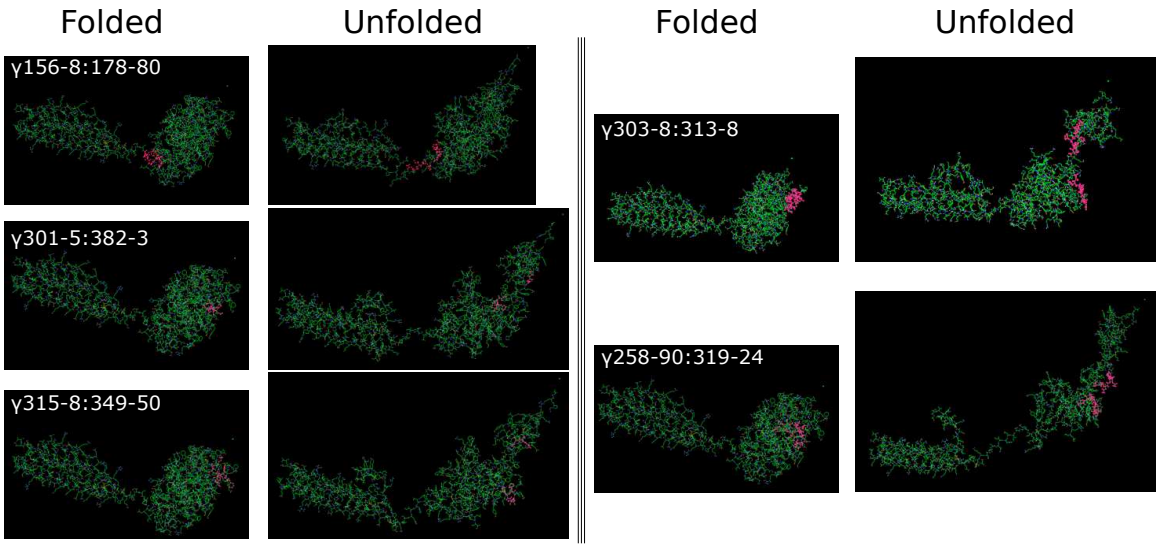

Figure 2.37: Images of native contacts implicated in force-clamp unfolding γ 156-8:178-80, γ 285-90:319-24, γ 301-5:382-3, γ 303-8:313-8, and γ 315-8:349-50. Purple region identifies the residues of interest before (left) and after (right) unfolding event.

associated with separation of the 'a' pocket. These two rupture events occur either at the same time or in the order listed. Sometimes occurring simultaneously with the previous two rupture events is the separation of native contacts γ 303-8:313-8 (Figure 2.37). In other simulations, this native contact will remain until the γ module has separated into 3 subdomains; however, it always produces an $\sim$30 Å extension. The rupture of native contacts γ 285-90:319-24 (Figure 2.37) usually occurs after previously mentioned interactions and as an independent unfolding event. After initial separation of the 'a' pocket region from the rest of the γ module, the native contacts γ 285-90:319-24 are located with the bulk of the γ module near the 'a' pocket. This unfolding event provides additional extension that separates the pocket region further from the rest of the γ module, $\sim$30 Å.

At longer extensions, the bulk of the γ module splits up into 3 subdomains. Rupture of native contacts γ 190-2:240-4 causes separation of the subdomain closest to the coiled-coil region and produces an extension of $\sim$25 Å. There are three sets of native contacts, γ 200-10:399-403, γ 204-6:240-8, and γ 245-9:277-81, that are consistently involved in the final separation of the γ module into the last 2 of 3 subdomains. The order at which these rupture events happen varies depending on the simulation, as discussed previously (Figure 2.33). However, these final extension events are likely not be measured in single-molecule AFM experiments because structural changes to the hole 'a' region would weaken the 'A-a' interaction and unfolding of the γ module can no longer be measured following rupture of the 'A-a' interaction in AFM experiments.

Simulated fibrin unfolding experiments showed γ module unfolding occurred through a series of steps - (1) reorientation of the protein along the axis of force, (2) separation of the 'a' binding pocket from the γ

module, (3) formation of three subdomains, and (4) final unfolding of the γ module and formation of beta strands near the 'a' pocket. This unfolding occurred through a variety of pathways with the most notable distinction being the order of formation of the three subdomains.

The total extension observed in these simulations was 30nm occurring through a variable number of steps always producing the same total extension. Extensions always present were an $\sim$3 nm, $\sim$12 nm, and $\sim$15 nm (Figure 2.36). The first extension was associated with reorientation of the γ module and the final $\sim$15 nm extension would not be observable in force-clamp experiments due to destabilization of the 'a' binding pocket. The middle $\sim$12 nm extension occurred in 1 to 3 steps of length $\sim$3, $\sim$3, and $\sim$6 nm, which are likely associated with observed unfolding steps in force-clamp experiments. There is variability in order observed unfolding; however, when the two smaller $\sim$3 nm extensions occur, they occur before the larger $\sim$6 nm extension. This indicates deviation from a Markovian model implying that some domains do not experience force equally to others over the course of the simulation. More work will need to be done to elucidate the differences between simulated and experimental kinetics of unfolding. Due to the similarity in lengths of each of these sections, it is difficult to explicitly identify subdomains associated with force-clamp extensions.

A variety of residues were implicated in unfolding events in the gamma module observed in simulation; however only γ 285-90:319-24, γ 301-5:382-3, γ 303-8:313-8, and γ 315-8:349-50 are likely to be observed in force-clamp experiments due to the their resulting extensions and location in the γ module. This method of analysis did not take into account the formation of new, strong contacts over the course of unfolding that could contribute to unfolding events observed in force-clamp experiments and further analysis would need to be performed in order to evaluate these effects.

Section 2.5: Conclusions and Future Work

In conclusion, I performed both constant-velocity and constant-force AFM force spectroscopy experiments to probe single-molecule fibrin unfolding through the 'A-a' knob-hole interaction. From these experiments, I acquired new information about the complex forced unfolding pathway of fibrin's γ module including the effect of different solution conditions, previously unseen intermediate states, complex unfolding kinetics, and residue contacts responsible for experimentally observed unfolding events.

Constant-velocity experiments, designed to explore the relationship between solution environment and the single-molecule mechanics of fibrin interactions, revealed that the single-molecule force rupture pattern depend on solution conditions. Specifically, (1) a correlation was established between conditions that suppress the forced dissociation characteristic of the 'A-a' knob-hole interaction and those that have been previously reported to inhibit fibrin polymerization (i.e., high temperatures and acidic pH), and (2) a relationship

was found between solution conditions that caused a decrease in the probability of a characteristic 'A-a' interaction contained event 4 and those associated with fine fibrin clots with thin fibers. Therefore, the extension of the γ module provided by forces applied to the 'A-a' knob-hole interaction are essential for the formation and integrity of fibrin fibers and the extension provided by single fibrin molecules through extension of the γ module has an impact on the size of fibers formed. Protofibrils have an inherent twist to them and may wrap around the fibrin fiber in order to form thicker fibers.(116; 137) The additional extension of the γ module could allow for the protofibrils to stretch permitting additional protofibril layers in thicker fibrin clots. In this way, SMFS experiments provide insight into the molecular mechanisms for larger scale clot behavior.

Constant-force experiments allowed for the investigation of low force unfolding domains and the direct investigation applied force's affect on unfolding kinetics. This research marks the first constant-force unfolding/unbinding study performed on fibrin and more broadly on protein unfolding produced through a force application to a physiologically relevant bond. Through the application of low forces over a prolonged time period, I observed fibrin γ unfolding through previously unseen intermediate states. Analysis of unfolding kinetics revealed the fibrin γ module unfolds through a complex energy landscape best described by glassy dynamics behavior, characterized by stretched-exponential unfolding. Monte Carlo simulations revealed that force-clamp experiments measured a fundamentally different unfolding pathway than previous constant-velocity experiments. Other molecules, such as ubiquitin,(87) have shown evidence of intermediate states and deviations from a simple two-state unfolding model; however, subdomains were not implicated in the observed behavior. This work marks the first systematic study into the role of subdomain unfolding as the source of deviations from the unfolding.

DMD simulations were used to visualize γ module domains unfolding as a result of constant force application to the 'A-a' knob-hole interaction. Simulated fibrin unfolding experiments showed γ module unfolding occurred through a series of steps - (1) reorientation of the protein along the axis of force, (2) separation of the 'a' binding pocket from the γ module, (3) formation of three subdomains, and (4) final unfolding of the γ module and formation of beta strands near the 'a' pocket. A variety of residues were implicated in unfolding events in the gamma module observed in simulation; however only γ 285-90:319-24, γ 301-5:382-3, γ 303-8:313-8, and γ 315-8:349-50 are likely to be observed in force-clamp experiments due to the their resulting extensions and location in the γ module.

The combination of force-clamp experiments, Monte Carlo simulations and DMD simulations elucidated fibrin γ module unfolding to a degree not previously achieved. The specific residues responsible for extension events observed in force-clamp experiments were identified through the use of DMD simulations. The extension events associated with γ 285-90:319-24 and γ 301-5:382-3 produced $\sim$3 nm extensions which together

produce the characteristic 6nm extension observed in force-clamp experiments. Monte Carlo simulations implicated the existence of multiple domains as the primary source of non-Markovian behavior observed in NEA analysis of force-clamp data. DMD simulations also showed multiple subdomains within the γ module, the earlier domains unfolding more rapidly than later domains. These simulations showed domains unfolding in order of their kinetic parameters (i.e., shorter lifetimes of conformational states earlier and longer lifetimes later) rather than the result of force-sheltered domains, which would produce short-lived conformational states following longer-lived conformational states. This level of detail into the mechanisms responsible for complex γ module unfolding would not have been possible without the combination of these there methods.

Preliminary experiments were performed to probe the reversibility of fibrin γ module unfolding. Because fibrin fiber extensibility is largely reversible,(73) the molecular mechanisms responsible for fiber extension must also be reversible. If unfolding of the γ module induced by force applied to the 'A-a' interaction contributes to the extensibility of fibrin fibers, then it may play a role in the reversibility. A variation of force-clamp called force quench allows for investigation of protein refolding under applied force.(138; 121; 139; 140; 141) Force-quench works by applying a constant force for a period of time to unfold the protein (just like force-clamp), then reducing the force for a period of time to allow the protein to refold, and finally the larger unfolding force is applied again to observe the presence or absence of unfolding events.

I performed preliminary force-quench experiments in which a 100 pN force was applied for 0.5 seconds to induce some unfolding in the γ module, followed by a 1 second 10 pN force application, and finally another 100 pN force applied until rupture of the 'A-a' knob-hole interaction. These forces and time scales were selected based on force-clamp experiments to be most likely to induce folding but still maintain the 'A-a' knob-hole interaction. Two sample force-quench curves are shown in Figure 2.38. In order for force-quench curves to provide useful information into unfolding, the curve must possess the following characteristic: (1) the first high force application must induce an unfolding event, and (2) the knob-hole interaction must remain intact through the final high force application. Because fibrin unfolding is inherently a stochastic process, these criteria dramatically reduce the number of force curves in a population that provide insight into unfolding. For this reason only 20 force-quench curves were collected and examined. Preliminary results indicated that 15% of the force curves exhibit refolding behavior, characterized by an unfolding step in both the first and second high-force application, for the initially investigated parameters. The majority of force-quench curves did not exhibit refolding as evidenced by a second unfolding step; however, some of these force curves displayed complex separation traces during the force-quench interval. More experiments should be performed in which the quenching force is adjusted in order to observe refolding behavior.

This collection of experiments informed our understanding of the mechanical properties of fibrin as they relate to blood clot formation and protein unfolding in general. In the larger scope of designing

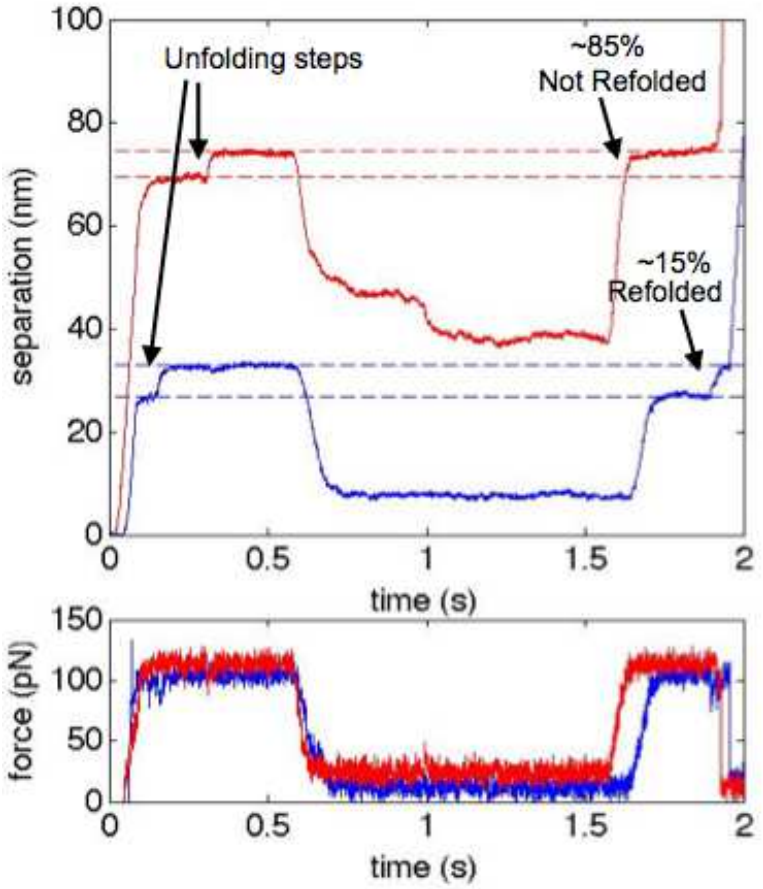

Figure 2.38: Representative force-quench results exhibiting both refolding and nonrefolding behavior of the γ module. (Top) separation-time traces acquired for force-quench experiment exhibiting refolding (blue) and no refolding (red). The percentage of refolded and not refolded traces are reported based on a population of 20 force-quench curves. (Bottom) Force-time plots of the 100 pN, 10 pN and 100 pN force pulses of 0.5 s, 1 s, and 0.5 s for each of the force-quench experiments. Note, the red and blue force curves have been offset slightly in force to allow better visualization of force data.

an instrument for mechanical investigation of cells, these experiments provide an ideal system on which to develop force application experimental methods and analysis pipelines which can be applied to single-molecule measurements on cells. In the next chapter I will develop experimental methods and analysis pipelines necessary for measuring the mechanical properties of cells.

CHAPTER 3: Understanding the Role of Nuclear Mechanics Using the Atomic Force Microscope for Single-Cell Force Spectroscopy Studies

Living cells possess the ability to sense, withstand and respond to external mechanical forces. These properties are essential to the physical integrity and biological function of the cell. The molecular mechanisms responsible for a cell's response to external force are especially of interest because of their downstream effects on gene expression, differentiation and motility. The nucleus itself has been implicated as a mechanosensor, with force-induced changes in nuclear structure directly affecting transcription; however, the process of mechanotransduction cannot be studied in isolation from cell mechanics.

The Atomic Force Microscope (AFM) has become ubiquitous in many cell mechanics studies, primarily due to its precision in force measurement (piconewtons), high spatial accuracy, and large dynamic range (hundreds of nanonewtons, depending on cantilever choice). In this chapter, I use the AFM to measure the mechanical properties of (1) two ovarian cancer cell lines with different known invasivity, (2) pancreatic cancer cells transfected with genes implicated in the epithelial-mesenchymal transition and (3) cytoplasts created by the removal of the nucleus from fibroblasts. Each of these studies provides insight into the role of nuclear mechanics, especially as it relates to mechanotransduction.

This chapter is comprised of the following key sections:

Section 3.1: Cell and Nuclear Mechanics Studies with the AFM

Mechanical forces play a crucial role in the growth and shape of virtually every tissue and organ in our bodies. However, relatively little is known about the mechanisms by which individual cells sense their mechanical environment and convert these mechanical cues into a biological response.

The transmission of mechanical force is essential to the physical integrity and biological function of healthy cells. Therefore, it is plausible to expect that deviations from normal cell mechanics and mechanotransduction may lead to various diseases. Indeed, researchers have found links between atypical mechanics of human cells,

and diseases and abnormalities such as cancer,(142; 143; 5; 144; 145; 146; 8) arthritis,(147) malaria,(148) and aging.(149; 150; 151) The molecular mechanisms responsible for the transmission of mechanical forces to the nuclear interior are of particular interest due to their downstream effects on gene expression, differentiation and motility. Recent findings have further supported the hypothesis that the nucleus itself may act as a cellular mechanosensor, bypassing the diffusion-based mechanosignaling through the cytoplasm to directly modulate the expression of mechanosensitive genes.(3; 32)

The process of mechanotransduction cannot be studied in isolation from cell mechanics, however. In order to understand how cells sense and respond, we must also understand how they deform and recover from physical disturbance. A cell's 'mechanical properties' broadly refers to a group of characteristics that define how a material responds to mechanical stimuli. Commonly, a material deformation in response to applied stress is reported as a modulus (e.g., Young's modulus) - the scaling between stress and strain of a solid material. Because cells are heterogenous materials composed of proteins, filaments and sub-cellular structures, one of the primary difficulties in cell mechanics is determining the origins of measured cellular mechanical properties. In particular, the nucleus is a significant contributor to whole-cell elasticity, which is stiffer than the cytoplasmic portion of the cell and results in mechanical response that deviates from models that define the cell as a simple, linear elastic material.(152; 153; 154)

Due to its versatility, the AFM is a prominent tool for the study of intrinsic cellular mechanical properties. The AFM possesses many qualities that are useful for biological studies, including (1) high vertical and lateral resolutions for precise force application and topographic information, (2) precise application and measurement of sub-nanonewton forces, and (3) the ability to probe a variety of sample geometries in natural conditions, such as buffer. The AFM can be used to directly manipulate cells to measure whole-cell and sub-cellular mechanical properties. A detailed description of AFM principles for cell mechanics studies can be found in Chapter 1 or instrument reviews.(155; 156). Briefly, AFM experiments are performed by applying force to the cell with a flexible cantilever, measuring small deflections as the cell is indented, and converting the deflections into units of force by approximating the AFM cantilever as a Hookean spring. The resulting force-indentation curves are then fit to an appropriate contact mechanics model, such as the Hertz model, to extract the Young's modulus of the cell or sub-cellular component.

In a step towards creating a versatile tool for understanding forces in biology and, more specifically, mechanotransduction, I describe in this chapter the the use of an AFM to measure the mechanical properties of single cells. I describe several experiments designed to understand cellular and nuclear mechanics in relation to cell function (mechanotransduction) and misfunction (cancer metastasis). Specifically, these experiments include:

1. determining the relationship between nuclear stiffness and migration in different ovarian cancer cell lines,

2. measuring subtle changes in the mechanical phenotype resulting from single genetic changes in pancreatic cancer cells and validating a new high-throughput cell mechanics assay, and

3. investigating the role of the changes in mechanical properties of de-nucleated cells on the aberrant mechanotransduction behaviors of cytoplasts.

These experiments require the development of a bead attachment protocol and data analysis pipeline discussed in Appendices I and D, respectively, to effectively and efficiently measure the desired mechanical properties. Overall, these experiments elucidate the role of nuclear mechanical properties in healthy mechanotransduction as well as the invasion and migration of cancer cell lines.

Section 3.2: Ovarian Cancer Cells Nuclear Stiffness Correlated to Metastasis

Cancer is characterized by a malfunction in the behavior of cells that undergo uncontrolled division, infiltrate and invade healthy body tissues, and migrate to distant sites throughout the body. Cancer cells possess the ability to successfully negotiate the metastatic process via complex and often contradictory physical interactions and mechanical properties.(157) As an example, cancerous tissue is stiffer than normal tissue,(144) but the cancer cells themselves are less stiff than healthy cells.(143) The correlation between a cell's ability to deform and the presence of different diseases is commonly accepted;(158) however, the mechanical properties of cells as a metric for understanding cancer have only recently become a focus of study.(143; 159; 145; 8; 146)

The emergence of the study of mechanical properties of cancer cells is partially due to the increase in information about the role of the nucleus in cell mechanics and mechanotransduction, especially as it relates to diseases.(160; 161; 162; 163; 32) The mechanical properties of the cell nucleus and their connection to the cytoskeleton play an essential role in migration.(164; 165) When a cell encounters constrictions in 3D migration, the stiffness and deformability of the nucleus has been found to be the rate-limiting factor.(164; 166) For this reason, the mechanical properties of the nucleus play a critical role in the spread of cancer cells through the basement membrane during metastasis. Therefore, studies of cancer cells should take into account the role of nuclear mechanics.

Another contributor to the increase in mechanical studies of cancer cells is the accessibility of a variety of biophysical techniques to probe the mechanical properties of cells, including membrane stretching, optical traps, micropipet aspiration, passive and magnetic beads, and atomic force microscopy. Owing to its versatil-

ity, the AFM has become a popular tool to study the intrinsic cellular mechanical properties associated with cancer cells.(167) A consequence of this variety in measurement techniques is the collection of sometimes contradictory measurements of mechanical properties such as stiffness. For instance, ovarian cancer cells have a range of reported stiffness values spanning several orders of magnitude (∼1 Pa to 10 kPa) depending on the employed technique.(8; 146)

The stiffness of ovarian cancer cell lines has been inversely correlated to migration and invasion;(8) however, these measurements have lacked precision in the locality of the mechanics measurement site, which is important for understanding the effect of the nucleus on mechanical measurements. In order to validate observed results with different mechanical techniques and, thus, reconcile currently differing stiffness measurements,(8; 146) I use the AFM to measured the mechanical properties of ovarian cancer cells with different known metastatic potentials such that I take into account the effect of the nucleus. Over the course of these investigations, I also measured an interesting effect of histone H2B fused green fluorescent proteins (GFP) on nuclear stiffness.

3.2.1: Experimental Methods

The day before AFM experiments, cells were plated in medium onto fibronectin-coated glass coverslips. Cells were plated onto the fibronectin-coated glass by trypsinization of a 50-90% confluent culture of SKOV3 and IGROV human ovarian cancer cell lines (from CISMM collaborator Professor Gerard C. Blobe at Duke University). The cultures were diluted back to about 30% confluence, and then an aliquot of cells was further diluted by at least 1/10 - 1/30 before plating in RPMI (Roswell Park Memorial Institute) medium with 5% serum and antibiotic/antimycotic at 1X. Cells usually attached within several hours, but were incubated overnight to allow cells to firmly attach before use.

On the day of AFM experiments, the samples were rinsed with fresh medium to remove loosely attached cells. The stiffness of the cells measured using an MFP-3D Bio AFM (Asylum Research, Santa Barbara, CA). For all AFM measurements, the cells were either unlabeled, stained on the day of the experiment with vital (live-cell) stain SYTO 82 nucleic acid label, or previously transfected with H2B-GFP. For the H2B-GFP samples, approximately 10-15% of cells possessed the fluorecently labeled nucleus desired. Then the sample was rinsed profusely with RPMI medium by removing liquid from the cloning ring, replacing with new medium, and repeating several times to remove loosely attached cells. And additional larger ring of vacuum grease was added onto gel surface concentric to the cloning ring to prevent spilling into the sensitive AFM electronics during the experiment. Then majority of solution was removed from the cloning ring, and the cloning ring removed from the gel surface. The sample was loaded on to the AFM stage and additional

medium added to form a small bubble in the inner vacuum grease ring.

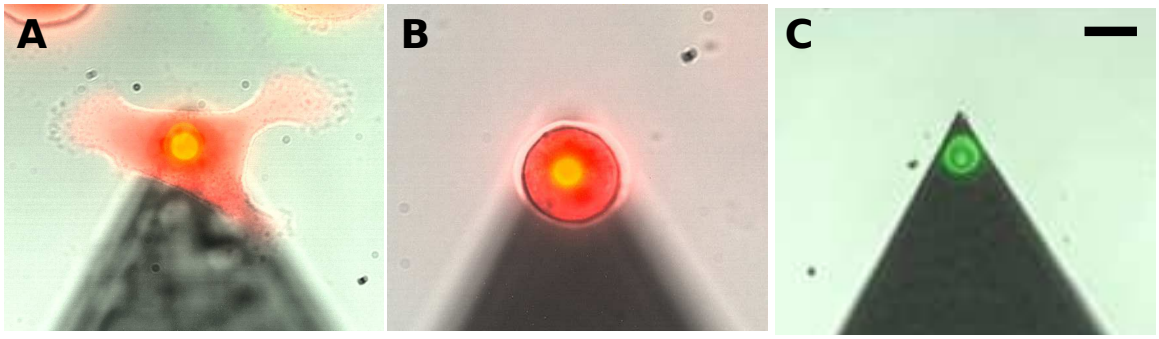

Figure 3.1: Images of cell indentation experiments. Overlaid, false-colored images of bright-field and two fluorescence images are shown for (A) SKOV, (B) IGROV, and (C) AFM tip. (A) SKOV and (B) IGROV images were taken immediately prior to AFM measurement over the nucleus with outline of the cell and triangular region of the cantilever from bright-field image (black and white), SYTO 82 throughout the cell but brightest in the nucleus (red), and 5 μm bead tip (green). Scale bar is 10 μm.

All experiments were performed using a TR400PSA cantilever with 5 μm yellow-green fluorescent polystyrene bead attached behind the pyramid tip using the protocol described in Appendix I. The cantilever spring constant (approximately 0.02 N/m) was measured in buffer using built in IGOR thermal tuning method after gluing the spherical probe, and prior to and following force measurements to ensure stability throughout experiments. The combined AFM optical microscope setup allows for precise positioning of the AFM probe over the desired region of the designated cells. Images of AFM experiment design, including attached bead and tip alignment, are in shown Figure 3.1. The beaded AFM cantilever was placed above either the center of the cell nucleus ('on-nucleus') or approximately 5 μm to the side of the nucleus ('off-nucleus'). The cantilever was moved at a velocity of 5 μm/s downward toward the cell until a trigger force of 0.5-1 nN (on-nucleus for IGROV and SKOV, respectively) or 0.1 nN (off-nucleus) was reached. The cantilever was then retracted at the same rate. For most cells, this was equivalent to $\sim$1.5 μm of indentation on-nucleus and $\sim$0.5 μm off-nucleus. Larger indentation were used on-nucleus to ensure that the mechanical properties of the nucleus contributed to the measured elastic modulus, while smaller indentations were used off-nucleus due to the smaller thickness of the cell at those locations. For each cell, ten force curves were collected at each location, separated by a 30 second dwell away from the cell surface. Force measurements were acquired for a minimum of 50 cells for each cell type over the course of three days of experiments.

Force curves were analyzed with custom MATLAB code to calculate the cell stiffness, described in detail in Appendix D. Briefly, the program identifies the contact point coordinates using a golden-section search in which a linear fit of the data to the left of contact point and a Hertz model fit to the data to the right up to a user defined maximum indent (on-nucleus $\geq$500 nm and off-nucleus 200-300 nm). The larger fit range

for on-nucleus measurements ensured that the nucleus contributed to the measured Young's modulus. The Hertz model is as follows:

$$F = \frac{4}{3}\frac{E\sqrt{R}}{(1-\nu^2)}\delta^{\frac{3}{2}} \tag{3.1}$$

where F is force, δ is indentation, E is elastic modulus, R is the tip radius, and ν is the Poisson's ratio. The point which attains the minimum total fitting error is selected as the contact point. Least squares fitting is applied to force-indentation data in the post-contact region of the force curve to the Hertz model to extract the Young's modulus of the cell. Then the cell types were compared with the standard t-test to determine difference.

3.2.2: Results

Examples of optical images obtained from previous on-nucleus cell indentation measurements are shown in Figure 3.1 for both SKOV and IGROV. The edges of the cell and triangular end of the cantilever can clearly be seen from the bright-field images (black and white). The cells have also been labeled with fluorescent SYTO nucleic acid stain, which is brightest in the nucleus but is also visible throughout the entire cell (red). The nucleus of the cells in the images shown in Figure 3.1 are directly below the AFM tip, which is false-colored green; however, due to the red green overlay, the tip appears yellow over the nucleus. These images show that the cells have a different morphology: the more invasive SKOV cells spread on the glass surface and frequently existing in single cell populations on the surface, while IGROV cells are more rounded and more likely to be found in clusters.

Representative force-indentation curves obtained from mechanical probing of individual cells are plotted in Figure 3.2A. The behavior of these curves is characteristic of their cell line. The primary cell lines of interest in this study were SKOV and IGROV; however, HEY cells have been used in both magnetic bead(8) and AFM experiments,(146) and are therefore a useful cell line for understanding the consistency and validity of our technique. Because the slope of each force-indenation curve is related to cell stiffness, differences between slopes for each cell indicate differences in stiffness between cells.

The force curves were analyzed with a Hertzian contact model to determine the corresponding Young's modulus of individual cells. Determination of the Young's modulus for HEY cells was straightforward, as the data were easily fit by the Hertz model (Figure 3.2A - solid green line) to yield a Young's modulus of 162 Pa for the shown curve. SKOV and IGROV cells exhibited more complex deformation, and the entire indentation depth could not be described by a single Young's modulus in the Hertz model. Shown in Figure 3.2 are two different Hertz model fits to the SKOV and IGROV data. Hertz model fitting is known to be sensitive to the determination of the contact point - the point where the tip comes into contact with the

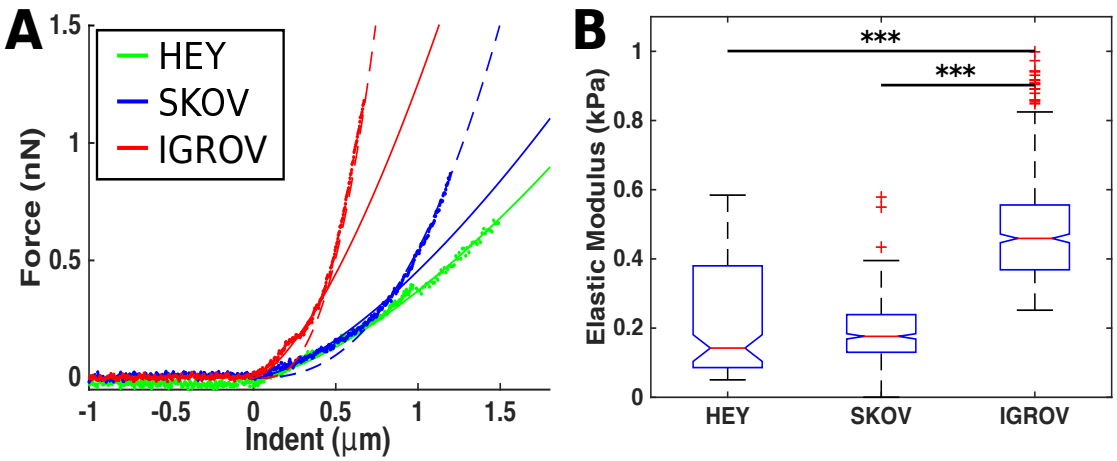

Figure 3.2: AFM stiffness measurements of ovarian cancer cells. (A) Representative force-indentation curves for HEY (green), SKOV (blue), and IGROV (red). The dots are actual data points from the force curve, and the solid line and dotted line are Hertz model fits to data with Young's moduli of 621 Pa (dashed red), 541 Pa (solid red), 550 Pa (dashed blue), 182 Pa (solid blue), and 162 (solid green). (B) Results of stiffness measurements for each cell type. Wilcoxon rank-sum test p-values established statistical significance between cells where *, **, and *** correspond to the $p<0.05$, $p<0.01$, $p<0.001$, respectively.

cell causing in the force curve - due to the subtlety of its identification on soft samples.(168) Within my MATLAB Hertz Analysis Package (Appendix D), I used a method to accurately find the contact points from soft samples developed by Lin et al.(169) The solid line is determined from a strict determination of contact point based on a deviation from baseline and shallow indentation depth Hertz fitting. The solid curve fits the data well for indentation depths of less than 0.7 μm and 0.5 μm for SKOV and IGROV cells, respectively. The dashed line is the Hertz model fit when the determination of the contact point is relaxed to allow for contact points at hundreds of piconewtons above baseline. The dashed curve fits the data well for deeper indentation depths but is a poor fit near the baseline. To avoid irreversible plastic damage to the cell, a nonlinear deformation regime, and effects from the underlying substrate,(156) all reported elastic modulus values are the result of fitting to the shallow indentation depth (solid lines). The data were fit to indentation depths of 300 nm and 500 nm for IGROV and SKOV cells, respectively, which correspond to approximately the same force application.

Some variability in force-indentation slopes and, thus, Young's modulus, is expected among individual cells from the same culture; therefore, measurements must be made using a sufficiently large data set that observations are indicative of the cell line. The consistency of SKOV and IGROV measurements was validated by comparing results for several days with different sample preparations. The results showed an expected variability in the stiffnesses of individual cells from the same line (Figure 3.3A). However, cells of the same type exhibited consistent elastic modulus distributions over several days with no significant difference

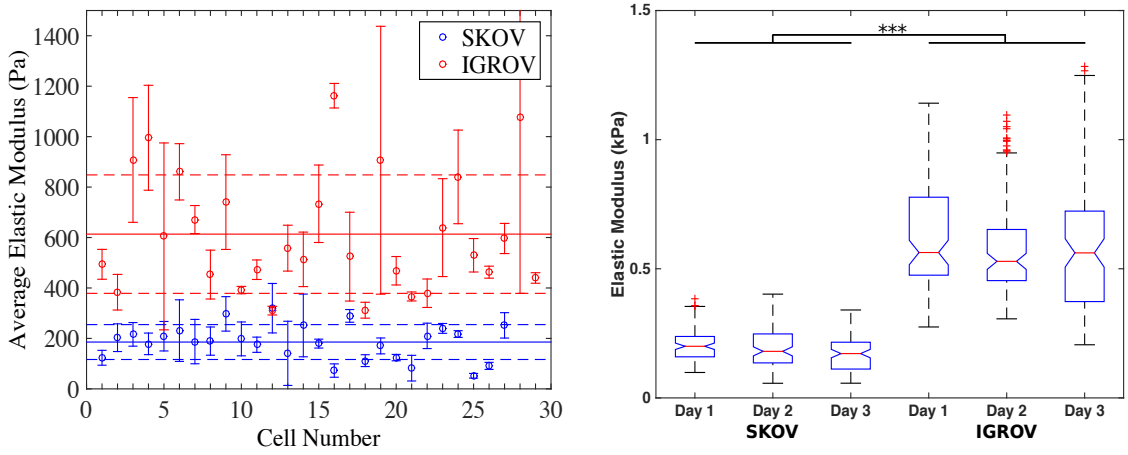

Figure 3.3: Reproducibility of AFM measurements of IGROV cells, which are stiffer than SKOV cells. (A) Average and standard deviation for the elastic modulus of each cell determined from Hertz model fit to all force curves acquired on-nucleus. Nearly 30 SKOV (blue) and IGROV (red) cells, all collected over the course of one day's experiments. The solid horizontal lines at ∼200 Pa and ∼600 Pa are the averages of SKOV and IGROV cells, respectively, with the standard error mean ranges shown with dashed lines. (B) Box plots of elastic modulus distributions for cells grouped by day. Wilcoxon rank-sum test p-values established statistical significance between days; the only significance was seen between SKOV and IGROV at $p<0.001$.

(Figure 3.3A). IGROV and SKOV cell populations on different days were significantly different in stiffness as determined by the Wilcoxon rank-sum test with p-values less than 0.001.

IGROV cells are significantly stiffer than SKOV and HEY cells. The distribution of Young's moduli for individual cells in each cell line is depicted in the box and whisker plots in Figure 3.2B. Each box plot represents the collection of the average elastic modulus for each cell, with the red line indicating the median of the data, the cental box representing the central 50% of the data, the notches setting the 25% and 75% quantile of the data, the Tukey whiskers indicating remaining data outside central box up to 1.5 times the height of the central box, and with all other remaining points marked by the red crosses as outliers. The large spread and lack of outliers represented for HEY could be representative of the cell line but is more likely the result of a lower cell count for this cell line. Only the force curves acquired on 10 cells are included for the HEY data set, as opposed to the 50 cells examined for SKOV and IGROV. HEY was included in these measurements due to its use in both magnetic bead and AFM measurements;(146; 8) it is therefore useful in understanding the relationships between existing reports on ovarian cancer cell stiffness as a marker of invasion potential. The measurement for average HEY stiffness is 216±89 Pa, a lower value than the reported 494±222 Pa reported by Xu et al.(146) but within a standard deviation of agreement. I also report the absolute Young's modulus of SKOV and IGROV cells to be 204±82 Pa and 578±123 Pa, respectively.

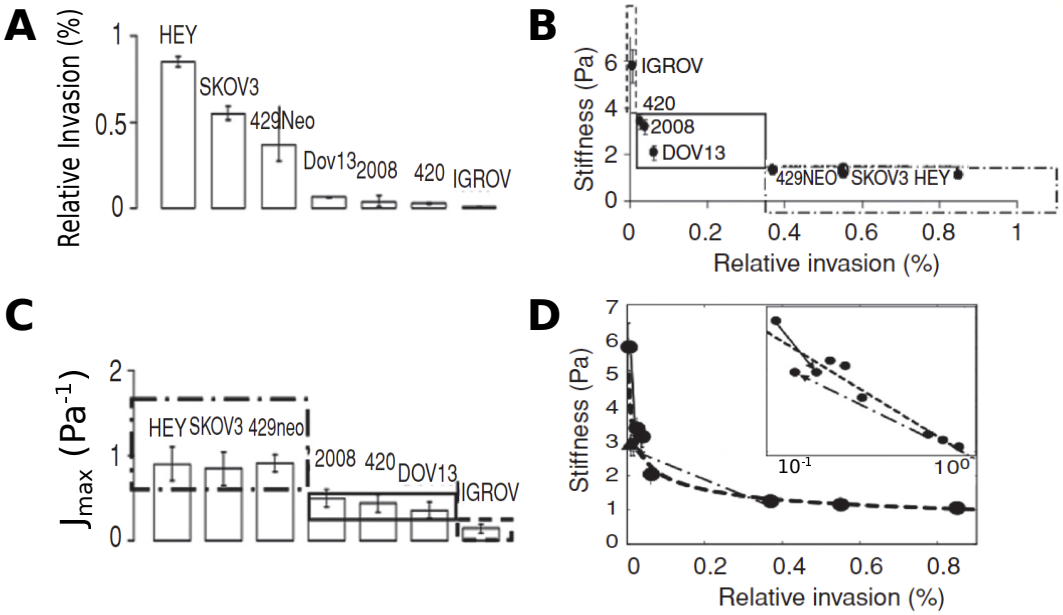

Figure 3.4: Stiffness correlates with invasion. (A) Invasion assays were conducted on the indicated cancer cell lines. Data represent the mean and standard error mean of three independent experiments. (C) Maximum compliance, where boxes indicate different scored regions based on relative invasion. (B) Stiffness values plotted relative to relative invasion, where the boxes represent the same scored regions as in C. (D) The same data as B with power law correlation. The inset shows power-law correlation on a log-log plot. Figures adapted from work published by Swaminathan et al.(8)

Previous studies performed in part by members of our lab demonstrated an inverse relationship between the stiffness of cancer cell lines and their relative invasion.(8) Figure 3.4 summarizes the results they found for a set of cells including SKOV and IGROV. Matrigel invasion assays showed the degree of invasiveness varied widely among individual lines (Figure 3.4A), with a two orders of magnitude change in invasivity between SKOV (∼0.65%) and IGROV (0.006%). Mechanical properties of the cancer cells measured using a 3DFM-magnetic tweezer system(170) found that the SKOV cell line was ten times more deformable than the IGROV cell line (Figure 3.4C). Using this data, the cancer cell lines were classified both by their stiffness and their invasiveness (Figure 3.4B), with both parameters falling into classes of low, medium, and high stiffness or invasiveness. Finally, a power-law relationship was identified relating these parameters (Figure 3.4D), the first evidence that metastatic potential measured through cancer cell invasion exhibits such an inverse power-law relationship with cell stiffness. These results exhibit the same inverse relationship between invasion and cell stiffness observed by Swaminathan et al.(8)

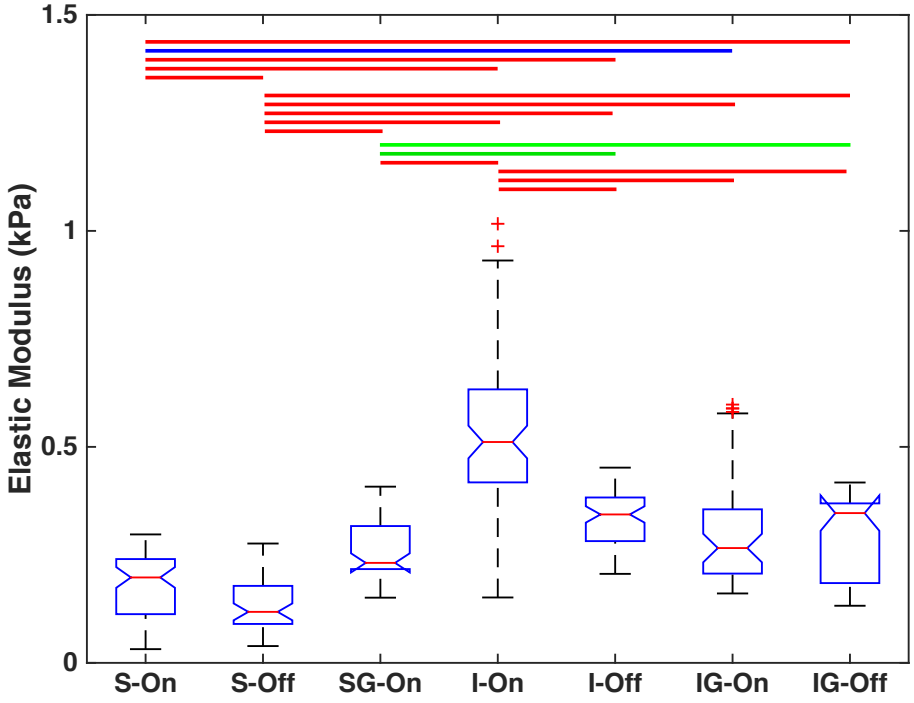

Figure 3.5: Cell stiffness measurements are dependent on location and grouping. Box plots of elastic modulus measurements for single SKOV cells on- (S-On) and off-nucleus (S-Off), groups of SKOV cells on-nucleus (SG-On), single IGROV cells on- (I-On) and off-nucleus (I-Off), and groups of IGROV cells on- (IG-On) and off-nucleus (IG-Off). Wilcoxon rank-sum tests established statistical significances between elastic modulus groups where $p<0.05$, $p<0.01$, and $p<0.001$ are represented by the blue, green, and red bars at the top of the plot, respectively

Up to this point, all AFM measurements reported were performed over the nucleus of single isolated cells. One of the benefits of using the AFM in lieu of magnetic bead measurements is the ability to probe different regions of the cell. With this additional degree of freedom, I gained insight into the role of different mechanical properties of components of the cell as they relate to cancer invasion. I performed AFM measurements at two locations – over the nucleus (on-nucleus) and one bead-diameter away from the nucleus (off-nucleus) – on at least 20 single cells. For single cells, the on-nucleus Young's modulus was significantly larger than the off-nucleus measurement (Figure 3.5). The contribution of the nucleus to AFM measured mechanics was most dramatic for SKOV cells, where the on-nucleus (S-On) measurement was twice that of the off-nuclues (S-Off), though a significant increase in stiffness was observed between IGROV on-nucleus (I-On) and off-nucleus (I-Off) measurements. Despite the reduced elastic modulus for the off-nucleus measurements for both cell types, the cells exhibited the same trend in stiffness both on- and off-nucleus: the IGROV cells were significantly stiffer than the SKOV cells.

Another factor which may play a role in cell stiffness is cell-cell interactions. To determine the impact of this factor, the stiffnesses of cells in groups were compared to those of singlet cells (Figure 3.5. The cells were plated onto glass with the intention of producing a sparse sample primarily consisting of single cells; thus, the elastic modulus reported for these cells in groups is the result of measurements on 10 cells for each condition. For the very few SKOV cells found in groups, the edges of the cells were not well defined; off-nucleus measurements were therefore not collected. IGROV cells were predisposed to growth in groups rather than existing as singlet cells. I was therefore able to locate groups of cells in which both on- and off-nucleus measurements were made. The on-nucleus elastic modulus for SKOV cells in groups (SG-On) was not significantly different from that of single SKOV cells (S-On); however, the on-nucleus elastic modulus for IGROV cells in groups (IG-On) was significantly smaller than that of single IGROV cells (I-On) and comparable to the elastic modulus of off-nucleus measurements (I-Off and IG-Off). Despite the changes in mechanics, both IGROV and SKOV cells were distinguishable in stiffness for all conditions.

The final parameter investigated was the effect of nuclear labels on the cells mechanical properties. An additional reason for choosing these cells was that their dramatic mechanical differences made them ideal candidates for a comparative study of strain propagation to the nucleus with the combined AFM and pathway rotated imaging system. This system and the demonstrative experiments performed are detailed in Chapters 4 and 5. An ideal method to clearly visualize the nucleus and internal structures for these studies would be to transfect the cells with H2B-GFP.(171) The results of H2B-GFP transfection on mesenchymal stem cells performed in CISMM collaborator, Professor Farshid Guilak's laboratory at Duke University (now at Washington University, Saint Louis) is shown in Figure 3.6A. Both the plan- and side-view images of the cell produced well-defined boundaries of the nucleus and structured regions within. The image quality of the

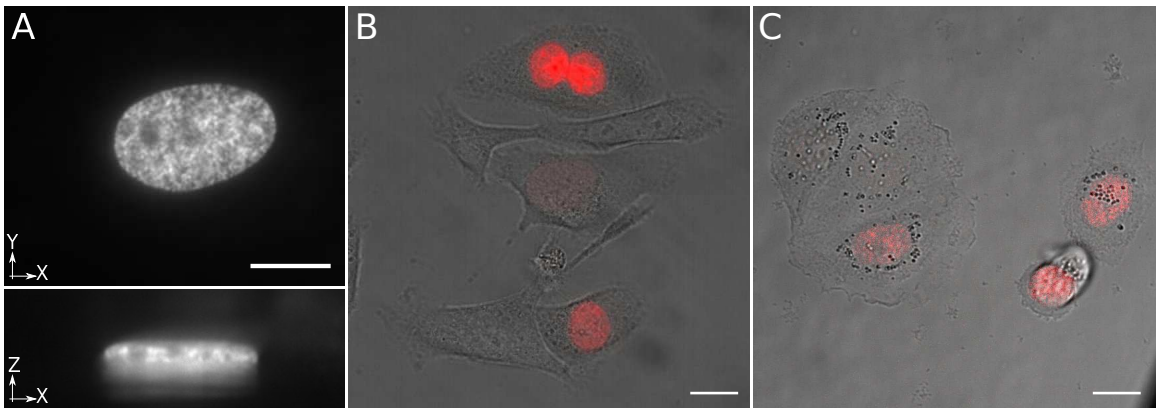

Figure 3.6: Fluorescent nuclei of H2B-GFP labeled cells. (A) MSC cell nucleus in standard microscope plan-view (top) and a pathway rotated side-view (bottom). More details on side-view imaging in Chapters 4 and 5. Fluorescence H2B-GFP (red) and bright-field (grey) overlaid images of (B) SKOV and (C) IGROV cells. All scale bars 10 μm

side-view image showed some background noise due to the use of broad rather than light sheet illumination, reflections off the glass surface correctable by plating onto a polyacrylamide surface, and the very thin nature of the MSCs nucleus height. However, the initial success of MSC imaging lead to the exploration of GFP-H2B transfection of both SKOV and IGROV cells.

Prior to performing any studies of cell deformation with our new side-view system (Chapter 4), changes in behavior of the ovarian cancer cells were noticed between H2B-GFP transfected and unlabeled cells. Both SKOV and IGROV cells were transfected with H2B-GFP (Figure 3.6B and C). The intensity of H2B-GFP in the nucleus was larger for SKOV cells than IGROV, indicating more GFP in the nucleus of SKOV cells. Moreover, the morphology of the transfected cells differed from unlabeled cells. This difference was most pronounced in SKOV cells, which became more rounded and more likely to grow in clusters than their unlabeled counter parts. Additionally, both cells seemed to divide more slowly, as they took longer to reach confluence. Therefore, I decided to perform on-nucleus stiffness measurements of the H2B labeled cells to determine if the H2B-GFP in the nucleus also effected the mechanical properties. Not all cells in a population were labeled, so on-nucleus AFM measurements were acquired for unlabeled and labeled cells in the same sample. The results of these measurements are in Figure 3.7. SKOV-H2B cells (SH2B) exhibited a significantly larger elastic modulus than the unlabeled SKOV cells. Moreover, the elastic modulus of SKOV-H2B cells was comparable to the elastic modulus of IGROV cells. Finally, on-nucleus AFM measurements of SYTO labeled SKOV and IGROV cells (SSyto and ISyto, respectively) validated that SYTO had no effect on elastic modulus for either cell type.

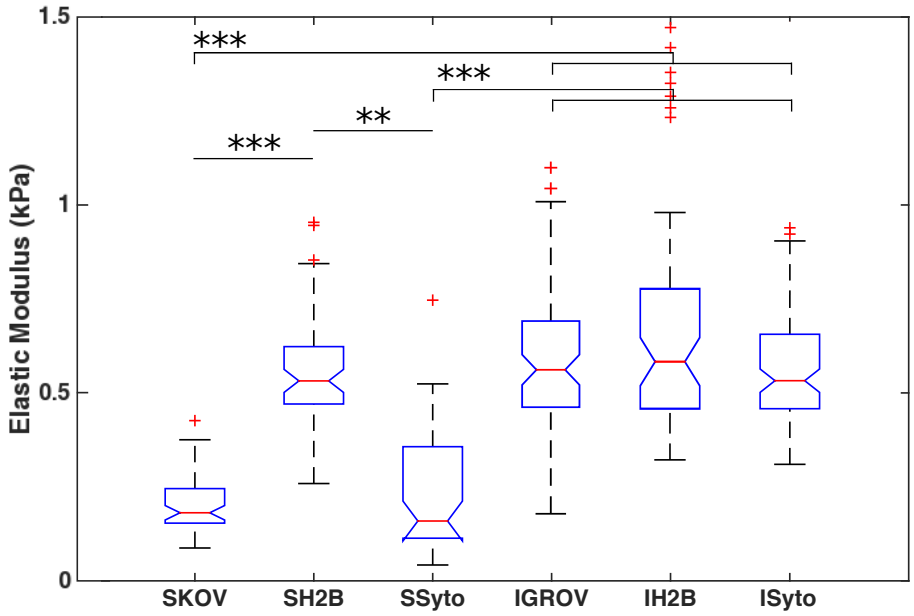

Figure 3.7: H2B-GFP affects the elastic modulus of SKOV cells. Box plots of elastic modulus measurements for unlabeld SKOV (SKOV), H2B-GFP SKOV (SH2B), SYTO labeled SKOV (SSyto), unlabeled IGROV (IGROV), H2B-GFP IGROV (IH2B), and SYTO labeled IGROV (ISyto). Wilcoxon rank-sum tests established statistical significances between elastic modulus groups where *, **, and *** represent $p<0.05$, $p<0.01$, and $p<0.001$, respectively.

3.2.3: Conclusions

The results of AFM measurements described in the previous sections mechanically distinguished ovarian cancer cells, IGROV, and the more invasive phenotype, SKOV. Specifically, the experiments showed that more invasive SKOV cells were softer than less invasive than IGROV cells. AFM on-nucleus and off-nucleus measurements were able to identify the same difference in stiffness, but the difference was more dramatic on-nucleus, implicating changes in nuclear mechanics related to invasion.

These are the first AFM indentation experiments on SKOV and IGROV ovarian cancer cells. The reported stiffness values are in general agreement with other AFM cell stiffness measurements(146) and the HEY cell measurement was within error of previously reported values.(146) These are not the first measurements to determine cell stiffness as a marker for metastatic potential in ovarian cancer cells. Previous experiment from our group by Swaminathan et al.(8) reported stiffness measurements with magnetic tweezers were inversely correlated with relative invasion of ovarian cancer cells, including SKOV and IGROV. We did not necessarily expect indentation experiments to yield the same correlation between stiffness and invasion as magnetic tweezers measurements due to the inherent differences in measuring stiffness. The AFM applies nanonewton forces to indent the cell and measure the bulk Young's modulus of the cell membrane, cytosol, cytoskeleton, and nucleus. In contrast, magnetic beads are attached to the cell membrane and measure the stiffness of the membrane and cytoskeleton. Despite intrinsic differences in the component of the cell measured, both techniques reflected a difference in mechanical properties reflective of the cell types' metastatic potential.

Due to the choice of AFM as a measurement technique, I was able to probe different regions of the cells to determine the contribution of the nucleus to cancer cell mechanics. AFM measurements showed the same inverse correlation between invasion and the mechanical properties of the cell in off- and on-nucleus measurements. AFM off-nucleus measurements yield an elastic modulus reflective of the cytoplasm, and to a lesser extent the membrane(172; 173) and molecular brushes (e.g., microvilli, microridges, glycocalyx).(174) Where as, AFM on-nucleus measurements yield a bulk elastic modulus reflective of contributions from the cytoplasm and nucleus. Because direct linkages between the cell membrane and nucleus (LINC complexes) can form, magnetic bead experiments may indirectly be probing the contribution of the nucleus to cell stiffness; however, it is difficult to tell whether differences in stiffness between cell lines are due to changes in cytoskeletal stiffness or to contributions from the mechanical nucleus, and changes are primarily attributed to changes in cytoskeletal stiffness. In contrast, with AFM measurements in two locations (on-and off-nucleus) we were able to indirectly observe mechanical differences between the nuclei of SKOV and IGROV cells. If the mechanical properties of the nucleus were unchanged and only the cytoskeleton and membrane were different, then both AFM (on- and off-nucleus) and magnetic bead experiments would observe a difference in

stiffness. However, because there are two measurement locations for AFM experiments, the stiffness increase on- and off-nucleus would be the similar for this scenario. Because we observe a larger change in stiffness on-nucleus, we concluded that the nucleus as well as the cytoskeleton of these two ovarian cancer cell lines are mechanically different. This could be an essential difference that allows SKOV cells to migrate more rapidly than IGROV cells throughout the human body. However, to confirm the validity of this interpretation and clarify deviations of AFM measurements from simple Hertzian behavior (Figure 3.2), information about subcellular structural deformation simultaneous with force data is required. The necessity of structural information in the direction of applied prompted the design and implementation of a combined AFM and pathway rotated imaging system, disucssed in Chapters 4 and 5.

High-resolution imaging of the nucleus and subnuclear structure of living cells has been achieved in cancer cells using a fusion protein of histone H2B and green fluorescent protein (GFP).(171) The H2B-GFP fusion protein incorporated in to the nucleus and the cells still went through the cell cycle; however, I observed a change in mechanical properties of transfected cells. I found that SKOV cells transfected with H2B-GFP exhibited a significantly larger elastic modulus than unlabeled SKOV cells. There was no apparent change in stiffness for transfected IGROV cells; however, these cells were less brightly labeled. This may indicate a density of label-dependent change in stiffness, the result of more protein in the nucleus increasing the Young's modulus. This could be investigated by determining the change in stiffness as a function of fluorescent intensity in the nucleus. Alternatively, the effect of H2B-GFP on the mechanical properties of the nucleus could be dependent upon cell line. More AFM indentation data is required to fully explore whether the change in stiffness is due to the cell line or concentration of H2B-GFP. The live-cell nucleic acid label SYTO did not have any effect on the apparent elastic modulus measured in AFM experiments. Therefore, experiments exploring nuclear deformation with simultaneous side-view imaging (Chapters 4 and 5) used SYTO to observe changes in nucleus and subnuclear structure. Initial results of comparisons of nuclear deformation between SKOV and IGROV cells using the new simultaneous AFM and side-view imaging technique can be found in Chapter 6 and Appendix K.

In conclusion, AFM measurements of cell stiffness identify a correlation between changes in cytoplasm and nuclear stiffness with reported migration and invasion. The relative stiffness of the nucleus presumably plays a role in the ability of SKOV cells to migrate more rapidly throughout the human body than the less invasive IGROV cells. Additionally, I observed an increase in nuclear stiffness as a result of H2B-GFP transfection into SKOV cells. Despite having little effect on the cell cycle, H2B-GFP effects the inherent mechanical properties of the nucleus. Thus, AFM measurements result in a greater understanding of ovarian cancer mechanics as related to invasion phenotypes and motivate future instrument design for simultaneous imaging in the direction off applied load.

In the next section, the AFM was used in a similar study to distinguish relatively subtle changes in the mechanical phenotype of pancreatic cancer cells resulting from single genetic changes. In addition to a mechanical understanding of cell response, the AFM provided an independent method of validation for a new high-throughput microscope.

Section 3.3: Mechanical Stiffness Correlates to Invasion in Pancreatic Cancer Cells.

As discussed in Section 3.2, cancer cells are often characterized by their ability to spread from one part of the body to another in a process referred to as metastasis. Studies have shown that not only is there a mechanical difference between healthy and cancerous cells,(157; 143) but there is also a relationship between the mechanical stiffness and relative invasiveness in multiple cancer cell types.(146; 175; 159; 176; 177; 8) Tumor of the pancreas is one of the most lethal forms of cancer in the developed world because of the difficulty of its early detection and its aggressive propensity for invasion, migration and metastasis.(5) Changes in mechanical deformability of the cells have been examined as possible pathways that facilitate easier migration and increased metastatic competence of pancreatic tumor cells(145; 178)

In a recent paper accepted to *Scientific Reports*, we presented an automated array high-throughput microscope (AHTM) capable of screening for changes in mechanical phenotype of cancer cells.(179) Over the course of this study, the AFM was used to validate characterization of relative compliance of human pancreatic ductal epithelial cells (HPDE), h-TERT transformed HPDE cells (HPNE), and four gain-of-function (GOF) constructs. The expression of GOF versions of a single gene involved in cancer biology produce detectable changes at the phenotypic level that can be measured using mechanical techniques. HPDE cells were stably infected with genes for H-Ras (HRASG12V),(180) Myr-AKT (myristolated-AKT),(181; 182; 183) Bcl2,(184; 185; 186) and TβRI,(187; 188; 189; 190) as well as wild-type BCL-2.(185; 186)

The results of this study were agreement with the results of the AHTM, AFM and invasion assay for distinguishing both the relatively subtle changes engendered by single genetic changes and the larger difference between normal and oncogene-expressing cells. The AFM results consistently resulted in a measured decrease in stiffness corresponding to cells with increased invasion results.

3.3.1: Experimental Methods

For details on preparation of gain-of-function cultures of HPDE cells and validation of activating pathway component expression in HPDE stable cells, please refer to publication Cribb et al.(179) Briefly, HPDE cells from Dr. Ming-Sound Tsao (University Health Network; Toronto, Canada) were infected with constructs obtained from Dr. Kris Wood(191) in Professor Gerard C. Blobe's lab and validation of activating pathway

was verified prior to AFM experiments. Then the day before AFM experiments, cells were plated in their preferred medium onto fibronectin-coated glass coverslips. On the day of AFM experiments, the samples were rinsed with fresh medium to remove loosely attached cells. The stiffness of all human pancreatic cells and variants were measured using an MFP-3D Bio AFM (Asylum Research, Santa Barbara, CA). For all AFM measurements, cell imaging was completed with bright-field optical microscopy by AFM combined inverted optical microscope (IX71, Olympus) so that cells were not fluorescently labeled.

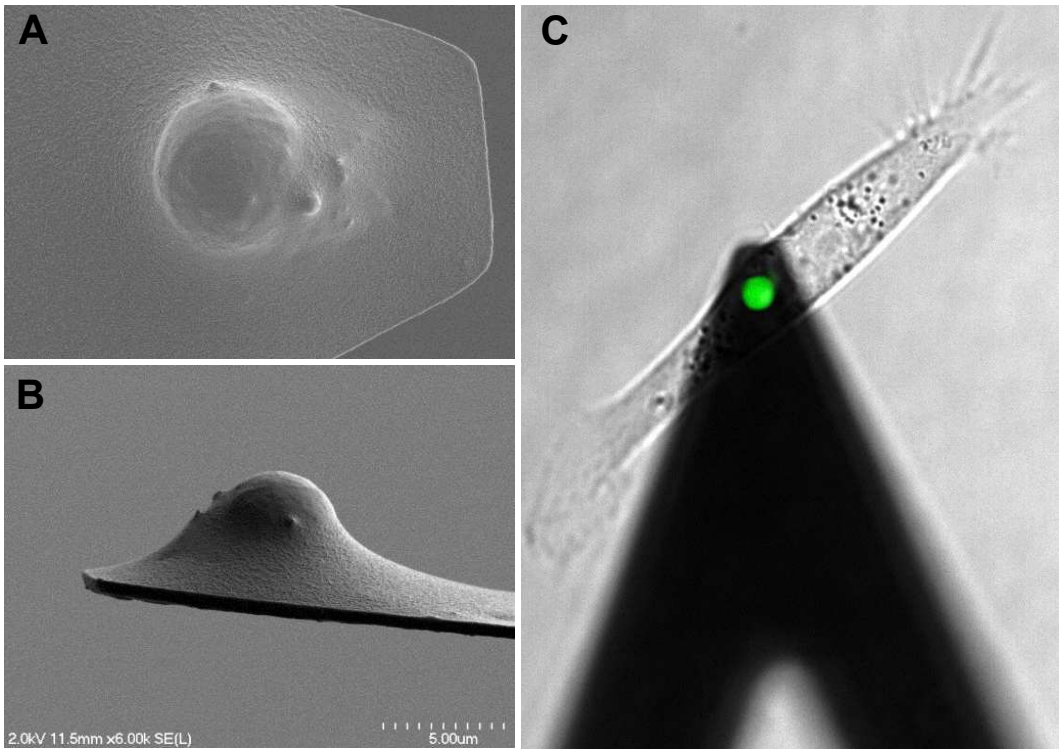

Figure 3.8: Scanning electron microscope images of 5 μm bead attached to TR400PSA pyramid tip from (A) top-view and (B) side-view. (C) Bright-field and fluorescence images overlaid to show the alignment of YG fluorescent bead over HPDE cell.

AFM force curves were collected and analyzed as previously described in Section 3.2.1 to determine the elastic modulus for each cell location. Images of AFM experiment design, including attached bead and tip alignment, are in Figure 3.8. The beaded AFM cantilever was placed above either the center of the cell nucleus ('on-nucleus') or approximately 5 μm to the side of the nucleus ('off-nucleus'). The cantilever was moved at a velocity of 5 μm/s downward toward the cell until a trigger force of 1 nN (on-nucleus) or 0.5 nN (off-nucleus) was reached. The cantilever was then retracted at the same rate. For most cells, this was equivalent to $\sim$1 μm of indentation on-nucleus and $\sim$ 0.5 μm off-nucleus. Smaller indentations were used off-nucleus due to the smaller thickness of the cell at those locations. For each cell, ten force curves were collected at each location, separated by a 30 second dwell away from the cell surface. Force measurements

were acquired for a minimum of 30 cells for each cell type over the course of two days of experiments. For the purposes of this study and comparison to other techniques, stiffness values were reported as compliance (1/stiffness).

Additionally, a standard Matrigel invasion assay and multiple passive bead rheology measurements on the AHTM system were performed with details described elsewhere.(179)

3.3.2: Results

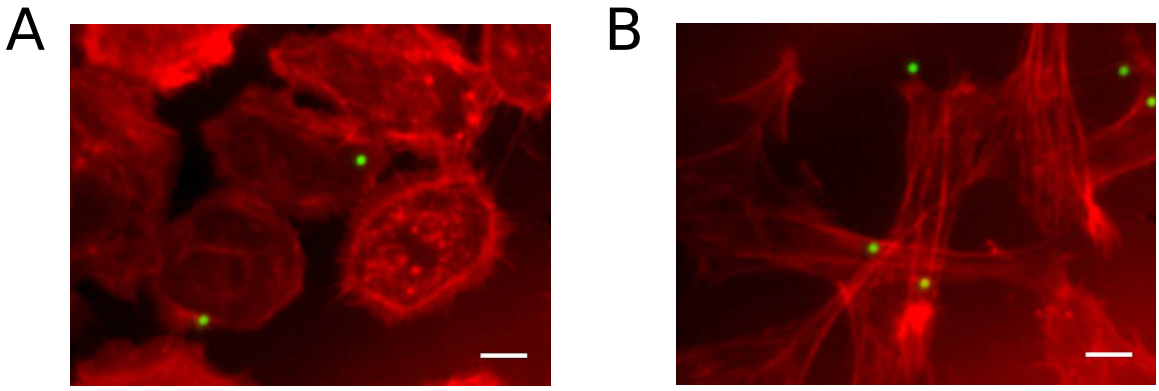

Figure 3.9: Imaging showing different morphology of HPDE and HPNE cells. (A) HPDE and (B) HPNE cells imaged with the AHTM in the 490 nm and 575 nm channels and merged in ImageJ. 2 μm YG beads are shown in green (12 ms exposure) and 568 alexafluor phalloidin stained F-actin in red (500 ms exposure).

Nearly all pancreatic cancer involves malignant transformation of pancreatic epithelial duct cells, and mutations in the KRAS oncogene are present in over 90% of metastatic pancreatic cancers.(192) We used HPNE cells as our model invasive cell line, comparing them to non-transformed HPDE cells. The HPDE cell line was originally derived from a normal pancreas portion and exhibits many features of normal pancreatic duct epithelial cells, including expression of wild type KRAS.(193) HPNE cels on the other hand express mutant KRAS associated with tumorigenesis. Figure 3.9 shows both cell types cultured onto a plastic-bottomed, 96-well plate, labeled with alexafluor phalloidin stained F-actin to clearly delineate actin filamints and cell boundaries, and decorated with fibronectin-coated 2 μm yellow-green microbeads. These images were acquired on the AHTM and clearly show the difference in morphology between the two cell lines. Similar differences were seen in AFM experiments except unlabeled cells were imaged in bright field.

Studies recently published by the Wood laboratory describe a GOF library of pathway-activating lentiviral constructs and its application of discovering pathways that confer resistance to targeted anticancer therapies.(191) To determine if mechanical changes in phenotype related to invasion, I used the AFM to measure stiffness of cells with 4 constructs from that library. The H-Ras (Ras pathway) and TGF-β receptor-

type I (TβRI; TGF-β pathway) GOF constructs were chosen based on their known effects as an oncogene and in initiating TGF-β signaling, respectively.(188; 190; 194; 189) Myristoylated-Akt (PI3K/AKT/mTOR pathway) and BCL-2 (intrinsic apoptosis pathway) GOF constructs were chosen because of their known roles as genes promoting growth and suppressing apoptosis during cancer progression.(182; 183; 185; 186)

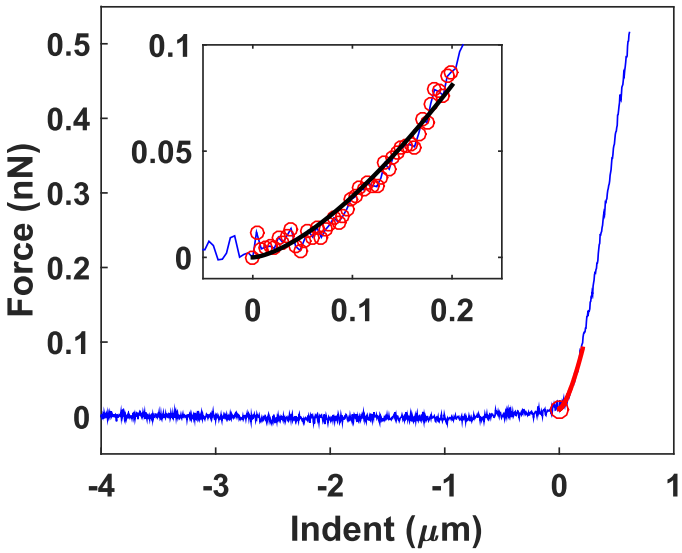

Figure 3.10: Force-indentation curve acquired over the nucleus of a CC cell. The larger plot shows the entire force-indentation curve (blue), contact point determined by custom MATLAB code (red circle), and the Hertz model fit (red line) for 200 nm indent. The inset shows a detailed view of the Hertz model fit (black) with an elastic modulus of 422 Pa to the data points from 0 up to 200 nm indent shown in red. The units on both the inset and main axes are the same

The result of a representative AFM measurement and analysis for a single force curve is shown in Figure 3.10. The data measured no force as the AFM tip approached the cell, then an increase in force as the AFM tip indents the cell. There was also a retraction portion of the curve (not shown) which exhibited little or no adhesion for all cell types. A Hertz model fit to force measurements on HPDE cells yielded average Young's modulus of $\sim$0.5 kPa. This measurement is in agreement with previously reported values for the same cell lines.(143; 195; 196) However, for ease of comparison with the other methods – invasion assay and AHTM – reported in this study, Young's modulus measurements were reported as their inverse, compliance, in units of 1/kPa. Therefore, HPDE cells have a compliance of 2 (1/kPa) with stiffer cells reporting a lower compliance and softer cells reporting a higher compliance.

AFM measurements were performed on HPDE, control construct (CC), four gain-of-function (GOF) constructs, and HPNE cell for $>$ 25 cells of each type in two locations (Figure 3.11). Wilcoxon rank-sum tests with Bonferroni-corrected p-values established statistical significances between constructs using AFM. The abbreviated labels HPDE (DE), construct control (CC), H-Ras (H-), Myristoylated-Akt (My), TβRI

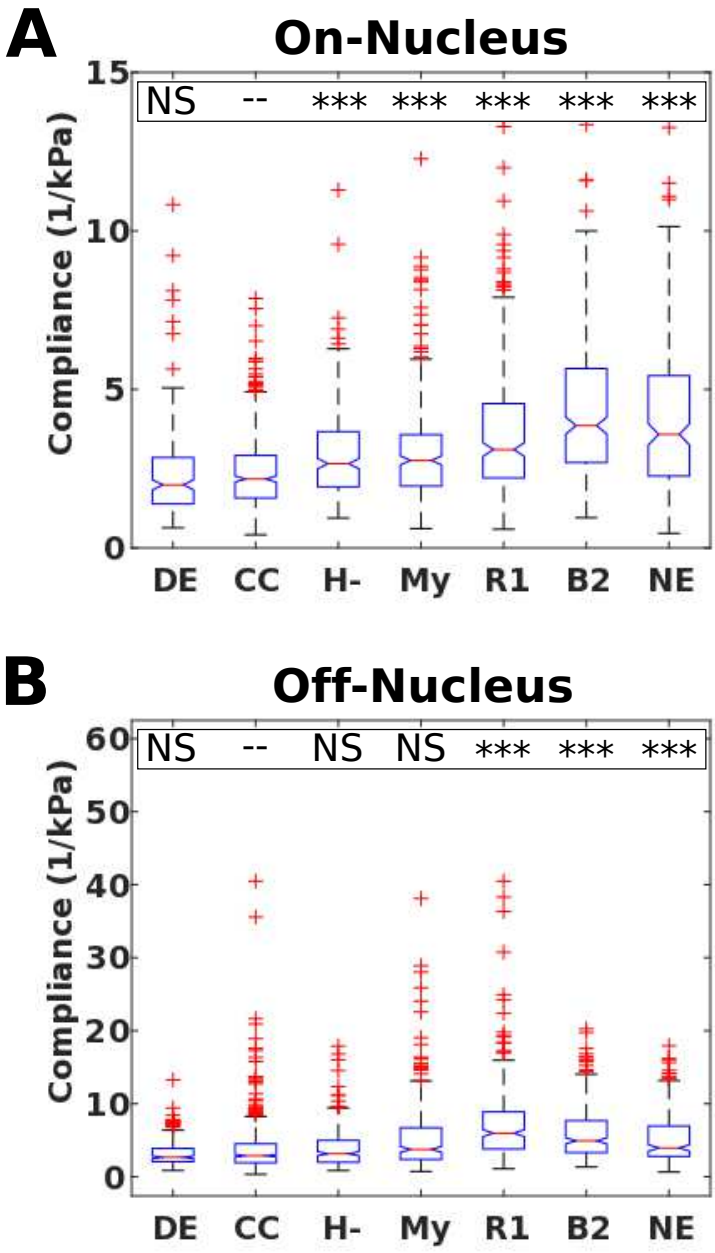

Figure 3.11: AFM compliance data for cells. (A) 'On-nucleus' compliance acquired with bead-tip directly over middle of nucleus and (B) 'off-nucleus' compliance acquired one one bead diameter away from the nucleus on each cell type. Wilcoxon rank-sum tests with Bonferroni-corrected p-values established statistical significances between constructs using AFM where *, **, and *** correspond to the $p<0.05$, $p<0.01$, and $p<0.001$, respectively. The abbreviated labels are HPDE (DE), construct control (CC), H-Ras (H-), Myristoylated-Akt (My), TβRI (RI), BCL-2 (B2), and HPNE (NE).

(RI), BCL-2 (B2), and HPNE (NE) were used for Figures and Tables. For 'on-nucleus' measurements, made with AFM bead-tip directly over the middle of the nucleus, the constructs generally displayed intermediate compliances between CC and HPNE, except for BCL-2 expressing cells which returned a larger median compliance than even HPNE cells. The difference between BCL-2 and HPNE cells, however, was not statistically significant at the 0.05 level. When inverted, the resulting median compliance values, which ranged between 2 and 4 (1/kPa), correspond to a stiffness of 500 Pa in the HPDE and CC cells, and to 250 Pa in the HPNE cells.(143; 195; 196) AFM 'off-nucleus' measurements, acquired one bead diameter away from the nucleus, produced large compliance (i.e., less stiff) and more spread in the reported for all cell types. Only BCL-2 and TβRI were significantly softer than the control with reported median compliance values larger than HPNE cells. The difference between these constructs and HPNE cells, was not statistically significant at the 0.05 level.

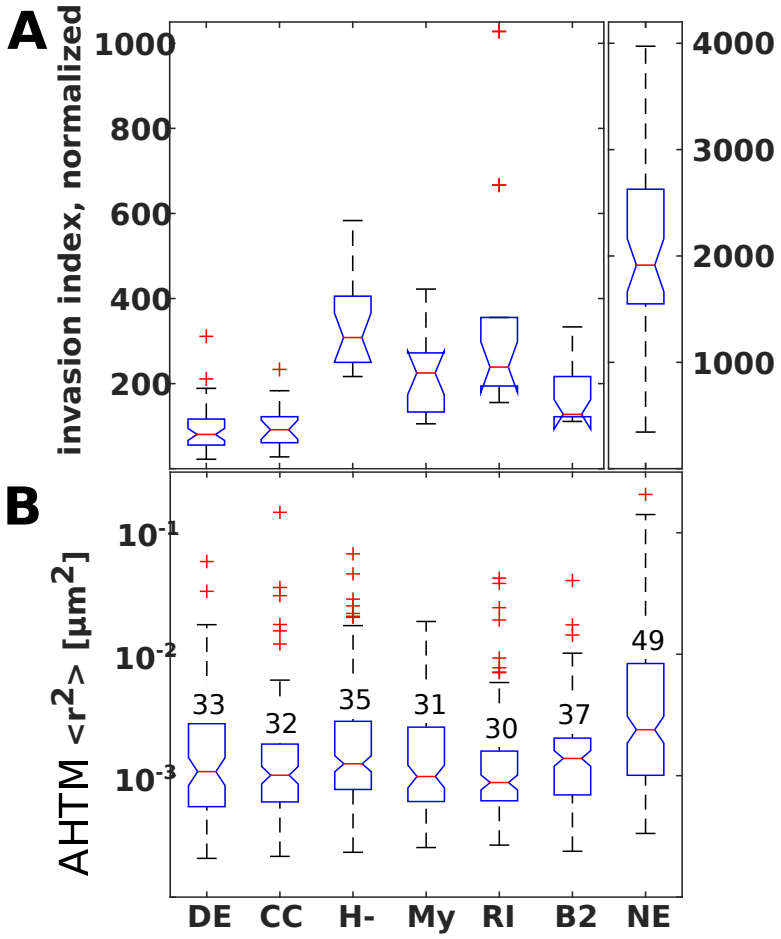

Figure 3.12: Results of comparative analysis methods - AHTM and invasion assay. (A) A standard Matrigel invasion assay reporting invasion index for each cell type and construct. (B) Passive bead measurements of median MSD at τ=1 second for each construct, as assessed using the AHTM. All significance values reported in Table 3.1.

Beause the primary goal of this research was validation of the AHTM, we compared AFM results to passive bead mean squared displacements (MSDs) measured on the AHTM and invasion assay results for the same conditions. AHTM results (Figure 3.12A) show an ∼16 nm (∼30%) increase in the median RMS value between cultures at both phenotypic extremes (CC vs HPNE), and a ∼5 nm increase between CC and H-Ras, myr-AKT, and BCL-2 and a lesser increase for TβRI. A standard Matrigel invasion assay (Figure 3.12B) concluded that while each construct increased invasion to an extent that was intermediate between CC and HPNE, all were significantly enhanced relative to CC ($p<0.01$). The invasion index exhibited a greater than order of magnitude increase between HPDE and HPNE cells. In terms of statistical significance, we summarized the data from each of the three assays relative to the CC controls in Table 3.1. The passive bead results from the AHTM and AFM results agreed in direction and significance for H-Ras, myr-AKT, and BCL-2. AHTM measurements of aggregate median values for TβRI-transfected we not significantly different from CC while the AFM showed a significantly increased median in compliance both on- and off-nucleus. The AFM on-nucleus results showed increases in compliance for the same conditions which produced increased invasion in the invasion assay results. However both AHTM and AFM off-nucleus measurements were only able to detect mechanical differences for a fraction of the conditions with increased invasion.

Technique	**DE**	**CC**	**H-**	**My**	**RI**	**B2**	**NE**
Invasion	NS	–	***	**	***	**	***
Passive bead	NS	–	***	***	NS	***	***
AFM on-nucleus	NS	–	***	***	***	***	***
AFM off-nucleus	NS	–	NS	NS	***	***	***

Table 3.1: A Table of significance values for the results of the invasion assays, AHTM analysis, and AFM measurements, where *, **, and *** correspond to the Bonferroni corrected p-values $p<0.05$, $p<0.01$, and $p<0.001$, respectively.

3.3.3: Conclusions

These AFM results show a difference in stiffness between non-transformed primary cells (HPDE) and their highly invasive phenotype (HPNE). Additionally, AFM on-nucleus measurements were able to identify more subtle changes in mechanical phenotype from the expression of single-gene GOF constructs. These constructs generally showed median compliance values between those seen for HPDE and HPNE phenotypes, with the exception of TβRI (RI) in off-nucleus measurements and BCL-2 (B2) in both off- and on-nucleus measurements. The same GOF constructs produced only a modest increase in invasion index and AHTM MSD measurements, with the exception of the TβRI AHTM measurement.

We did not expect that all constructs used in this study would necessarily show a more compliant

phenotype. For example, My-AKT and BCL-2 expression promotes the ability of cancerous cells to multiply without undergoing apoptosis, but these expressions are not known to alter the mechanical phenotype of pancreatic cancer cells directly. The statistical significance found in the AFM compliance measurements may indicate an important mechanical change that indirectly accompanies the expression of these genes.

Additionally, the AFM results validated the AHTM as a technique for screening changes in the mechanical phenotype of cancer cells. Table 3.1 summarizes that, with one exception, the assays performed consistently in the sense that increased compliance and invasion, and levels of significance were in agreement for cell type. By binning AHTM results according to their direction of change and significance, the system achieves a reliable and rapid method of characterizing changes in mechanical phenotype. It is notable that AFM and AHTM produced largely consistent results despite different mechanical measurement. The AFM applies nanonewton forces to indent the cell and measure bulk compliance of the cell membrane, cytosol, cytoskeleton, and even nucleus effects. On the other hand, the AHTM measures the thermal motion of 2 μm beads attached to the cell membrane, thus probing the membrane and cytoskeleton properties less invasively.

The ability to distinguish differences in cell stiffness due to GOF constructs adds to the growing abundance of data correlating mechanical properties of the cells with the relative invasivities; however, a considerable benefit of this study was the the validation of the AHTM. Data acquisition with the AHTM will facilitate further development of cell mechanics assays that probe the pathways responsible for many cancer phenotypes, as well as the effects of chemotherapeutic drugs.

In both the examination of ovarian (Section 3.2) and pancreatic cancer cells, the nuclear mechanics is correlated with invasion and migration of the cell lines. Therefore, it is clear that the mechanical properties of the nucleus play a fundamental role in cancer metastasis. In order to better understand the role of nuclear mechanics, the next study examines the intrinsic mechanical properties and force response of cytoplasts - cells without nuclei.

Section 3.4: Mechanosensing in Cytoplasts

Continued research throughout the past decades has led from the idea of a single mechanosensor to the realization that there are a variety of mechanosensitive elements to sense applied forces and substrate stiffness, including stretch-activated ion channels in the plasma membrane and conformational change in proteins at focal adhesions and inside the cytoskeleton.(3; 4; 33; 34) This signaling can happen through a chemical signal cascade, mechanical force propagation or a combination of these.

The transmission of mechanical forces to the nuclear interior modulate gene transcription, either directly or indirectly. Recent findings have further bolstered the hypothesis that the nucleus itself may act as a

cellular mechanosensor, bypassing the diffusion-based mechanosignaling through the cytoplasm to directly modulate expression of mechanosensitive genes.(3) Isolated nuclei experiments (Figure 3.13A) have shown that mechanotransduction is not restricted to cell surface receptors and adhesions but can occur directly at the nucleus.(9) The process of mechanotransduction to the nuclear interior depends on the mechanical properties of the nucleus and its physical connectivity to the surrounding cytoskeleton. The mechanical properties of the nucleus are provided by the nucleoskeleton and the nucleoplasm (containing DNA, nucleoli, nucleoplasmic lamin, etc.). The nucleus is connected to the cytoskeleton by LINC complexes - Linker of the Nucleoskeleton and Cytoskeleton. This connection is essential for a broad range of cellular functions including, but not limited to, nuclear movement, cytoskeletal organization, cell polarity, cell migration and mechanosensing.

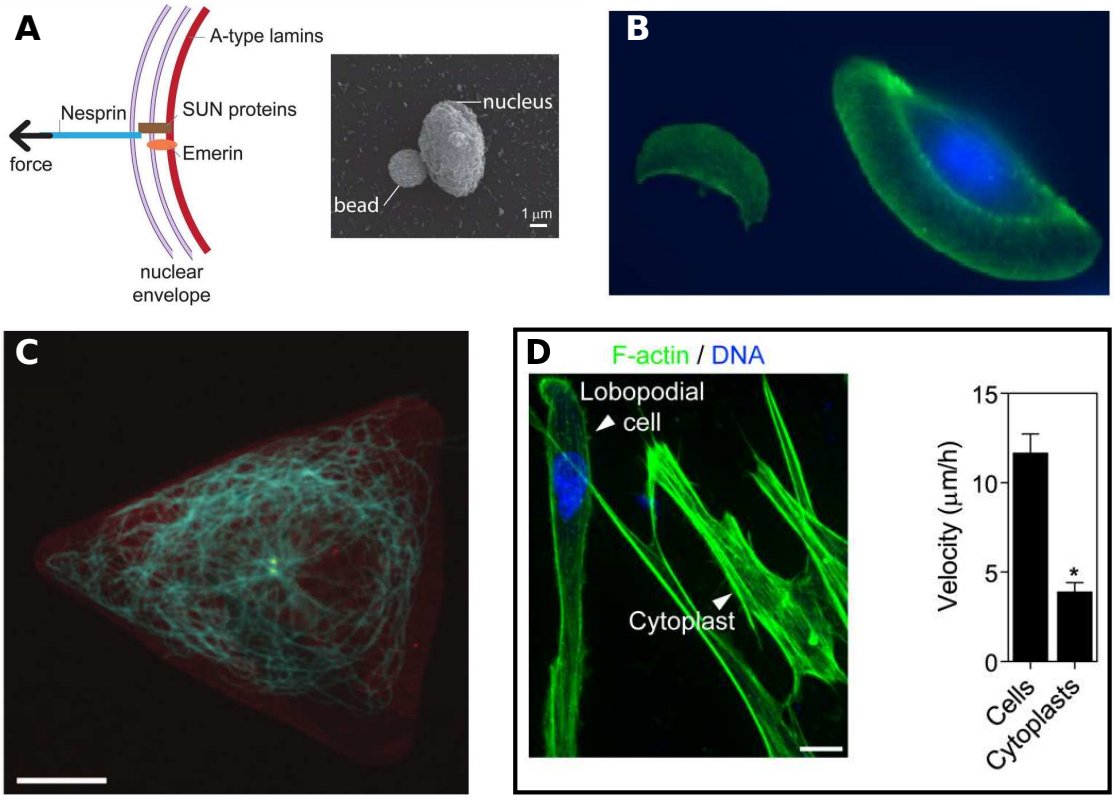

Figure 3.13: The nucleus plays a role in cell sensing, polarity and migration. (A) Guilluy, et al. measured stiffening of isolated nuclei in response to force applied to nesprin-1. Diagram and scanning electron micrograph of experiment shown.(9) (B) Hirsch, et al. observed a moving cytoplast (left) was closer in appearance to keratocyte (right) than fibroblast. Actin labeled in green and nucleus in blue.(10) (C) Bornens found that the nucleus-centrosome axis is a marker of cell symmetry breaking, except in cytoplasts where the centrosome sits precisely at the center and the microtubule network is symmetrically distributed.(11) (D) Petrie, et al. showed that enucleated fibroblasts (cytoplasts) adhere to the matrix but migrate more slowly than intact cells in 3D matrix. All shown scale bars are 10 μm.(12)

To study the role of the nucleus in motility, polarity and mechanosensing, David Graham, a graduate

student working with Professor Keith Burridge and Professor James Bear at UNC, is studying cells without nuclei - cytoplasts. Cytoplasts are formed through the removal of the nucleus from healthy fibroblasts in a process known as enucleation. Mass enucleation of cells is accomplished by centrifugation through a density gradient in the presence of cytochalasin, an inhibitor of actin polymerization. Upon centrifugation, cell nuclei move to the long, thin cytoplasmic stalks, which subsequently break down, generating membrane-bound cytoplasts and karyoplasts, the portion containing the nucleus with a small amount of cytoplasm.

Cytoplasts possess many of the same characteristics as their fibroblast precursor, including the ability to move, produce mature focal adhesions, exert force, and align their cytoskeleton in the direction of flow. However, they also possess a number of differences that highlight the importance of the nucleus in normal cellular function. First, the motion of cytoplasts are strikingly different than their intact counterparts. Fibroblasts produce protrusions and retractions of lamellipodia, while cytoplasts move in a crescent-moon shape characteristic of keratocytes (Figure 3.13B).(10) Second, centrosome positioning in migrating cells is altered. The centrosome positioning in cultured cells is tightly controlled, where the nucleus-centroscome axis is a marker of cell symmetry breaking in fibroblasts. When adhering to a micro-patterned region, intact cells reproducibly attach with the centrosome in a 2 μm diameter area directly behind the nucleus; enucleated cells adhere to the same pattern, but the centrosome sits precisely at the center (Figure 3.13C).(11) Finally, even though both cells adhere to a three-dimensional matrix, cytoplasts migrate at less than half the speed of intact cells.(12)

Additional work, heretofore unpublished by Graham and coworkers, points to aberrant mechanotransduction in cytoplasts as the source of many of these differences. In these studies, cytoplasts did not sense differences in substrate stiffness as determined by cell area measurements on different stiffness substrates. Durotaxis studies, discussed in Appendix E, measured the relative motion of intact fibroblasts and cytoplasts on a gradient stiffness gel. Due to the lack of forward motion, cytoplasts were determined to be unable to durotax (i.e., sense and respond to substrate rigidity). Magnetic bead experiments showed a lack in stiffening response of cytoplasts due to externally applied force.

The goal of AFM measurements of the mechanical properties of cytoplasts was to determine if aberrant mechanotransduction behaviors were the result of changes in intrinsic mechanical properties of the cell due to removal of the nucleus. To investigate this, stiffness measurements were performed for the center of cytoplasts, intact fibroblasts nuclear region and intact fibroblasts cytosol region. Additionally, the change in stiffness for each cell type and region was investigated with an unfunctionalized tip to corroborate magnetic bead results.

3.4.1: Experimental Methods

A mix of intact fibroblasts and cytoplasts was sparsely plated into a cloning ring on a glass coverslip and brought to our lab by David Graham prior to experiments. The samples were rinsed with and experiments performed in room temperature HEPES buffered F12/DMEM (Thermo Fisher Scientific - Liverpool, NY).

AFM force curves were collected and analyzed as previously described in Section 3.2.1 to determine the elastic modulus for each cell location. Force measurements on cells were performed in two locations on fibroblasts and one location cytoplasts (Figure 3.14 – over the nucleus of fibroblast (red asterisks), near the nucleus of the fibroblast over a thick region of the cytoplasm we are calling the midzone (blue asterisks), and over the thickest part in the center of the cytoplast (green asterisks). The order of collection for fibroblasts over the nucleus and midzone was alternated with no observable effect on the elastic modulus due to the order of force collection. Force curves were collected with a vertical ramp size of 5 μm and ramp speed of 1 μm/s. Indention of the cell was performed to a trigger point of 1 nN for over nucleus measurements and 0.5 nN for midzone and cytoplast measurements. These trigger point values were chosen to produce an indentation depth of $\sim$ 10-20% the region height. Approximately 10 force curves were collected in each location with a 5 second dwell between each force curve. Additionally, experiments were performed with the AFM cantilever held at constant force for a 4 second dwell in contact with the cell and 6 second dwell away from the cell. These were designed for a more direct comparison to magnetic bead pulling experiments; however, no significant difference in modulus behavior was observed between this and initial experiments with no surface dwell.

3.4.2: Results

Data was collected over the course of three days each, with separate sample preparations of fibroblasts and cytoplasts plated onto glass. Multiple sample preparations ensured that any trends observed were not reflective of a single sample preparation population, but indicative of the cell types. On each day, at least five cells of each type were measured with a series of ten force curves separated in time by five seconds. The order of collection for fibroblasts over the nucleus and midzone was alternated – first ten curves were collected over the nucleus, followed by ten over the midzone, and then the opposite order (midzone and then nucleus) for the next cell – with no observable effect on the elastic modulus due to the order of force collection.

The result of comparing all data to determine the absolute elastic modulus for each cell type/location is shown in Figure 3.15. The midzone of intact fibroblasts was significantly softer than cytoplasts and the nuclei of intact fibroblasts, but no significant difference was observed between the stiffness of cytoplasts and

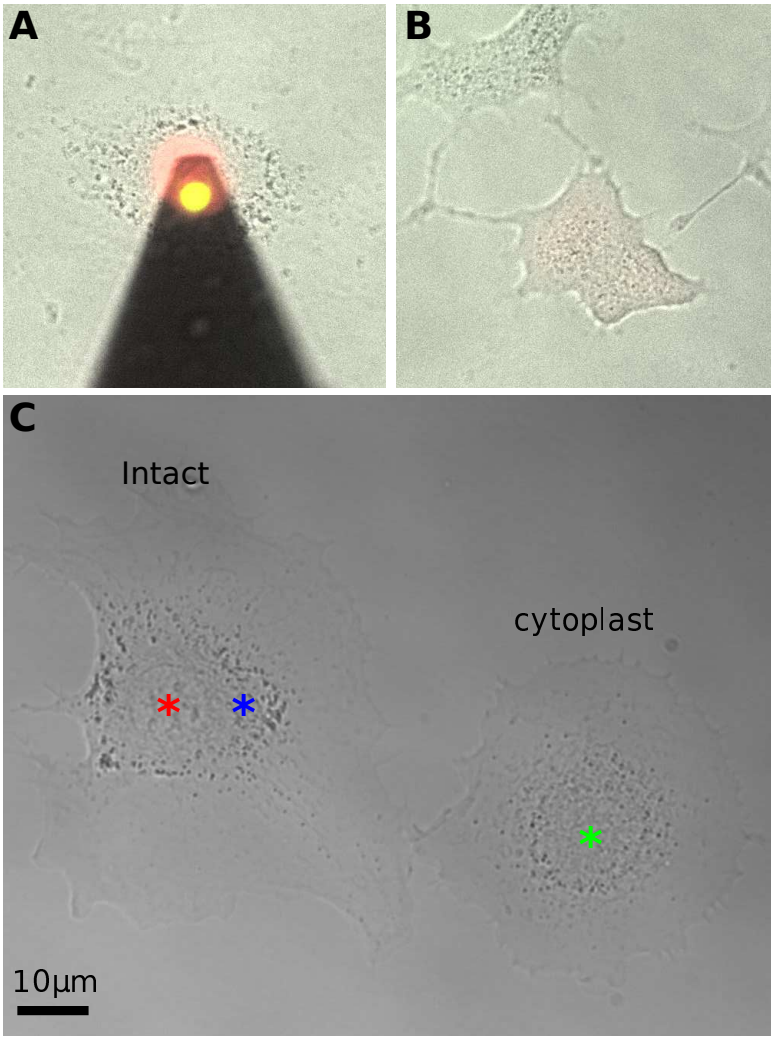

Figure 3.14: AFM stiffness measurements of intact fibroblasts and cytoplasts. (A) Overlaid bright-field, red fluorescence, and green fluorescence image of AFM cantilever over fibroblast with intact nucleus. In bright-field image, the AFM cantilever is a large black triangle and the outline of the entire fibroblast can be seen. The nucleus labeled with TD tomato is false-colored red and a 5 μm yellow-green fluorescent bead attached to the end of an AFM cantilever is false-colored green. (B) Overlaid bright-field and red fluorescence image of cytoplasts, showing that some cytoplasts lacking the nucleus are uniformly labeled with TD tomato. (C) Bright-field image of fibroblast with intact nucleus and cytoplast, as labeled. Locations for AFM measurements are denoted with asterisks –over the nucleus of intact fibroblasts (red), over the midzone of intact fibroblasts (blue), and over the center of the cytoplast (green).

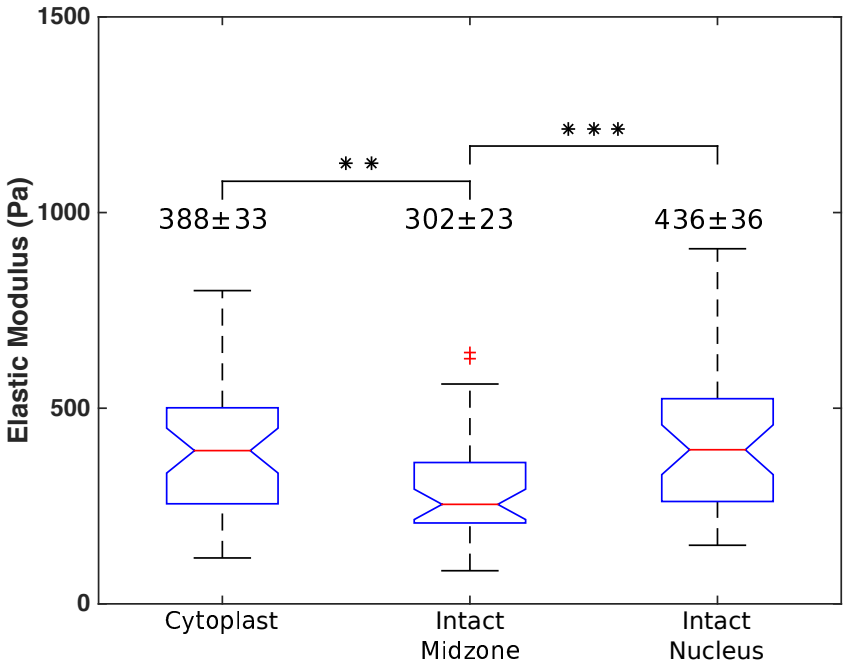

Figure 3.15: Box plot of the elastic modulus for cytoplasts, over the nucleus of intact fibroblasts, and over the midzone, one bead diameter away from the nucleus, of intact fibroblasts. Each box plot represents the collection of average elastic modulus for each cell, with the red line indicating the median of the data, the cental box representing the central 50% of the data, the notches setting the 25% and 75% quantile of the data, the Tukey whiskers indicating remaining data outside central box up to 1.5 times the height of the central box, and all other remaining points marked by the red crosses as outliers. Asterisks (*,**, ***) represent significance values of $p < 0.05$, 0.01, 0.001 as determined by the Wilcoxon rank-sum test. The average elastic modulus and standard deviation for each type are shown above each box plot.

stiffness measured over the nuclei of fibroblasts.

Comparisons were made to confirm the differences observed were characteristic of the cell types, and not due to variations between sample preparations on different experiment days, cloning rings or outlier cells. The results of this analysis can be found in Appendix F. Briefly, the results showed the distribution of elastic modulus for each cell type are consistent over multiple days and cloning rings; therefore, measurements of the elastic modulus of each cell type/location could be directly compared across days.

All results up to this point assume that there is no change in the stiffness of the cell over the course of subsequent force measurements. For each cell type/location, up to 10 force curves were acquired and analyzed to measure stiffness. In order to investigate the force response, I normalized the elastic modulus of each force curve in a series to the elastic modulus of the first force curve. An increase in stiffness is greater than one and a decrease in stiffness is less than one. A statistics comparison was performed for multiple day force response data, found in Appendix F. When force parameters were adjusted parameters were adjusted to mimic magnetic bead pulling experiments with a force application dwell time of 4 seconds and a 6 second pause between subsequent force curves (similar to the on-time for the magnetic bead experiments). No force response is seen for cytoplasts or fibroblasts on-nucleus (Figure F.3); however, the midzone fibroblast measurements show an increase in their stiffness with multiple force applications.

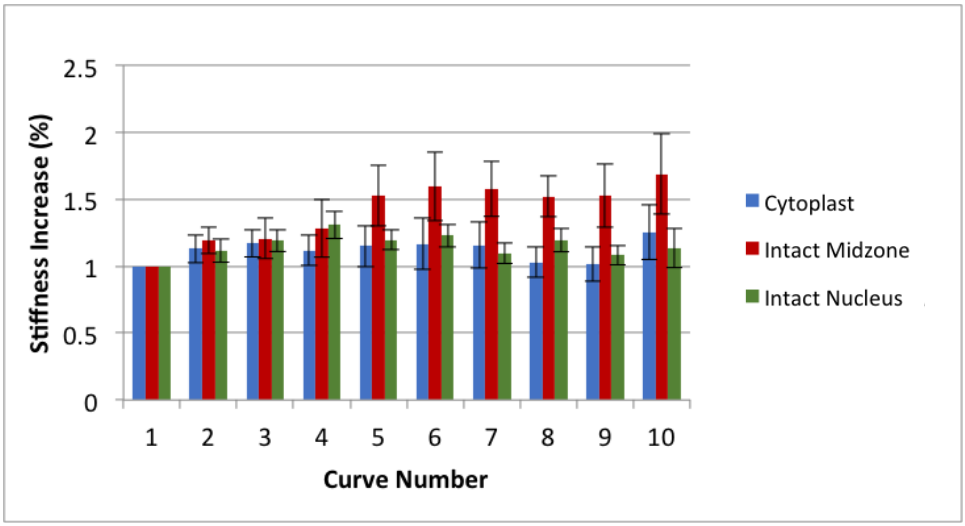

Figure 3.16: Average stiffening of cells reported as values normalized to the first force curve for AFM measurements in which dwell parameters were set to mimic magnetic bead pulling experiments (i.e., AFM cantilever held at constant force for a 4 second dwell in contact with the cell and 6 second dwell away from the cell).

3.4.3: Conclusions

In conclusion, I have successfully measured several mechanical properties of cytoplasts and intact fibroblasts. The results of AFM stiffness measurements were Young's modulus values of 388±33 Pa for cytoplasts, 302±23 Pa for the midzone of fibroblasts, and 436±36 Pa for the nuclei of fibroblasts. Distributions of over 500 Young's modulus measurements showed the intact fibroblast midzone was significantly softer than the cytoplasts and the nuclei of intact fibroblasts. These results were consistent over several sample preparations and across days of data collection, thus are considered representative of the cell types. Similar stiffness values for cytoplasts and measurements made over the nucleus of fibroblasts indicate that the primary contributor to the stiffness measured over the nucleus was the cytoplasm surrounding the nucleus, rather than the nucleus itself. To probe nuclear stiffness, future experiments would need to be performed with a larger indentation depth to guarantee that the indentation of the nucleus would contribute to the stiffness measurement. These results were unexpected because the cytoplast region probed was assumed to have a similar makeup to the midzones of intact fibroblasts. These results reveal that the centers of cytoplasts are stiffer than the midzones of fibroblasts due to either a fundamentally different makeup (e.g. more material was left behind after nucleus removal than originally suspected) or an underlying structural difference from their fibroblast precursor (e.g. a stronger, symmetric cytoskeletal network similar to that shown in Figure 3.13C was formed in cytoplasts).

Magnetic bead experiments showed a lack in stiffening response of cytoplasts due to externally applied force. Therefore, the AFM force response experiments were designed to elucidate whether the stiffening response was due to the location of bead attachment. However, no concrete conclusions about stiffening response could be drawn from subsequent AFM force curves on the same cell. When all data was taken into account, there was a slight stiffening of all cell types/locations. When AFM parameters were set to mimic magnetic bead experiments, there was an increase in force response for the midzone of intact fibroblasts. This may indicate that cytoplasts and the nuclei of fibroblasts do not stiffen in response to force application, but instead the midzone of the fibroblast is stiffening as a result of force. However, because the midzone region of fibroblasts is thinner than the cytoplasts or fibroblasts over the nucleus, subsequent force curves in this region could be displacing cytoplasm material, and the substrate below the cells (glass) may therefore contribute to the apparent stiffness. Further investigation of the effects of indentation depth would be required to determine the veracity of this hypothesis. These results may corroborate magnetic bead experiments performed by David Graham, where the stiffening response observed is primarily contributed by cytoplasm region (specifically, cytoplasm regions not on top of the nucleus). This is likely the case, because the functionalized beads in magnetic bead experiments tend to attach on the flat regions of the cell farther

from the nucleus. Any discrepancies between the results yielded in these two techniques are likely due to the fundamental differences in the experiments. Magnetic beads are functionalized to form focal adhesions at the cell surface, and the formations of these focal adhesions access different mechanotransduction pathways than the interaction of an uncoated AFM tip indenting the cell. Future AFM experiments using an AFM tip functionalized to mimic magnetic beads could be used to probe the differences between stiffening results reported by indenting and pulling experiments. Alternatively, other AFM techniques for measuring force response, such as monitoring the amplitude change of an AFM cantilever on top of the cell over time to measure a change in amplitude indicative of a change in stiffness, would be better suited to explore this mechanical property.

Our AFM results indicate that the previously observed aberrant mechanotransduction behaviors were not the result of changes in intrinsic mechanical properties of the cell due to the removal of the nucleus. This is supported by similar stiffness measurements for cytoplasts and intact fibroblasts and by force response that suggests a stiffening response of the cytoplasm of fibroblasts but not cytoplasts. These results indicate that previously observed aberrant mechanotransduction behaviors observed for cytoplasts were not the result of changes in intrinsic mechanical properties of the cell due to removal of the nucleus, but instead are solely due to changes in mechanosensing due to the removal of the nucleus.

Section 3.5: Conclusions and Future Work

In this chapter, I investigated purely mechanical measurements of cells and, more specifically, the nucleus, using the AFM. This was accomplished via several experiments designed to understand cellular and nuclear mechanics in relation to cell function (mechanotransduction) and misfunction (cancer metastasis). The results of these experiments elucidate the importance of nuclear mechanical properties to healthy cell function, as follows:

1. In Section 3.2, I showed that AFM stiffness measurements of ovarian cancer cells were inversely correlated with invasion assay. Differing from previous techniques, I was able to probe different regions of the cells to determine the contribution of the nucleus to cancer cell mechanics. AFM measurements showed the same inverse correlation between invasion and the mechanical properties of the cytoplasm (off-nucleus) and nucleus (on-nucleus) between the two cell lines, indicating the role of the nucleus in a cancer cell's ability to spread throughout the body.

2. I found that H2B-GFP fusion protein incorporated into the nucleus has an effect on the mechanical properties of the nucleus. I found that SKOV cells transfected with H2B-GFP exhibited a significantly

larger elastic modulus than unlabeled SKOV cells. More AFM indentation data is required to fully explore whether the change in stiffness is due to the cell line or to the concentration of H2B-GFP. However, the effect of H2B-GFP on nuclear mechanical properties must be taken into account in future experiments.

3. In Section 3.3, I showed that AFM stiffness measurements of pancreatic cancer cells were inversely correlated with invasion. The AFM was used to distinguish non-transformed primary cells (HPDE) from their highly invasive phenotype (HPNE). AFM on-nucleus measurements were able to identify more subtle changes in mechanical phenotype from the expression of single-gene GOF constructs used to produce detectable changes at the phenotypic changes relevant to cancer biology. These AFM results validated our laboratory's array high-throughput microscope for screening changes in the mechanical phenotype of cancer cells.

4. In Section 3.4, I measured the relative stiffnesses and force responses of fibroblasts and cytoplasts. AFM measurements resulted in a similar Young's modulus for cytoplasts and intact fibroblasts. Initial force response measurements suggest a stiffening response to indentation from the cytoplasm of fibroblasts but not cytoplasts. These results indicate that previously observed aberrant mechanotransduction behaviors observed for cytoplasts were not the result of changes in intrinsic mechanical properties of the cell due to removal of the nucleus, but instead are solely due to changes in mechanosensing due to the removal of the nucleus.

The experiments in this chapter illustrate the use of the AFM for understanding cell and nuclear mechanics for a wide range of cell biology research. However, key metrics for understanding cell response to mechanical stimuli, such as the rearrangement of the cytoskeletal and nucleoskeletal structure, induced strains, and biochemical distributions, were not examined. In the next chapter, I discuss a unique imaging system that combines an AFM with both vertical light-sheet illumination and a new imaging technique called PRISM - Pathway Rotated Imaging for Sideways Microscopy - designed specifically to acquire structural information during the application of stress in the direction of applied load with accompanying piconewton resolution force measurements.

CHAPTER 4: Combined Atomic Force Microscopy and Pathway Rotated Imaging for Sideways Microscopy

Key metrics for understanding cellular response to mechanical stimuli include rearrangement of the cytoskeletal and nucleoskeletal structure, induced strains and biochemical distributions; however, extracting structural information during an applied stress is limited by our ability to image cells under load. In order to study the mechanics of single cells and subcellular components under load, I have developed a unique imaging system that combines an AFM with both vertical light-sheet illumination and a new imaging technique called PRISM – Pathway Rotated Imaging for Sideways Microscopy. The combined AFM and PRISM system simultaneously delivers the quintessential imaging of cell deformation in the direction of applied force and piconewton resolution force measurements. The additional inclusion of light-sheet microscopy improves the signal-to-noise ratio by illuminating a sub-micron thick layer of the cell.

This chapter is comprised of several key sections:

4.1 Combined AFM and Optical Microscopy

4.2 Pathway Rotated Imaging

4.3 Vertical Light-Sheet Illumination

4.4 Conclusions and Future Work

Section 4.1: Combined AFM and Optical Microscopy

Living cells exist in a complex physical environment where they must withstand and respond to a wide range of mechanical forces.(197; 33; 198; 199; 4) However, much is still unknown regarding the mechanisms by which individual cells sense mechanical signals and then transduce them into changes in intracellular biochemistry and gene expression. This continual process of sensing, transmission and response is known as mechanotransduction and is essential for the maintenance of normal cell development and function. Mapping the mechanical, structural, and biochemical processes involved in mechanotransduction requires instrumentation that provides the ability to

1. apply and measure pN-nN forces,
2. image cellular structure dynamically in the direction of applied load,
3. and relate these two measurements with a high degree of temporal certainty.

Studies focused on the mechanics of single cells, subcellular components and biological molecules are rapidly progressing due to an array of techniques for studying cell mechanics, including the AFM, optical tweezers, particle tracking, magnetic beads, micropipette aspiration, micropillar arrays, and substrate stretching. Though there are benefits and drawbacks to each of these techniques, the AFM, developed as a high-resolution imaging tool, has become prevalent in the cell biology community for its use in force spectroscopy. Force manipulation induces a rapid response from cells via shape change, remodeling of the cytoskeleton and calcium signaling; these phenomena all depend on frequency, duration, magnitude and location of applied force.(200; 13; 201; 202) Increasingly, the AFM is the instrument of choice for a variety of reasons, including (1) its ability to directly apply and simultaneously acquire high accuracy measurements of forces, (2) its broad functional range of applied forces and resolution, and (3) its ability to operate in concert with a multitude of optical microscopy modalities.

A detailed description of AFM principles can be found in Section 1.2 and in instrument reviews.(155) Briefly, the AFM records the motion of a flexible cantilever with a tip at its end as it interacts with a sample. To measure elasticity, the tip of the AFM cantilever is pressed against the cell while applied force and cell deformation are monitored. For an in depth review of the AFM and other techniques in cell mechanics, see Rodriguez et al.'s review. (155)

Chapter 3 describes how an AFM system is useful for providing insight for a wide range of mechanical cell biology questions. However, the described measurements were taken without acquiring structural information during the application of stress. Traditionally, this measurement is performed by coupling force measurements with brightfield and epifluorescence microscopy, techniques that provide an image of the specimen along a plane parallel to the surface (referred to here as 'plan-view').

As described above, the AFM is well-suited for use in cell biology experiments due to its ability to be combined with optical microscopy techniques. The Asylum MFP-3D-BIO AFM used for the experiments described herein is a commercial, fully-capable AFM integrated with an inverted optical microscope, with a proven track record for cell mechanics studies.(203; 204; 205; 206; 207; 208; 209; 210; 211; 212) Studies that combine forces and imaging have shown the rapid mechanical response of cells through shape changes, the remodeling of the cytoskeleton, and calcium signaling; these phenomena all depend upon frequency, duration, magnitude and location of applied force.(200; 13; 201; 202)

Despite the insight that plan-view epifluorescence provides, the imaging method is limited because the forces are applied in the z-direction, perpendicular to the imaging plane. Thus, the most substantial cellular deformations and structural rearrangements are likely aligned with the applied force. Acquisition of key structural information during applied stress therefore remains limited by the system's inability to image cells under load in the direction of applied force.

There are two approaches for overcoming this limitation – confocal microscopy and the use of custom side-view imaging chambers.

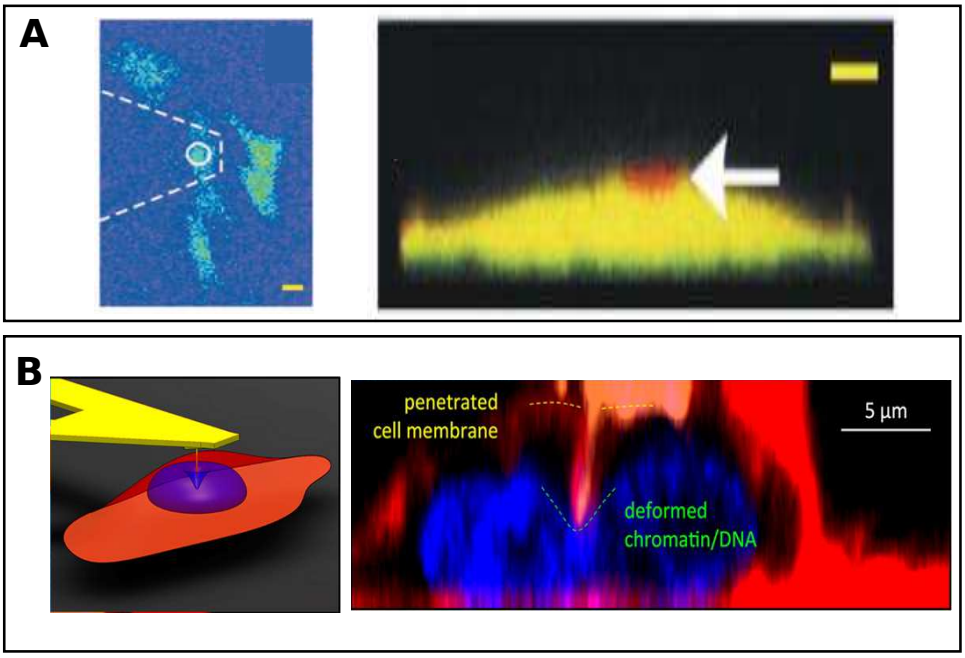

Figure 4.1: Combined AFM and Confocal Imaging. (A) Plan-view (left) and a zx-slice (right) of confocal stack for osteoblast loaded with calcein-AM. (Right) One image was taken before indentation (red) and one during indentation (green), and both images were superimposed. The area displaced by indentation is shown in red. Scale bar is 10 μm. Figures adapted from Charras et al.(13) (B) Illustration of experiment (left) and Z-stack confocal images (right) of a human bladder cancer cell with AFM needle tip indentation. (Right) Red membrane and blue nucleus label show cell membrane and nuclear envelope penetration resulting in deformed chromatin. Figures adapted from Liu et al.(14)

The first approach to obtaining side-view images of the sample while applying and measuring forces has been to combine AFM with confocal microscopy, which works by creating a stack of plan-view images and reconstructing the 3D structure from which a vertical slice can be obtained.(213) Some examples of combined AFM force measurements and confocal imaging are depicted in Figure 4.1; the measurements were performed to understand both strain-induced calcium response(13) and nuclear mechanical properties *in situ*.(14) The deficiencies of this method are (1) the poor axial resolution compared to planar resolution, best seen in Figure 4.1, and (2) the duration (several seconds) required to collect image stacks for 3D reconstruction of an xz-slice.(213)

To overcome these limitations, scientists have employed a second approach to obtaining images of AFM-applied force – directly utilizing a side-view imaging path. A direct view of the cell from the side facilitates the direct measurement of force-induced changes and an improved z-axis resolution. These systems require the construction of custom force spectrometers, sample chambers, and imaging systems to allow for both

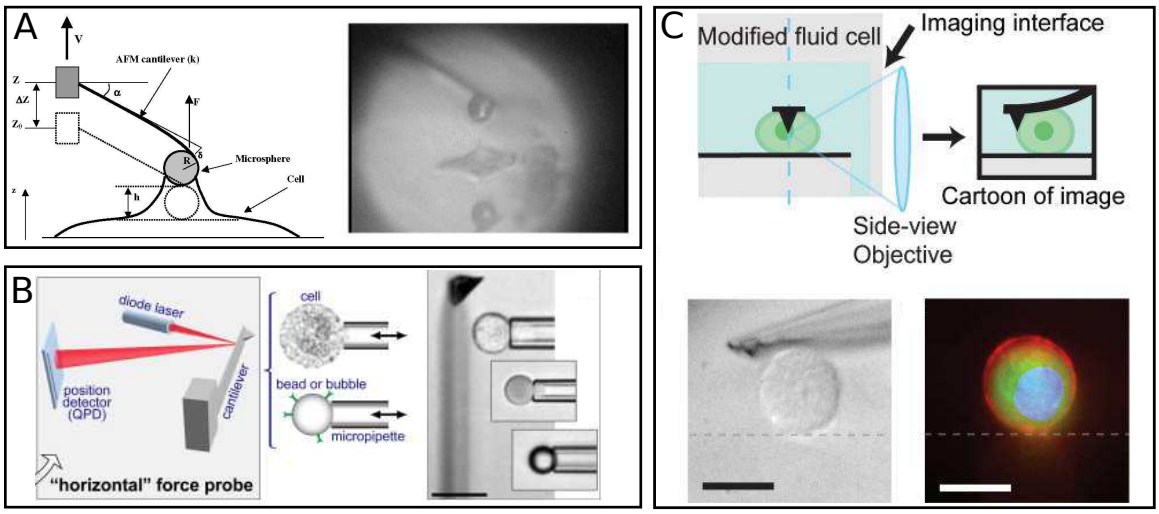

Figure 4.2: Combined AFM and Side-View Imaging. (A) Typical stretching experiments on Chinese hamster ovary (CHO) cells, where force measurements are extracted from images. (B) A custom-built horizontal force on the stage of an inverted microscope. A variety of pipette-held test objects can be translated to or from the stationary cantilever by a closed-loop piezo actuator. (C) Custom side-view chamber built for AFM measurements. (Top) Schematic of system. (Bottom) Brightfield and merged images taken in epi-fluorescence for a U2OS cell. Scale bars are 20 μm. Images (A), (B), and (C) are modified from Canetta et al.(15), Ounkomol et al.(16), and Chaudhuri et al.(17), respectively.

force measurements and imaging of the cells in media. Such systems have been used to measure viscoelastic properties during cell stretching,(15) cell compression,(16; 17) and cytoskeletal rearrangement,(17) as depicted in Figure 4.2. Although side-view imaging path techniques allow for combined force measurement, improved z-axis resolution, and potentially faster imaging than confocal imaging, several drawbacks exist in current systems. There is often a loss in force sensitivity due to the custom design of the system, especially in systems that rely upon the images to track the tip motion of the AFM cantilever and calculate force. Designing these custom systems is time-consuming and imposes restrictions upon the sample geometry.

In this context of the field of mechanotransduction, I have developed a unique imaging system that combines a standard AFM system with both vertical light-sheet (VLS) illumination and a new imaging technique called PRISM – Pathway Rotated Imaging for Sideways Microscopy (Figure 4.3). The system facilitates the high-speed imaging of cell deformation, resulting in sub-micron structural motion in the direction of applied force with accompanying fully synchronized piconewton-resolution force measurements, which can be applied to versatile sample geometries. In the following sections, the two major innovations of the new system are discussed: (4.2) Pathway Rotated Imaging for Sideways Microscopy and (4.3) Vertical Light-Sheet Illumination.

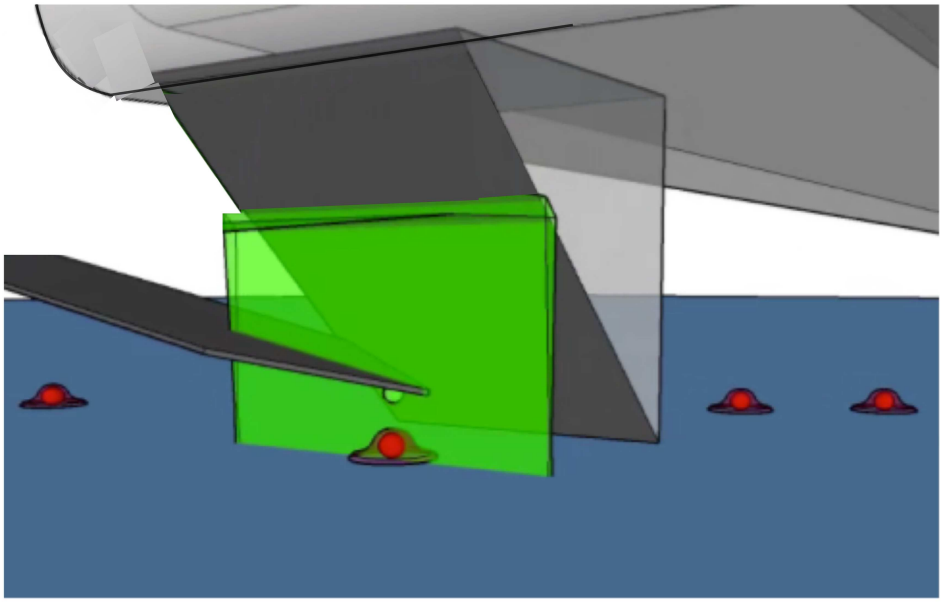

Figure 4.3: To-scale SketchUp illustration of the combined AFM-PRISM-VLS system, including 5 μm yellow-green fluorescent bead Norland attached to ArrowTL1 AFM cantilever, 180 μm micro-prism with reflective hypotenuse attached to capillary tube, $\sim$1 μm VLS, and several cells with SYTO-labeled nuclei (red) on glass.

Section 4.2: Combined Pathway Rotated Imaging for Sideways Microscopy and Force Spectroscopy

PRISM, Pathway Rotated Imaging for Sideways Microscopy, is a new imaging technique that enables real-time, side-view imaging on a standard microscope system and can be coupled with a standard AFM for simultaneous force measurement. PRISM is an adaptation of previous methods including (1) single lens theta confocal microscopy, where a single lens combined with a mirror unit yields improvements to axial and volume resolution,(214; 215) and (2) the use of specially fabricated specimen substrates or chambers that achieve both top and side-views for a variety of samples.(216; 217; 218; 219; 220; 221; 222)

The principle behind PRISM is straightforward: a 45° reflecting optic is freely positioned next to a fluorescently-labeled cell in the field-of-view (FOV) of a standard epifluorescence imaging system. When the objective is moved upward, the imaging plane moves upwards in z, and the traditional horizontal slices of the image stack are obtained (often referred to as an 'image stack' or 'z-stack'). As the objective translates upward, the imaging plane eventually intercepts the reflecting optic, which rotates the plane into a vertical object plane. Continuing to move the objective upward, the now vertical object plane sweeps across the cell, creating lateral slices of the specimen. The sequences of images, plan-view and then side-view, appear on

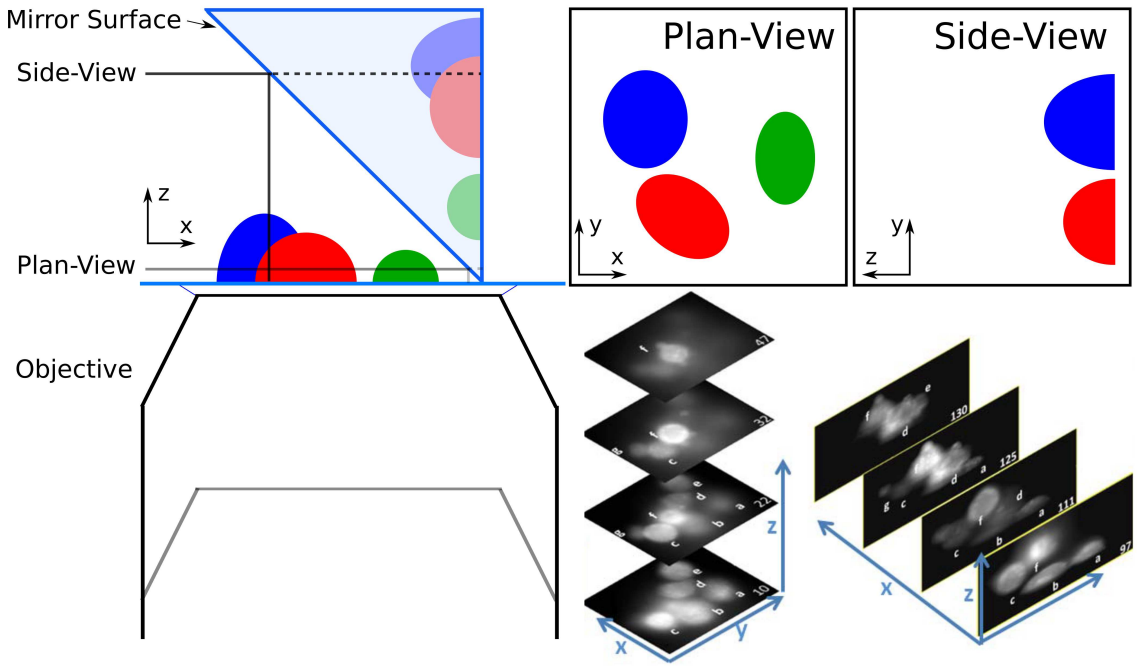

Figure 4.4: PRISM image formation illustration and demonstration. A cartoon of the PRISM imaging system showing mirror surface of prism, objective, and cells (red, blue, and green for illustrative purposes). Both the plan- and side-view imaging planes are shown on the left, with their corresponding objective height, and on the right, as they would appear in common widefield microscope camera. (Bottom-Right) PRISM demonstration imaging piled cells in both plan- and side-view

an unmodified traditional widefield microscope camera with the side-view images appearing to the side of the FOV and for higher objective positions. A PRISM imaging schematic and demonstration is depicted in Figure 4.4. Note that, in the demonstrative images, the cell that appears brightest in the highest plan-view slice is also in the top of the side-view slices, and the other cells can be similarly identified.

Using the PRISM imaging system, the objective can be focused to the side-view imaging plane for acquisition of high-resolution, high-speed images in the xz-plane (i.e., in the direction of applied force).

4.2.1: Implementation

The central design challenge for the PRISM-AFM system is physically positioning the PRISM reflecting optic into the FOV of the standard microscope near the AFM cantilever without incurring a loss of force sensitivity or imposing undue restrictions on sample geometry. This requirement results in constraints on choices of AFM cantilever, necessitates modifications to the existing AFM assembly to accommodate the placement of PRISM optics, and necessitates a novel reflecting optic and mounting/manipulation method so that it can be easily incorporated into the AFM system. Further, once the physical requirements are satisfied, the AFM and camera data require software synchronization in order to reliably interpret simultaneous measurements.

The first physical parameter taken into consideration is the spatial clearance allowed between the AFM cantilever holder and the coverslip when the AFM tip is fully engaged, shown in Figure 4.5. This requirement is accommodated by modifying the AFM cantilever holder and by choosing a 180 μm 45° reflecting optic and mount.

For the unmodified cantilever holder, the lowest point in the system limiting insertion of PRISM-reflecting optic is the polished quartz window. The unmodified clearance is approximately 300 μm, but ultimately depends on the choice of cantilever and the placement of the AFM cantilever chip in the holder. To increase this distance, shims were added below the cantilever chip and flexible screw down spring clip (see Figure 4.5). The superluminescent diode (SLD) passes through the optical window, reflects off the back of the AFM cantilever, and back through the optical window into the AFM head to measure small displacements in cantilever position, as described in detail elsewhere (Section 1.2). Moving the cantilever further from the window risks potentially reducing the reflected SLD signal measured by the detector; however, after implementation of the shims, a <10% reduction in signal for up to 500 μm shim thickness was observed. The cantilever holder, modified with shims below the cantilever chip and spring clip, allow for a clearance of nearly 1 mm.

Next, the 45° reflecting optic and mount were chosen so that they would fit in the allowed space and

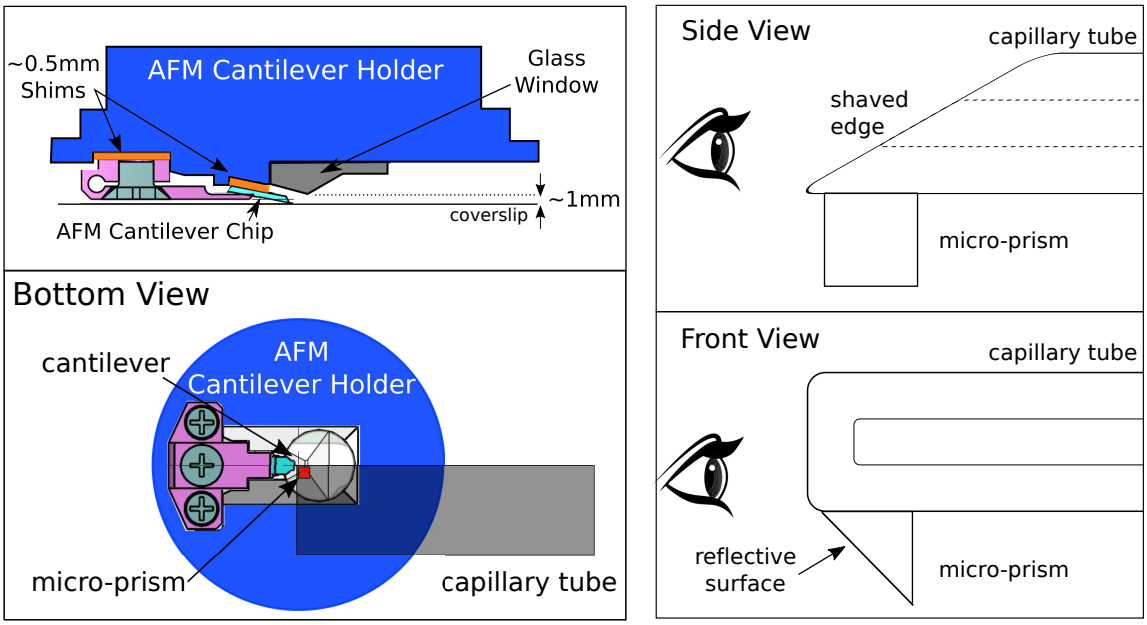

Figure 4.5: Modifications to AFM cantilever holder and micro-prism mounting. (Top-Left) Side-view cutaway image of cantilever holder with ∼1 mm clearance between the glass window (grey and glass coverslip due to use of shims (orange). (Bottom-Left) The bottom view of micro-prism (red) placed near AFM cantilever, as would be seen by an inverted optical microscope. All elements are drawn to scale except micro-prism, which is shown larger to clearly identify its location. (Top-Right) Side-view image of micro-prism mounted on bottom of shaved capillary tube. The eye indicates the direction from which the front-view image is drawn. (Bottom-Right) Front-view of micro-prism on capillary tube, where the eye indicates the direction from which the side-view image is drawn.

have clearance to move vertically. A 180 μm right-angle prism with coated hypotenuse (Precision Optics Corporation, MA) was adhered to a capillary tube with UV-cured Norland Optical Adhesive 81 (Norland Products Inc., NJ). Both the prism and capillary tubes were chosen because they were small enough to accommodate the space provided between window and cantilever. The capillary tube has additional benefits of (A) optically transparency, allowing for the prism to be positioned in close proximity to the AFM cantilever without concern of damaging the AFM tip, and (B) sufficient rigidity to lift the prism off of the glass (or polyacrylamide-coated glass). The total height of the capillary tube (300 μm) and micro-prism (180 μm) is approximately 500 μm with adhesive, which easily fits in the nearly 1 mm clearance allowed between cantilever holder and glass coverslip, as illustrated in Figure 4.5. A prism mounted onto a capillary tube could be easily lifted from the glass surface and positioned relative to the AFM tip and specimen with the aid of a 3-axis micro-manipulation stage. This implementation places the prism just above the specimen so the substrate can be freely translated to locate cells of interest. Future experiments in this system will require temperature control; therefore, an additional mounting arm was designed and 3D-printed to be used with the MFP-3D BioHeater Closed Fluid Cell (Asylum Research, CA). More on the the PRISM-BioHeater setup can be found in Appendix J.

Both modifications to the AFM cantilever holder and choices in prism mounting allow for coupling of the AFM and PRISM imaging system with no loss in sample versatility.

The second physical parameter considered when designing the system is SLD path and signal. As previously described (Section 1.2), the SLD light reflected off the back of an AFM cantilever is used to detect the small deflections generated when the AFM tip interacts with the specimen of interest. To avoid interfering with the SLD path, which would reduce our system's force sensitivity, I chose the longest commercially available AFM cantilevers and shaved down the end of the capillary tube. After experimenting with a variety of cantilevers, I determined that a minimum cantilever length of 450 μm was required to allow ample room for SLD alignment on the back of the cantilever. For the experiments described herein, both Arrow-TL1 and TL-CONT (Nanosensors) tipless cantilevers were chosen based on their spring constants. Additionally, the front portion of the capillary tube was shaved back prior to prism attachment to avoid interference with the SLD light path (Figure 4.5).

These two considerations allow for the implementation of PRISM imaging without affecting the force sensitivity or versatility of AFM measurements. The position detection resolution of the system is thermally limited and unaffected by pathway rotated imaging path. A power spectrum of an Arrow TL1 cantilever under the PRISM apparatus was indistinguishable from the power spectrum acquired in solution prior to PRISM alignment (Figure 4.6).

The final task for simultaneous side-view imaging and force measurement is enabling synchronization of

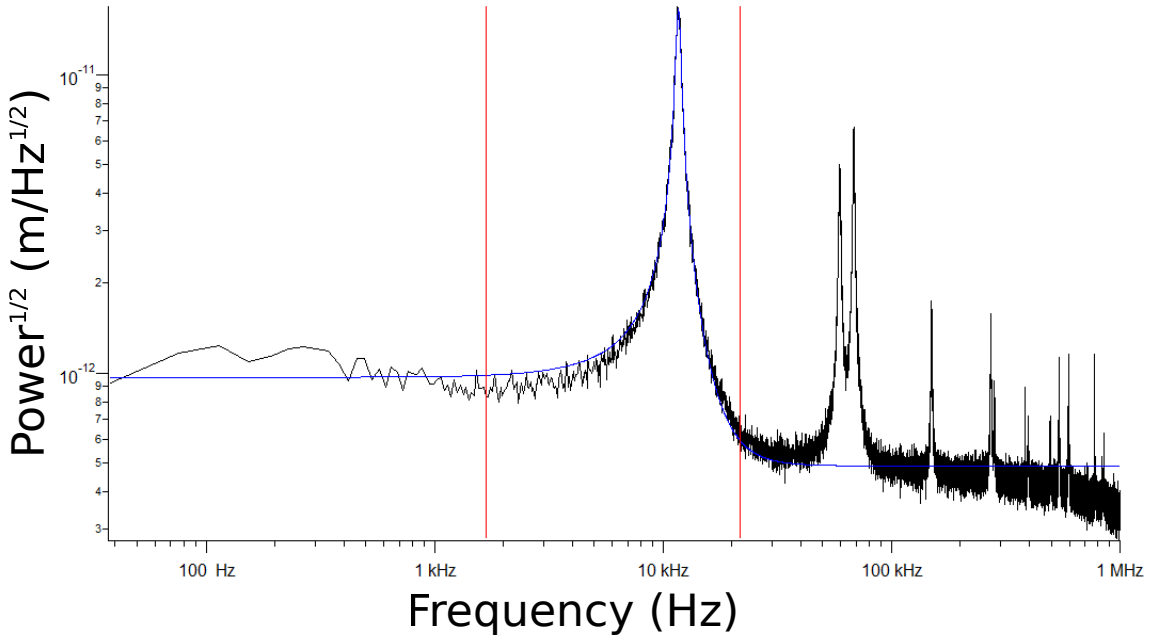

Figure 4.6: Cantilever power spectrum showing thermally-limited detection of cantilever in water under the PRISM apparatus. The best function to the first resonance of the power spectrum is shown in blue. The calculated spring constant based on this fit was 21 pN/nm, which is within manufacturer specifications of 20 pN/nm.

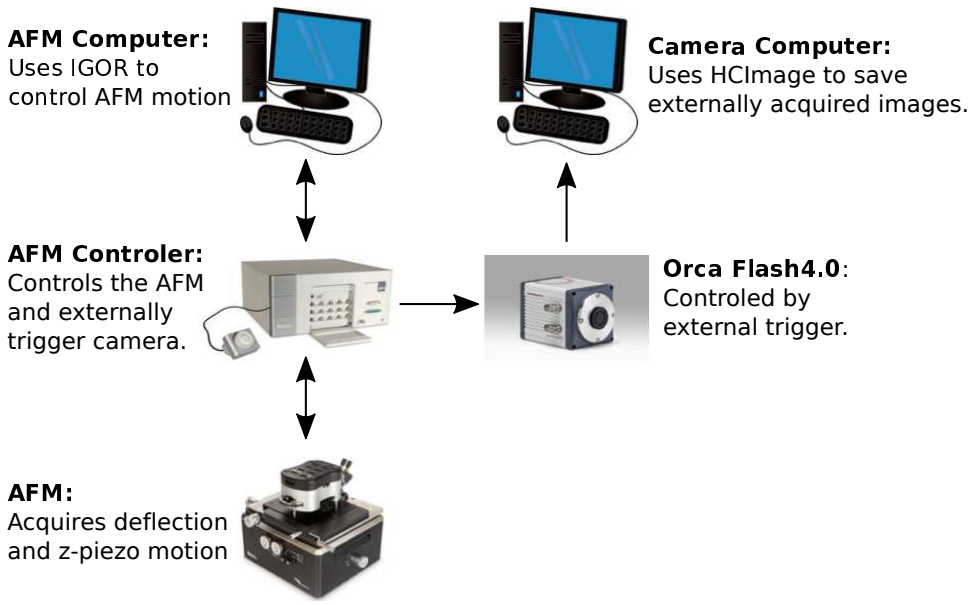

Figure 4.7: AFM-camera synchronization signal flow. Double-headed arrows indicate a flow of data in both directions.

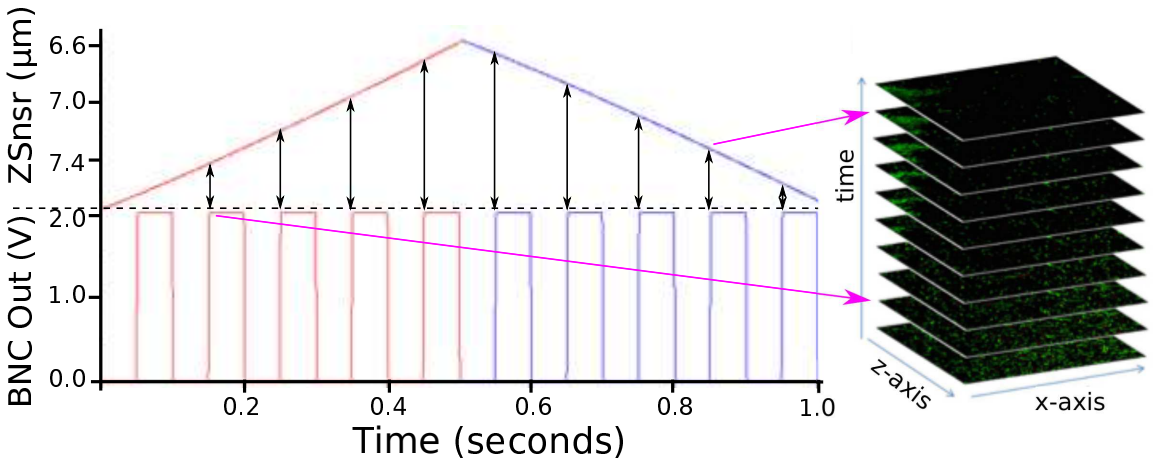

Figure 4.8: Sample synchronized AFM and 10 fps image data. The AFM software acquires both Z sensor (and deflection) data from the AFM and BNC output voltage used to signal the camera. These pulses recorded in AFM software can be used to directly relate force data to images acquired with the pulsed voltage.

the high-speed imaging and AFM data acquisition. This was accomplished by utilizing the AFM controller as an external trigger for the Orca Flash 4.0 camera. Figure 4.7 shows the signal flow for synchronized data collection. The AFM computer uses IGOR code to send information to control AFM motion and receive collected deflection and Z-sensor data through the AFM controller. The AFM controller can both send information to the AFM head and scanner, and also output voltage signals using one of its BNC outputs. By writing a voltage pulse wave for the BNC output into the AFM's standard, constant-velocity force curve IGOR control code, the AFM controller to externally signals the Orca Flash 4.0 camera. The camera must be set to externally edge trigger from within HCImage software. Because the camera signals on the increasing edge of the voltage signal, the force and image data was resolved to better than 1 ms of simultaneous force data. This resolution was determined by pulsing the SLD for a precise indicator in both force data and images. Sample data is shown for 10 fps in Figure 4.8.

4.2.2: Characterization

To measure the resolution of the side-view images acquired with PRISM, the point spread function (PSF) of sub-pixel microspheres was measured. Characterization samples were prepared by incubating 20 nm red fluorescent beads with SKOV cells, then rinsing and fixing the sample using formaldehyde. Two PSF stacks were acquired for each bead analyzed on the system – a plan-view z-stack and a side-view x-stack. Then, each image stack was analyzed by fitting a Gaussian function to the intensity profile in each axis direction through the maximum intensity pixel. The results for plan-view and PRISM-view PSF characterization of a

single bead are shown in Table 4.2. These values were within 15% of the theoretical resolution of the system. Similar results were achieved for at least 10 other beads for which plan-view and PRISM-view stacks were acquired. These results demonstrate that our system provides a z-resolution in PRISM side-view images comparable to the X and Y resolution achieved in standard plan-view imaging. A detailed description of PSF calculations and tilts measured in the PRISM system can be found in Appendix H.

PSF	Plan-View FWHM	PRSIM-View FWHM
x	0.332 μm	0.870 μm
y	0.305 μm	357 μm
z	0.947 μm	**321 μm**

Table 4.1: PSF values reported as the full width at half maximum of Gaussian fit to intensity profile along the given axis.

The final step to characterize the combined AFM and PRISM system was the simultaneous acquisition of force-indentation data and side-view images of deformation. A sample was prepared by plating SKOV, ovarian cancer cells, onto polyacrylamide gel coated glass coverslip. The polyacrylamide gel was added to the sample preparation to remedy imaging artifacts, including the reflection of fluorescent label off the glass coverslip in side-view images and imaging difficulties associated with chips or reflective-coating issues on the bottom edge of the micro-prism. Once the cells had firmly attached to the polyacrylamide surface (usually 24 hours after plating), the cells were labeled with SYTO 83 orange fluorescent nucleic acid stain (ThermoFisher Scientific). The cells were then rinsed and loaded onto the AFM scan stage, and the AFM beaded tip and PRISM apparatus were positioned near the cell in the microscope FOV. Prior to the experiment, 5 μm yellow-green fluorescent microspheres were attached to tipless cantilevers (Arrow TL1 for this data set) using the protocol described in Appendix I. Using a large beaded tip provided the dual advantage of exhibiting the most consistency in treating cells as a homogenous elastic medium,(223; 224) and increased separation between the contact point of tip on cell and the broad cantilever to prevent blocking imaging of this key area.

Once the above-mentioned components of apparatus were loaded and properly positioned, the objective was focused to the side-view imaging plane and the above procedure for synchronized data acquisition was implemented. The result was simultaneously acquired piconewton force-indentation data and PRISM side-view images of ovarian cancer cell deformation. Figure 4.9 shows the resulting force data and a single image acquired during the approach portion of the force curve. These data made evident two areas that required improvement: (1) there was substantial bleaching of the sample over the course of the experiment and (2) the signal-to-noise of the image was insufficient for distinguishing subcellular components. Both of these problems were the result of the illumination plane moving up with the imaging plane as the objective was focused up from plan-view to side-view, requiring the use of unfocused high intensity light to achieve PRISM-

view images. To increase the signal-to-noise and improve the imaging of our system, I implemented vertical light-sheet illumination.

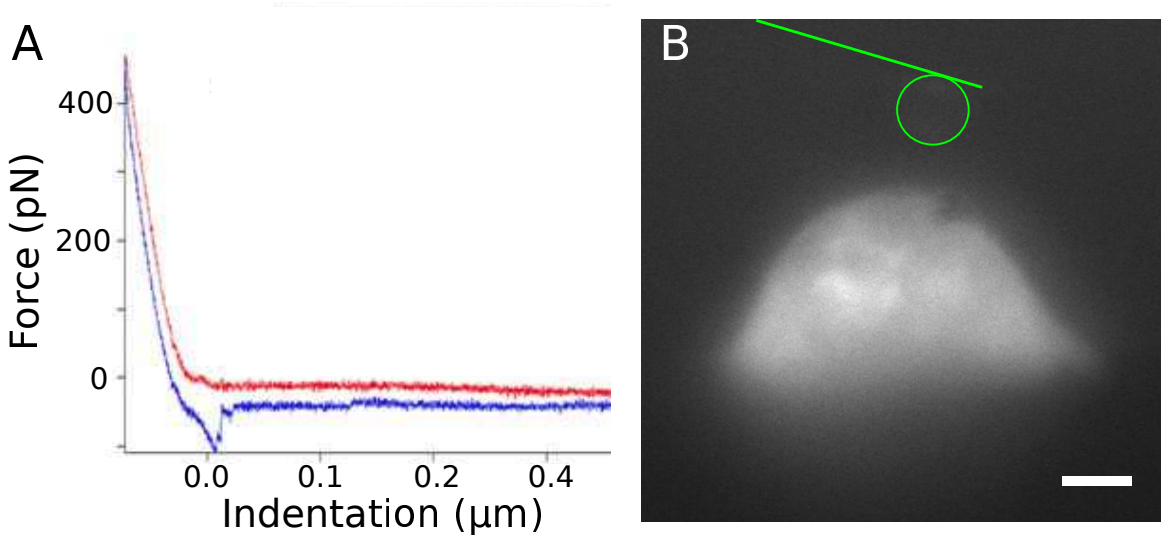

Figure 4.9: Combined AFM and PRISM system demonstration. Simultaneous (A) AFM force-indentation curve - approach in red and retract in blue - and (B) PRISM side-view image of ovarian cancer cell with SYTO 83 DNA stain. Green outline shows location of beaded AFM cantilever for this particular image. Scale bar is 5 μm. Higher quality images produced with the incorporation of VLS illumination are in Figures 4.15 and 5.3

Section 4.3: Vertical Light-Sheet Illumination

The contribution of out-of-focus fluorescence to an image is a common problem in standard fluorescence microscopy which is often overcome through the use of a thin planar sheet of light that only illuminates the fluorescence in the region of interest. This technique is often referred to as light-sheet fluorescence microscopy (LSFM) or single/selective plane illumination microscopy (SPIM). Though the technique was first described in a 1903 publication by Siedentopf and Zsigmondy,(225) LSFM (originally called ultramicroscopy) has experienced a recent surge in use due to its applications for biological imaging. LSFM can reduce out-of-plane fluorescence in the imaging of labeled tissues, cells, and single-molecules.(226; 227; 228; 225; 229) Use of a thin sheet of light allows researchers to image sample volumes faster than current methods, image larger samples, produce well-registered optical sections suitable for three-dimensional reconstruction, and reduce light dosage associated with photobleaching and phototoxicity. Frequently, this is accomplished using a twin objective configuration, where the objectives are juxtaposed at 90° angles to illuminate the region surrounding the detection objective.(230; 231; 228; 225)

Unlike conventional light-sheet microscopy where the sample is illuminated with a light-sheet parallel to

the surface to provide optical sections in the XY plane (plan-view), the PRISM imaging plane is vertical and thus requires a vertical light-sheet (VLS) to illuminate the specimen. Additionally, PRISM imaging requires both lateral and axial positions of the VLS to precisely align the illumination and imaging planes. I designed a variant of light-sheet microscopy in which VLS illumination and PRISM-imaging are accomplished using the same objective.

4.3.1: Implementation

The properties of lasers as propagating Gaussian beams are fundamental to light-sheet fluorescence microscopes and are discussed in detail in Appendix G. I designed the optics system (see Figure 4.10) to be placed externally to the microscope body and to operate in conjunction with the microscope's tube lens and imaging objective to produce the desired light-sheet dimensions. The optics layout begins with the laser: a 532 nm diode-pumped solid state green laser diode (Thorlabs, Inc.) with a circular beam output.

The light then passes through a series of spherical lenses and two cylindrical lenses to produce a beam with a sheet cross section (i.e., >100 μm along one axis and <1 μm along the other axis). To form a light-sheet at the specimen, the laser beam is focused only along one axis using cylindrical lenses to form a line-focus (as opposed to the point focus produced by spherical lenses). In Figure 4.10, the beam behavior in orthogonal directions is denoted by red and blue lines. The red lines correspond to the sheet width axis (w_s in the sheet illumination inset) and are affected by spherical lenses and cylindrical lenses (denoted by f_{CW}). The blue lines correspond to the sheet depth axis (d_s in the sheet illumination inset) and are affected by spherical lenses and cylindrical lenses (denoted by f_{CD}). The first two lenses, f_{SL1} and f_{CD1}, are spaced apart a distance equal to the sum of their focal lengths and act as a tube lens on the sheet depth axis. Likewise, the first and third lenses, f_{SL1} and f_{CW1}, act as a tube lens on the sheet width axis because the middle cylindrical lens, f_{CD}, has no effect on the beam properties on this axis. The lateral mirror, placed in a 4f configuration, permits lateral movement of the light-sheet without affecting other light-sheet properties. The following series of cylindrical mirrors adjust the orthogonal parameters to the desired dimensions.

In this light-sheet design, I have employed an optical technique of axial displacement presented by Botcherby et al.(232; 233; 234) This method of axial displacement was originally designed for rapid imaging, which required remote focusing. This arrangement involves a plane mirror and high NA objective in an ideal 4f configuration with the imaging objective. The plane mirror reflects the rays from the intermediate image space back into the objective and through a beam splitter to direct the rays toward the final tube lens and imaging place. By moving the plane mirror (or axial mirror), it is possible to change the plane on which the sheet waist is focused without introducing spherical aberration.

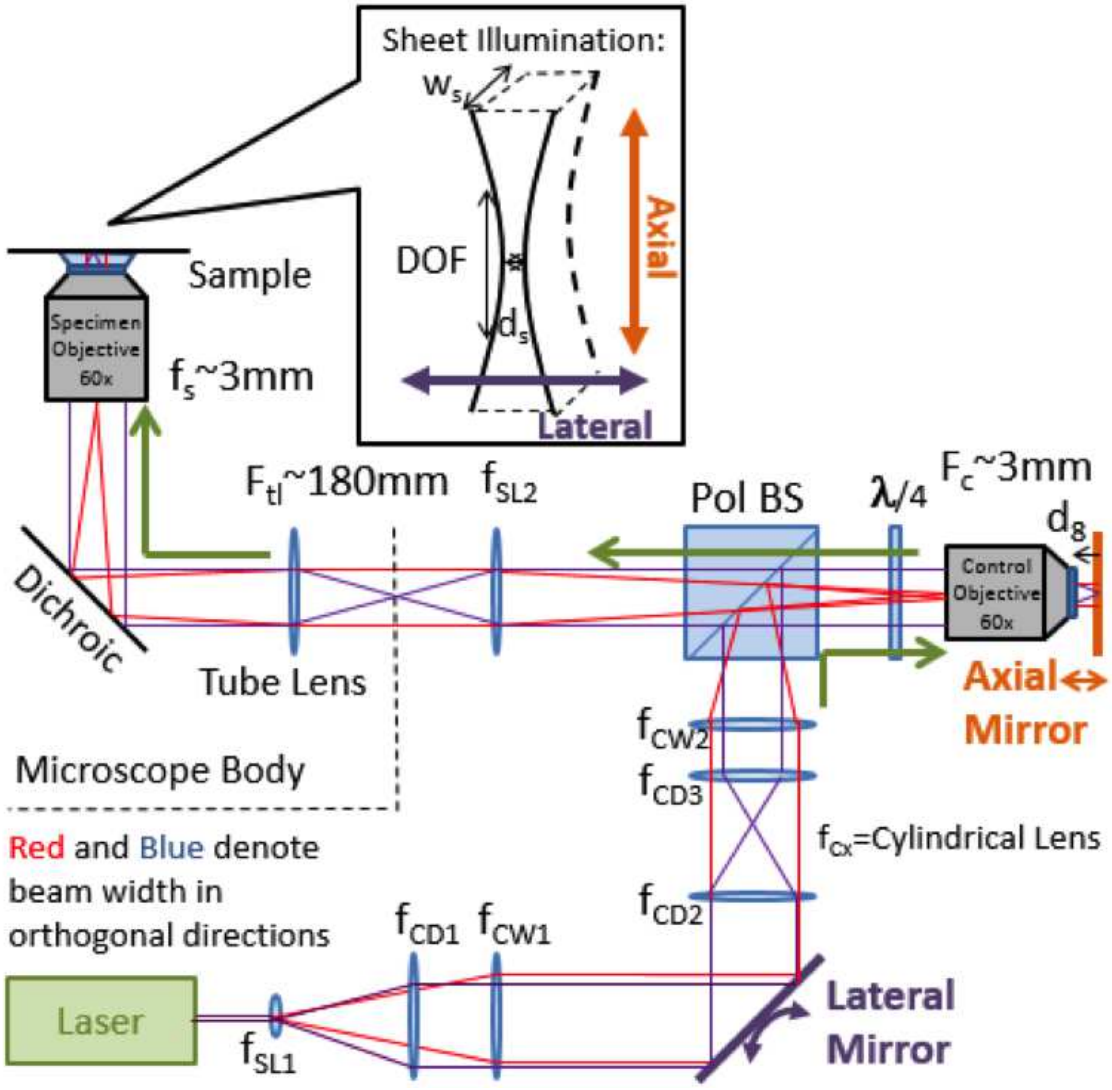

Figure 4.10: Schematic of VLS optical layout. The system consists of a series of spherical lenses (f_{SL1}, f_{SL2}, and f_{tl}, cylindrical lenses oriented either along the sheet waist axis (f_{CD1}, f_{CD2}, and f_{CD3}) or along the sheet length axis (f_{CW1} and f_{CW2}), control and specimen objectives, axial and lateral mirrors, and polarized beam splitter. A dichroic was used in the place of a standard plane mirror to allow excitation wavelength to be reflected and the epifluorescence emission wavelength to pass through. The lateral mirror provides lateral displacement of the laser illumination in the sample plane. The control objective and the axial mirror are used for remote axial translation of the light-sheet up and down relative to the sample plane.

The final step in coupling the external optics to the standard inverted optical microscope of the AFM MFP-3D Bio system required the replacement of the internal mirror for changing imaging pathways with a dichroic. The dichroic reflects the 532 nm laser light that enters the microscope body through right-side port and passes through the epi-fluorescence produced by the sample. By removing the dichroic from the light path, the microscope system still permits broad illumination of the sample.

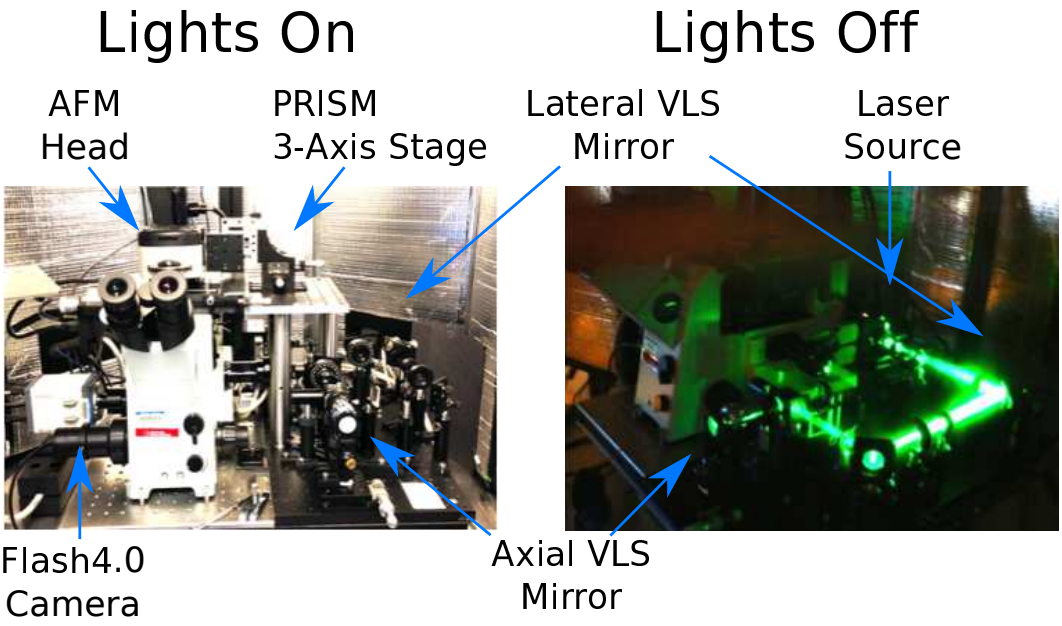

Figure 4.11: Image of completed AFM-PRISM-VLS system. The left image shows the AFM head on top of the inverted optical microscope, the 3-axis micromanipulation stage on which the capillary tube PRISM assembly is mounted, and the VLS optics to the right of the microscope. The right image illustrates the beam's transition from a circular shape to a flat sheet upon entering the microscope and was created by performing a long exposure image of the optics path while allowing liquid nitrogen condensed water vapor to scatter the laser light.

The completed system can be seen in Figure 4.11. The entire system – AFM, optical microscope, and light-sheet optics – fits inside the BCH-45 acoustic enclosure and on the Herzan AVI series vibration isolation platform (Asylum Research), where the standard granite top was replaced with a lighter breadboard to accommodate weight restrictions. The requirements of acoustic and vibration isolation are essential to maintaining the force sensitivity of the AFM force measurements.

4.3.2: Characterization

Characterization of VLS illumination requires (1) measuring the light-sheet parameters, such as beam waist and depth of field, and (2) establishing improved image quality via its implementation in an experimental context.

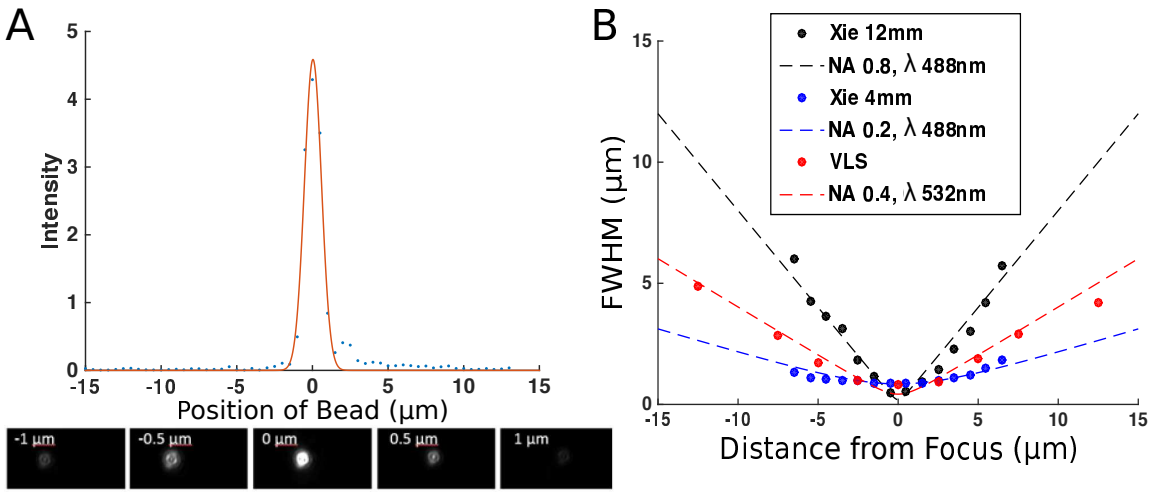

Figure 4.12: Vertical light-sheet characterization. (A) Intensity of 20 nm fluorescent bead sample illuminated by VLS as a function of the lateral position translated by the AFM scan stage. Sample images of a 20 nm fluorescent bead sample illuminated by VLS as it is translated through the sheet are shown below. (B) FWHM of the VLS as a function of axial mirror position, which provides a measure of the sheet depth of field.

I measured the beam width as a function of depth by scanning fluorescent beads through the light-sheet using the AFM scan stage and mapping their intensities as a function of position. The characterization specimen was created by drying a sparse dilution of beads in ethanol onto a glass coverslip. The sample was then loaded onto the AFM scan stage and was passed through the light-sheet in increments of 0.5 μm. Fluorescence intensity from the beads increased as the beads passed through the light-sheet, and subsequently decreased as they receded from the beam wast. For each image, the intensity profile of each bead was determined via fitting to a Gaussian distribution. These intensities were plotted as a function of scan stage position, and then the distribution was fitted to a Gaussian distribution to determine the FWHM as a measure of sheet width (Figure 4.12A). The axial mirror position was then moved, and the process was repeated. In this way, the width of the beam as a function of axial position was determined. The result was a beam waist of 0.9 μm and a corresponding depth of focus (DOF) of $\sim$10 μm for our system.

Figure 4.12B compares the light-sheet produced by our system with those of other leading systems in the field. The theoretical resolution of each system is depicted by a dashed line, with additional detail provided in Appendix G. The light-sheet produced by Xie et al.(229) for single-molecule imaging was controlled by the size of the aperture on the back of the illumination objective. Increasing the aperture size reduced the size of the beam waist; however, this also resulted in a decrease of the DOF, or the distance over which the sheet width is uniform. Depicted in Figure 4.12B are sheet profiles produced by two aperture diameters in the Xie system (black = 12 mm and blue = 4 mm) and our system (red). The large aperture configuration

produces a beam waist narrower than our VLS; however, the DOF is only a few microns and would not be useful for full cell measurements. In contrast, the smaller aperture configuration produced a beam waist slightly larger than ours and with a very large DOF. The latter configuration was used for all single-molecule transcription factor studies in the Xie paper (229) as it consistently illuminated a large enough section of the specimen. Taking specimen size into consideration, our light-sheet parameters are competitive with other light-sheet systems, and possess the depth of field and sheet width to acquire PRISM images of cells.

Next, I endeavored to compare imaging quality between broad illumination and VLS illumination in PRISM images. To test the change in image quality, 20 nm beads were incubated with ovarian cancer cells (SKOV) to serve as point sources and background that could be analyzed in the PRISM images. The resulting plan- and side-view images can be seen in Figure 4.13. The plan-view image shows a false color overlay of broad (red) and VLS (green) illumination. The broad illumination makes it apparent that the entire cell is decorated with 20 nm beads that contribute to out-of-focus fluorescence, while the sheet illumination excites a thin band of the cell several bead-diameters thick. To produce PRISM side-view images, the objective focus was raised until the imaging plane was rotated by the 45° reflecting optic to acquire a side-view image of the cell. Raising the objective to change the imaging plane also increased the height of the VLS so that the beam waist was well above the cell. Therefore, before acquiring PRISM-VLS images, the light-sheet was returned to the specimen using the axial mirror. Adjusting both the axial and lateral positions of the VLS is crucial for achieving high quality side-view images with the PRISM imaging system.

The dramatic improvement in the signal-to-noise ratio and, thus, the ability to resolve point sources is apparent when comparing the PRISM-view broad and VLS illumination in Figure 4.13. The increase in signal-to-noise ratio is evidenced by a dip in the signal over the middle of the cell corresponding to the nucleus, where the engulfed beads were not able to reach, and at the periphery of the cell. To quantitatively characterize the change in signal, a plot profile through the same region of the cell for each illumination method was compared. While the maximum intensity measured through beads within the cell were unchanged, the nucleus region exhibited a drop in out-of-focus intensity by over 50%. Due to the reduction in background noise, the ability to resolve single beads in the cell is now possible with VLS illumination. Furthermore, there was a significant reduction in photobleaching during a time-series acquisition due to the reduction in intensity required for PRISM imaging (this phenomenon is less dramatic and more difficult to convey in still images). A similar improvement is observed in signal-to-noise ratio with VLS applied on live cell stains (Figure 4.14).

Coupling VLS illumination to the AFM-PRISM system resulted in improved imaging quality by reducing out-of-plane fluorescence.

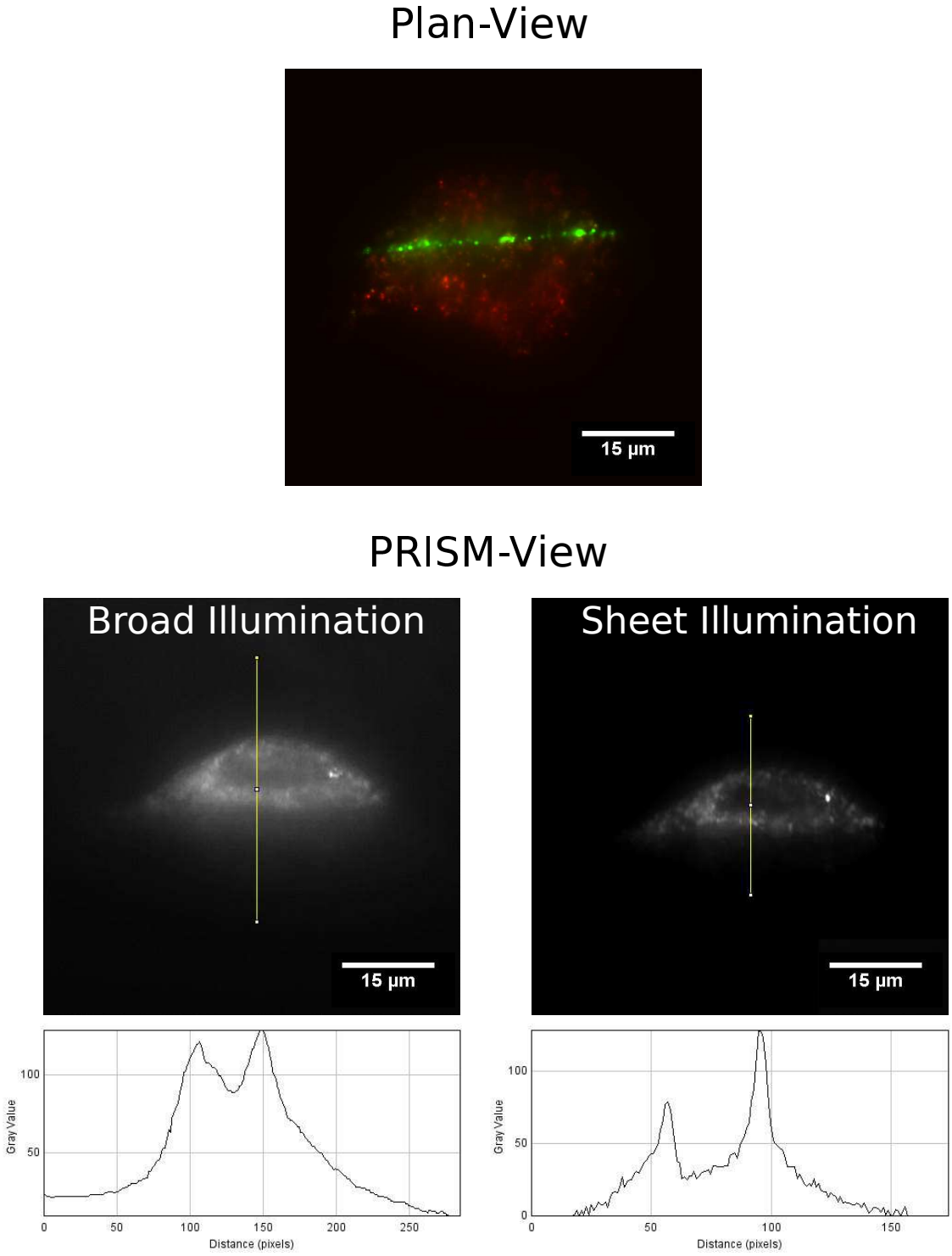

Figure 4.13: Vertical light-sheet (VLS) illumination improves imaging of ovarian cancer cells labeled with 20 nm fluorescent beads. (Top) False colored plan-view image of broad (red) and VLS (green) illumination of 20nm bead-labeled cells. (Bottom) PRISM-view images of the same cell with both broad and sheet illumination. Intensity profiles for the yellow line in each image.

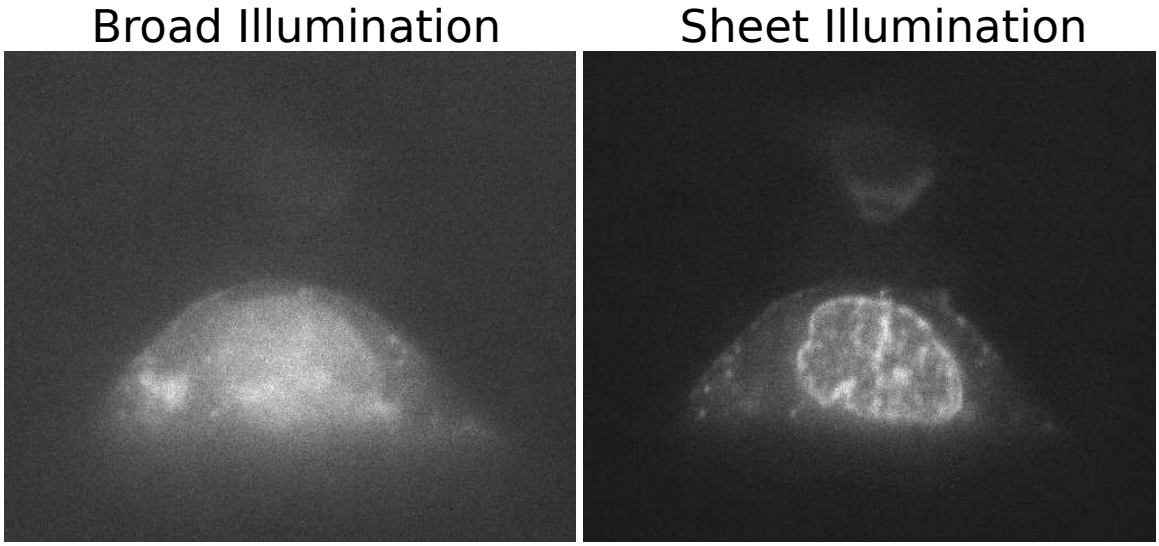

Figure 4.14: Vertical light-sheet (VLS) illumination improves imaging of ovarian cancer cells labeled with membrane (Vybrant) and nucleic acid (SYTO83) labels. PRISM-view images of same exposure time for the same cell with (left) broad and (right) sheet illumination show a dramatic improvement in signal-to-noise with VLS illumination.

Section 4.4: Conclusions

Our microscopy system integrates and synchronizes force measurements with powerful high-frame-rate side-view imaging, a technique that significantly improves upon the current state of the art for cell mechanics studies. This improvement was accomplished by coupling the AFM with a pathway rotated imaging technique and vertical light-sheet illumination. This combination facilitated high frame rate imaging in the XZ plane without restricting sample geometry or compromising the piconewton-resolution force data capabilities of the AFM.

A to-scale illustration of the cell experiment illustrates the versatility in our experimental setup and depicts the relative scales of the instruments involved at the sample (Figure 4.3). The results of one of the first live cell experiments from the completed AFM-PRISM-VLS system can be found in Figure 4.15. Ovarian cancer cells (SKOV) were labeled with SYTO 82, a red fluorescent nucleic acid stain, which is brightest in the nucleus of the cell and even shows structure within the nucleus. Overlaid images for broad (Figure 4.15F) and light-sheet (Figure 4.15G) illumination show the outline of the cell and Arrow-CONT cantilever (black and white), the SYTO-labeled nucleus (red), and 5 μm yellow-green fluorescent bead tip on the AFM cantilever. Prior to PRISM imaging, the AFM bead tip is aligned over the center of the nucleus and the light-sheet is positioned to be directly under the bead where force is applied. Then, simultaneous force and image data (Figure 4.15) is acquired as (A) the bead approaches, (B) contacts the cell, (C) indents the nucleus until a force trigger is achieved, (D) the cantilever maintains that deflection for a pre-defined dwell

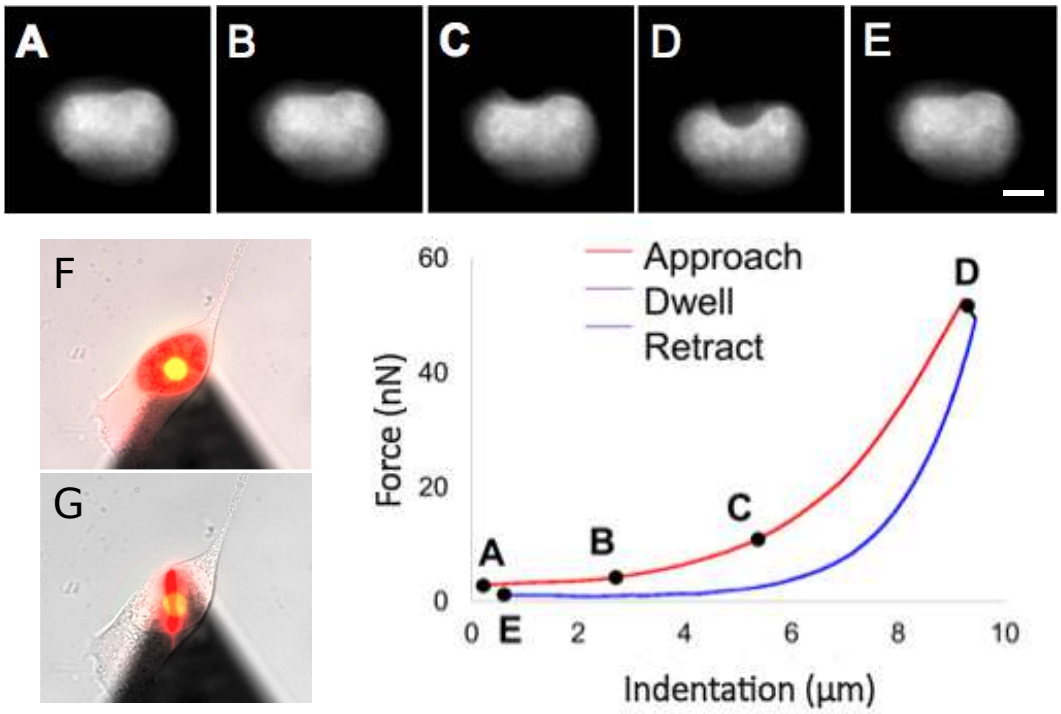

Figure 4.15: Sample experiment performed on a SKOV cell. Images A-E are select PRISM-view images from a video of the SKOV cell deformation acquired simultaneously with AFM force data. Plan-view images F and G are false-colored red, green and bright-field, and are of the same cell and AFM cantilever in broad and sheet illumination, respectively. The bottom-right plot is the force-indentation curve simultaneously acquired with the corresponding images indicated. Figure 5.3 depicts a cell with more internal nuclear structure due to a change in label.

time and (E) retracts from the cell. The side-view images in Figure 4.15 are frames from a movie and, due to efforts made in synchronizing the AFM and camera controls, their corresponding locations in the AFM force curve can be directly matched. Where the side-view images provide visual context for any irregularities in force-indentation curves, the force data measures cell stiffening effects as described in Chapter 3. The images also show movement of sub-nuclear structure due to the applied force, the focus of Chapter 5, where I use this system to better understand the mechanisms responsible for mechnaotransduction.

In conclusion, the combined AFM, PRISM and VLS system is ideally suited for studying the mechanical, structural and biochemical responses involved in mechanotransduction. The optics for pathway rotated imaging and vertical light-sheet illumination were incorporated with minimal modifications to the commercially available AFM-microscope system and restrictions to specimen geometry. This unique system provides the ability to

1. apply and measure pN-nN forces,
2. acquire high-speed and high-resolution images of cellular structure dynamically in the direction of applied load,
3. and relate force and image data with a high degree of temporal certainty.

While designing and implementing this system, several considerations and goals for future systems should be taken into account:

- As illustrated by Galland et al.(235) and Gebhardt et al.(229), a 45° reflecting optic can be used to rotate a light-sheet to the horizontal. In this way, the light-sheet in our system could also be oriented horizontally for use in low background plan-view imaging.
- In the current design, both the lateral and axial motion of the VLS are manually controlled. Adjusting these parameters manually introduces vibrations into the system and limits the precision of adjustments. Therefore, in future designs of the system, steps should be taken to implement computer-controlled axial and lateral motion. Computer controlled sheet motion would add the ability to efficiently acquire high-resolution image stacks in both PRISM and plan-view for 3-dimensional image reconstruction to our system.
- An important parameter in imaging cells is the ability to incorporate multiple wavelength fluorophores to help elucidate mechanisms involved in mechanotransduction. In future versions of the VLS microscope, the back port of the microscope should be used to allow for the use of multiple wavelengths of excitation and emission light through the use of the filter wheel. This is not possible through the right side port as the microscope must be broken down in order to exchange dichroics.

Technique	AFM + Inverted Optical Microscope	AFM + Confocal	AFM + Other Side-View Techniques	AFM + PRISM	AFM + PRISM + VLS
Force Resolution (pN)	✔	✔	✔	✔	✔
Versatile Sample Geometry	✔	✔	X	✔	✔
High Frame Rate Imaging (ms)	✔	✔	✔	✔	✔
Plan-View Imaging	✔	✔	✔	✔	✔
Side-View Imaging	X	✔	✔	✔	✔
Side-View Resolution (sub-micron)	X	X	✔	X	✔
High Frame Rate Side-View Imaging (ms)	X	X	X	X	✔

Table 4.2: Comparison of current techniques for simultaneous AFM force measurements and side-view, high frame rate imaging. The criteria for a versatile force measurement and side-view imaging system are listed in the column. A green checkmark indicates that the technique accomplishes the task and a red 'X' indicates that the technique cannot accomplish the task. The orange checkmark indicates that only some techniques are able to maintain piconewton force resolution. The orange 'X's indicate that the techniques have not satisfied the criteria, but this is not directly due to the inability of the instrument to acquire high frame rate imaging.

In the next chapter, investigations of the mechanics of single cells and subcellular components under load using the combined AFM-PRISM-VLS system will be described.

CHAPTER 5: Application of the Combined Atomic Force Microscopy and Pathway Rotated Imaging System

In the previous chapter, I discussed the development of a combined atomic force microscopy (AFM) and pathway rotated imaging for sideways microscopy (PRISM) system. In this chapter, I describe the use of this system to investigate the mechanics of single cells and subcellular components under load. This experiment included the acquisition of simultaneous cell mechanics measurements with high speed, side-view images of intracellular motion. From these experiments, the structural components of the cell responsible for changes in cell mechanics were identified and direct mechanical linkages between the cell membrane and the nucleus investigated.

This chapter is comprised of the following sections:

Section 5.1: Background on Mechanotransduction to the Nucleus

Living cells possess the ability to sense, withstand, and respond to external mechanical forces. These properties are essential to the physical integrity and biological function of the cell. Mechanical forces are critical regulators of the growth and shape of virtually every tissue and organ in our bodies. However, there is still much unknown about the mechanisms through which individual cells sense these mechanical signals and convert them into changes in biochemistry and gene expression - a process known as mechanotransduction.

The molecular mechanisms responsible for a cell's response to external forces are especially of interest due to their downstream effects on gene expression, differentiation and motility.(33; 34) Mechanotransduction pathways are mediated by the conformational changes in load-bearing subcellular structures which result in activation or deactivation of biochemical signaling pathways in response to mechanical stress.(45) Previous experiments have led to the identification of pathways that signal from the membrane to the nucleus through the passage of cytoplasmic components such as transcriptional co-activators into the nucleus.(45; 236; 237; 238; 239)

However, it has recently become clear that nuclear structures may respond directly to mechanical tension

via force propagation through the cytoskeleton.(3) This understanding of direct mechanical response is the result of the discovery of LINC (Linkers of Nucleoskeleton and Cytoskeleton) complexes, through which the nucleus is physically connected to the cytoskeleton and, thus, the cell surface.(240; 241) The direct mechanical linkage between the nucleus and the cytoskeleton is proposed to facilitate the propagation of signals to the nucleus in only a few micro-seconds.(3) In this way, the nucleus itself may therefore be a mechanosensor with force-induced changes in nuclear structure directly affecting transcription.(162) However, the effect of intracellular and nuclear motion due to external force has not yet been fully explored.

Even though the cellular response to controlled mechanical inputs is important in a variety of biological processes, the specific molecular mechanisms underlying the observed response are not well understood, partly because of the lack of appropriate experimental tools. Key metrics for understanding cell response to mechanical stimuli include the rearrangement of the cytoskeletal and nucleoskeletal structure, induced strains and biochemical distributions; however, structural information during applied stress is limited by the ability to image cells under load. In Chapter 4, I discussed a unique imaging system that combines an atomic force microscope (AFM) with both vertical light-sheet illumination (VLS) and a new imaging technique called PRISM – Pathway Rotated Imaging for Sideways Microscopy – designed to study the mechanics of single cells and subcellular components under load,. The combined AFM and PRISM system facilitates the imaging of cell deformation in the direction of applied force with accompanying piconewton resolution force measurements. The additional inclusion of light-sheet microscopy improves the signal-to-noise ratio achieved by the illumination of a thin layer of the cell.

Using the system developed and described in Chapter 4, here I demonstrate the use of an instrument that combines atomic force microscopy with a side-view fluorescent imaging path that enables high frame rate imaging of cellular deformation along the axis of loading. Force resolution 10 s of piconewtons, $\sim$ 300 nm xz-plane image resolution, and 10 ms time resolution were directly observed in the study of intracellular (and intranuclear) motion due to force applied to focal adhesions at the cell membrane. Specifically, I utilize the combined AFM-PRISM-VLS system to investigate mechanical mechanisms underlying the deformation or adhesion of SKOV ovarian cancer cells to a fibronectin-coated AFM tip. In Chapter 3, SKOV cells were investigated as one of a set of cells exhibiting mechanical properties (i.e., stiffness measured with passive bead, magnetic bead and AFM measurements) and mechanical response (i.e., softening measured with magnetic beads) correlated to their metastatic potential. This chapter focuses on the detailed analysis of datasets acquired for a *single cell* to fully showcase the capabilities of the system and the new insights on cell deformation accessible from the analysis of this unique data. Additional datasets of similar quality to those reported here have been acquired (Appendix K) and will be the focus of further research, now that there exists a method for interpreting these data.

Our system is the first to allow simultaneous AFM force measurements with side-view imaging of sub-cellular motion with a z-direction image resolution comparable to high-quality plan-view, xy-resolution at high frame rates of 50 fps. The utility of this measurement was demonstrated for (1) identifying the structural components of the cell responsible for changes in apparent depth-dependent mechanical properties and (2) identifying direct mechanical linkages between the cell membrane and the nucleus. Experiments were performed by indenting a cell with a fibronectin-coated AFM tip and then retracting the AFM tip while simultaneously collecting sub-nanonewton AFM force data with millisecond-synchronized ∼300 nm resolution imaging in the direction of applied force. Because mechanical properties of the cell were determined from indentation AFM data and adhesion strength was determined from retraction AFM data, the experiments were broken down into (1) indentation and (2) adhesion data. Due to our simultaneous side-view image technique, I was able to clearly determine the physical changes in the cell associated with changes in apparent stiffness measured in force data. Specifically, nuclear deformation and strains primarily located at the top of the nucleus were correlated with a 1.5-fold increase in stiffness measured with a Hertz model fit to force-indentation data. The image z-axis resolution and millisecond synchronization allowed me to detect sub-micron motion of the cell membrane and nucleus corresponding to force-rupture events of membrane adhesion to the fibronectin-coated AFM tip. These adhesion results indicate a relationship between the strength of surface adhesions and direct mechanical linkage from the cell membrane to the nucleus. Through the detailed analysis of these datasets, I illustrate the power of the integrated force measurement and synchronized high frame rate, side-view imaging system for cell mechanics studies.

Section 5.2: Experimental Methods

5.2.1: Materials, Sample Preparation, and Tip Functionalization

All reagents were purchased from Thermo Fisher Scientific (Liverpool, NY) unless noted otherwise.

Cells were sparsely plated onto fibronectin-coated polyacrylamide (PA) gels. Gels were prepared to achieve 50-60 kPa stiffness, using a ratio of the 4:3:3 50mM HEPES, 40% acrylamide, and 2% methyl-bis. Gelation was activated by the addition of 0.004 N,N,N',N'-tetramethylethylenediamine-1, 2-diamine, and 0.012 10% ammonium persulfate. The gels were prepared onto 24x50 mm glass coverslips (Corning #1.5), previously UV-cleaned and then vapor treated with 1,3,5,7-tetravinyl-1,3,5,7-tetramethylcyclotetrasiloxane. After catalyst addition, 10 μL of gel solution was placed in the center of the coverslip and rapidly covered with a HMDS (hexamethyldisilazane) vapor-treated 22x22 mm coverslip to compress the gel and spread it evenly on the coverslip. The gel was allowed to partially dry in a sterile biological safety cabinet before removing the 22x22mm coverslip from the top of the gel.

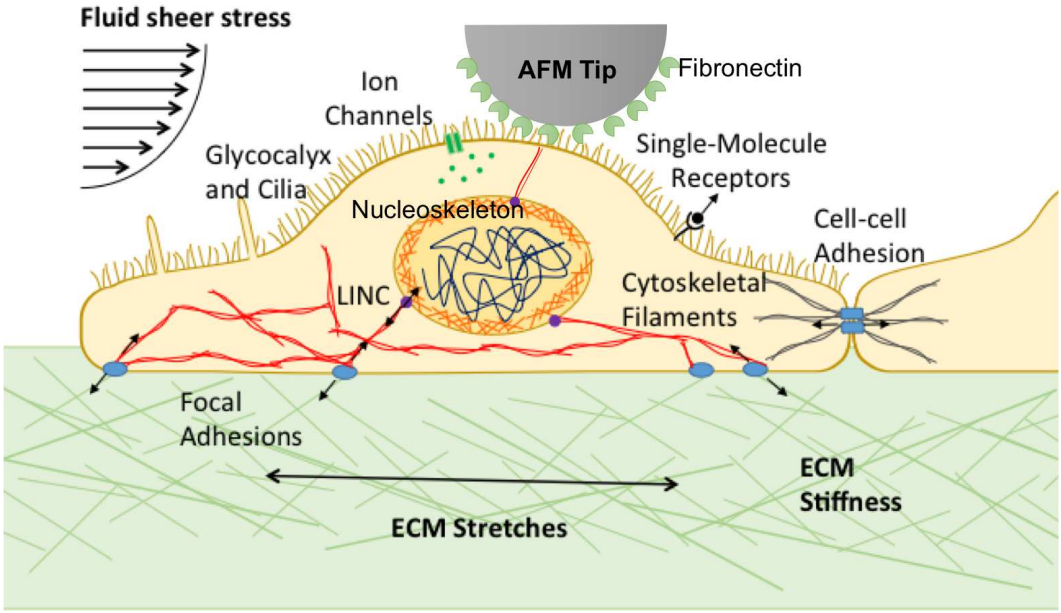

Figure 5.1: Experiment design for single cell mechanotransduction studies. Note that the complex mechanical environment surrounding the cell (e.g., fluid shear, extracellular matrix, cell-cell adhesions) is not a part of this experiment but rather a reflection of all the types of forces that a cell can experience. The fibronectin-coated AFM tip is brought into contact with the cell over the nucleus. Indentation of the cell can be used to measure direct deformation of cellular and subcellular components, and focal adhesions formed between the tip and cell can be used to measure adhesion.

To attach fibronectin to the gel, sulfo-SANPAH (N-sulfosuccinimidyl 6-(4'-azido-2'-nitrophenylamino)hexanoate) was disolved in DMSO (dimethylsulfoxide, cell culture grade) at ∼1 mg/mL and spread into a 1 cm diameter circle with a pipet tip in the center of the gel. The excess solution was removed from the gel sample. Then with the gel inside the biological safety cabinet, the UV light was turned on for ∼10 minutes or until the sulfo-SANPAH color turned from orange-red to slightly brown. The sulfo-SANPAH was then rinsed with 3 successive applications and removals of PBS (phosphate buffered saline). Then 0.01 mg/mL fibronectin in PBS was placed onto the same location with enough solution to barely cover the same area. The UV light was again turned on for 5 minutes to allow crosslinking of the fibronectin onto the gel surface. After removal of the fibronectin solution and while relatively dry, a 1 cm glass cloning cylinder was added to the gel with thin layer of vacuum grease and sterile cell media was used to rehydrate the gel. The vacuum grease serves the dual purpose of preventing buffer leakage during overnight incubation and AFM-PRISM experiments.

Cells were plated onto the gels by trypsinization of a 50-90% confluent culture of SKOV3 human ovarian cancer cell lines (from Gerald Blobe's lab at Duke University). The cultures were diluted back to about 30% confluence, and then an aliquot of cells was further diluted by at least 1/10 - 1/30 before plating in RPMI (Roswell Park Memorial Institute) medium with 5% serum and antibiotic/antimycotic at 1X. Cells usually attached within several hours, but were incubated overnight to ensure firm attachment.

On the day of the experiment, cells were stained with vital (live-cell) stains for SYTO 82 or 83 nucleic acid label, MitoTracker mitochondria and cell membrane label, and/or Vybrant cell membrane label. The sample was rinsed profusely with RPMI medium by removing liquid from the cloning ring, replacing with new medium, and repeating several times to remove loosely attached cells. A larger secondary ring of vacuum grease was added onto the gel surface concentric to the cloning ring. The majority of solution was removed from the cloning ring, and the cloning ring removed from the gel surface. Finally, the sample was loaded onto the AFM stage and additional medium added to form a small bubble in the inner vacuum grease ring.

In parallel, fibronectin was physiosorbed onto the surface of the AFM cantilever with 5 μm polystyrene bead tip. Bead attachment to cantilever procedure is described in Appendix I. Briefly, a 5 μm polystyrene bead (Corpuscular, NY) was attached with Norland Optical Adhesive (Norland, NJ) to a TL CONT tipless cantilever (Novascan Technologies, IA). The AFM cantilever is loaded into the AFM cantilever holder and while on the holder approximately 10 μL of 0.01 mg/mL fibronectin in PBS was placed on the end of the cantilever where bead was attached. The solution is allowed at least 15 minutes to physiosorb onto the polystyrene bead before rinsing the AFM tip with medium and loading into the AFM head.

5.2.2: Simultaneous AFM and Image Data Collection

The cantilever and sample were loaded onto the AFM, and experiments were performed in medium bubble formed between substrate and AFM cantilever holder. Care was taken throughout the experiment to avoid any media leakage onto the AFM system, which could possibly damage the electronics because of the salts and liquid in the medium.

Using the AFM micromanipulation stage, I selected a single SKOV cell firmly attached to the gel, with spreading behavior representative of the cell line and sufficiently fluorescent in plan-view. Each of these parameters was important due to the small number of cells in each sample. Next, the AFM tip was positioned over the nucleus of the selected cell. The AFM tip and cell were then jointly positioned such that the VLS illuminates the region of the cell directly under the AFM tip. Finally, PRISM was positioned $\sim$ 50 μm from the AFM tip to avoid contacting the cell or AFM cantilever. Once all the physical parameters were in place, the imaging objective height was raised to find the pathway rotated side-view imaging plane. Because adjusting the height of the objective also changed the position of the narrowest part of the light sheet, the VLS no longer illuminated the sample. To compensate for this, the VLS was translated back down to the cell using the axial adjustment mirror in the VLS optics (Figure 4.10). Once the imaging and illumination planes were aligned, the IGOR software was used to acquire a standard constant-velocity force curve and externally trigger the ORCA Flash4.0 CMOS camera (Hamamatsu Photonics K.K., Japan), as previously described in Section 4.2.

5.2.3: AFM Data Analysis

AFM data were typically collected at 100kHz. The resulting data was used to determine the mechanical properties of cells and adhesion forces between a cell and fibronectin-coated AFM tip from the indentation or retraction portions of the force curve, respectively.

Force curves were analyzed with custom MATLAB code to calculate the Young's modulus, a measure of cell stiffness. The code is described in detail in Appendix D. Briefly, the program identifies the contact point coordinates using a golden-section search, which attains the minimum total fitting error for a linear fit of the data to the left of the contact point and a Hertz model fit to the data from the contact point to the right, up to a user defined maximum indent. Least-squares fitting is applied to the force-indention data in the post-contact region of the force curve to the Hertz model in order to extract the Young's modulus of the cell.

Additionally, measurements of the adhesion forces formed between the cell membrane and fibronectin-coated AFM tip were collected. The retraction portion of the AFM force-indentation curve contains rupture

peaks created when the AFM tip pulls against attachments to the cell membrane. As the cantilever continues to move away from the surface, the force applied to these attachments increases until a rupture or intracellular rearrangement occurs. The heights of these rupture peaks are related to the strength of the interactions, whose resulting ruptures produce the drop in force.

5.2.4: Image Analysis

PRISM-view images of the SKOV cell labeled with a membrane dye (Vybrant) and a nucleus (Syto) stain illustrate cell motion due to applied load. Images were acquired with 300 nm resolution at 50 fps. Motion of the cell membrane and subcellular components such as the nucleus were measured using kymograph and difference image analysis.

Kymograph Analysis: A kymograph is a traditional and effective method of measuring movement in cell biology, e.g., dynamic assembly of microtubules or motor proteins in axions.(242; 243) A kymograph is a time-space plot created by extracting a long, thin, rectangular region from each image in a time-lapse series. The rectangular region-of-interest (ROI) is pasted sequentially side-by-side to make a montage of the region over time. The result is a series of bright lines corresponding to different fluorescently labeled regions of the cell - the cell membrane, nuclear membrane and intracellular/intranuclear punctate regions. If the rectangular region is aligned along the axis of applied load (z-direction), the oblique white regions in the kymograph correspond to movement of the fluorescent regions over time, with slopes related to the velocity of the region's motion. Moreover, relative separations can be related to intracellular/intranuclear strain resulting from applied load.

A vertical ROI directly below the AFM tip was selected (Figure 5.2A). Kymographs of image stacks were created with the ImageJ KymographyReslice plugin (Figure 5.2B). Then, using custom MATLAB code, the position of the bright regions of the kymograph were tracked in time. Each peak was tracked through the image stack using Gaussian fitting, with initial estimates of peak positions provided manually by the user for the first frame (Figure 5.2C). The result of tracking the bright regions with the Gaussian tracker can be seen in Figure 5.2D. This analysis is applicable to any dataset collected on the system.

Difference Imaging: Image differencing is an image processing technique used to identify changes between images, calculated by finding the difference between each pixel in two images, and generating a resulting difference image. Then, imaging thresholding was applied to filter out background noise; additionally, an area filter was applied when necessary to omit areas of the image that clearly contain no cell movement data. This technique was used to identify regions of motion within the cell associated with AFM measured force-rupture events when looking at a broader region of the cell than could be captured using a kymograph.

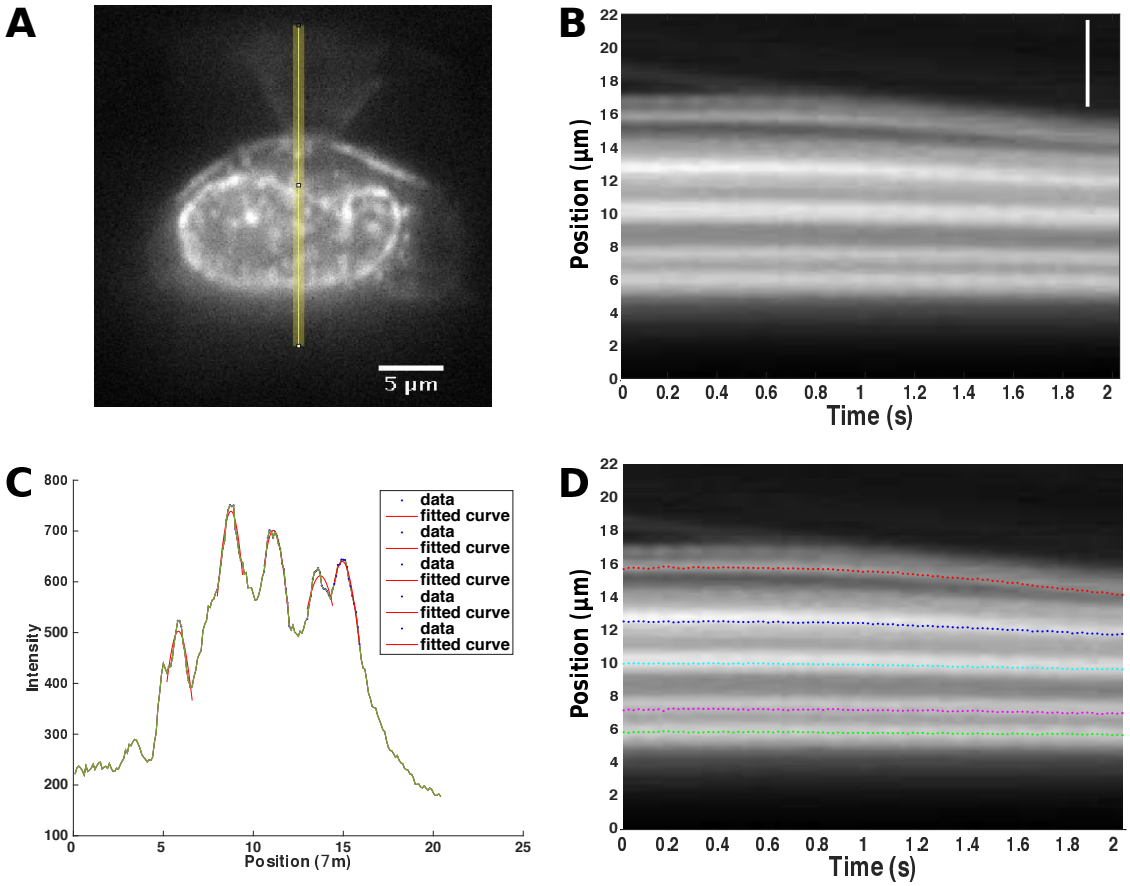

Figure 5.2: Kymograph analysis of deformation images of SKOV cell. (A) Representative side-view image sequence with vertical sliced section as the region-of-interest directly through the AFM tip center. Labeled regions of the cell - Syto 83 (nucleus) and Vybrant (cell membrane) - and the AFM bead-tip can be seen in this image. (B) Kymograph of the yellow ROI over the course of the approach portion of the dataset. (C) Gaussian fits to each of the 5 user-identified fluorescence intensity peaks for a single time point. (D) The result of Gaussian fits to each of the time points was a line for the top cell membrane (red), top of the nucleus (blue), and bottom of the nucleus (green). There are two additional lines (cyan and magenta) corresponding to punctate labels within the nucleus.

Section 5.3: Deformation and Adhesion Experiments

5.3.1: Simultaneous AFM and Image Data Collection

The power of our system for cell mechanics studies is the integration of force measurement with force-synchronized high frame rate imaging in the direction of applied force (z-direction). This was accomplished through two major innovations, discussed in detail in the previous chapter (Chapter 4): (1) Pathway Rotated Imaging for Sideways Microscopy (PRISM) and (2) Vertical Light Sheet (VLS) Illumination. Briefly, PRISM employs an $\sim 45^{\circ}$ reflecting optic near the cell to provide a side-view of the cell and VLS provides illumination for only the vertical plane imaged by PRISM. An advantage of the freely positioned reflecting optic was the ability to combine the imaging system with a commercially available AFM, without loss of sensitivity, for standard cell mechanics measurements. These combined innovations enable high frame rate side-view imaging capability with simultaneous AFM force measurements.

The results for a standard constant-velocity AFM measurement on our system are shown in Figure 5.3. The simultaneous side-view images of a SKOV cell labeled with membrane (Vybrant) and nuclear (Syto) stains illuminate cell motion due to applied load with an image resolution of $\sim$300 nm in the z-direction and 10 ms time resolution, limited by exposure time.

All experiments discussed in this chapter were performed with constant-velocity AFM measurements due to their prevalence in cell mechanics studies; however, simultaneous force and image data could be acquired with the AFM operated in constant-force (i.e., force clamp) or custom-programmed (e.g., force-quench or constant-velocity reversibility) modes, such as those used for the single-molecule studies described in Chapter 2. Over the course of a typical AFM experiment, the force curve has four ROIs indicated in the plots of Figure 5.3 by different colors - the approach (blue), surface dwell (magenta), retract (red), and final dwell (magenta), always in that order. Both plots in Figure 5.3 are different representations of the same dataset depicting different information contained in AFM data about the force changes as a function of time or indentation over the course of the experiment.

First, the AFM cantilever moves toward the cell (Figure 5.3A), contacts the cell membrane (Figure 5.3B), and indents the cell until the cantilever achieves a predetermined deflection or force value (Figure 5.3C). For this dataset, the predetermined deflection or force value, often called a trigger point, was 1.5 nN. All of the AFM measurements up to reaching the predetermined force trigger, including both the approach and indentation, are commonly referred to as 'approach' data and are shown in blue on the plots in Figure 5.3. Cell mechanics and structural deformation are examined in greater detail in Section 5.3.2.

Then, a feedback loop is used to maintain a constant cantilever deflection and, thus, constant force

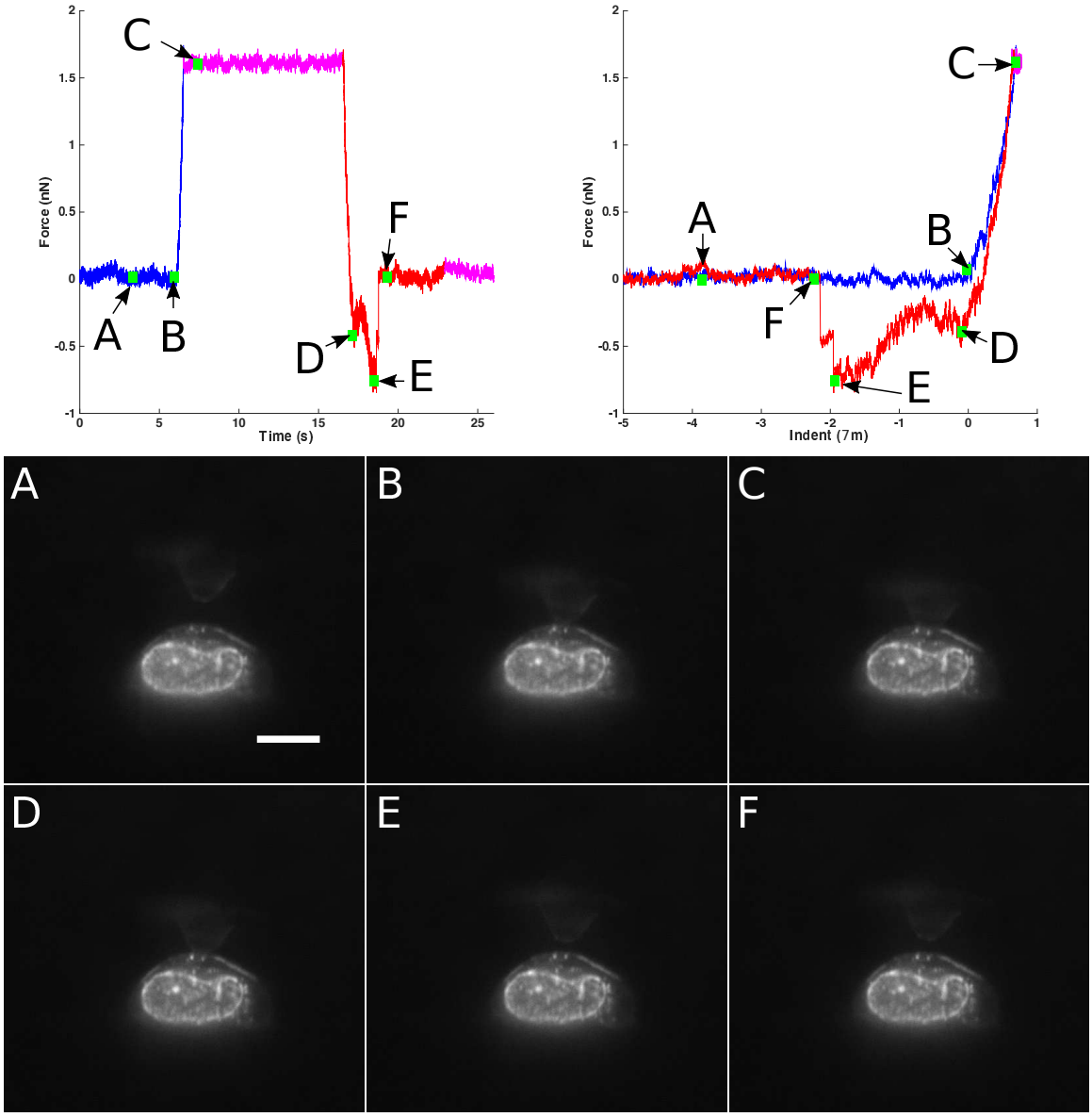

Figure 5.3: Simultaneous AFM force data and images. AFM deflection and z-piezo data was converted into force and indentation to produce force-time (Top-Left) and force-indentation (Top-Right) curves, which can be partitioned into several regions - approach and indent (blue), retract and adhesion (red), and dwells at constant deflection either at the surface or away from the cell (magenta). [A-F] Simultaneously acquired images of Syto83 and Vybrant labeled SKOV cell at a rate of 50 fps. Scale bar indicates 10 μm. Their location in the force curves are marked.

applied to the cell, for a defined dwell time of usually a few seconds. In Figure 5.3, the dwell time (shown in magenta) was 10 seconds.

At the end of the indentation dwell, the AFM cantilever is moved away from the cell surface at a constant velocity; this portion of the curve is commonly referred to as the 'retract' data and is red in the plots in Figure 5.3. As the base of the cantilever is moved away from the cell at a constant-velocity, the AFM tip is held down by adhesion formed between the fibronectin-coated bead and the cell membrane (Figure 5.3D and E). The detachment of cell-tip adhesion occurs through several discrete ruptures, each on the order of nanonewtons. The first drop in force between the tip and cell membrane (Figure 5.3D) is associated with a separation of ~ 0.7 μm; however, there is still unlabeled attachment evidenced by the increase in force up to the next, larger force peak (Figure 5.3E). The final rupture of adhesions between the tip and cell allow the cantilever to return to its native position of zero force (Figure 5.3F), which is maintained for the rest of the retract portion of the force curve. Adhesion rupture events and associated strain are examined in greater detail in Section 5.3.3.

After fully retracted from the cell surface, an additional dwell period elapses away from the cell surface (plotted in magenta in Figure 5.3) to allow sufficient time for all attachments between the tip and cell to rupture (though not necessary for this particular dataset). This final dwell time has the additional benefit of continued signals to the camera for image capture, which allow for measuring relaxation of the cellular structures after force-rupture.

For this data representation, positive force values in force curves are associated with the AFM tip bent upward while applying force to the cell, and negative force values are the result of the cell pulling down on the AFM tip as the cantilever is moved away from the cell. Data will often be plotted inversely when the adhesion forces are of primary interest. However, for consistency, the data for this chapter orients indentation forces as positive and adhesion forces as negative.

For the first time, our system features simultaneous AFM force measurements with side-view imaging subcellular motion with a z-direction image resolution comparable to typical plan-view, xy-resolution at high frame rates of 50 fps. Because so much information can be extracted from a single force curve and image time series, detailed analysis of representative cells was performed in two parts - (1) deformation and (2) adhesion. From these respective analyses insight was gained on (1) the structural components of the cell responsible for changes in cell mechanics and (2) direct mechanical linkages between the tip and cell membrane to subcellular components.

5.3.2: Indentation Data

As an initial demonstration of the combined AFM and pathway rotated imaging system, I probed the passive mechanical response of cells to an applied load. Force-indentation data with a specific inflection point where the apparent stiffness of the cell, as calculated with the Hertz model, changed was observed. I used the high-speed, side-view image capabilities our system provided to identify strains in subcellular components that gave rise to the change observed in force data.

Externally applied mechanical stress can induce changes in the cell, such as cytoskeletal stiffening and activation of growth factors.(244; 245; 246; 247) Recent findings have suggested that the nucleus itself may act as a mechanosensor, bypassing the diffusion-based mechanosignaling through the cytoplasm to directly modulate expression of mechanosensitive genes.(3) The AFM is an ideal tool for further investigating the role of mechanical stress in cells because it allows for both the measurement of the mechanical properties of a cell and the precise application of an applied load for understanding stress response of a cell.

The process of obtaining cellular stiffness using the AFM typically involves fitting the acquired force indentation curve with the Hertz model (Equation 3.1 for a spherical indenter) to extract the elastic modulus. The Hertz model assumes that strains are small and within the elastic limit, the surfaces are continuous (i.e., the tip is small compared to the cell), and the surfaces are frictionless (i.e., no adhesion). As a result, cell stiffness measurements made using the Hertz model applied to AFM data are effective measurements that includes contributions from different cellular components, including the cell membrane, actin cortex, cytoskeleton, and nucleus, each with their own mechanical properties.(248; 156) Researchers have attributed deviations in AFM force-indentation results from Hertzian behavior to the contribution of subcellular components (such as molecular brushes, the actin cytoskeleton, microtuble network, intermediate filaments and nucleus) to the measured stiffness.(248; 14; 142; 249; 250; 251) AFM experiments have been combined with confocal imaging to elucidate the component responsible for the deviations(248); however, these experiments either lack sufficient force sensitivity or image resolution - both in time and space - to fully explore this matter.

Therefore, the distances over which applied forces affect the cell and subcellular components remain unclear; this is especially true in reference to the rearrangement of the nucleus and subnuclear structure, as this likely leads to more general phenotypic effects. The mechanical deformation of the cell was probed with simultaneous sub-nanonewton resolution force data and millisecond imaging to measure the sub-micron deformations. The imaging system provided the ability to identify strains in subcellular structural components, while force synchronization facilitated the identification of subcellular components responsible for deviations of force data from Hertzian behavior.

Results:

Figure 5.4A shows the approach portion AFM force-time curve and representative images (C-E) from a 50 fps image sequence of the cell during deformation, indicating successful cell deformation measurements taken by our system.

The approach curve has two distinct regions with different slopes, suggesting two regimes to the force measurement. The change in slope does not directly correlate to a difference in stiffness regimes, because stiffness is determined from the relationship between force and indentation. However, because the experiment was performed with constant z-piezo motion (i.e., constant-velocity force spectroscopy), there is a direct relationship between the slope and stiffness. This is further confirmed by fitting the Hertz model (Equation 3.1) to the different regions of the force-indentation curve (Figure 5.4B). Region I, the indentation region of 0 to ~ 0.6 μm, possessed an elastic modulus of 2.9 kPa and region II, the indentation region of approximately 0.6 to 1.8 μm, possessed an elastic modulus of 3.9 kPa - a nearly 1.5-fold difference in the elastic modulus of each region.

Similar observations have been reported by Carl et al.,(252) Kasas et al,(253), and Sokolov et al.(174) on BQ2, COS, and human cervical epithelial cells, respectively. These authors considered the cell as a mechanically multilayered structure in which the first layer represents the actin cytoskeleton and/or molecular brushes (e.g., microvilli, microridges, glycocalyx) and the second layer represents the intermediate filament and microtubule network. This work was supplemented by chemical alteration of the cell or finite element modeling to confirm their assumptions; however, there were no direct observations of deformation responsible for the mechanical response regimes. Due to the simultaneous side-view image technique, I was able to clearly determine the physical changes in the cell associated with changes in apparent stiffness measured in force data.

The side-view images (Figure 5.4 C-E) clearly showed the positions of the cell membrane, nucleus boundaries and punctate structures within the cytoplasm and nucleus. Due to the clarity of imaging, the relative positions of these cellular components were tracked and correlated to force data to elucidate the mechanism behind the difference in these elastic regions. This was accomplished by tracking the positions of intensity peaks in a kymograph as a function of time (Figure 5.2).

Two key components contributing to the bulk mechanical properties of the cell are the cytoplasm and nucleus. Each of these regions are clearly identified in the side-view images (Figure 5.5A). There exists a thin cytoplasm region below the nucleus which could not be labeled with the current cell staining. To observe the absolute motion of the nucleus and membrane relative to the PA gel, an additional layer of fluorescence under the cell would be necessary. Despite lacking a clear marker for the bottom surface of the cell, the motion of Gaussian fits to the bottom membrane (Figure 5.5 B green) of the nucleus was 239 nm over the

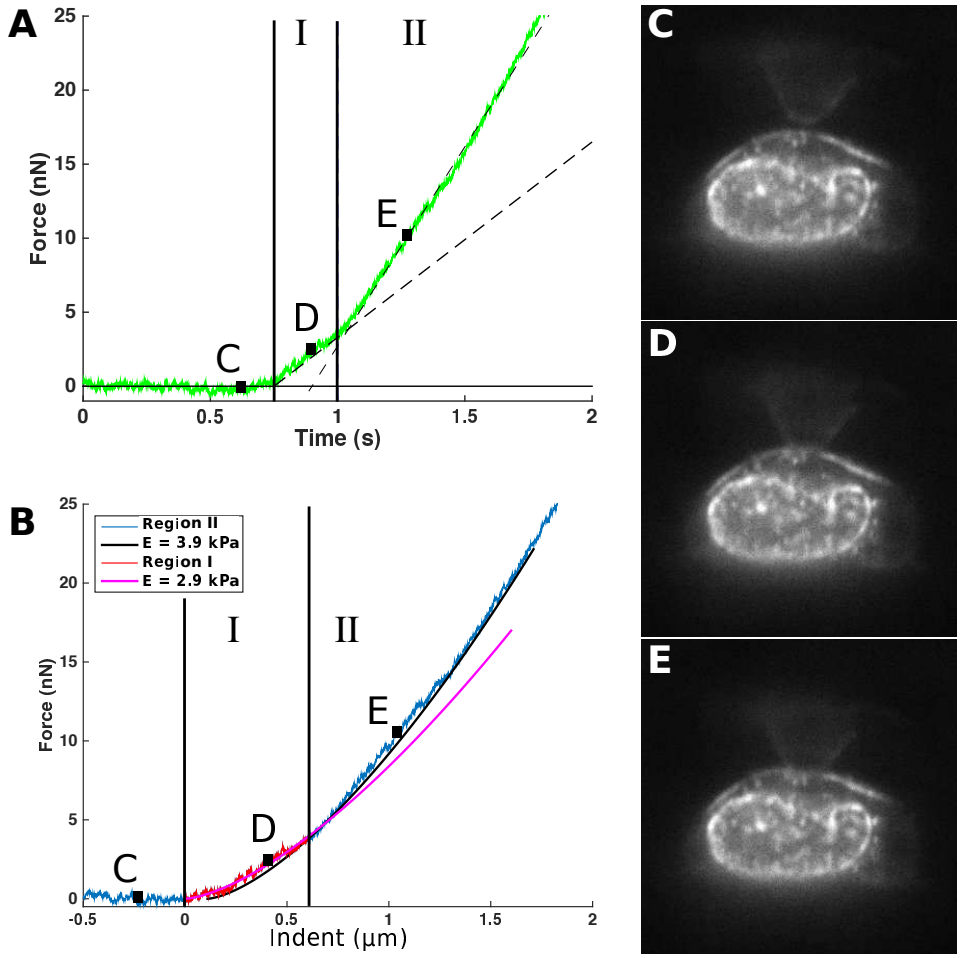

Figure 5.4: Simultaneous AFM force data and side-view images of cell deformation. (A) Force-time plot with different slope regimes (I and II) with dashed lines to illustrate the difference in slope. (B) Force-indentation data fit to a Hertz model for each of the regimes identified in the force-time plot. (C-E) Sample images from a time sequence acquired simultaneously with force data, as identified on the force curves.

time course of indentation, less than the resolution of the imaging determined from point spread function analysis (Section 4.2). Therefore, the bottom of the nucleus was unaffected by AFM force deformation and was a fixed point reflective of substrate rigidity compared to the cell.

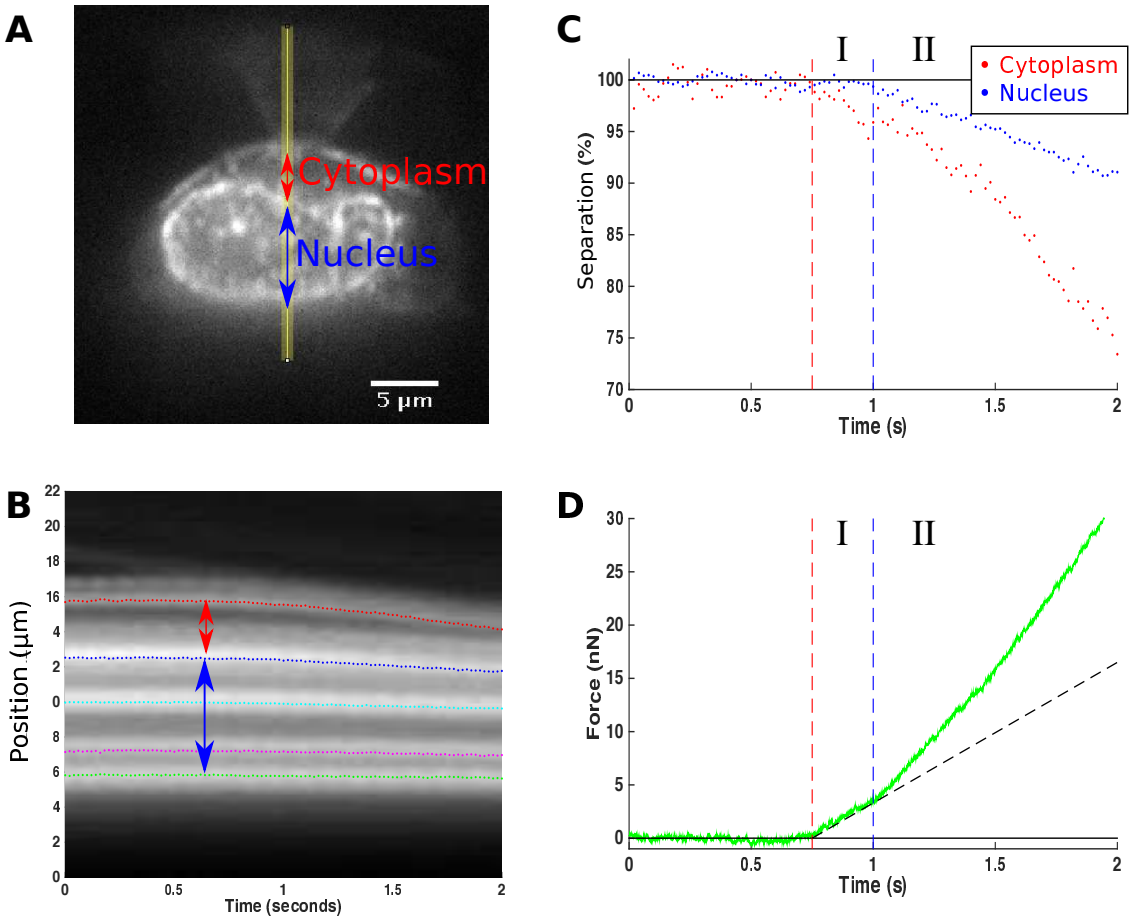

Figure 5.5: Change in force regime associated with compression of SKOV cell cytoplasm (blue) and nucleus (red). (A) Representative image from a side-view image sequence of SKOV cell labled with membrane (Vybrant) and nucleus (Syto83) label. Vertical ROI directly below the AFM tip shown in yellow, cytoplasmsol height indicated in blue and nucleus height indicated in red.(B) Kymograph of the yellow ROI over the course of the approach portion of the dataset with Gaussian tracked intensity peaks. (C) Membrane height above top of nucleus accounts for the cytoplasm region (red) and nucleus height is measured from top to bottom of nucleus (blue). These separation values were normalized to their initial position and tracked over the course of the time sequence. (D) Corresponding force-time data showing the two ROIs.

The height of the cytoplasm (red arrow) and nucleus (blue arrow) was tracked over the course of the kymograph (Figure 5.5 B and C). I found that, for region I (identified in the force-time curves as the region from the initial contact point of AFM tip with cell to the change in slope), I only observed compression of the cytoplasm region of the cell. In region II, compression of the cytoplasm continued and compression of the nucleus occurred at a slower rate.

The Hertz model has been widely used to determine cell elasticity; however, this model does not account for different mechanical properties of subcellular structures. Several methods, including the brush model (223) and depth-dependent Hertz fitting(253; 19), have been used to account for the mechanical complexity of the cell. In a simplified view, a force-indentation curve on a soft, homogenous sample could be fitted with the Hertz function to determine modulus; however, if a harder material is inside the sample, the curve will deviate to a stiffer elastic modulus at depths that reflect the position of the stiffer material (Figure 5.6). This harder inclusion model is a nearly accurate description of my results, exhibiting compression of both the nucleus and cytoplasm at different rates contributing to the stiffness measurement in region II. This model also predicts that, upon deformation, both the materials exhibit some motion. Our side-view imaging system indicates that the nucleus of the cell did not exhibit any compression until the region II stiffness regime. This deviation indicates a more complex mechanical system at play. The behavior of reaching a threshold force or pressure prior to deformation is reminiscent of energy barriers observed in a variety of biological experiments (e.g., unfolding potential in single-molecule studies).(245) However, the nuclear motions in region I may have been too subtle to detect, or unlabeled regions of the cell may have contributed to the complexity of SKOV deformation. More measurements and analysis are therefore required to definitively understand whether the cell can be represented as multilayered-Hertzian structure.(19)

Another possible contributor to complex force-indentation curves is cell deformation beyond the elastic regime covered by the Hertz model and into plastic deformation. Plastically deformed material no longer retains its original form after the removal of external forces. Due to the large deformations caused by AFM indentations of the SKOV cell, there was potential for measuring plastic deformation of the cytoplasm or nucleus. To determine whether this was the case, I compared the cytoplasm and nucleus heights (shown in Figure 5.5A) before indentation, during indentation dwell, and after retraction of the AFM tip. For the retraction case, I waited until 1 second after the final rupture event to measure heights in order to ensure that adhesion between the tip and cell membrane would not obscure the results. Height values reported in Table 5.1 reveal that heights before and after the force deformation of the SKOV cell are in agreement. The reported errors are the standard deviations of Gaussian fits to intensity profiles for 10 frames in each region; however, all of these deviations are less than the side-view z-resolution of 0.3 μm. Because these measurements were made in the direction of applied force, the largest strains and, thus, the highest potential for plastic deformation, are also along this axis. As a result, I observed no plastic deformation of either the nucleus or the cytoplasm regions of the cell over the course of these indentation experiments. However, this does not rule out plastic deformation of unlabeled subcellular or sub-nuclear components.

The final measurement performed for the deformation dataset was a preliminary strain measurement. Because previous investigations of AFM-induced strain in cells focused on long-timescale (seconds to minutes)

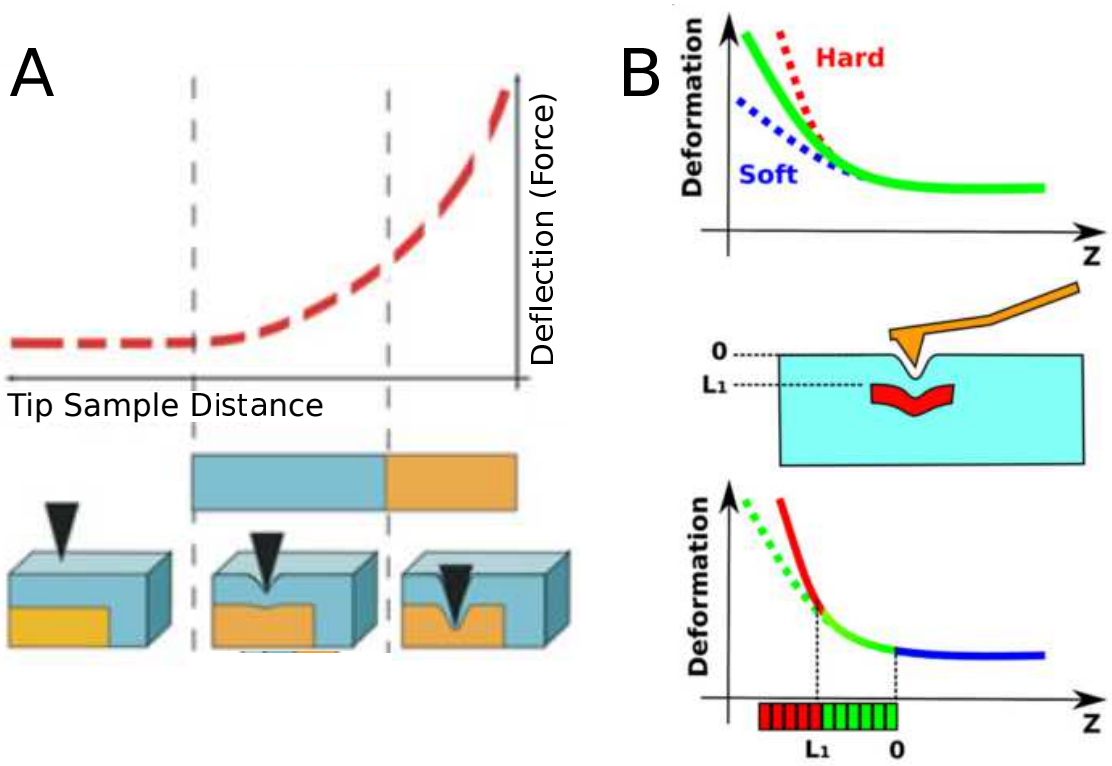

Figure 5.6: Material deformation models with different stiffness regimes. (A) Schematic representation of stiffness as effected by depth for a multilayer material. Figure modified from Radotic et al.(18) (B) Schematic illustrating the effect of a hard inclusion on the mechanical properties measured in force curve. Figure modified from Roduit et al.(19)

	Before	During	After
Cytoplasm	3.15 ± 0.04 μm	2.57 ± 0.05 μm	3.11 ± 0.05 μm
Nucleus	6.80 ± 0.01 μm	5.93 ± 0.01 μm	6.80 ± 0.01 μm

Table 5.1: Height values of the cytoplasm and nucleus regions of the cell identified in Figure 5.5 before indentation, during indentation dwell, and after retraction of the AFM tip from the cell surface. The reported deviations of values are the standard deviations of height measurements resulting from Gaussian fits to intensity profiles for 10 frames in each region.

force-induced deformations and remodeling of the cell as observed in plan-view,(200) information about strain during the short-timescale (milliseconds) and the direction of applied force are lacking. Because kymographs do not take into account the lateral movement of fluorescent cell label, I analyzed the region of the cell directly below the AFM tip - the only region of the cell for which there is predominantly z-motion (Figure 5.7A). The fluorescent regions were tracked on the kymograph with the same Gaussian fitting protocol, and the regions were identified in increasing order, as they are further away from the tip.

A plot of the percent strains induced in each of these reasons at each time point (Figure 5.7) revealed that strains in the deformed cell decreased further from the point of compression. The largest change in percent compression is visible in Region 1 of the cell corresponding to the cytoplasm region above the nucleus. Both Regions 2 and 3 also exhibited increased induced strain over the course of the indentation. Only Region 4 showed large fluctuations in the percent strain due to the relatively small initial length (Figure 5.7D) and less well-defined illumination of the bottom boundary of the nucleus. Due to this contribution of noise to the measurement for Region 4, there was no measurable change in strain due to the AFM tip. The majority of compression observed in the nucleus and associated with a change in stiffness measured in force data was the result of motion at the top of the nucleus. The application of further image tracking analysis and strain models would provide a detailed insight into the propagation of strain from AFM tip through the cell and sub cellular components.

Discussion:

As an initial demonstration of the combined AFM and PRISM system, I used the high speed image acquisition to identify physical components responsible for deviations of force-indentation data from a simple mechanical model. I probed the mechanical deformation of the cell with simultaneous sub-nanonewton resolution force data and millisecond imaging to measure the sub-micron deformations.

These simultaneous measurements allowed for the identification of nucleus deformation corresponding to deviations of force-indentation data from simple mechanical models. Though these were not the first AFM measurements to report two stiffness regimes in AFM force data, they are among the first to have image data that inform the mechanisms responsible for the change in apparent elastic modulus. The high speed and side-

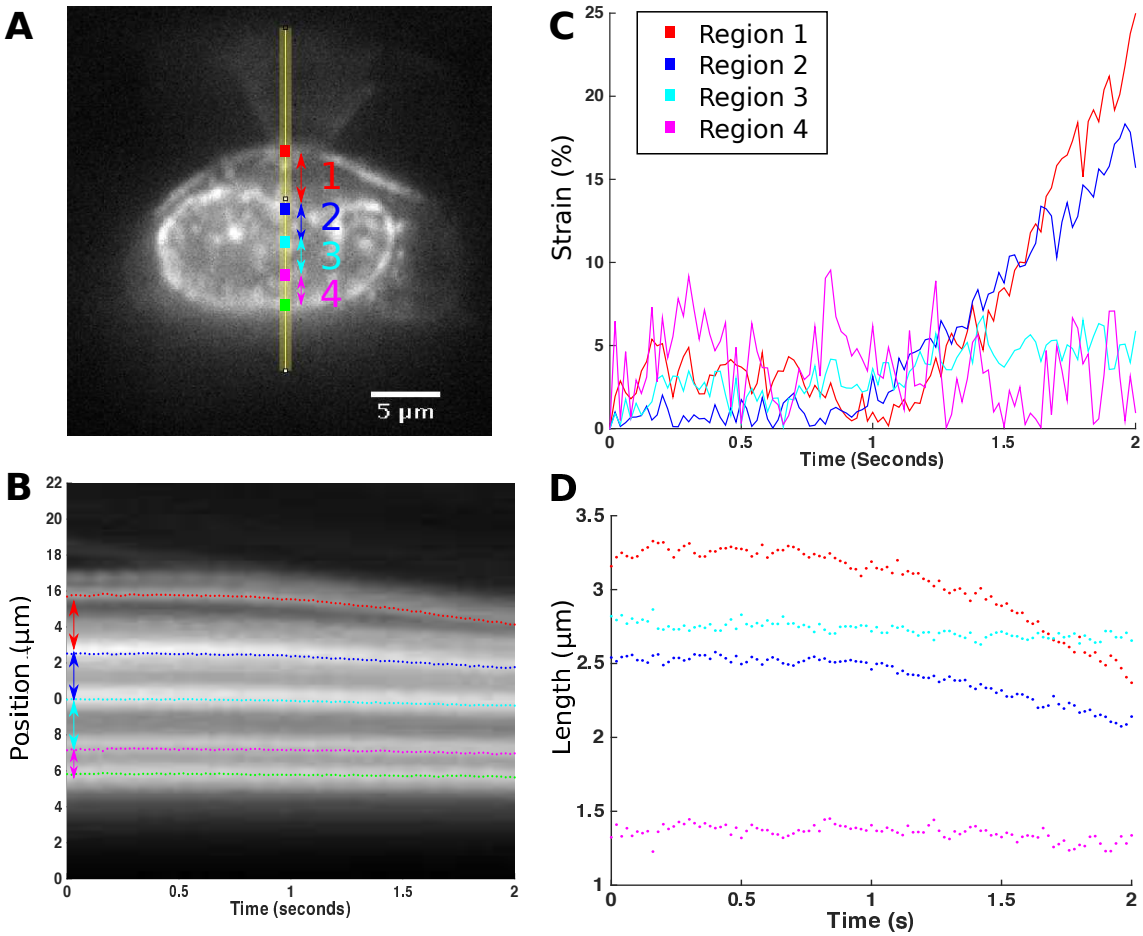

Figure 5.7: Strain decreases further from tip. (A) Representative image from a side-view image sequence of SKOV cell labled with membrane (Vybrant) and nucleus (Syto83) label. Subsequent separations between cell membrane, nucleus boundaries, and punctate labels have been labeled with different numbers and colors. (B) Each of the regions identified are the separation between lines in the kymograph. (C) Plot of induced strain and absolute length of each of the regions due to deformation of the cell with AFM tip.

view imaging allowed for millisecond distinction between the compression of the cytoplasm associated with one stiffness and the initial compression of the nucleus contributing to a stiffer apparent modulus. Moreover, the sub-micron resolution in imaging allowed for measurements of induced strain propagation through the nucleus. These strains identify the top of the nucleus as the major source of deformation and, thus, induced strain contributing to mechanical measurements. These measurements are consistent with finite element models of the AFM deformation of an elastic material with harder inclusion (i.e., the nucleus).(19)

Further work should be done to examine more force curves of a similar nature or with different anomalous force patterns to elucidate the mechanisms responsible for the details in force response. More datasets exist for similar experiments and just require the necessary time for analysis. Additionally, the collected data would benefit from more sophisticated methods of tracking deformation and, especially, strain propagation throughout the entire cell, rather than in just the region below the AFM tip. I have explored the possibility of incorporating spatiotemporal image correlation spectroscopy (STICS), but this requires further optimization for useful analysis with the datasets.

5.3.3: Adhesion Data

Next, I imaged the motion of subcellular structures due as force applied to adhesions between a fibronectin-coated AFM tip and cell surface.

The nucleus is physically connected to the cell surface through the cytoskeleton and the LINC (Linkers of Nucleoskeleton and Cytoskeleton) complexes, allowing rapid mechanical stress transmission from adhesion to the nucleus through a process known as mechanotransduction. These changes have been proposed to affect signaling within the nucleus over a few microseconds.(3) Abnormal cellular response to mechanical stimuli has been correlated with disease states, including cancer.(8) However, the effect of intracellular and nuclear motion due to external force applied only at the cell surface has not been fully explored.

Experimental studies of mechanotransduction have been performed by directly applying force to surface integrins with ligand-coated micropipettes and magnetic particles, or physically deforming protein-coated substrates.(250; 254; 255) These experiments presented evidence of force-dependent changes in internal structures visualized inside the cytoskeleton and nucleus. These measurements unequivocally confirm the existence of long-range force propagation in living cells; however, they do not fully investigate the length and time scales over which direct mechanical linkages in the cell transmit force. Current experiments have been limited in force-feedback or imaging capabilities to fully address this question. The capture of force data over the course of an experiment is necessary to understand the strength of adhesion and mechanical changes. Additionally, high frame rate and high-resolution imaging is necessary to understand cell response

to external forces propagated through the cytoskeleton, producing sub-micron displacements in milliseconds or faster.

In contrast to previous experiments,(250; 254; 255) I probed the length and time scales of intracellular motion due to forces applied at the cell surface with simultaneous sub-nanonewton resolution in force data and millisecond imaging to measure the sub-micron deformations. A fibronectin-coated AFM tip in our system was used to promote the formation of focal adhesions between the AFM tip and cell to study the retraction portion of the AFM curve with both force-rupture data and side-view imaging. These simultaneous measurements allow for the precise correlation of force-rupture of adhesions to the cell membrane with membrane, intracellular, nuclear and intranuclear motion. Larger rupture events ($\geq$ 2 nN) sometimes produced nuclear and intranuclear motion, and smaller rupture events ($<$ 2 nN) only resulted in membrane motion. This suggests that stronger adhesions are more likely to form direct mechanical linkages to the nucleus. Clearly, locally applied forces through cell membrane adhesions have a significant effect on the structural arrangement of the cell, and our unique system provides further insights into the mechanisms involved in cell signaling through mechanotransduction.

Results:

Figure 5.8A shows a typical AFM force-indentation curve between fibronectin-coated AFM bead-tip and SKOV cell. Fibronectin promotes the adhesion between the bead and cell membrane, and is associated with the formation of focal adhesions. The retract portion of the force curve contains numerous peaks associated with the rupture of attachments between the tip and cell, resulting in a sudden drop in force. Often referred to as force-rupture events, these peaks are produced when the cantilever - moving away from the substrate at a constant velocity - exerts an increasing force on the attachments between the bead and cell until the attachment breaks suddenly, releasing the bead and allowing it to move upward, thus decreasing the force applied to the AFM tip. This is in contrast to sliding or nonspecific tip interactions, which would exhibit a prolonged period with little to no change in force or a gradual drop in force.(256)

In this dataset, I was able to distinguish 10 force-rupture peaks, ranging in peak height from 0.1 nN up to nearly 10 nN. Each rupture peak was associated with motion in the side-view images of the SKOV cell labeled with membrane (Vybrant) and nucleus (SYTO 83) dye.

As an initial analysis, a kymograph for the vertical region directly under the AFM tip was acquired as the majority of strains and, thus, motion would be expected in this region (Figure 5.8B). The kymograph of this region (Figure 5.8C) showed 5 clear bands of fluorescence - the tip moves from indenting the cell at time zero to detached from the cell and out of the FOV at 4 seconds; the cell membrane (red), which shows large fluctuations where the membrane is becoming detached from the tip; the top (green) and bottom (magenta) of the nucleus; and one intranuclear punctate region. Gaussian curve fitting for each time point

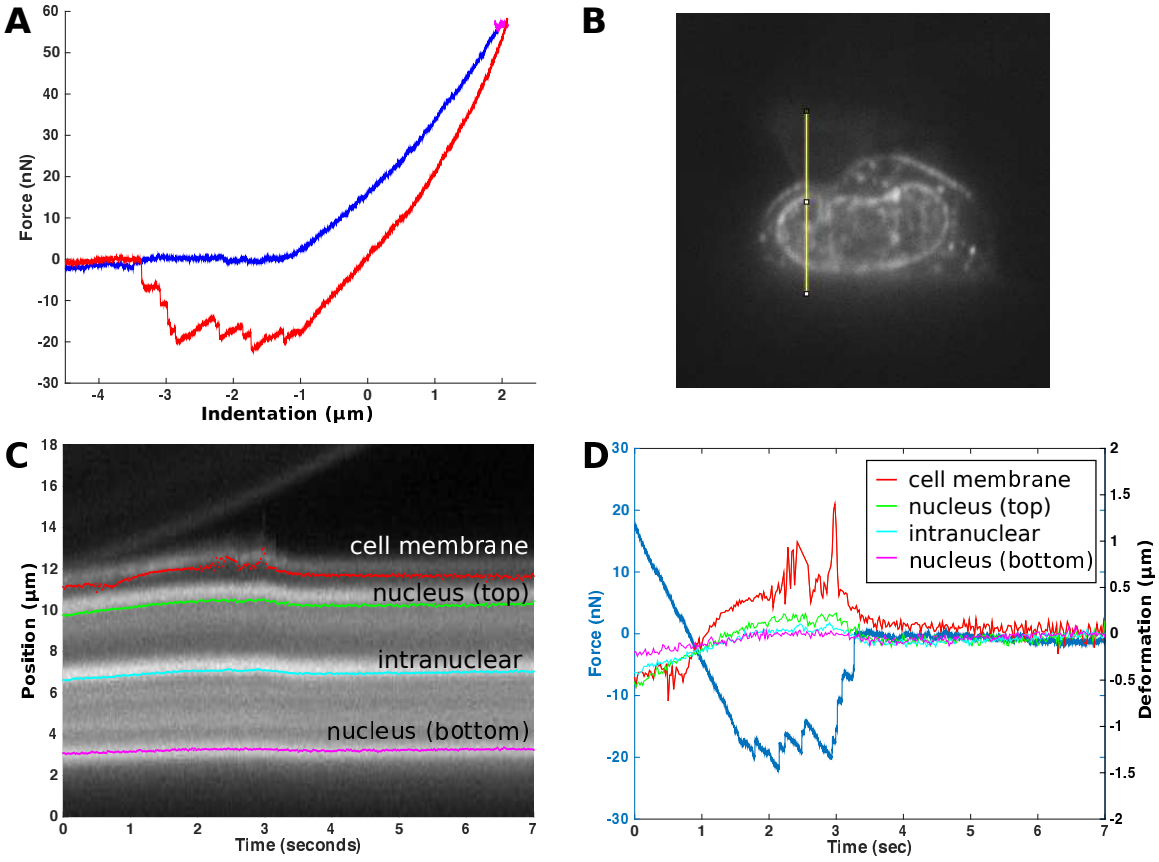

Figure 5.8: Simultaneous force and image data acquired for adhesion between fibronectin-coated AFM tip and SKOV ovarian cancer cell. (A) AFM force-indentation showing a number of adhesion events on the retract portion of the curve (red). The approach and surface dwell are shown in blue and magenta, respectively. (B) Representative image from the simultaneously acquired image time sequence. The vertical yellow line was selected for creating a kymograph of cell motion over the course of the retract curve (C). (C) The kymograph shows motion of the AFM tip off the cell surface eventually leaving the FOV at ~ 4 seconds, and several bright fluorescent regions of the cell - cell membrane (red), top of nucleus (green), punctate region within nucleus (cyan), and bottom of nucleus (magenta) - tracked with my gaussian peak tracker. (D) Time synchronized force (blue - left axis) and displacement (red, green, cyan, magenta - right axis) are displayed on the same plot.

in the kymograph was used to track the four intensity lines corresponding to regions of the cell. Due to the sub-millisecond synchronization of the AFM and camera, displacement data from the kymograph could be plotted along with force data to observe correlated motion and force-rupture events. Figure 5.8D shows force data (blue) on the left axis and displacement data (red, green, cyan, magenta) on the right axis. The displacement data acquired from the kymographs was centered on the portion of the dataset - after the AFM tip was completely detached from the cell and no force was applied - to make visualization easier.

These results showed membrane and nucleus motion correlated with AFM force data. Recall the convention mentioned in Section 5.3.1 where negative values in the force curve correspond to force applied to the AFM tip by the cell when bending the cantilever towards (or against) the surface. More negative values in the force curve map to stronger forces applied to the cell-tip attachments. As the force applied to the AFM tip increases (becomes more negative, Figure 5.8C), the cell membrane and, to a lesser extent, the top of the nucleus are displaced upwards until the attachments to the AFM tip were ruptured, which produced a drop in force applied to the AFM tip (becomes more positive, Figure 5.8C) and a drop in membrane height. Moreover, the upward displacement of the cell membrane drops in synchrony with two of the force-rupture peaks, implying that these force-rupture events were the result of membrane detachment from the AFM tip. *This demonstrates that the detachment of cell adhesion from the AFM tip, characterized by force-rupture peaks in AFM data, are correlated to a dramatic movement of the cell membrane.*

From these kymograph results, there are multiple peaks in the force-rupture pattern that do not appear to produce motion in the cell. However, visual inspection of the image time sequence indicate that there was motion occurring in locations not captured by the kymograph.

Therefore, I used difference imaging to identify motion in the entire XZ image correlated to force-indentation data. Figure 5.9 presents the retract potion of the same force-indentation curve as Figure 5.8 with simultaneous side-view images. Five of the larger rupture events identified in the force curve (C-G) were determined to produce motion of the cell from visual inspection of the data. To identify regions of the cell with motion correlated to force-rupture events, difference images were taken between the image acquired at the top of the force peak (solid circle) and the image acquired at the bottom of the force peak (open circle, following the peak image by at least 3 frames, 60 ms). The images were subtracted, and a threshold was then applied to reduce the background signal produced by random fluctuations. Finally, an area filter was imposed to further ensure that only the regions that moved between the top and bottom of the peak were visualized. Figure 5.9 C-G displays the image acquired at the top of the force peak and the regions of motion determined from image difference analysis in green.

The image series and analysis shown in Figure 5.9 is a series of detachments where the AFM tip produced both force-rupture events and cell motion. Following the indentation and surface dwell portions of the force

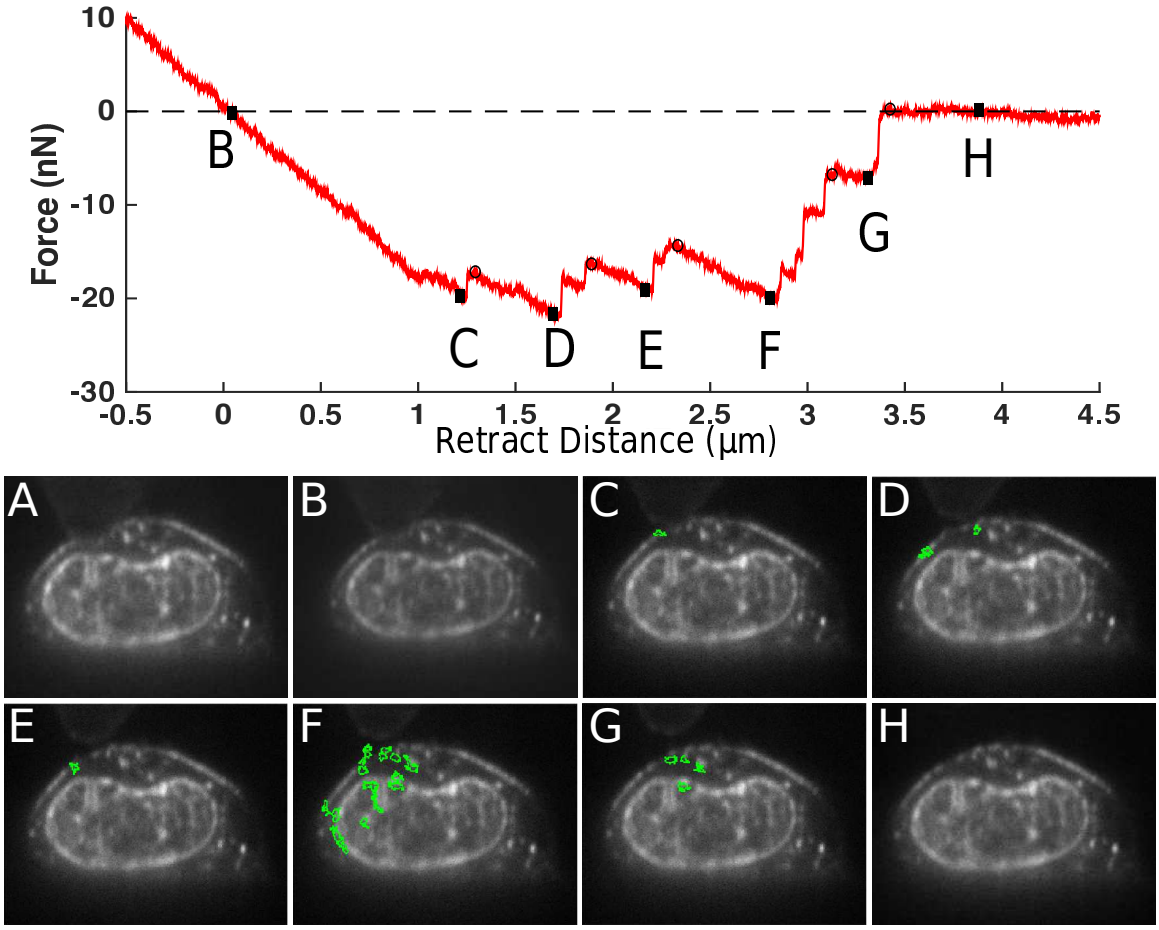

Figure 5.9: Measurement of adhesion between fibronectin-coated AFM tip and SKOV ovarian cancer cell measured by simultaneous AFM and PRISM imaging system. (Top) Retract portion of force-indentation curve with points corresponding to force-synchronized images (B-H) identified. These images correspond to (A) the first data point in the retraction curve and the position of maximum cell indent, (B) the point of zero force application to the cell, (C-G) force-rupture peaks, and (H) after all rupture events. The green regions in the peak images (C-G) outline the regions of motion determined from difference images occurring between the top of the peak and the first image at the bottom of the peak (identified with an empty circle and following the peak by at least three frames). A closer examination of Peaks F and G can be found in Figure 5.10.

curve, the retract curve began in the position of maximum indentation (Figure 5.9A). The AFM tip was most visible in image A in the top-left while indenting the cell, but is also seen in images A-H moving further up in the same region until fully out of the FOV in image H. Then, the cantilever was moved away from the surface at a constant speed until the AFM tip was no longer pushing into the cell and a position of zero force application was reached (Figure 5.9B). The zero force position on the retract curve did not necessarily occur at the same indentation depth as the zero force position on the approach curve due to the viscoelastic nature of the cell. Between position B and Peak C,the AFM tip applied force to the cell through its adhesions to the cell membrane, ultimately stretching the cell body upward (away from the substrate). This produced an upward motion of the cell membrane, nucleus, and punctate cytoplasm or intranuclear regions. Peaks C-G (Figure 5.9C-G) correspond to rupture events, presumably where adhesions broke contact between the cell membrane and AFM tip, with the final rupture peak (G) resulting in the total detachment of the AFM tip from the cell surface and a return to a zero applied force for the remainder of the curve (Figure 5.9H).

Peak C rupture occurred when the cell membrane partially detached from the left-side of the AFM tip, forming a gap between the labeled membrane and the AFM tip. Subsequent upward motion of the membrane in that region conveyed continued adhesion, supported by more force-rupture events producing further detachment on that side of the AFM tip.

Where only membrane motion was recorded for Peak C's detachment series, Peak D's rupture recorded detachments from the middle and right side of the AFM tip. A closer examination reveals that the middle then the right detachment occurred, where the right detachment produced the smaller unlabeled peak following Peak D. The same gap was observed between the labeled cell membrane and the AFM tip. Motion was observed in the cell membrane and punctate regions of the cytoplasm just below the tip. Peak E rupture resulted from the detachment of the membrane from the left-side of the AFM tip, with membrane motion similar to the location of Peak C.

The most dramatic motion was produced during Peak F through a series of smaller rupture events. Peak F consisted of the largest force drop of 13.2 nN displayed in Figure 5.9 and also the most observable motion in the cell (Figure 5.9F), most notably motion of the nucleus boundaries and intranuclear punctate regions. A closer examination of data following Peak F is shown in Figure 5.10. For these images, difference imaging was performed between subsequent frames with a lower threshold value, determined from differences acquired after returning to baseline, applied to make it possible to capture motion due to the smaller rupture events (green). Peak F rupture occurred through 5 smaller force drops identified as F, F0, F1, F2, and F3. At Peak F, I observed the existence of a short-lived extension of fluorescently-labeled membrane, which broke from the tip, which resulted in a 0.9 nN force drop, and was no longer prominent in the following frame (F0). A larger view of the extension, measured at a length of 1.8 μm, is displayed in Figure 5.11. In the frame

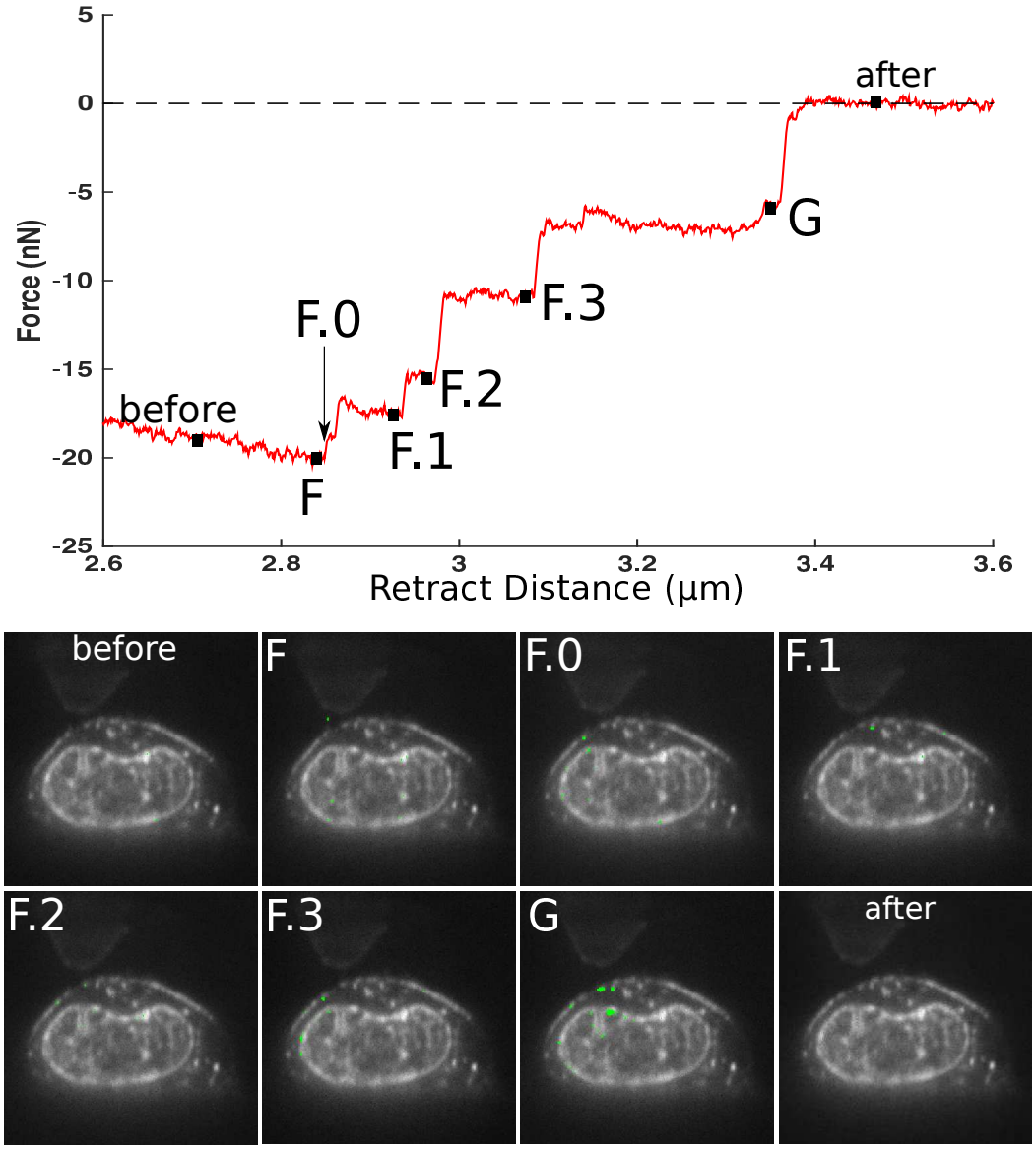

Figure 5.10: Closer examination of Peak F and G from Figure 5.9. (Top) Portion of force-indentation retract curve containing Peaks F and G with points corresponding to force-synchronized images identified. No point is shown for F.0 because this is the frame immediately following Peak F. Between F.0 and F, there is the extension of a 1.8 μm fluorescent region of the cell membrane. Green regions in peak images show regions of motion determined from difference images occurring between subsequent images.

immediately following the detachment of the membrane tether (F0), a drop in the cell membrane and the nucleus region was observed directly beneath and to the left of the AFM tip. Peaks F1 and F2 corresponded to motion in the cell membrane under and to the left of the tip, respectively. Because these two peaks occurred close to each other in time (and frames), some motion was observed in the same location for both peaks. Peak F3 was correlated with the motion of the cell membrane and nucleus - a similar region to F0 but with additional nucleus motion on the left side.

The final rupture peak, Peak G, corresponds to a final detachment of the AFM tip from the cell membrane. Peak G correlated with a sudden drop in the cell membrane and nucleus region directly under the AFM tip. Just prior to Peak G, a 1.8 μm separation between the fluorescently labeled membrane and the AFM tip (Figure 5.11) was observed. This separation was first noted following Peak C and continued to increase over the course of the force curve. Though there are still obvious attachments between the AFM tip and cell, evidenced by the complex force-rupture pattern and corresponding cell motion, these attachments are not labeled so the direct attachments between the tip and cell could not be directly observed. Following the final rupture event, the cell and AFM tip no longer experienced force from the interaction between each other. As a result, the AFM tip returned to a zero force baseline, and the simultaneous images showed no motion (Figure 5.9H and 5.10after)

Only the final rupture peaks F and G resulted in measured motion in the nucleus, which indicate that, despite the rupture of the membrane attachments during initial force-rupture events, the key attachments linking directly to the nucleus are unaffected. Moreover, the strongest interactions between the fibronectin-coated tip and cell membrane formed direct linkages to the nucleus.

Thus, the PRISM imaging path enabled me to correlate the AFM force-rupture events with intracellular motion and interpret connections formed directly to the nucleus.

Discussion:

This experiment demonstrated the successful utilization of the combined AFM and PRISM system to study intracellular motion that occurs when forces are applied through focal adhesions on the cell membrane. The system's high frame rate acquisition of side-view images and force synchronization facilitated precise correlation between force rupture of adhesions to the cell membrane with membrane, intracellular, nuclear and intranuclear motion.

The reported rupture forces range from less than 1 nN up to 10s of nN, with a total change in force application of 20 nN over the course of the experiment. These adhesion strengths are in agreement with literature reports of cell adhesion to fibronectin, which range from sub-nannonewton(257) for a few molecules to hundreds of nanonewtons for a $1\mu m^2$ focal adhesion. I observed membrane extensions associated with sub-nanonewton and nuclear motion associated with larger ($\geq$ 2 nN) rupture events.

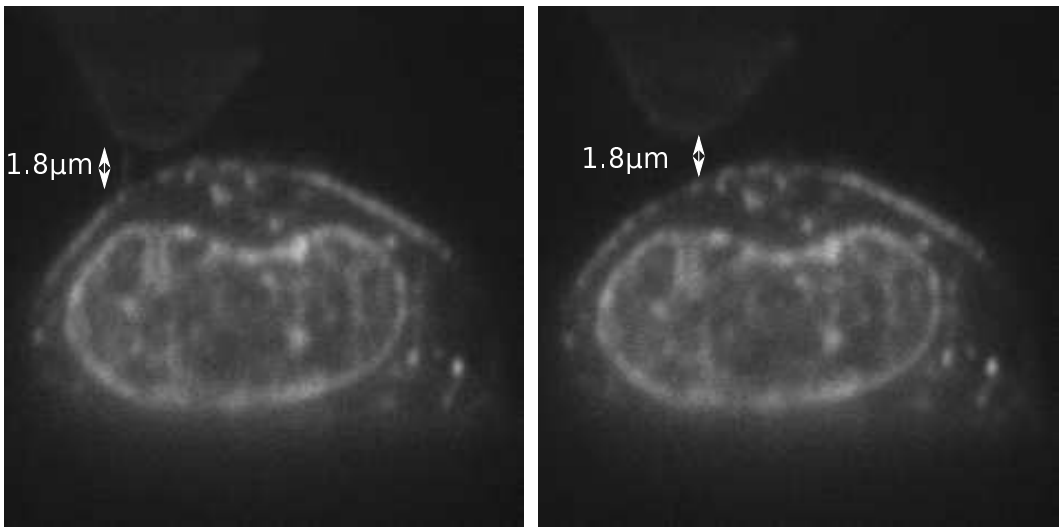

Figure 5.11: (Left) Short-lived 1.8 μm tether produced at Peak F. (Right) Separation between tip and substrate just prior to final rupture event at Peak G.

Larger rupture events ($\geq$ 2 nN) sometimes produced nuclear and intranuclear motion, while smaller rupture events ($<$ 2 nN) resulted only in membrane motion. Experiments have already shown that forces applied to the cell membrane produced changes in the cell shape(17), internal structure,(255) and nucleus;(250) however, they were unable to resolve specific rupture events and, thus, the strength of interactions associated with direct mechanical linkage from membrane to the nucleus. Only the final rupture peaks F and G (Figure 5.9), resulted in measured nuclear motion. Membrane rupture during the initial force-rupture events left the key attachments linking directly to the nucleus unaffected. Moreover, the strongest interactions between the fibronectin-coated tip and cell membrane formed mechanical linkages directly to the nucleus.

Because of the system's heightened z-axis image resolution, I was able to resolve the formation of a 1.8 μm fluorescent membrane extension and even an unlabeled region of the cell membrane when the AFM tip disengaged from the cell body. The adhesion force contributed by the fluorescent membrane extension is much smaller than other forces measured between the tip and membrane. Weaker adhesion forces are consistent with reports of membrane tethers as unsupported membrane attachments at a few discrete points,(17; 258; 259) whereas the attachments between cell membrane and tip not producing tethers are stronger and are likely linked directly into the cytoskeleton. However, the rupture of the tether correlated to a relaxation of the nucleus, so cytoskeletal attachments to the membrane near the formation of the tether still link nuclear motion to membrane motion. The unlabeled region between the cells and the AFM tip could be associated with the unlabeled fibronectin coating the AFM tip and the glycocalyx layer of the SKOV cell. Fibronectin has a persistence length of 160nm,(260) and it is therefore unlikely to be responsible for much of

the unlabeled region. Conversely, the reported values for the glycocalyx surrounding the cell membrane range from a fraction of a micron(261) up to 11 microns.(262) These reported values depend greatly on cell type; because I was unable to locate a reported value for SKOV cells, future experiments should be performed to label the glycocalyx and measure the height of this region, perhaps with fluorescent wheat germ agglutinin. However, I observed stronger interactions than typically reported for glycocalyx interactions, so a more complex interaction is likely, and future experiments could be targeted at understanding this region of attachment.

The side-view imaging path enabled me to correlate the AFM force measurements and force-rupture events with membrane and intranuclear cell motion. Due to the high frame rate imaging and force synchronization, I attributed membrane motion with all force-rupture events, and nuclear motion with larger rupture forces. Additionally, the increased z-axis image resolution of the system allowed me to resolve membrane extensions and an unlabeled region which would not have been possible with such techniques as combined AFM and confocal imaging. Clearly, locally applied forces through cell membrane adhesions have a significant effect on the structural arrangement of the cell; our unique system provides further insights in to the mechanisms involved in cell signaling through mechanotransduction.

Section 5.4: Conclusions and Future Work

The power of the AFM-PRISM-VLS system for cell mechanics studies is the integration of force measurement with synchronized high frame rate imaging in the direction of applied force (z-direction). This was accomplished by coupling our AFM with PRISM imaging and VLS illumination, discussed in detail in Chapter 4. This system enables high frame rate, high-resolution side-view imaging of cell motion without restricting sample geometry or compromising the piconewton resolution force data capabilities of the AFM. In this chapter, the system was applied to investigate single cell mechanics and mechanotransduction.

The results of a standard constant-velocity AFM measurement on our system are shown in Figure 5.3. The simultaneous side-view images of a SKOV cell labeled with membrane (Vybrant) and nucleus (Syto) stains illuminate cell motion due to applied load with an image resolution of ~ 300 nm in the z-direction and 10 ms time resolution, limited by exposure time. The AFM-PRISM-VLS system provides novel measurements by combining simultaneous AFM force measurements with side-view imaging of subcellular motion. The system benefits from a z-direction image resolution comparable to high-resoltuion xy-resolution at high frame rates of 50 fps. I demonstrated the utility of this measurement for (1) correlating details in the force curves with structural events within the cell and (2) investigating direct mechanical linkages between the cell membrane and the nucleus. Because mechanical properties of the cell were determined from indentation AFM data and

adhesion strength was determined from retraction AFM data, the experiments were broken down into (1) indentation experiments and (2) adhesion experiments.

In my indentation experiments, I observed that nuclear deformation correlated to a change in AFM force-indentation stiffness regime. The simultaneous measurements allowed for the identification of nucleus deformation corresponding to different stiffness regimes in the force-indentation data. Though these were not the first AFM measurements to report multiple stiffness regimes common in AFM force data, they are among the first to have image data that informs statements about the mechanisms responsible for the change in apparent elastic modulus. The high speed and side-view imaging provided millisecond temporal resolution between compression of the cytoplasm associated with one stiffness and initial compression of the nucleus contributing to a stiffer apparent modulus. Moreover, the sub-micron resolution in imaging allowed for measurements of induced strain propagation through the nucleus. These measurements identify the top of the nucleus as the major source of deformation and, thus, induced strain contributing to mechanical measurements. These measurements are consistent with finite element models of AFM deformation of an elastic material with harder inclusion (i.e., the nucleus).(19)

Further work should be done to examine more force curves of a similar nature or with different anomalous force patterns to elucidate the mechanisms responsible for the deviations in force response. Additionally, the collected data would benefit from more sophisticated methods of tracking deformation and, especially, strain propagation throughout the entire cell (e.g., spatiotemporal image correlation spectroscopy)

In the adhesion experiments, I observed force disparities in the rupture events between tip and substrate which produced nuclear motion, and those that only resulted in membrane motion. A force-rupture event of at least 2 nN was required to observe nuclear motion, indicating the strongest interactions between the fibronectin-coated tip and cell membrane formed direct linkages to the nucleus. Moreover, the larger force-rupture events producing nuclear motion were the final events in the force curve, suggesting that, despite rupture of the membrane during initial force-rupture events, the key attachments linking directly to the nucleus were unaffected. These are observations for a specific cell, and a larger dataset is required to understand trends in mechanotransduction for this cell line.

Additionally, I observed the formation of a 1.8 μm fluorescent membrane extension due to applied force, as well as an unlabeled region between cell membrane and tip through which force was still applied. The adhesion force contributed by the fluorescent membrane extension is much smaller than other forces measured between the tip and membrane, signifying that the attachments between cell membrane and tip not producing tethers are stronger and likely linked directly into the cytoskeleton. Both the observations of the fluorescent membrane extension and unlabeled region were only possible due to the z-axis resolution of the AFM-PRISM-VLS system.

Additional experiments are needed to determine the underlying mechanisms involved in the direct transmission of force from focal adhesion at cell membrane to the nucleus and understanding the tip-cell attachment in the unlabeled region. These adhesion results were only possible due to the high frame rate acquisition and side-view resolution, which allowed me to precisely correlated force-rupture events associated with adhesion of the AFM tip to the cell membrane to membrane, intracellular, nuclear, and intranuclear motion.

As an initial demonstration of the combined AFM and PRISM system, I identified the structural components of the cell responsible for changes in cell mechanics and investigating direct mechanical linkages between the cell membrane and the nucleus. I probed the mechanical deformation of the cell with simultaneous sub-nanonewton resolution force data and millisecond imaging to measure the sub-micron deformations.

This set of experiments demonstrates how I used the integrated force measurement and synchronized high frame rate, side-view imaging system for cell mechanics studies to accomplish the following goals:

- This system is the first to acquire sub-nanonewton AFM force data with millisecond synchronized ~300 nm resolution imaging in the direction of applied force.
- Due to the image quality and synchronization, I was able to correlate nuclear deformation with an increased apparent stiffness, as described by Hertz model fit to AFM data.
- I was able to measure intracellular and intranuclear strains to determine a region specific response to externally applied force.
- Though not the first to measure multiple stiffness regimes in AFM force data, I am the first to correlate the continuous change in stiffness regime with nuclear deformation.
- I detected sub-micron motion of the cell membrane and nucleus as the result of surface adhesion ruptures.
- I indicate a relationship between the strength of surface adhesions and direct mechanical linkage from the cell membrane to the nucleus.
- I observed extensions of fluorescent membrane only possible due to the z-axis resolution of the AFM-PRISM-VLS system.

I anticipate that the combined PRISM and AFM system will be useful in studies of cell mechanics, cell contractility, and phagocytosis. The system can provide particular insight when protein localization or subcellular rearrangement will help reveal mechanisms involved in, or underlying responses to, mechanical forces. However, in order to fully utilize the potential of this system, a larger parameter space that includes

the incorporation of multiple color labels and single-molecule techniques should be incorporated. The next chapter focuses on a summary of work done to date, plans for additional experiments, and design concerns for the next version of the AFM-PRISM-VLS system.

CHAPTER 6: Summary and Future Work

The overall goal of this presented dissertation work was to design and develop a tool for providing combined force measurement and imaging capabilities necessary to advance cell biophysics research. This need motivated the design and implementation of the combined AFM-PRISM-VLS system to facilitate the imaging of cell deformation in the direction of applied force with synchronized piconewton resolution force measurements. Additionally, experimental procedures and data analysis pipelines for single-cell and single-molecule force spectroscopy were developed.

This chapter is comprised of several key sections:

6.1 Summary

6.2 Future Work

6.3 Conclusion

Section 6.1: Summary

The forced rupture of the fibrin 'A-a' knob-hole interaction, a crucial bond in the initial stages of fibrin polymerization, was investigated using the AFM to perform SMFS experiments. As described in Chapter 2, both constant-velocity and constant-force SMFS experiments were used to examine the complex forced unfolding pathway of fibrin's γ module.

Because fibrin polymerization and clot structure is known to be dependent upon the solution environment, I sought to understand how various solution factors affect the interactions involved in fibrin polymerization at the single-molecule level. In Section 2.3, I determined that AFM constant-velocity SMFS experiments were sensitive enough to detect changes in 'A-a' interaction forced unfolding due to changes in solution conditions (i.e., calcium and NaCl concentration, pH, and temperature). Single-molecule experiments performed at high temperatures and acidic pH solution conditions also associated with the inhibition of fibrin polymerization and resulted in a decreased probability of observing γ module unfolding and a decrease in the rupture force for the fibrin 'A-a' knob-hole interaction. Additionally, the ability of the hole to maintain function under extension (characterized by an additional extension event) was decreased by every perturbation to solution condition. The destabilization of the hole 'a' binding pocket was reversible by adding a molar excess of Ca^{2+}, which is hypothesized to stabilize hole 'a' through the $\gamma 1$ calcium-binding site.(105). In this way, the

SMFS experiments explored protein function.

Because constant-velocity experiments provide an indirect relationship between force application and protein unfolding, low force unfolding domains can be overlooked and unfolding kinetics may be misinterpreted. In Section 2.4, I found that AFM constant-force SMFS were able to detect previously unobserved intermediate states and fundamentally different unfolding kinetics than revealed by constant-velocity experiments. Additionally, molecular dynamics simulations were used to determine which domains within the γ module were associated with extension events. Through the application of low forces over a prolonged time period, I observed fibrin γ unfolding through previously unseen intermediate states, an infrequent occurrence in SMFS.(87) These intermediate states are characteristic of fibrin unfolding deviant from the all-or-none, two-state Markovian process observed in multimodular mechanical proteins.(126; 130; 87) Analysis of unfolding kinetics revealed the fibrin γ module unfolds through a complex energy landscape best described by glassy dynamics behavior, characterized by stretched-exponential unfolding. Moreover, force-clamp experiments and Monte Carlo simulations of unfolding indicate that the unfolding kinetics of subdomains within the γ module are the primary contributor deviations from two-state behavior, contrary to the force protected domains model motivated by constant-velocity experiments. Constant-force probing of the 'A-a' interaction exposes a fundamentally different unfolding pathway than previous force-ramp experiments. Through a series of control experiments performed by Laurel Averett, single-molecule fibrin extensions were associated with extension of the γ module (1) and calorimetry experiments proved the existence of at least three subdomains within the γ module;(132; 133) however, these experiments were unable to determine specific regions associated with observed extension events. Therefore, I analyzed molecular dynamics simulations of γ module unfolding to determine specific residues associated with forced extension events measurable through 'A-a' interaction experiments. Specifically, DMD simulations revealed separation of the 'a' binding pocket from the rest of the γ module and separation of the remain γ module into subdomains as responsible for extension events.

Because fibrin fiber extensibility is largely reversible,(73) the molecular mechanisms responsible for fiber extension must also be reversible. Preliminary force-quench experiments were performed to probe the reversibility of fibrin γ module unfolding as a contributor to the extensibility of fibrin fibers. A fraction of the force-quench curves exhibited refolding of the γ module, as evidenced by a second unfolding step; moreover, many of these force curves displayed complex separation traces during the force-quench interval. More experiments should be performed in which the quenching force is adjusted in order to observe refolding behavior.

This collection of experiments informed our understanding of the mechanical properties of fibrin as they relate to blood clot formation. In the larger scope of designing an instrument for mechanical investigation

of cells, these experiments provided an opportunity to develop force application experimental methods and analysis pipelines which can be applied to single-molecule measurements on cells. Additionally, they provide insight into force-induced protein unbinding and unfolding behavior as it contributes to mechanical signaling within the cell.

Because a crucial part of how cells sense and respond to their environment are the mechanical properties of the cells themselves, I measured the whole cell's mechanical response to externally applied large forces and strains. In Chapter 3, I performed several experiments designed to understand cellular and nuclear mechanics in relation to cell function (mechanotransduction) and misfunction (cancer metastasis). In Section 3.2, AFM stiffness measurements of ovarian cancer cells were inversely correlated with invasivity. Differing from previous techniques, I used the AFM to probe different regions of the cells to determine the contribution of the nucleus to cell mechanics measurements. Both on- and off-nucleus (cytoplasm) measurements showed the same inverse correlation between invasion and stiffness; however, on-nucleus measurements produced a larger change in apparent stiffness indicating a change in nuclear stiffness as well as cytoplasmic. Additionally, I found that H2B-GFP fusion protein incorporated into the nucleus has an effect on the mechanical properties of the nucleus. SKOV cells transfected with H2B-GFP exhibited a significantly larger elastic modulus than unlabeled SKOV cells. More AFM indentation data is required to fully explore whether the change in stiffness is due to the cell line or to the concentration of H2B-GFP. However, the effect of H2B-GFP on nuclear mechanical properties must be taken into account in future experiments. In Section 3.3, I showed AFM stiffness measurements of pancreatic cancer cells were inversely correlated with invasivity. The AFM was used to distinguish non-transformed primary cells (HPDE) from their highly invasive phenotype (HPNE). AFM on-nucleus measurements were used to identify more subtle changes in mechanical phenotype from the expression of single-gene GOF constructs used to produce detectable changes at the phenotypic changes relevant to cancer biology. These AFM results validated our laboratory's array high-throughput microscope for screening changes in the mechanical phenotype of cancer cells. In Section 3.4, I measured the relative stiffnesses and force responses of fibroblasts and cytoplasts. AFM measurements resulted in a similar Young's modulus for cytoplasts and intact fibroblasts. Initial force response measurements suggest a stiffening response to indentation from the cytoplasm of fibroblasts but not cytoplasts. These results indicate that previously observed aberrant mechanotransduction behaviors observed for cytoplasts were not the result of changes in intrinsic mechanical properties of the cell due to removal of the nucleus, but instead are solely due to changes in mechanosensing machinery caused by the removal of the nucleus.

The preceding cell mechanics measurements revealed the contribution of the nucleus to the mechanical properties of a variety of cells. The experimental techniques and the data analysis methods developed during cell mechanics experiments can be applied to a variety of AFM experiments designed for understanding

cell and nuclear mechanics for a wide range of cell biology research. Moreover, deviations from Hertzian mechanics behavior for AFM measurements performed over the nucleus indicate nuclear contributions to stiffness measurements. However, these experiments lacked the imaging capabilities necessary to identify the contribution of the nucleus to apparent changes in stiffness.

The necessity to measure and apply piconewton forces, and simultaneously acquire structural information during applied force in the direction of applied load motivated the development of a unique imaging system that combines AFM, PRISM, and VLS. In Chapter 4, I described the design, implementation and characterization of the combined AFM-PRISM-VLS system. The combined AFM and PRISM system simultaneously delivers imaging of cell deformation in the direction of applied force and piconewton resolution force measurements with the additional inclusion of VLS illumination to improve image quality. The system has the force sensitivity to measure piconewton resolution forces and the dynamic range to apply up to several nanonewtons of force to the sample. The PRISM imaging and VLS illumination facilitated high-speed and high-resolution images of cellular structure dynamically in the direction of applied load with z-axis resolution comparable to plan-view resolution. Synchronization of the force and imaging systems facilitated high-speed data collection with sub-millisecond temporal precision.

In Chapter 5, I demonstrated the utility of the combined AFM-PRISM-VLS system for single-cell studies. The system provided simultaneous AFM force measurements with tens of piconewton of force resolution, $\sim$ 300 nm xz-plane image resolution, and 10ms time resolution in the study of intracellular (and intranuclear) motion due to force applied at the cell surface. With these measurements, I identified the structural components of the cell responsible for changes in apparent depth-dependent mechanical properties and direct mechanical linkages between the cell membrane and the nucleus. In Chapter 3, SKOV cells exhibited a depth-dependent stiffness over the nucleus determined the Hertz model. Due to our simultaneous side-view image technique, I was able to clearly determine the physical changes in the cell associated with changes in apparent stiffness measured in force data. Specifically, nuclear deformation and strains primarily located at the top of the nucleus were correlated with a 1.5-fold increase in stiffness measured with a Hertz model fit to force-indentation data. Additionally, I investigated force propagation of cell-tip adhesions evidenced by rupture events in force curves and structural motion of the cell in PRISM images. Using the improved image z-axis resolution and millisecond synchronization, I detected sub-micron motion of the cell membrane and nucleus corresponding to force-rupture events of membrane adhesion to the fibronectin-coated AFM tip. These adhesion results indicated a relationship between the strength of surface adhesions and direct mechanical linkage from the cell membrane to the nucleus. Through the detailed analysis of these datasets, I illustrated the power of our integrated force measurement and synchronized high frame rate, side-view imaging system for cell mechanics studies.

We anticipate that the combined AFM-PRISM-VLS system will be useful in studies of cell mechanics and mechanotransduction studies from the single-molecule to the single-cell level.

The experimental techniques and analysis tools developed in this thesis can provide a full picture of mechanical signaling from conformational changes to a single-molecule through structural changes induced throughout the cell over a range of time scales. The system can provide particular insight when protein localization or subcellular rearrangement will help reveal mechanisms involved in or underlying responses to mechanical forces.

Section 6.2: Future Work

In order to fully utilize the potential of this system, future designs should incorporate multi-color imaging, automation of sheet motion, and 3-dimensional image reconstruction.

An important parameter in imaging cells is the ability to incorporate multiple wavelength fluorphores to elucidate different mechanisms involved in mechanotransduction. For example, in Chapter 5 the illumination of cell membrane, nucleus and actin cytoskeleton would provide further information on strain propagation during both deformation and adhesion of the SKOV cell to fibronectin-coated tip. Stronger direct mechanical linkages from cell membrane through cytoskeleton to the nucleus are hypothesized for the large final adhesion rupture events. Having a labeled cytoskeleton would allow for explicit visualization of this linkage. In order to facilitate multiple wavelengths, future versions of VLS illumination will use the back port of the microscope for illumination and two-color simultaneous imaging system. The current design for our system has the VLS illumination entering the microscope from the right side port. This port was designed as an alternative imaging pathway for a camera, and the illumination pathway operates using a dichroic in place of the standard reflecting mirror. To change wavelengths in the current configuration would require disassembling the microscope body in order to exchange dichroics. The back port of the microscope will allow for the use of multiple wavelengths of excitation and emission light by taking advantage of appropriate filters in the standard filter wheel. On the imaging side, a Gemini image splitting optic can be incorporated to obtain two-color simultaneous images. This will allow for the rapid acquisition of multicolor images without the need to switch lasers or filter sets and incorporation of FRET imaging capabilities into the system.

As illustrated by Galland et al.(235) and Gebhardt et al.(229), a 45° reflecting optic can be used to rotate a light sheet to the horizontal. In this way, the light sheet in our system could also be oriented horizontally for use in low background plan-view imaging. This type of reflected light sheet microscopy has been used in single-molecule imaging of transcription factor binding to DNA in live mammalian cells.(229) Then our combined system could facilitate single-molecule imaging of fluorescently labeled proteins in response to

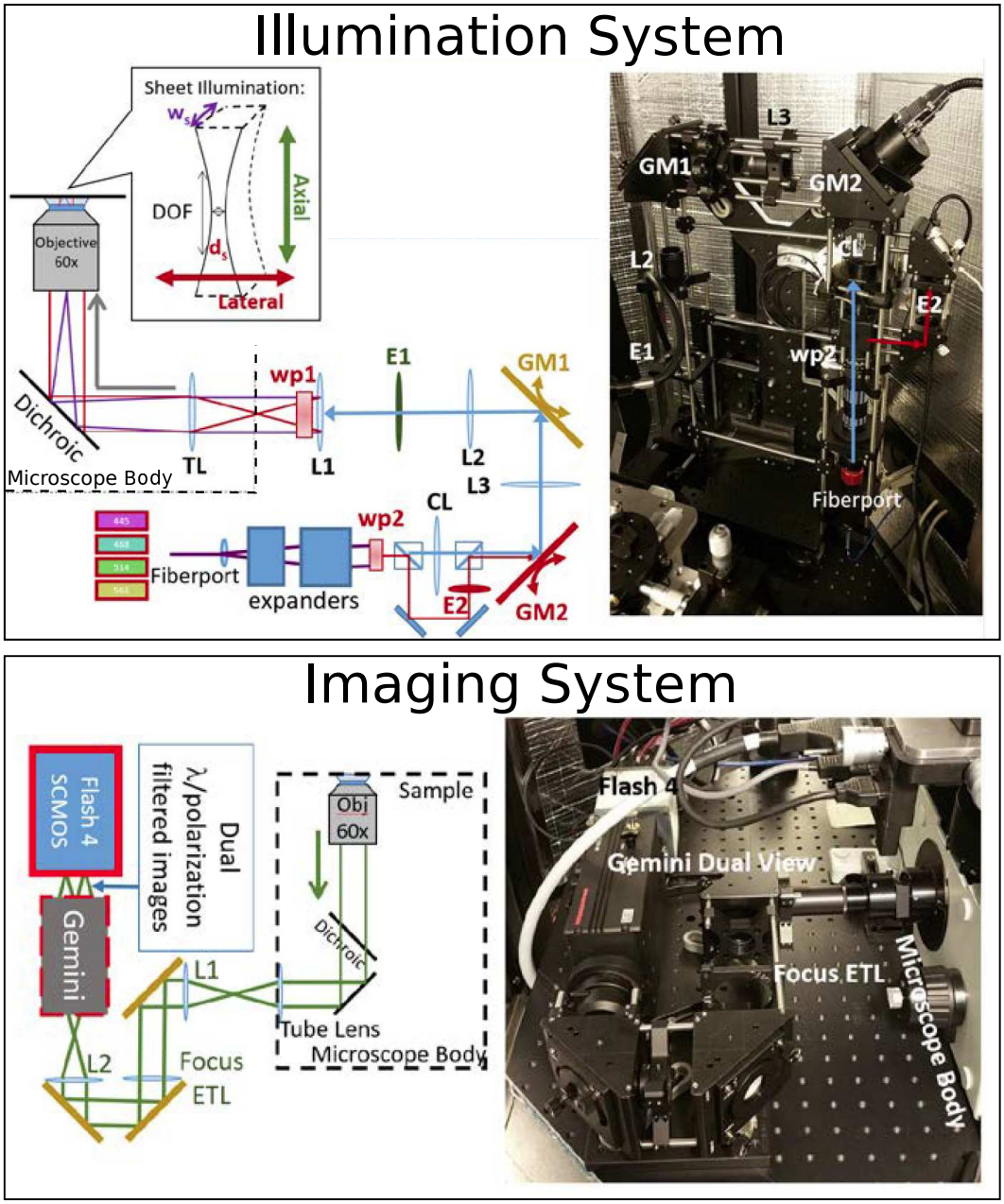

Figure 6.1: Next generation of VLS illumination and imaging systems for combined AFM-PRISM-VLS system. (Top) Schematic and image of completed next-generation illumination system with key components labeled in both schematic and image. Key improvements in the new system include a multi-wavelength light engine, the use of the rear illumination port of microscope; and computer-controlled electrically tunable waveplates (WP1, WP2), lenses (E1, E2) and galvanometer mirrors (GM1, GM2). (Bottom) Schematic and image of completed next-generation imaging system with key components labeled in both schematic and image. Key improvements in the new system include remote focusing electrically tunable lens (ETL) and Gemini image splitting optic.

single-molecule interactions on living cells.

Another important improvement for the next generation system will be the removal of manual controls of parameters such as sheet axial and lateral position, and alternating between broad and light sheet illumination. Automating these operations has the dual benefit of reducing mechanical vibrations and improving the speed at which adjustments can be performed. Computer controlled sheet motion would add the ability to efficiently acquire high-resolution image stacks in both PRISM and plan-view for 3-dimensional image reconstruction to our system. This is accomplished in the next generation of the PRISM-VLS system by incorporating electronic waveplates (WP), electrically tunable lenses (ETL), and galvanometer mirrors (GM). The illumination type (broad or VLS) can be rapidly switched by activating the polarizing WP to alternate between the cylindrical lens path producing the light sheet or a spherical lens producing a broad illumination. When operated in VLS mode, the ETL allows for the axial adjustment of the position of the sheet focus and the galvanometer mirror moves the light sheet perpendicular to the plane of its sheet (lateral). On the output side of the microscope, a focusing ETL is employed to change the focus of the imaging section without physically adjusting the objective position. The combination of VLS and imaging ETLs adds the ability to efficiently acquire high-resolution image stacks in both PRISM and plan-view for 3-dimensional image reconstruction to our system.

The next generation system, with improvements described above, has been installed and is undergoing characterization by graduate student Evan Nelsen. I acquired the first PRISM-view multicolor images shown in Figure 6.2.

Future experiments building on the work presented in this thesis should include multicolor labeling of a cell to elucidate mechanotransduction pathways due to force applied to focal adhesion. In Chapter 5, I observed motion of the nucleus due to forces applied to adhesions formed at the cell surface. The rapid transmission of mechanical forces from the cell membrane through the cytoskeleton and into the nucleus facilitated by LINC complexes, has been proposed to have a direct affect on cell response to external stimuli by directly effecting gene expression in the nucleus.(163; 162; 3) The propagation of force through this direct connection could be imaged with the new combined AFM-PRISM-VLS system. By functionalizing the AFM tip to promote the formation focal adhesions to the tip (similar to the method described in Chapter 5), the AFM can be used to apply force to the cell surface. The choice of protein coating the tip could play a role in strength and mechanical linkages formed by the focal adhesion and could thus be a variable parameter effecting mechanotransduction. Labeling the actin cytoskeleton and nucleus with different fluorescent labels would make it possible to track structural changes along the cytoskeleton and into the nucleus. Because our system could be synchronized to within signaling limits of the software involved ($< 1\mu$s), this would make possible the first imaging of direct mechanical signal transduction from cell surface to nucleus. Other experiments could

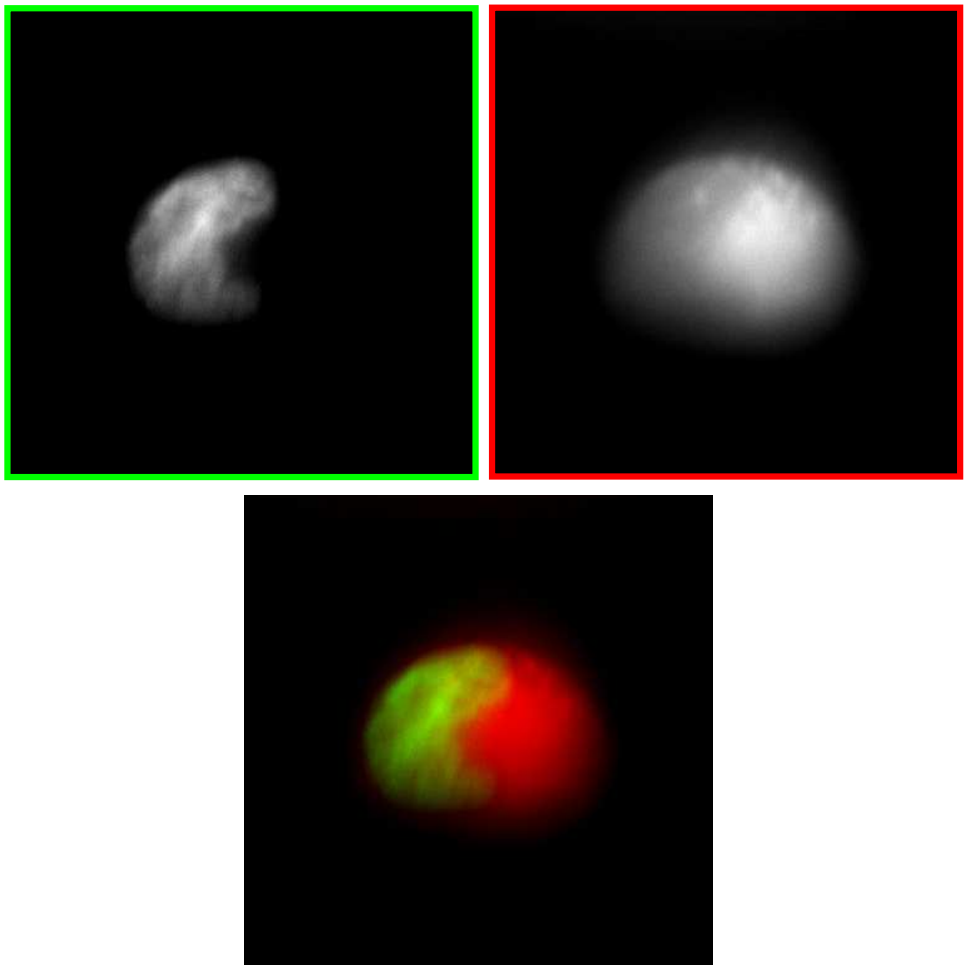

Figure 6.2: SKOV cell labeled with green nucleic acid (SYTO16) and red membrane (MitoTracker) stains acquired with different wavelength light sheet in PRISM-view. The nucleus (top-left) and membrane (top-right) images were acquired separately and then overlaid (bottom) to visualize the entire cell. Simultaneous acquisition of both wavelengths required later implementation of split side-by-side imaging.

include measuring chemical signaling in relation to force applied with an AFM tip to determine distances over which stress activated ion channels are effected, now accessible due to the image resolution provided by the PRISM imaging path. Most investigations of mechanotransduction pathways would be benefited by the ability to take rapid, high-resolution correlated to precisely applied force measurements.

Mechanical measurements of ovarian cancer cells (Chapter 3) showed that less invasive IGROV cells were stiffer than the more invasive SKOV cells. Force curves acquired on these cells also showed two stiffness regimes. So to determine the source of the stiffness difference and stiffness regimes, PRISM-images of deformation were acquired to observe differences in nuclear deformation due to applied force. Preliminary experiments with PRISM-imaging showed that over the same indentation depth (as a percentage of cell height), the change in aspect ratio of the nucleus for the two cells differed (Figure 6.3). In Figure 6.3, PRISM-view images representative of indentation for SYTO-labeled SKOV and IGROV nuclei are shown. These images were acquired prior to addition of VLS illumination and lack the resolution observed in later experiments (Chapter 5). The force curve acquired simultaneously with IGROV indentation is shown in Figure 6.3 with the corresponding image locations identified. A similar curve was acquired for the SKOV cell and the depicted images represent similar indentation depths. Shown in the bottom-right of Figure 6.3 is a plot of change in aspect ratio for each of the cells shown. This was calculated by tracking the vertical height directly below the AFM tip and the width across the widest portion of the nucleus. The result of tracking the change in aspect ratio for each nucleus type is a larger change in aspect ratio for SKOV cells than IGROV cells. If the nucleus of each cell were strictly an elastic material (as assumed by the Hertz model), then the same indentation depth should result in the same change in aspect ratio. This deviation indicates a more complex underlying mechanism for strain propagation than a simple elastic model. Altered lamin expression has been reported in many cancers, where the resulting increase in nuclear deformability could enhance the ability of cells to transit tight spaces during metastasis.(32) The structure and deficiency in nuclear lamin could be responsible for the difference in aspect ratio observed between these two cell lines. This possibility leads to an interesting series of experiments now accessible with the AFM-PRISM-VLS system. By labeling lamin and the cytoskeleton, differences (and similarities) in force transmission between these two cell lines can be investigated. These experiments would provide valuable insight into the mechanisms responsible for force transmission and direct mechanical signaling in cancer cells.

All future work on our system would benefit from more rigorous data analysis methods to calculate strain maps, flow fields, diffusion and (un)binding rates. We have begun to understand spatiotemporal image correlation spectroscopy (STICS) as a means of analyzing PRISM-view images using a package provided to us through collaboration with the Wiseman Lab. STICS is a method of image correlation spectroscopy that does not separate the spatial fluctuation analysis from the temporal to obtain flow vectors, or the direction in

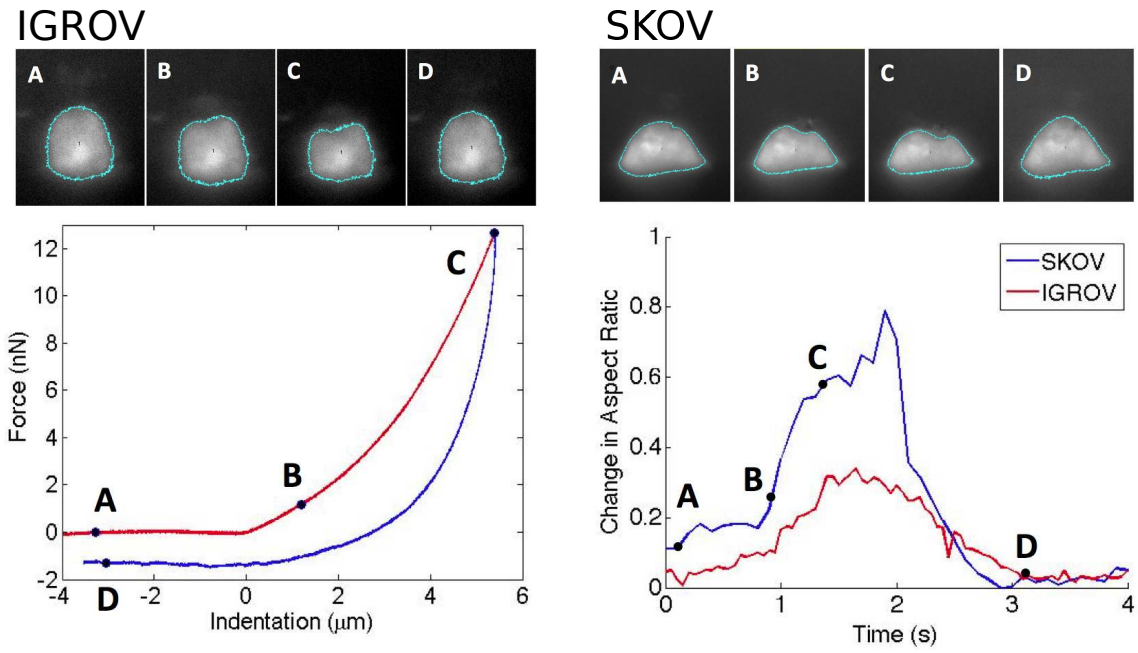

Figure 6.3: SKOV and IGROV deformation comparison. Representative PRISM images of SYTO-labeled nucleus from time series acquired during (top-left) IGROV and (top-right) SKOV cell deformation. (Bottom-Left) Force-indentation curve for IGROV indentation with points corresponding to images labeled. A similar indentation curve was acquired for the SKOV cell and images shown were acquired at similar depths. (Bottom-Right) Change in aspect ratio of cell nuclei over the course of indentation curve for IGROV (red) and SKOV (blue) cells as determined from a ratio of cell height to cell width calculated from time series.

which particles are exiting the correlation areas if directed flux is present.(263; 264) This method of analysis would provide data on the motion of subnuclear regions over the course of a combined AFM-PRISM-VLS experiment. For example, the position of different chromosome territories (spatial ordering of chromosomes) in the nucleus is believed to regulate transcriptional activity.(265) Under load, the nucleus deforms which changes the proximity of chromosome territories, specifically moving the gene-poor chromosomes localized near the periphery of the nucleus toward the active center of the nucleus, a process that could lead to altered transcription. Furthermore, this would allow for a validation of the hypothesis that nuclear lamin determines the sensitivity and timescale of nuclear reorganization in response to stress.(265) This could be a future area of investigation; however, the current analysis is sensitive to edges produced by boundaries, especially those created by an AFM tip (Figure 6.4). Therefore, more work is required to implement this or other analysis methods for determining induced strain.

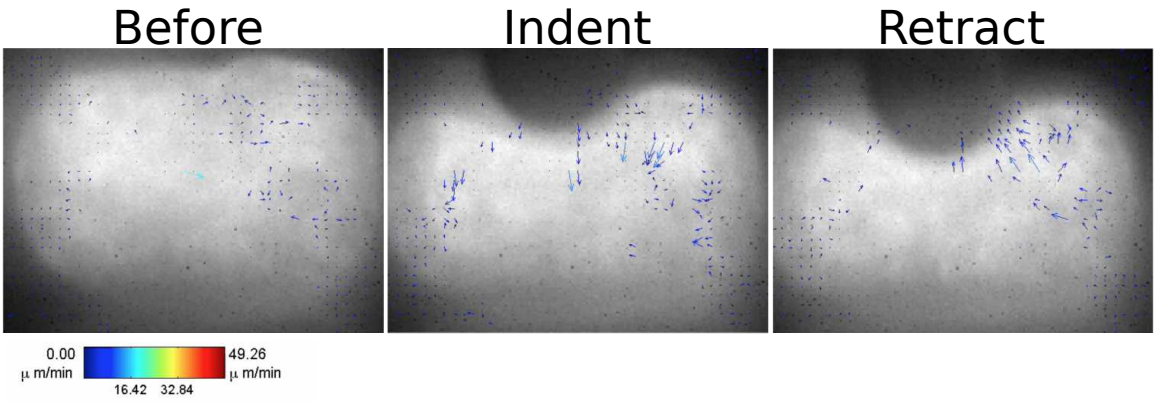

Figure 6.4: Initial application of STICS analysis to Syto-labeled SKOV nucleus data set. Analysis was applied to the entire time series, and show here are three representative images taken before indentation, during indent and during retraction of the AFM tip. The before image gives an idea of background thermal noise measured with STICS. During indent, the majority of fluorescent regions are moving down and away from the AFM tip. During retract, the bright labels are moving up toward the retracting tip. Locations not in close proximity to the AFM tip move as a result of applied load; however, different regions of motion are observed during indentation and retraction, indicating that different regions of the nucleus may deform reversibly (or not).

Section 6.3: Conclusion

Collectively, this dissertation has detailed the strategies and implementations of experimental procedures and data analysis pipelines for single-cell and single-molecule force spectroscopy. This included single-molecule study of forced fibrin unfolding through the specific 'A-a' interaction. The unfolding mechanism observed in SMFS experiments was shown to be mediated by a variety of solution conditions known to effect full clot structure, including calcium and NaCl concentration, temperature and pH. Additionally, constant

force applied to the 'A-a' interaction was shown to unfold the γ module through a different unfolding pathway characterized by an observable intermediate unfolding step and unfolding kinetics dominated by the kinetic parameters of individual domains, rather than the force-protected nature of these domains. When these experimental results were combined with the results of molecular dynamics simulations, I was able to attribute unfolding to specific residues which may be associated with clotting dysfunction. In the future, the mechanical response of single fibrin molecules to force may elucidate the source of mechanical properties of fibrin networks. Single-cell mechanics studies indicated the significance of the nucleus to a cell's mechanical properties, including mechanotransduction, for a range of cell types and revealed a depth dependance to apparent stiffness. However, standard cell mechanics measurements lack the ability to measure key metrics for cell response, such as nuclear deformation, in the direction of applied force. Therefore, I developed a combined AFM-PRISM-VLS system that facilitates high-resolution, high-speed imaging in z-direction synchronous with AFM force measurement. With this system, I was able to identify nuclear deformations associated with the change in apparent stiffness observed in AFM force-indentation data and nuclear motion due to force applied through adhesions at the cell surface. Longer-term goals for this instrument are to investigate how external mechanical stimuli (specifically single-molecule interactions) alter gene expression, motility, and differentiation.

APPENDIX A: Single-Molecule Force-Clamp Analysis

In order to efficiently collect enough data on fibrin unfolding at different forces, I created an analysis pipeline to take force-clamp data and determine the start and end of steps in the separation-time curve. From these data points, relevant parameters such as step height, total extension, and lifetime can be calculated and compared for different clamping forces.

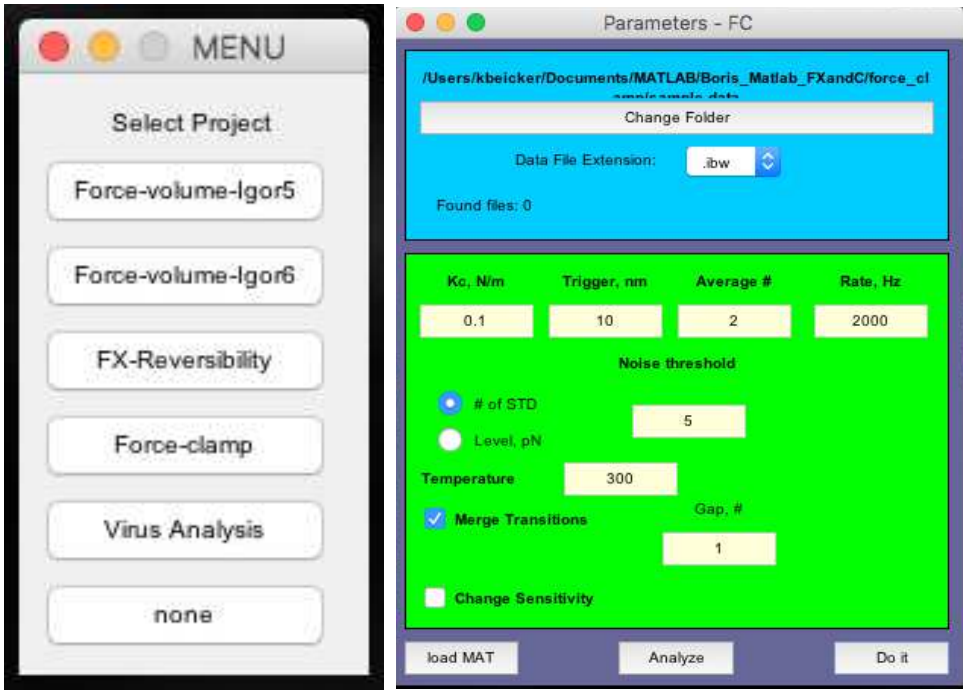

Figure A.1: Data analysis package for a range of data types. (Left) The panel for selection of data and analysis type. Not shown here is the selection for 'Cell Mechanics' analysis as discussed in Appendix D. (Right) GUI for selection IGOR wave parameters to read ibw files into MATLAB. This panel is the same for Force-Volumes in Igor 5 and 6, FX-Reversibility, and Force-Clamp selections.

The first window encountered when running the package allows the user to select the data type to be analyzed (Figure A.1 Left). Selections include 'Force-Volume-Igor5', 'Force-Volume-Igor6', 'FX-Reversibility', 'Force-Clamp', 'Virus Analysis', 'Cell Mechanics', and 'None'.

The first four items have modifications to the code to allow the analysis package to take in a variety of different data formats. 'Force-Volume-Igor5' This selection allows the user to analyze data collected on older versions of Asylum software for which the peak-finder analysis was initially designed. This analysis package was written in Professor Boris Akhremitchev's lab at Duke University (his lab has since moved to the Florida Institute of Technology) and a more detailed discussion can be found in Laurel Averett's thesis (1). Briefly, the software identifies force rupture peaks for all curves collected in a standard force map. 'Force-Volume-Igor6' performs the same analysis as discussed above for newer AFM force maps in which the

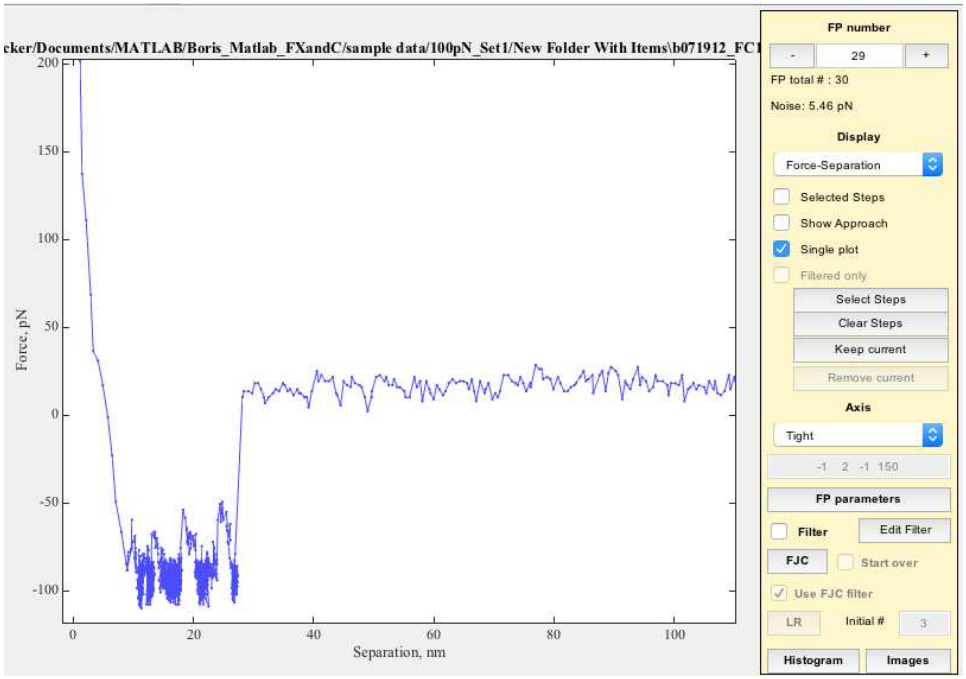

Figure A.2: Typical GUI for peak selection generated by running analysis in Figure A.1 Right.

data is saved in a different structure. I applied a simple modification to the above code to allow the analysis package to seamlessly read in the new data structure. 'FX-Reversibility' and 'Force-Clamp' both required a more in depth overhaul of the analysis packages due to the entirely different data structure associated with custom programed waves for data collection. However, the result was similar - a data analysis package for peak selection. 'FX-Reversibility' reads in data from constant-velocity SMFS reversibility experiments, in which the AFM tip is retracted a set distance away from the surface, returned toward the surface, and then retracted again through rupture. In the case of force-clamp data, this part of the data analysis was initially used to filter out force traces with no interaction events; however, was obsolete in later iterations and instead opened directly into the Step-Finder GUI. The force-clamp selection works for both force-clamp and force-quench experiments. All of these selections open a parameter panel for reading AFM data into MATLAB (Figure A.1 Right). The results of running this panel is a GUI (similar to Figure A.2) which allows the user to go through the force curves and look at curves with peaks (or steps) selected. The output file from this can be used to determine peak separations, force rupture values, and fit protein unfolding models (e.g., the freely jointed chain).

The 'Virus Analysis' and 'Cell-Mechanics' selections both open GUIs for analysis similar to that described in Appendix D. 'Virus Analysis' is a more primitive version without the depth of analysis or versatility offered by the Cell Mechanics analysis GUI discussed in Appendix D. The final selection – 'None' – simply closes

the window.

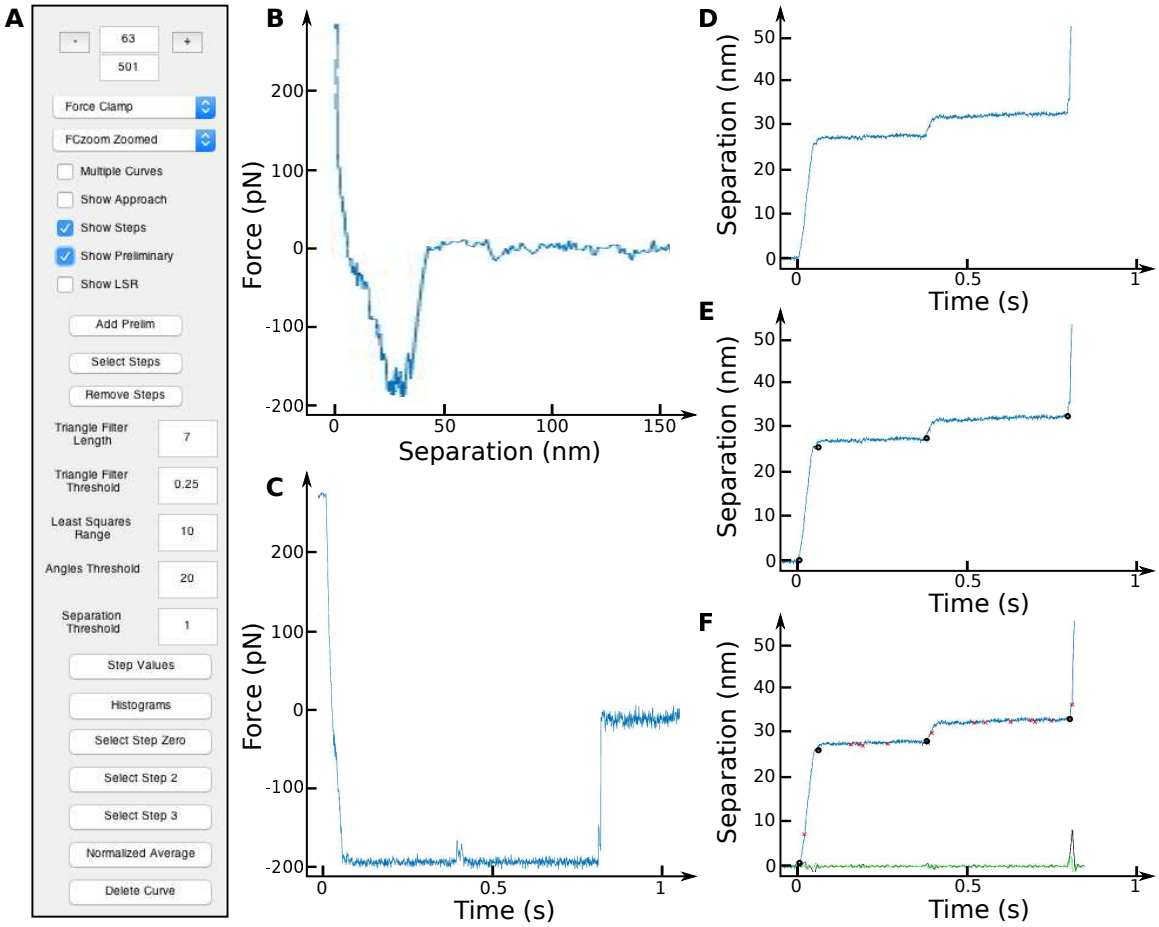

Figure A.3: The Step-Finder GUI panel and results. (A) Panel showing the range of displays and parameters that can be used for analysis of force-clamp results. Data can be plotted as (B) force-separation, (C) force-time, and (D) separation-time. (E) By selecting 'Show Steps', the step-finder analysis uses a trapezoidal filter to find the points of inflection in separation-time traces (black open circles). (F) For a deeper understanding of possible missed steps of the effects of modifying parameters, selecting 'Show Preliminary' shows the guesses for steps (red 'x's) and the results of multiple trapezoidal filters for inflection points (green and black trace). The buttons at the bottom of the tools panel (A) are for analysis of steps in data points and can produce a variety of plots.

For force-clamp analysis, I developed an automated step selection method using trapezoidal filters which is referred to as Step Finder. After the Igor data has been run through the code developed by the Akhremitchev lab to produce a matlab file, the Step Finder code uses a trapezoidal filter, angle requirements, separation requirements, and manual input to determine the separation-time steps for large data sets. The use of a trapezoidal filter is heavily based on techniques for identification of time pulses in radiation measurements by Jordanov et al(266) which are remarkably similar to separation-time traces in force-clamp experiments. The following is an explanation of several key parameters as they relate to the Step Finder GUI:

1. **Filter Length:** This gives the length of the applied smoothing filter. Two examples are shown in Figure A.4.

    - *Box Filter:* This sums values for length and is ideal for smoothing data. This was not used in this analysis package.
    - *Triangle Filter:* This was used up to the third filtering step of force-clamp data. The sum of the first window is subtracted from the sum of the second window, which results in smoothed data due to the length of the window and numerical differentiation due to the difference.

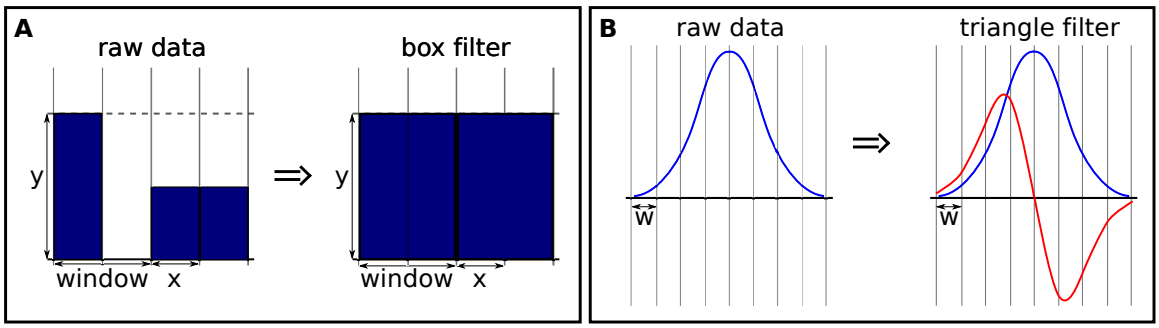

Figure A.4: Illustration of results of applying a (A) box filter and (B) triangle filter to raw data sets.

2. **Filter Threshold:** This is the minimum value applied to the filter results to consider a point a step due to the change observed. Multiple filters were applied and this threshold is applied to the third filtering pass, similar to an inflection point derivative.

    - The second triangle filter applied to the wave function gives points of inflection where curve crosses the zero.
    - The third triangle filter gives a magnitude of change and thus the certainty of a step existing.

3. **Least Squares Range:** This is the number of data points to the left and right of steps found using only the triangle filter over which the least squares algorithm is applied (Figure A.5). Least squares fitting finds best-fitting curve by minimizing the sum of the squares of the offsets of points from the curve.

4. **Angle Threshold:** This parameter makes sure we don't just have a noisy baselines by requiring a minimum angle between the two least squares fits (Figure A.6).

5. **Separation Threshold:** This threshold makes sure that a noisy baseline is not an issue on a step plateau. Therefore separations associated with steps must be outside of the noise of a step plateau (Figure A.7).

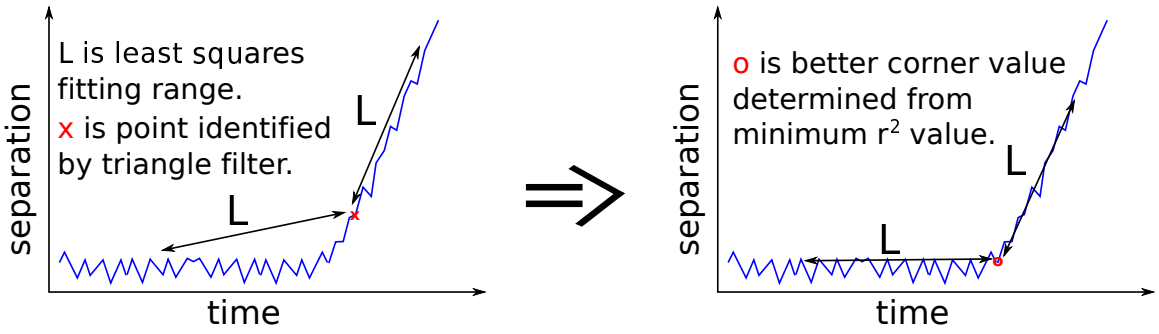

Figure A.5: Illustration of the application of the least squares filter.

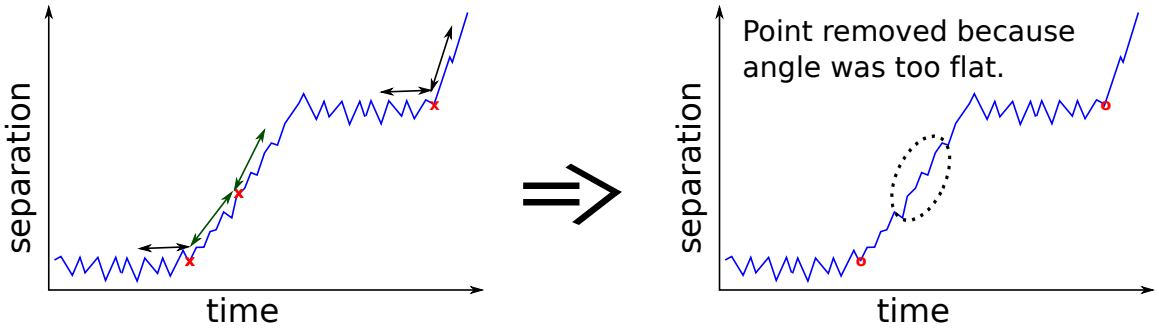

Figure A.6: Illustration of the application of the angle threshold.

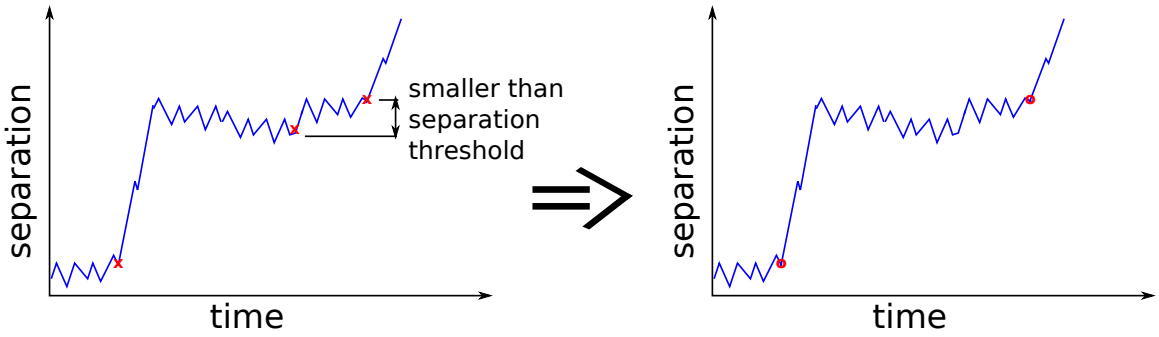

Figure A.7: Illustration of the application of the separation threshold.

6. **Manual Addition or Removal of Steps:** The view also has the ability to manually add or remove steps as long as they are recognized as preliminary steps in the triangular filter.

From this analysis package GUI, individual step height values, histograms of steps in data sets and normalized ensemble averages (NEAs) can directly be determined. Additionally the output for step locations can be used for further post-filtering analysis. The code can be acquired from the University of North Carolina at Chapel Hill Center for Computer Integrated Systems for Microscopy and Manipulation.

APPENDIX B: Two-State Unfolding

The simplest representation of protein unfolding assumes that a molecule may belong to only two states, the folded state and the unfolded state. In reference to force-clamp, the protein would unfold in a single step from folded to unfolded state, where a single exponential describes the probability of unfolding. This can be mathematically derived from a Poisson distribution.

A Poisson distribution expresses the probability of a given number of events occurring in a fixed interval of time (or space) if these events occur with known average rate and independently of the time since the previous event (Markovian). This is ideal for representing the probability of unfolding individual protein domains that have an intrinsic unfolding rate. The probability of obtaining exactly n successes in N trials is given by the limit of the binomial distribution:

$$P_p\left(n \mid N\right) = \frac{N!}{n!\left(N-n\right)!} p^n \left(1-p\right)^{N-n}$$

where p is the probability of success for each of n independent yes/no experiments. If we concern ourselves with the probability of not unfolding, then for two-state unfolding the number of successes would be zero ($n = 0$). So the distribution of events not unfolding is

$$P_p\left(0 \mid N\right) = \left(1-p\right)^N$$

Because events occur with a known average rate, we can define an expected number of 'successes' (i.e., unfolding events):

$$v = N \cdot p \rightarrow p = \frac{v}{N}$$

So the probability of not unfolding, can be determined by looking at a large sample size ($\lim N \rightarrow \infty$):

$$P_{\frac{v}{N}}\left(0 \mid N\right) = \left(1 - \frac{v}{N}\right)^N$$

$$P_v\left(0\right) = \lim_{x \rightarrow \infty} \left(1 - \frac{v}{N}\right)^N = e^{-v}$$

However, we are interested in the probability of unfolding as a function of time

$$P_{UF}\left(t\right) = 1 - e^{-v} = 1 - e^{-\alpha t}$$

Usually single-molecule force spectroscopy experiments are performed on polyproteins of the same single domain proteins.(87; 130) Therefore, all unfolding events are representative of unfolding the same domain and two-state unfolding can be readily applied to describe them.

APPENDIX C: Monte Carlo Simulations of Protein Unfolding

Single-molecule protein unfolding experiments, such as atomic force microscope force-clamp experiments, have prompted extensive theoretical and computational work in order to extract a protein's kinetic, energetic, and structural properties. Molecular dynamics simulations (such as, steered molecular dynamics discussed in other sections of this thesis) provide insights into the structural changes during force-induced protein unfolding; however, these simulations involve time scales that are orders of magnitude smaller than those of the experiment and the parameters used in the calculations are often neither controllable nor measurable experimentally.(267) As a result, to understand force clamp spectroscopy experiment results I used a Monte Carlo simulation approach based on a simple two-state kinetic model for the protein.

A Monte Carlo simulation is used to invesigate the 'time dependence' of a model for which change does not proceed in some rigorously predefined fashion (e.g., according to Newton's equations of motion) but rather in a stochastic manner which depends on a sequence of random numbers which are generated during the simulation. Running the same simulation with a different sequence of random numbers will not give identical results but will agree with previous simulations within some 'statistical error'. For force-clamp protein unfolding, this means I can simulate a variety of separation-time unfolding trajectories in order to determine kinetic parameters.

Fibrin γ module unfolding deviates from the single exponential unfolding behavior characteristic of simple two-state unfolding. This deviation could result from a variety of characteristics unique to the γ module including the presence of multiple subdomains with different unfolded lengths and unfolding rates, and protein conformation such that weaker domains are protected from force application through the 'A-a' knob-hole interaction. Monte Carlo simulations are an ideal method for determining the source of fibrin's deviation from the simple two-state unfolding model and establishing the appropriate model for extracting kinetic parameters from experimental force-clamp results.

Section C.1: Methods

In force-clamp experiments, the AFM tip is moved away from the substrate until a constant force is applied to the protein. When protein domains unfold, the force applied to the cantilever is reduced and the tip must move away from the substrate again to maintain the constant force. In this way, a constant force on the protein is maintained throughout a force-clamp experiment.

To simulate the separation-time traces produced by force-clamp experiments, I need to calculate the probability that individual protein domains will unfold. The Bell-Evan's model(119) describe the unfolding rate of a protein as a function of applied force

$$k_U = k_0 e^{'fracF\Delta x k_B T} \tag{C.1}$$

where k_0 is the unfolding rate in the absence of an external force and Δx is the distance between native state and the transition state along the pulling direction. The likelihood of one protein domain in the molecule unfolding is related to the unfolding rate by

$$p = \Delta t \cdot k_U \tag{C.2}$$

So the probability of at least one of a group of N_f identical folded domains to unfold in a given time step can be found from the binomial distribution

$$P = 1 - (1 - p)^{N_f} \tag{C.3}$$

To determine if the unfolding happens at a particular point in time, P is compared with a randomly generated number uniformly distributed between 0 and 1. If P is larger than the random number, a domain unfolds and the applied force and population of states are recalculated. Otherwise, no unfolding occurs and the state remains unchanged. Additional parameters, such as domain length and unfolding order can be applied for exploring variations in separation-time traces.

The protein polymer is assumed to be stretched in the direction perpendicular to the surface with joints between domain groups lying along the line between surface tether point and the position of the time. Interactions between different parts of the polymer and between the chain and surface are not considered. For simplicity, the rapid elastic extension and relaxation of the protein chain is consider to be insignificant.

Custom MATLAB analysis code was written to explore several domain parameters and configurations for fibrin's γ module:

1. A series of the same domains (to mimic polyprotein experiments)

2. Multiple domains with the same kinetic parameters but different unfolded lengths

3. Multiple domains with the same unfolded length but different kinetic parameters

4. A series of the same domain with preferred unfolding order (to simulate force protected domains)

Section C.2: Results

The simplest case for protein unfolding is a single domain unfolding due to an applied force. So, it is in this case that I check the validity of our Monte Carlo simulations. In Figure C.1, simulated data exhibit an exponential probability of unfolding over time for all applied forces and the unfolding rate increases for higher pulling forces. When just 50 curves were averaged to produce the normalized ensemble average, a stair step pattern is present in the probability of unfolding curve. This is the result of individual unfolding events being distinguishable when averaging a small number of curves. The same behavior was seen in experimental data. When the number of curves averaged was further increased to 500 curves, the individual stair step unfolding events were no longer evident in the normalized ensemble average and the exponential behavior of the probability of unfolding was unmistakable.

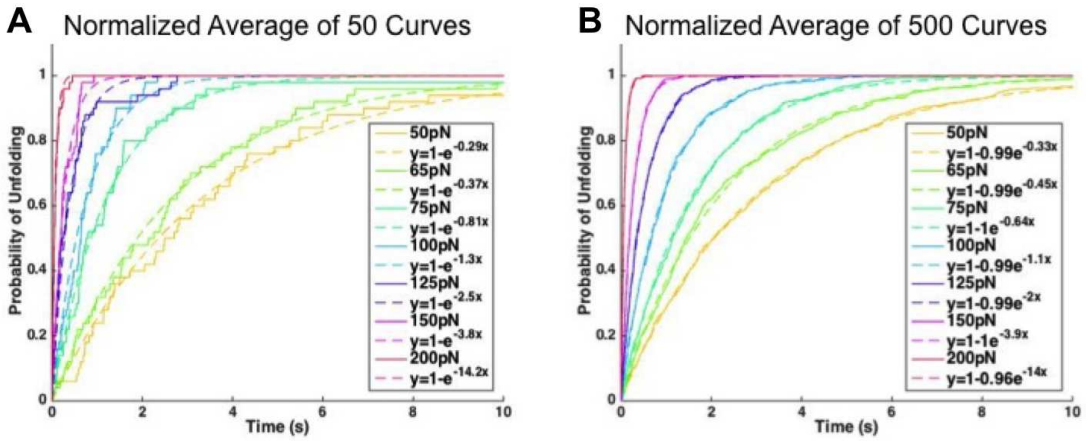

Figure C.1: Monte Carlo Simulation of Single Domain Protein Unfolding. These plots show the normalized ensemble average of (A) 50 curves and (B) 500 curves as a function of time created from simulations of single domain unfolding.

Additionally, I tested the validity of our simulated unfolding trajectories by assessment of the kinetic parameters extracted using Bell's Model. To do this, normalized ensemble averages of 500 unfolding trajectories were created at each unfolding force, and a single exponential curves was fit to each normalized ensemble average. Then log of the exponent was plotted versus pulling force and fit with a line, so that kinetic parameters could be extracted using the log of the Bell-Evan's Model (C.1):

$$\ln(k_U) = \ln(k_0) + \left(\frac{\Delta x}{k_B T}\right) F \tag{C.4}$$

The Bell-Evan's model accurately returned the input parameters for the Monte Carlo simulation (Figure C.2), further validating the simulated data.

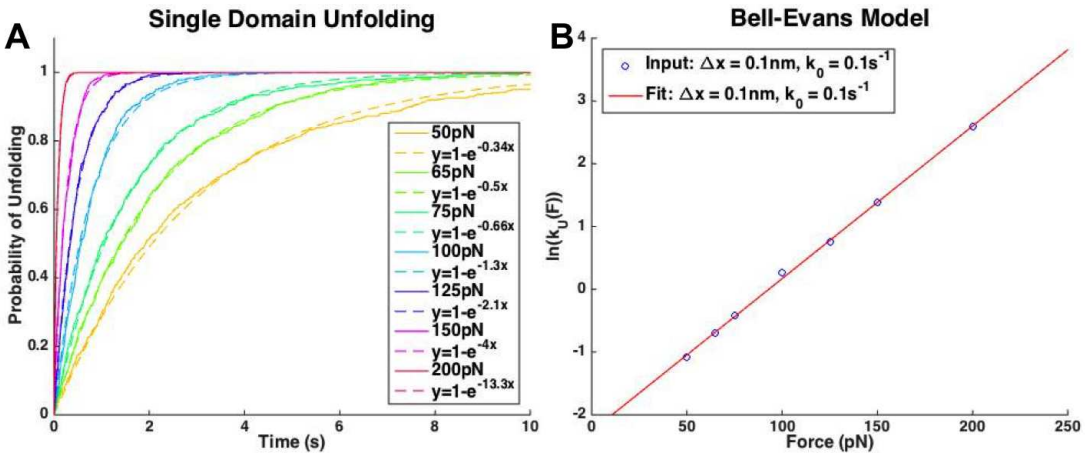

Figure C.2: Determining Kinetic Parameters with the Bell-Evan's Model. (A) Normalized ensemble average plot of 500 curves created from Monte Carlo simulation of single domain unfolding. (B) Plot of the natural log of the exponents calculated by fitting the probability of unfolding versus the force (blue circles) and a linear fit to these data points (red line).

However, fibrin γ module unfolding observed in AFM force-clamp experiments was distinctly non-exponential in nature. So, fibrin γ module unfolding is more fundamentally complex than the forced unfolding of a single protein domain.

C.2.1: Polyprotein-like Unfolding

Since the fibrin γ module was shown to unfold in a series of steps, it is possible that multiple domains unfolding produced the deviations. This was unlikely because many single-molecule force spectroscopy experiments are performed using polyproteins, multidomain proteins composed of repeats of the singular protein domains. Polyproteins typically contain between 6 and 12 domains and have been shown to capture unfolding kinetics of single proteins in AFM force-clamp experiments using the normalized ensemble average.(87) I used our Monte Carlo simulations to validate that multiple domains could still be readily described by exponential behavior independent of the number of domains.

Monte Carlo simulations of a multi domain protein were calculated by determining the probability of unfolding for a number of independent protein domains where each experiences the same force. This means that at any given time, each domain has a probability of unfolding defined by application of the Bell model. The results of simulations for 100 pN constant force unfolding for a single-domain, two-domain, and ten-domain protein (Figure C.3), exhibit exponential unfolding behavior characteristic of a two-state unfolding system. Moreover, the probability of unfolding was not dependent on the number of domains as made evident by the same single exponential fit to all three data sets.

From this I can conclude that fibrin's non-exponential unfolding behavior is not the result of simply having several of the same subdomains. However, the domains unfolding as part of fibrin's γ module unfolding could have different unfolded lengths or kinetic parameters (i.e., distance to transition state and steady-state unfolding rate).

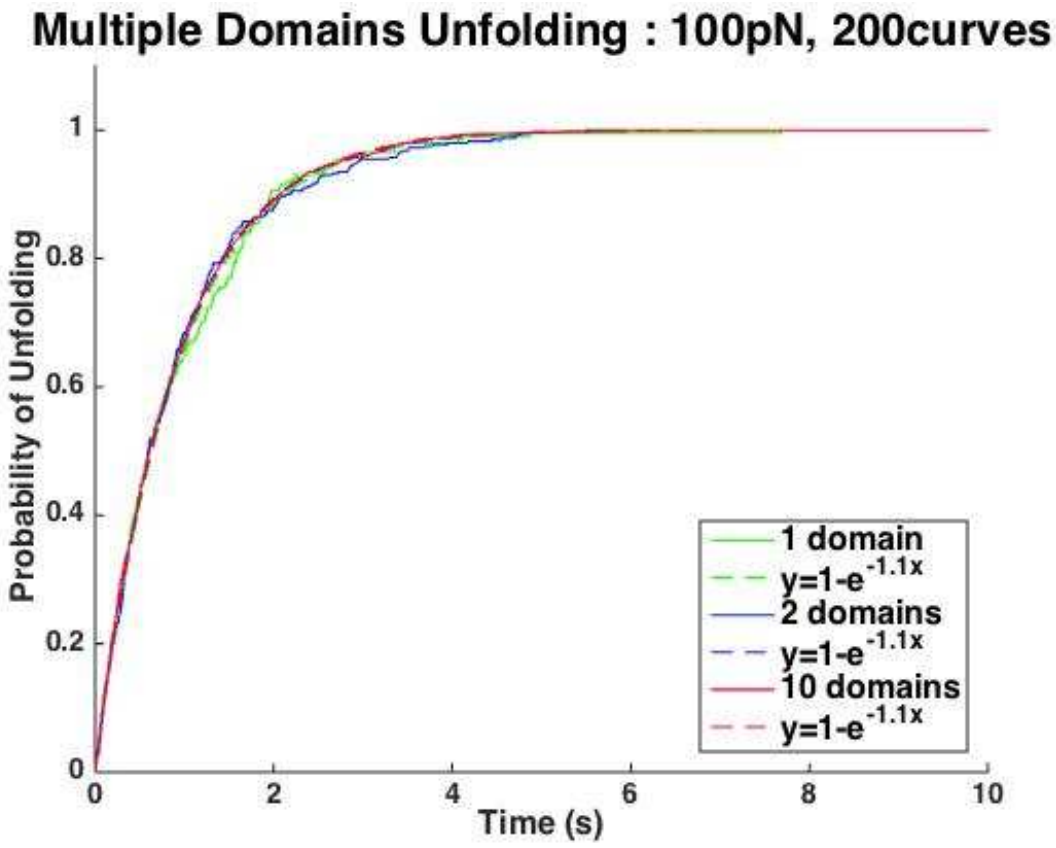

Figure C.3: Monte Carlo Simulation of Multi-Domain Protein Unfolding. These plots show the probability of unfolding at 100 pN clamping force displayed as a normalized ensemble average of 200 curves for a single domain (green), a two-domain (blue), and a 10-domain (red), where each domain has the same unfolded length, with single exponential fits.

C.2.2: Different Domain Lengths

Another factor that could contribute to the non-exponential unfolding behavior observed by fibrin's γ module is a difference in unfolded length of each domain within the γ module. This possibility is unlikely because the unfolding steps observed in force-clamp experiments were all approximately the same length of 3.3 nm. However, Monte Carlo simulations of domain unfolding make it simple to investigate the effect that domain length has on unfolding kinetics observed in experiments. So domain length was investigated a source of the γ module's deviation from exponential unfolding.

Monte Carlo simulations were run for two domains of increased difference in unfolded length. Once again, the domains were treated as independent with the same kinetic parameters. One domain for each of the protein variations was given the unfolded length of 1 nm. The other domain was assigned the unfolded length of 1 nm, 5 nm, and 10 nm for each variation of protein geometry. The results of simulations for 100 pN constant force unfolding of 500 curves for each of these domain lengths (Figure C.4), exhibit exponential unfolding behavior characteristic of a two-state unfolding system. Moreover, the probability of unfolding was not dependent on the length of the unfolding domains as made evident by the same single exponential fit to all three data sets.

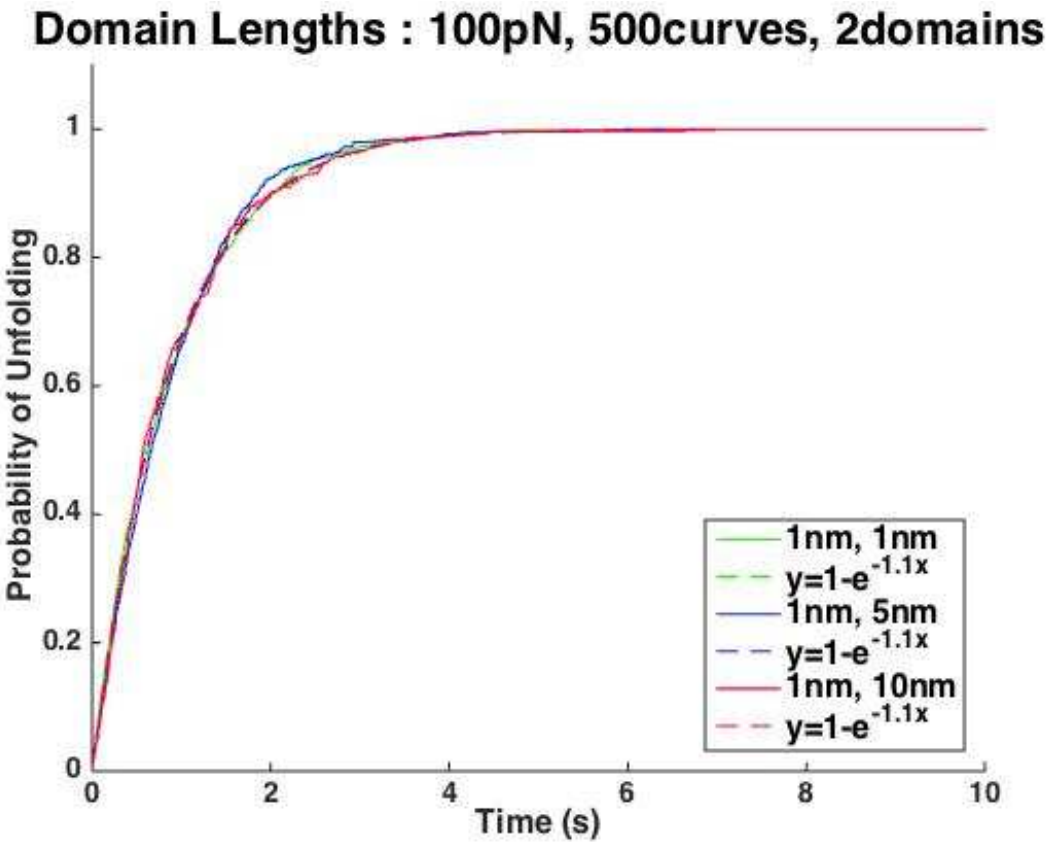

Figure C.4: Monte Carlo Simulation of Multi-Domain Protein Unfolding with Different Domain Lengths. These plots show the probability of unfolding at 100 pN clamping force displayed as a normalized ensemble average of 500 curves for a protein consisting of two 1 nm domains (green), a protein consisting of a 1 nm and 5 nm domain (blue), and a protein consisting of a 1 nm and 10 nm domain (red), with single exponential fits.

C.2.3: Different Kinetic Parameters

Unlike a polyprotein, unfolding in a native protein may have different kinetic parameters (i.e., steady state unfolding rate, k_0 and distance to transition state, Δx) and differences in these factors produce deviations from the simple two-state model. I showed for a simple system with two unfolding domains changes to either k_0 or Δx produced deviations from single exponential unfolding behavior (Figure C.5). More over, these differences were the same for both k_0 and Δx where at shorter time scales the probability of unfolding is under estimated by a single exponential fit and over estimated at longer time scales.

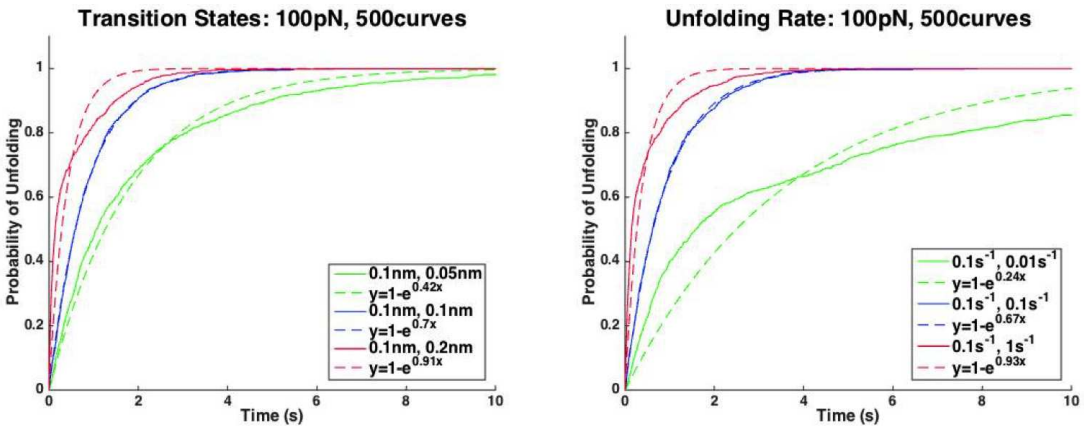

Figure C.5: Monte Carlo Simulation of Multi-Domain Protein Unfolding with Different Kinetic Parameters. These plots show the probability of unfolding at 100 pN clamping force displayed as a normalized ensemble average of 500 curves for a protein consisting of two 1 nm domains with varied (A) distance to transition state and (B) steady-state unfolding rate for the second domain. A single exponential fit to each data set is shown with a dashed line.

The deviations observed in Monte Carlos simulations (Figure C.5) were more pronounced but similar to the deviations seen in force-clamp AFM experiments (Figure 2.28). This indicates that a difference in the kinetic parameters of unfolding domains is responsible for deviations from single exponential unfolding of fibrin's γ module.

If the unfolding protein is known to have two domains with different kinetic parameters that will unfold over the course of a force-clamp experiment, then the unfolding can be described by the sum of two exponential fits. Using the Monte Carlo simulations, I tested the ability to calculate kinetic parameters from a two exponent fit to the normalized ensemble average. Unfolding was simulated for a range of forces, normalized ensemble averages for each force were fit with the sum of two equally weighted exponents then the exponents (ordered by largest and smallest) as a function of force were fit using Bell's model to extract the force-free kinetic parameters. The results for different unfolding rates and distances to transition state are shown in Figure C.6 and Figure C.7, respectively. From these simulations it is clear that I accurately determined the

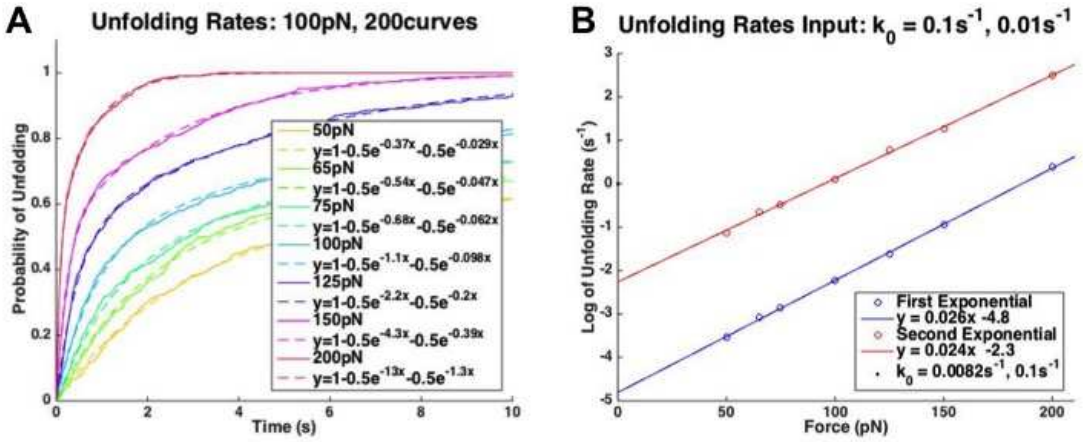

Figure C.6: Different Unfolding Rate for Multi-Domain Protein. (A) The probability of unfolding a protein consisting of two 1 nm domains with different k_0 of 0.1 s^{-1} and 0.01 s^{-1} at forces ranging from 50-200 pN calculated from a normalized ensemble average of Monte Carlo results with two exponential fit. (B) Exponential values plotted as a function cla'mping force, fit with Bell's model to determine k_0 (last value displayed in legend).

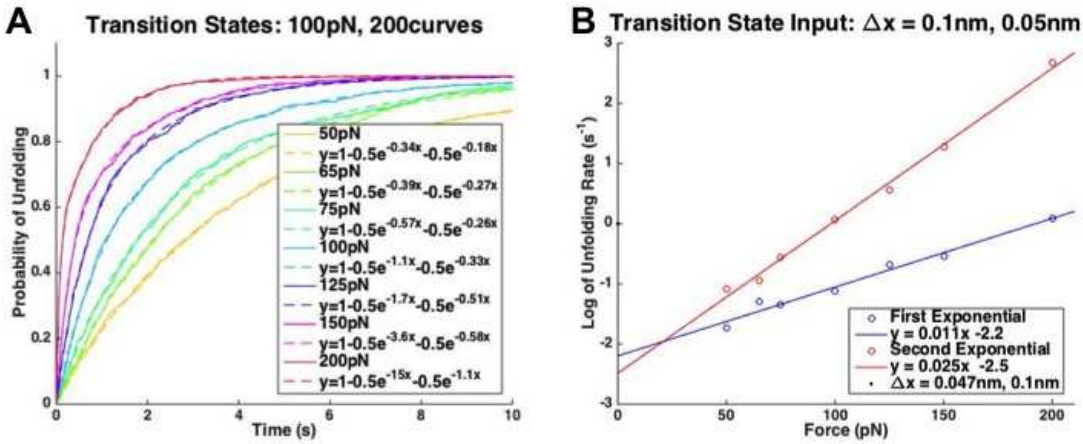

Figure C.7: Different Transition State Distances for Multi-Domain Protein. (A) The probability of unfolding a protein consisting of two 1 nm domains with different Δx of 0.1 nm and 0.05 nm at forces ranging from 50-200 pN calculated from a normalized ensemble average of Monte Carlo results with two exponential fit. (B) Exponential values plotted as a function clamping force, fit with Bell's model to determine the Δx (last value displayed in legend).

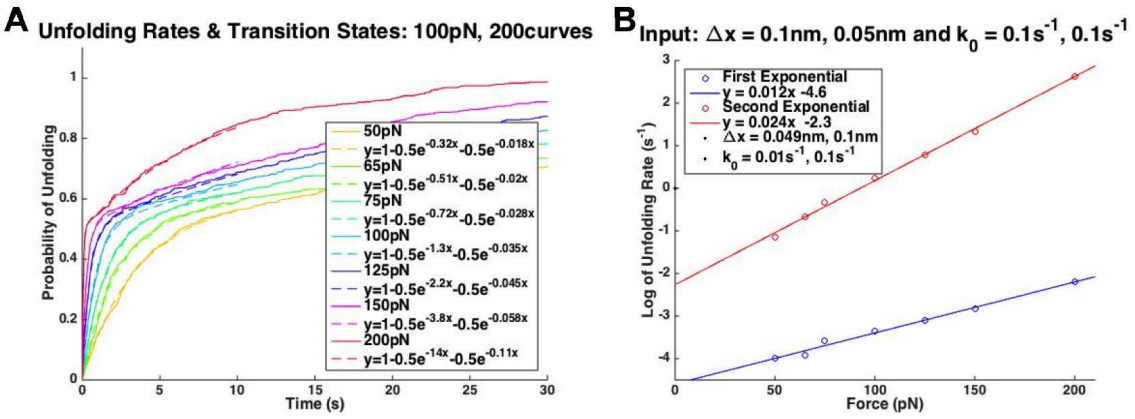

Figure C.8: Monte Carlo Simulations of Multi-Domain Protein with Domains of Different k_0 and Δx. (A) The probability of unfolding a protein consisting of two 1nm domains with different k_0 (0.1 s^{-1} and 0.01 s^{-1}) and Δx (0.1 nm and 0.05 nm) at forces ranging from 50-200 pN calculated from a normalized ensemble average of Monte Carlo results with two exponential fit. (B) Exponential values plotted as a function clamping force, fit with Bell's model to determine the k_0 and Δx (last values displayed in legend).

kinetic parameters of each domain by fitting the normalized ensemble average with the sum of two exponentials. This was verified for a range of unfolding rates (0.001-1 s^{-1}) and transition state distances (0.05-0.2 nm) – not shown. Additionally, if both force-free unfolding rate and distance to the transition state are different for each unfolding domain, both parameters can be extracted using the sum of two exponentials (Figure C.8).

However, this method is only a viable method of interpreting AFM results when the number of unfolding domains for the molecule is known. In the case of the fibrin γ module, there are a range of unfolding domains (2-4 domains) that may unfold prior to 'A-a' knob-hole rupture. With multiple domains and thus multiple exponents, exponential fits become more sensitive to input parameters and less reliable for determining kinetic parameters for each domain. Usually a reasonable assumption for multiple unfolding rates is a single rate constant because slow exponents will contribute strongly to the probability of unfolding where as faster rate constants will not be seen in the probability of unfolding curve. This being said, with the appropriate analysis, others have extracted information about the number of intermediate unfolding states can be extracted from fits using the gamma function equation.(130)

C.2.4: Ordered Unfolding Events

Fibrin γ module unfolding is additionally complex because some domains are likely protected from unfolding due to force applied through the 'A-a' knob-hole interaction (reference toy model section). By treating each unfolding domain as a two state unfolding event but requiring the domains to unfold in a specific order,

a Monte Carlo simulation of ordered domain unfolding was constructed similar to unfolding simulations described above. All simulations were preformed with the same equilibrium unfolding rate and distance to transition state (0.1 s^{-1} and 0.1 nm).

The result of sequentially unfolding domains is a deviation from single exponential protein unfolding (Figure C.9A). The more force-sheltered domains in the protein sequentially unfolded, the larger the deviation from the expected single exponential behavior (Figure C.9B). The deviations produced in Monte Carlo simulations differ from fibrin force-clamp experiments (Figure 2.26) with lower probability of unfolding observed at short timescales and larger probability of unfolding at longer time scales compared to single exponential fit. ***This suggest that despite the presence of force protected domains in fibrin's γ module postulated by constant-velocity experiments, these are not the dominant factor contributing to deviations from simple two-state, single-exponential unfolding.***

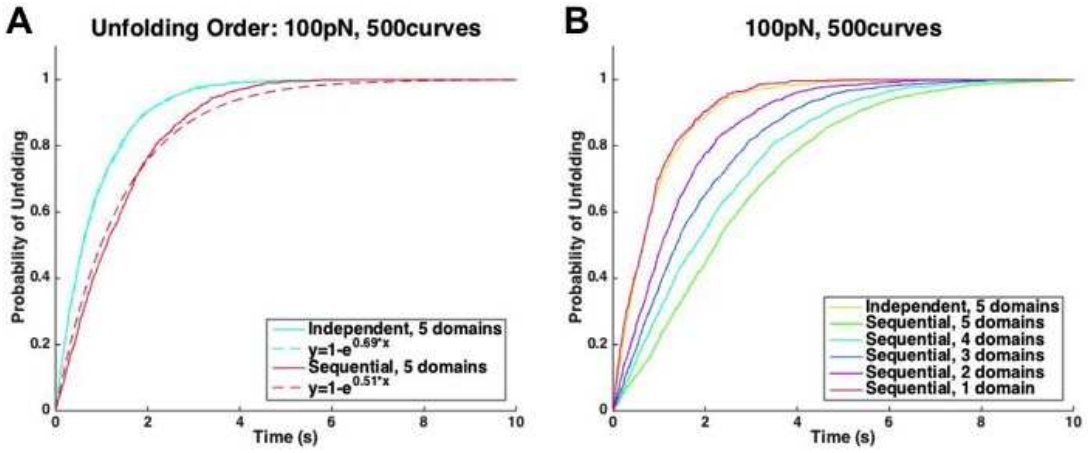

Figure C.9: Monte Carlo Simulation of Multi-Domain Protein Unfolding. (A) These plots show the probability of unfolding at 100 pN clamping force displayed as a normalized ensemble average of 500 curves for a protein consisting of five 1 nm domains occurring either independently, as previously described, or in a sequential order due to force protected domains. (B) The effect of the number of sequential domains on probability of unfolding curve. A single exponential fit to each data set is shown with a dashed line.

Section C.3: Conclusions: Glassy Dynamics to Describe Fibrin γ Module Unfolding

Monte Carlo simulations allowed us to test a range of possible sources for fibrin gamma module deviation from the simple two-state, single exponential behavior used to describe a smooth energy landscape for protein unfolding. Parameters, such as the number of domains and the domain length, did not effect single exponential unfolding of our simulated protein; however, both changes in domain kinetics and force-protected domains produced deviations in the probability of unfolding from the single exponential behavior.

The deviations from single-exponential unfolding observed due to domain kinetics more closely resembled experimental results of AFM force-clamp experiments on fibrin than the order of domain unfolding. ***This suggests that constant-force unfolding of fibrin does not produce the same results of force-sheltered domains as observed in constant-velocity experiments.*** Instead domains are allowed to unfold in a natural sense in time without increasing force application to the domains, thus giving results more sensitive to the kinetic parameters of the individual domains. Multiple exponentials could be used to determine kinetic parameters for individual domains with in the γ module; however, with multiple domains and thus multiple exponents, exponential fits become more sensitive to input parameters and less reliable for determining kinetic parameters for each domain. Therefore, a model that takes into account both the presence of intermediate states and varied domain kinetics is necessary to interpret the results of AFM force-clamp experiments of fibrin.

Another method of analyzing molecules with complex unfolding pathways is to determine average kinetic parameters of fibrin's γ module by using a glassy dynamics model of protein unfolding. A complex or "rugged" energy landscape is often proposed as a model for protein unfolding under equilibrium conditions;(7; 268; 269; 270) however under non-equilibrium conditions, such as in force-clamp experiments, protein unfolding is often assumed to have a smooth energy landscape.(271) First proposed by Frauenfelder, the glassy model of multiple traps in the native protein landscape is described by a stretched exponential function:(129; 272)

$$P_{UF}(t) = 1 - e^{-(\alpha t)^{\beta}} \tag{C.5}$$

where α is the unfolding rate at for the probability of unfolding curve and β is the stretching exponent. Ideally to be used to describe AFM force-clamp unfolding of fibrin's γ module, this function would need to encompass deviations due to kinetic parameters and ordered unfolding.

To test this model for protein unfolding on a protein with domains of different kinetic parameters, domain unfolding was simulated for a range of forces, normalized ensemble averages for each force were fit with the stretched exponential function then the exponent as a function of force was fit using Bell's model to extract the force-free kinetic parameters. The results for different unfolding rates and distances to transition state are shown in Figure C.10 and Figure C.11, respectively. From these simulations, the ensemble average kinetic parameters determined from the stretched exponential fits were between the kinetic parameters of each domain with k_0 skewed toward the slower unfolding rate and Δx about average. A stretched exponential satisfactorily describes a range of k_0 and Δx when one parameter is held constant (Figure C.12); however, when both parameters are adjusted deviations from this model become apparent (Figure C.13).

To test this model for protein unfolding on a protein with domains of different kinetic parameters, domain

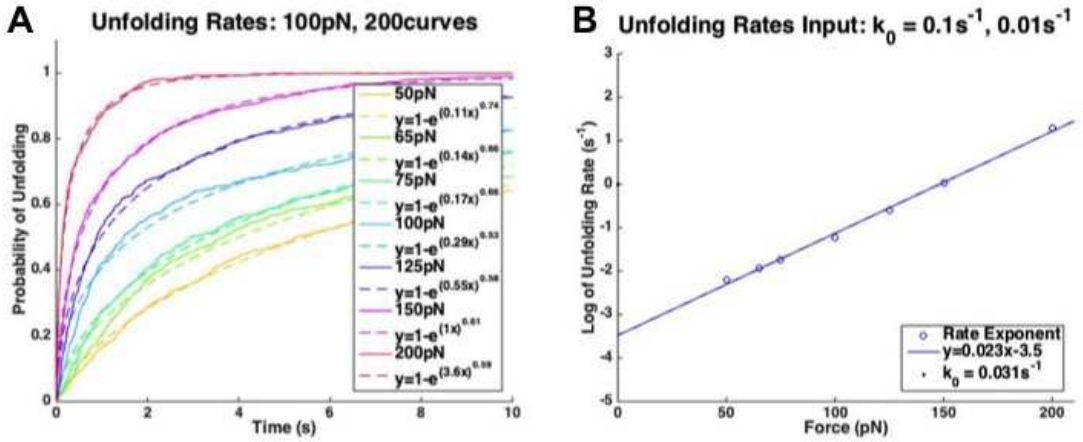

Figure C.10: Stretched Exponential on Different Unfolding Rate for Multi-Domain Protein. (A) The probability of unfolding a protein consisting of two 1 nm domains with different k_0 of 0.1 s^{-1} and 0.01 s^{-1} at forces ranging from 50-200 pN calculated from a normalized ensemble average of Monte Carlo results with stretched exponential fit. (B) Exponential values plotted as a function clamping force, fit with Bell's model to determine k_0 (last value displayed in legend).

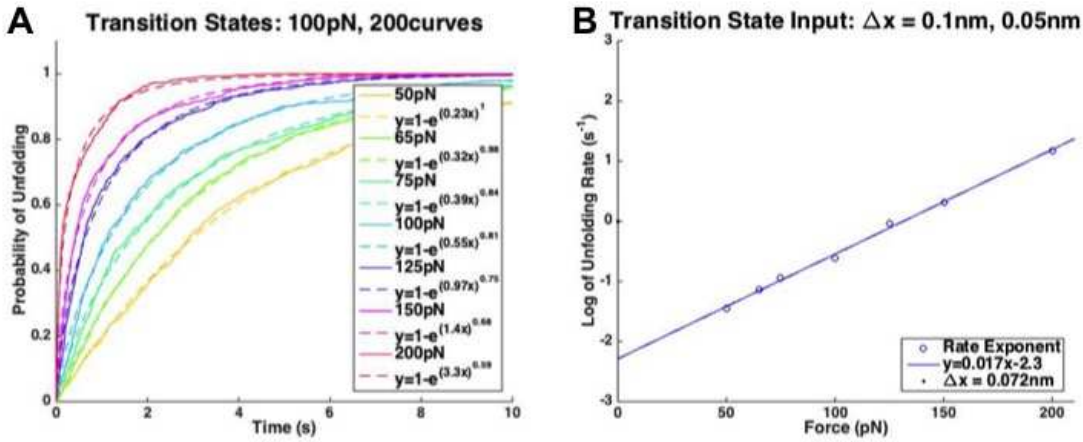

Figure C.11: Stretched Exponential on Different Unfolding Rate for Multi-Domain Protein. (A) The probability of unfolding a protein consisting of two 1 nm domains with different k_0 of 0.1 s^{-1} and 0.01 s^{-1} at forces ranging from 50-200 pN calculated from a normalized ensemble average of Monte Carlo results with stretched exponential fit. (B) Exponential values plotted as a function clamping force, fit with Bell's model to determine Δx (last value displayed in legend).

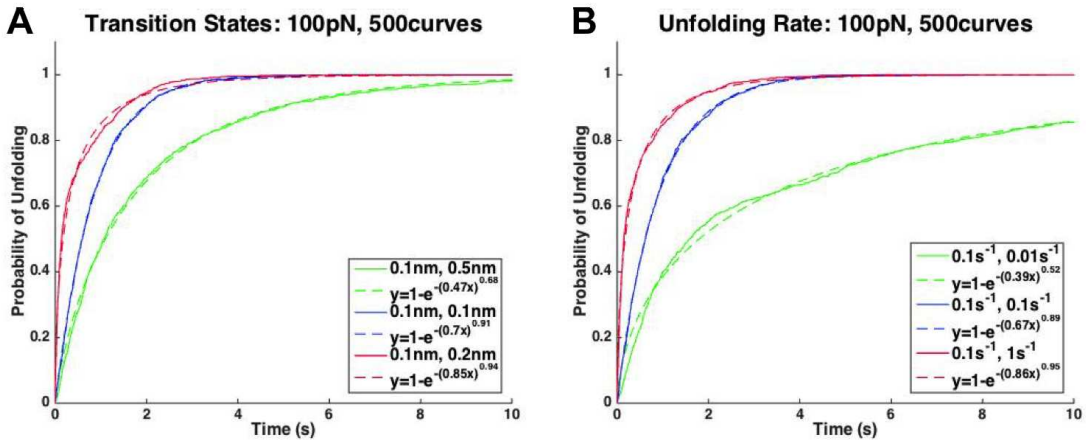

Figure C.12: Stretched Exponential on Different Transition State Distances for Multi-Domain Protein. The probability of unfolding a protein consisting of two 1 nm domains with (A) different Δx of 0.1 nm and 0.05 nm and (B) different k_0 (0.1 s^{-1} and 0.01 s^{-1}) at forces ranging from 50-200 pN calculated from a normalized ensemble average of Monte Carlo results with stretched exponential fit..

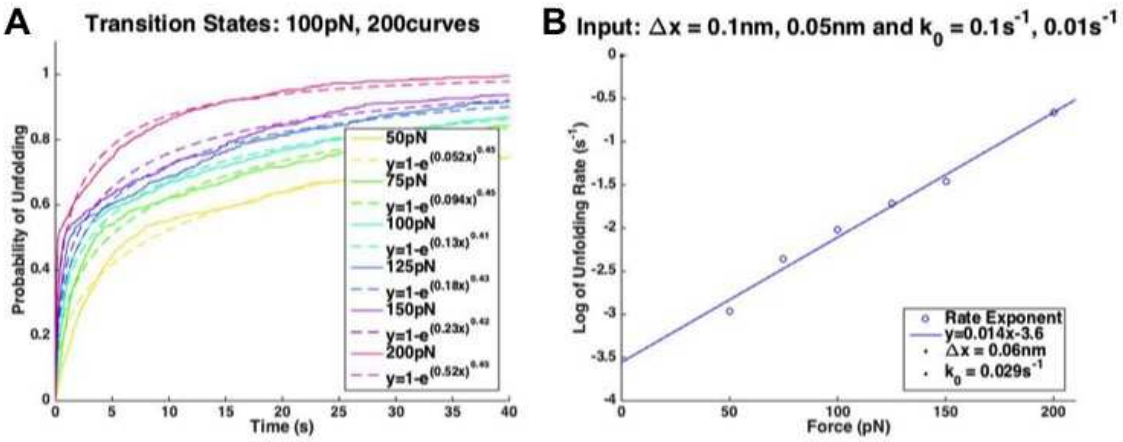

Figure C.13: Stretched Exponential Fit to a Multi-Domain Protein with Domains of Different k_0 and Δx. (A) The probability of unfolding a protein consisting of two 1 nm domains with different k_0 (0.1 s^{-1} and 0.01 s^{-1}) and Δx (0.1 nm and 0.05 nm) at forces ranging from 50-200 pN calculated from a normalized ensemble average of Monte Carlo results with a stretched exponential fit. (B) Exponential values plotted as a function clamping force, fit with Bell's model to determine the k_0 and Δx (last values displayed in legend).

unfolding was simulated for a range of forces, normalized ensemble averages for each force were fit with the stretched exponential function then the exponent as a function of force was fit using Bell's model to extract the force-free kinetic parameters. This is only a reasonable approximation if you are assuming that a large number of small and complex wells can be treated as a single well - in a way smoothing the curve. The results for stretched unfolding rates was an exponential dependence on force as expected with the Bell model. Additionally the resulting k_0 and Δx values fall between the input parameters, as expected skewed toward the slower unfolding rate. ***Therefore, using a stretched exponential to describe the complex unfolding behavior observed in fibrin and applying the Bell model to extract kinetic parameters works as an acceptable approximation, skewed toward the slower unfolding rate and smaller distance to transition state.***

Ideally, what could be done is the Monte Carlo simulations could be used to iteratively calculate and fit to get parameters to determine the kinetic parameters for each domain. This however, would require further work to understand how to extract these parameters from simulations. From these simulations I was able to determine that the presence of force protected domains in fibrin's γ module postulated by constant-velocity experiments are not the dominant factor contributing to deviations from simple two-state, single-exponential unfolding. The deviations are more likely produced by a different kinetic parameters associated with unfolding domains. These can be approximated by a single 'rough' unfolding domain by using stretched exponentials to determine force dependence of fibrin domain unfolding.

APPENDIX D: Hertz Analysis Package

Mechanical properties, especially stiffness, of individual cells are critical for many biological processes including cell growth, motility, division, and differentiation.(273) Additionally, changes in cell mechanical properties are associated with disease conditions, such as cancer.(159; 143; 175) The Atomic Force Microscope (AFM) is one of several techniques that provides a way to reliably measure the stiffness of living cells. The use of the AFM for cell mechanics measurements is the focus of Chapter 3, which contains several specific cell mechanics experiments. The basic principle for these experiments is an AFM tip is used to indent a cell and measure the applied force from the bending of the AFM cantilever. Once the data is acquired, the Hertz model is fit to a force-indentation curve to determine a quantitative measure of material stiffness.

Over the course of these experiments, it became evident that an analysis pipeline was required to accurately and efficiently extract stiffness measurements and make comparisons in these large data sets. Therefore, I developed custom MATLAB data analysis routine specifically tailored to cell mechanics experiments. Briefly, the program identifies the contact point coordinates using a golden-section search in which a linear fit of the data to the left of contact point and a Hertz model fit to the data to the right up to a user defined maximum indent. The point which attains the minimum total fitting error is selected as the contact point. Least squares fitting is applied to force-indentation data in the post-contact region of the force curve to the Hertz model to extract the Young's modulus of the cell. A series graphical user interfaces (GUIs) were used to improve flexibility and user friendliness when working with large data sets.

What follows is a users guide for our custom MATLAB GUI based analysis package complete with screen captures and discussions of behind-the-scenes calculations. The code can be acquired from the University of North Carolina at Chapel Hill Center for Computer Integrated Systems for Microscopy and Manipulation.

Section D.1: Hertz Analysis Pipeline

The overarching procedure for data collection and analysis is as follows.

1. Acquire data with AFM (Igor). The data will be saved as single force curves (ibw) or force maps (ARDF).

2. Open MATLAB and navigate such that the current folder is the 'Hertz Analysis' folder. This package was written to run on MATLAB 2013a. If you are running a version of MATLAB earlier than MATLAB 2013a, there may be standard MATLAB functions that are not included in your library. For example, strsplit is not a standard function in MATLAB 2010 – this function has been included in the standard Hertz Analysis Package. Additional functions identified as missing will be added to the standard

package.

3. Use the Hertz Analysis GUI to determine the elastic modulus of each force curve, discussed in more detail in Section D.2.

   We recommend grouping IGOR force curves into different folders by individual cell and experimental condition on that cell (e.g., on nucleus, off nucleus, velocity, force trigger), and grouping folders by cell type and day of experiment. This grouping is not necessary for running the analysis software; however it is helpful for organization and later comparative analysis.

   The result of running the Hertz Analysis GUI on the ibw files is a single MATLAB file containing the elastic moduli of all the force curves in the folder, as well as the goodness of fit and all the force-indentation data. Additionally, a figure of the elastic modulus for each force curve is saved. Hertz analysis is repeated for each folder.

4. Then all of the single MATLAB (Fit_Results) files of the same type need to be collected into the same folder. For me this usually means collecting each of the Fit_Results (containing the elastic moduli of all the force curves on a single cell) into a folder, so that all the SKOV cell data taken over the nucleus is in the same folder – ten cells means ten files.

5. Then the results of Hertz Analysis GUI can be combined (over many days, types of cells, regions, etc.) into a single MATLAB file using the load_HertzModuli function or the Compare Data GUI. This allows for a single file to be saved and various comparisons to be made.

6. Comparisons of the elastic modulus between different sample types and days can be checked using the Compare Data GUI, discussed in more detail in Section D.4. This GUI allows for statistical comparisons and creation of some of the most revealing plots about trends in data.

Section D.2: Hertz Analysis GUI

This GUI allows the user to load in raw AFM (z sensor and deflection) data in the form of ibw files and fit the data with the appropriate hertz model to get the elastic modulus of the force curve.

To open the Hertz Analysis GUI, type 'HertzAnalysis_GUI' into the MATLAB command line. The GUI can be seen in Figure D.1A.

1. The first button on the GUI, 'File Path:', allows the user to load the file containing all ibw files to be analyzed. This code has also been modified to take in ARDF files; however, this capability is MATLAB version dependent.

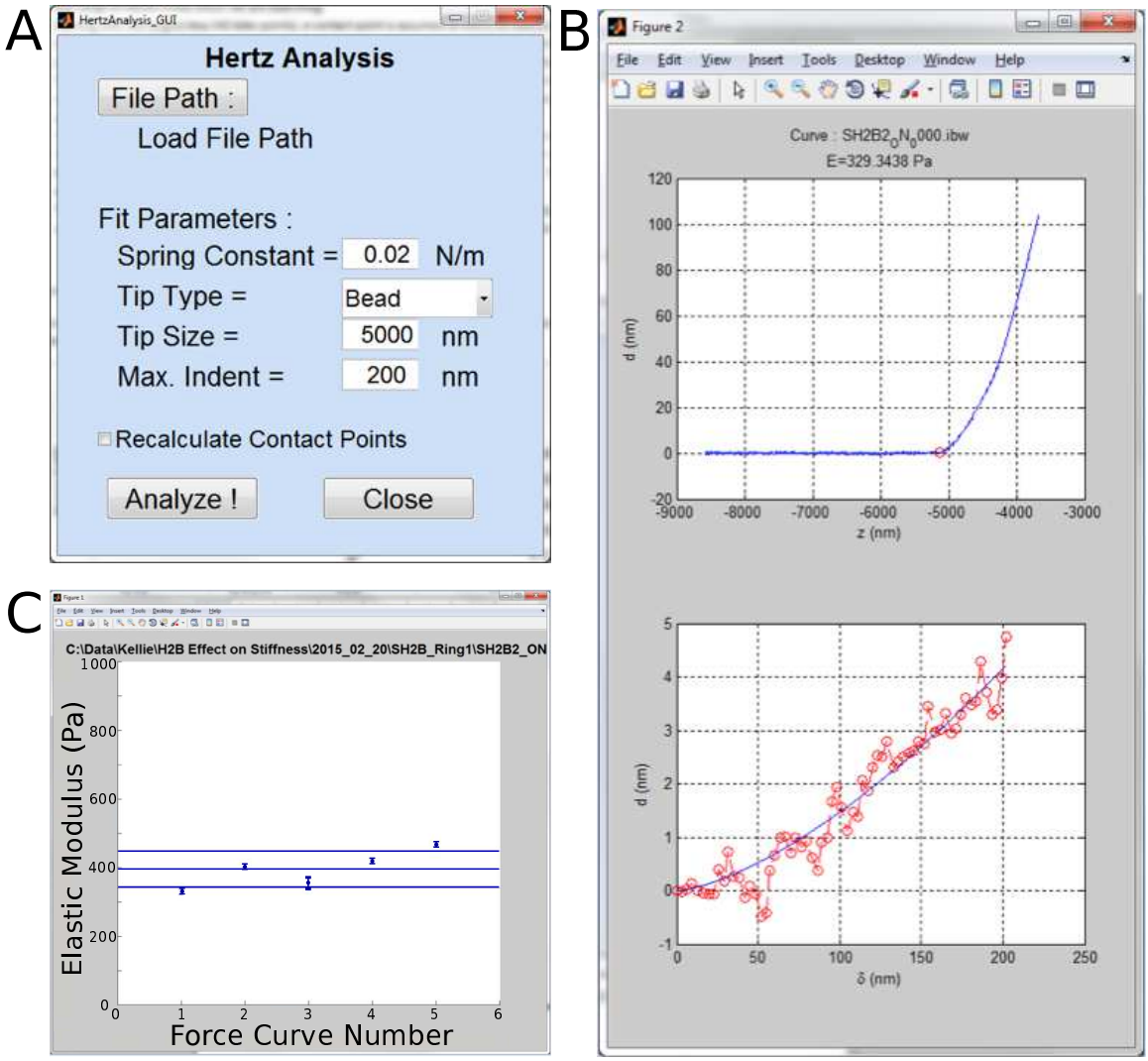

Figure D.1: Hertz Analysis GUI and review panels. (A) Screen capture of Hertz Analysis GUI. (B) Review plot for Hertz model fit to data, where the top plot shows the contact point and the bottom plot shows the hertz model fit to the specified indentation depth. (C) Plot of elastic modulus with goodness-of-fit error bars and average/standard deviation lies for the data set.

2. 'Load File Path' will change to reflect the folder from which you will be analyzing data. If you are going to be changing file paths frequently, it maybe useful to change opening file location – simply modify line 177 of HertzAnalysis_GUI function.

3. There are a variety of fit parameters that can be adjusted for the specific experiment. Briefly, they are the spring constant of the cantilever in N/m, the tip type – either cone or bead, the tip size – the half angle in degrees for cone tip or the diameter of a bead tip in nm, and the maximum indent depth that will be fit when determining the elastic modulus.

4. Pressing 'Analyze!' will cycle through each of the curves briefly showing a plot of deflection-zPiezo with contact point and best fit hertz curve (Figure D.1B). After all the force curves are shown, a plot of elastic modulus with goodness of fit error bar for each curve is shown (Figure D.1C). Additionally on the plot are the average and standard deviation of the set. Then the analyzed data and figure are saved to the same folder from which the data was loaded. More information of fitting protocol in Section D.3.

5. Selecting the 'Recalculate Contact Points' check box will allow the user to select an estimate for the contact point of poorly fit curves (you'll know them when you see them). There are prompts for the entry of '1' for yes or '0' for no by the user to recalculate curve or mark the curve as a poor fit as the program cycles through curves.

From this point different data sets can be compared using the Compare EMods GUI.

Section D.3: Fitting Hertz Model

Behind the Hertz Analysis GUI, the AFM force-indentation data is fit with a Hertz model in a method similar to that reported in JOVE by Thomas, et al.(168) Here is a quick description of the major functions involved in fitting the force-indentation data with the hertz model.

One of the primary parameters leading to uncertainty and poor estimation of the elastic modulus of a material is determination of the contact point. Our contact point is determined by a function, contactpoint4, which acomplishes the following:

1. The deflection data is smoothed using an moving average filter.

2. An initial guess for the contact point is the halfway point.

3. A "golden-section search" is performed, in which the contact point can be found by successively narrowing the range of values inside which we are searching. An illustration of this method can be seen

in Figure D.2.

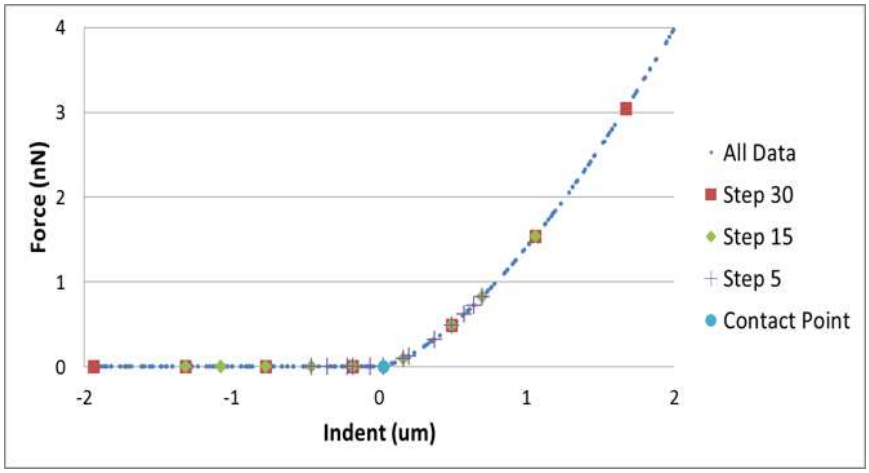

Figure D.2: Illustration of the golden-section search used to determine contact point when fitting force-indentation data with the Hertz model.

(a) Starting with the largest step (40 data points), a contact point is assumed at every 40 data points for the limits of the force curve (first data point, last data point). For each of these contact points, the hertz model is fit to all data to the right of the contact point and for Model=2, a line is fit to the data to the left of the contact point. The error in these fits is assigned to the estimated contact point. The point with the least error is the new center for fitting data, so the bounds are adjusted; the lower limit is set to twice the step size below the chosen point and the upper limit is set to twice the step size above the chosen point.

(b) Then the step size is reduced to the next smaller step size (20 data points), and a contact point is assumed at every 20 data points for the limits defined by the previous search. All data in the force curve is fit for each of these assumed contact points and the best contact point is chosen by the least error in fits. The limits are adjusted and the process repeats.

(c) This process is repeated until the step size is a single data point. The result of this final search is the index value for best guess for the contact point of the force curve. The index is output from this function.

During step 3, the function 'afmcntp' is used to calculate the elastic modulus for data with a given contact point. This function performs a least squares fit to the force-indentation curve with specified contact point and indentation value determine the elastic modulus of the force-indentation curve from the Hertz model:

$$F = \frac{4}{3}\frac{E\sqrt{R}}{(1-\nu^2)}\delta^{\frac{3}{2}}$$

where F is force, δ is indentation, E is elastic modulus, R is the tip radius, and ν is the Poisson's ratio.

Section D.4: Compare EMods GUI

This GUI allows the user to compare elastic moduli and combine data sets previously analyzed with Hertz Analysis GUI. This is useful for determining changes occurring between different days of experiments or cell lines.

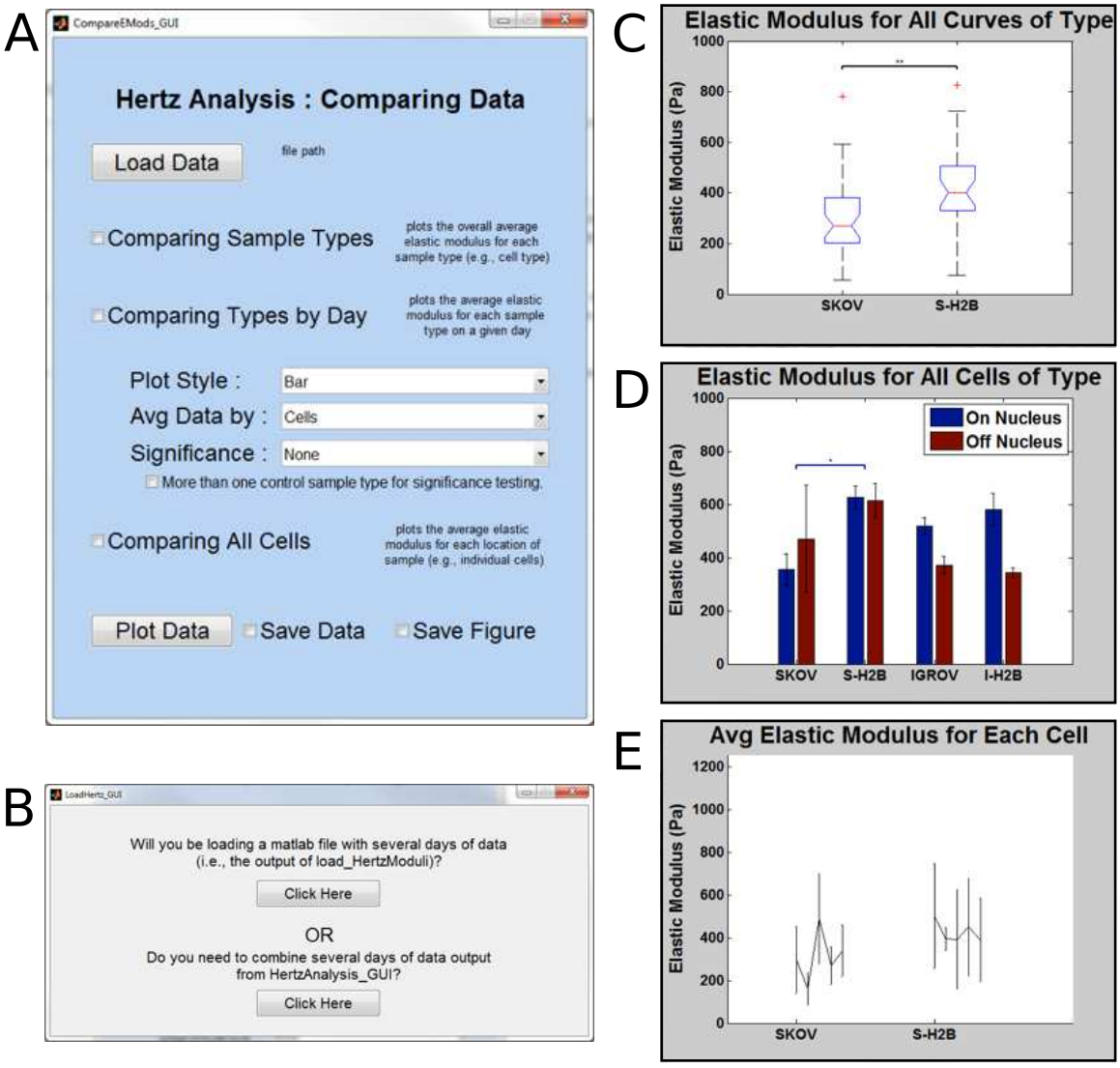

Figure D.3: Compare EMods GUI and resulting figures. (A) Screen capture of Compare EMods GUI. (B) Screen capture of window guiding user to load files. (C) Box plot resulting from compare sample types with ttest for significance. (D) Bar plot resulting from comparing types by day. For this plot, the 'day' is actually 'On Nucleus' and 'Off Nucleus'. (E) Plot resulting from comparing all cells with average elastic modulus and standard deviation of each cell.

To open the Compare Elastic Modulus GUI (Figure D.3A), type 'CompareEMods_GUI' into the MATLAB command line.

1. The 'Load Data' button will open an additional GUI that allows the user to choose between (1) loading a MATLAB file of previously combined data output from load_HertzModuli or (2) being walked through combining data of several samples (cells), types, and days (Figure D.3B.

2. Selecting the second option, runs the load_HertzModuli function which prompts the user for a series of inputs at the command window. Alternatively, the user can type 'load_HertzModuli()' into the command line to execute only the combination of data.

3. There are three types of plots that can be created with the Compare EMods GUI. The user simply need select the box next to the figure desired before selecting 'Plot Data'.

   (a) Comparing Sample Types: This compares the average elastic modulus for a single type of sample over multiple days. Additional selections may be made for the plot style, average parameter and significance. Shown Figure D.3C is a set of sample data in the form of a box plot with ttest performed.

   (b) Comparing Sample Types by Day: This shows the averages of each elastic modulus for each day and allows comparison with in days. Because there is only one day of data in the sample set, Figure D.3D shows a different sample set where 'On Nucleus' and 'Off Nucleus' measurements are treated as separate days.

      i. For both the 'Comparing Sample Types' and 'Comparing Sample Types by Day', plots can be displayed as bar, box or scatter plots with error bars.

      ii. There are two ways that the averages can be calculated: (1) These averages can be calculated by taking the average of the average elastic modulus of each cell. The error bars on these plots show the standard error of the data. (2) These averages can be calculated by averaging all the force curves. The error bars on these plots show the standard deviation of the data.

      iii. There is the option of calculating significance. Currently the only significance test employed is the t-test but additional statistic tests could be added. Selecting a significance test will prompt the user for input in the command window as to which cell type (or types if the 'more than one control sample' box is checked) is the control cell for analysis.

   (c) Comparing all Cells: This shows the average elastic modulus and standard deviation on each sample - or cell in my case -from averaging the elastic modulus of each force curve (Figure D.3E). This can be kind of a crazy plot to look at because its many colors and a lot of information all

at once, but is useful for identifying outliers and checking out what could be going on behind the scenes.

4. Pressing 'Plot Data' will plot the figure(s) of the selected checkboxes. If Save Data or Save Figure is selected, then the user will be prompted for save location and name.

The code can be acquired from the University of North Carolina at Chapel Hill Center for Computer Integrated Systems for Microscopy and Manipulation.

APPENDIX E: Calibration of Gradient Stiffness Gels for Durotaxis Studies

Many cellular functions, such as cell proliferation, migration, spreading, morphology, and stem cell differentiation, are modulated by external cues provided by the cell's environment.(274; 275; 276) Chemical and stiffness gradients in the microenvironment, e.g., extracellular matrix, contribute to important cell processes that determine cell function and fate.(277; 273) There are a variety of 'taxes' associated with the movement of cells in response to an external stimulus (Figure E.1). Chemotaxis is the movement of cells in response to a chemical stimulus. Haptotaxis is a subset of chemotaxis in which the chemical attractant is bound to substrate, e.g, a protein density gradient in the extracellular matrix. Mechanotaxis is the movement of cells in response to a mechanical stimulus, e.g. fluid flow. Durotaxis is a subset of mechanotaxis that refers specifically cell response to substrate rigidity, e.g. a stiffness gradient in the extracellular matrix.

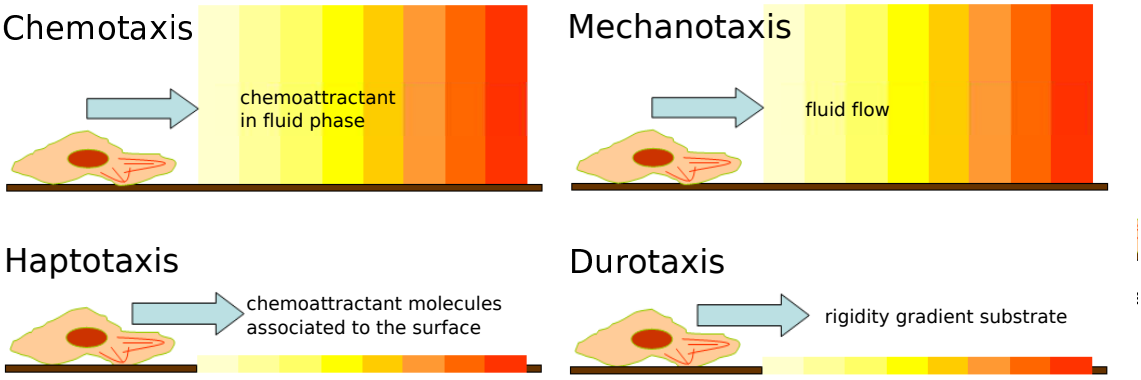

Figure E.1: Types of tactic behavior. Figure modified from Kohidai, L.(20)

Sreeja Asokan is interested in separating the role of haptotaxic, and chemotaxic cell behavior especially in reference to the Myosin II signaling pathway. To accomplish this goal, she makes use of protein and stiffness gradients in a microfluidic environment. In order to understand the durotaxis component, a precise calibration of the gradient stiffness substrates is required.

Hydrogels with stiffness gradients for studying cell mechanics are typically made by either changing the crosslinker ratio(21) or exposing the crosslinker to an irradiation gradient(22) (Figure E.2). The gels for which this protocol was designed were made with the latter method using a gradient opacity mask to produce gels with gradient stiffness in the range of 1-100 kPa.

Polyacrylamide (PA) gels were made by Sreeja in James Bear's lab then brought to our lab for measurement. We used a TR400PSA pyramid cantilever with Norland attached 5 μm bead as described elsewhere (reference bead attachment protocol). The PA sample was loaded on to the AFM scan stage such that the gradient is along the x-axis and water was added on to the sample. All measurements were performed in

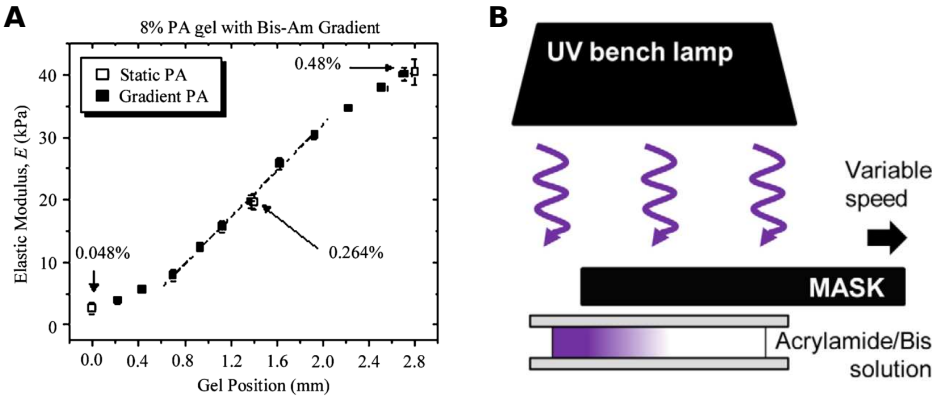

Figure E.2: Methods for making gradient stiffness gels. (A) Elastic modulus measurements on a PA gel made with Bis-Am gradient. Modified from Engler et al.(21) (B) Cartoon illustration of PA gel with moving mask used to create different cosslinking times and produce gradient stiffness. Modified from Sunyer et al.(22)

liquid to prevent dehydration of gel. Several force curves were performed before characterizing the substrate in order to determine ideal force curve parameters. For the reported measurements, a force trigger of 2 nN and velocity of 5 μm/s were used.

Measurements were taken at 0.5 mm intervals along the gradient (x-direction) to get a good representation of the range and rate of the stiffness change. These intervals are larger than the motion accommodated with the piezo controlled scanning stage. So the x-axis motion was accomplished with the manual adjustment knobs.

To collect a representative measure of stiffness for the sample, several force curves were acquired in the y-direction as well. The y-axis motion was in the range of scan stage piezo motion so the Asylum Macro Builder was used for efficiency and consistency. The MacroBuilder interface allows the AFM user to set up and run a sequence of measurements without having to perform complex IGOR programming.(23) A sample MacroBuilder program and the standard set of functions can be seen in Figure E.3. Briefly, the MacroBuilder interface should first set the Y-parameter to zero. Then open a for-loop to run through 3 to 5 iterations corresponding to different y-positions (these correspond to asterisks on FIGURE E.5A) in which the program acquires several single force curves and increments the y-position by 20 μm. If you are unsure which direction in the IGOR interface (x-direction or y-direction) corresponds to motion of your sample on the scan stage, find a mark on your sample surface and make large changes to the x- and y-positions on the Main Panel of the Force Panel. The key 'macro' functions and their order can be seen in Figure E.4.

Using MacroBuilder and the manual stage adjustment all force curves are collected by manually adjusting the y-position knob, running the MacroBuilder protocol, and then repeating for the desired length of the gradient. Once all force curves are collected, they are analyzed with custom MATLAB code discussed in

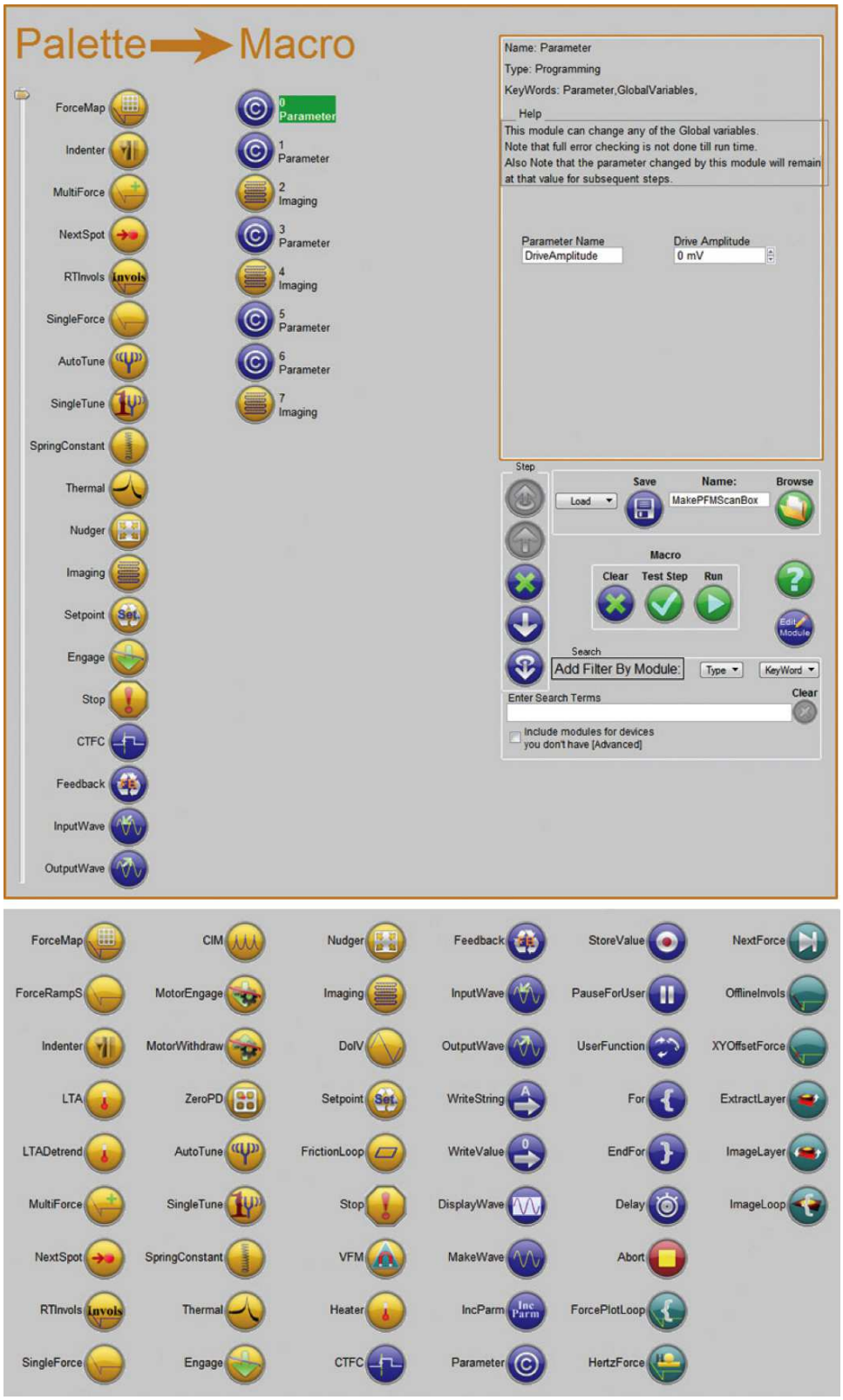

Figure E.3: (Top) Sample of MacroBuilder interface with program for automated piezo-response force microscopy. (Bottom) Standard MacroBuilder "Modules" available to users. Images from Asylum MacroBuilder data sheet.(23)

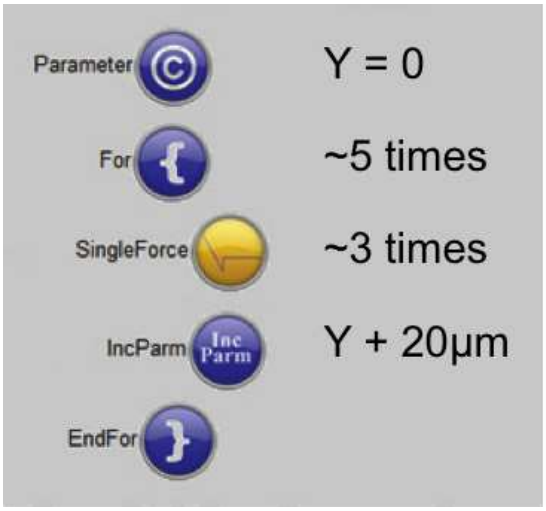

Figure E.4: Basic MacroBuilder scheme for key 'macro' functions involved in gradient measurement described.

detail elsewhere (Appendix D). Briefly, the code fits each curve with the Hertz model to extract the elastic modulus, then groups the curves so that there are a collection of moduli at each y-position, and returns the average elastic modulus for each location (Figure E.5).

The result for one such sample, shown in Figure E.5C, was a stiffness gradient of ~4 kPa/mm, ranging from softest at 10 kPa to control region receiving full intensity light at 85 kPa. This method can be easily applied to a variety of sample types with different gradients by adjusting in the AFM cantilever, the x- and y-increments, or force curve parameters.

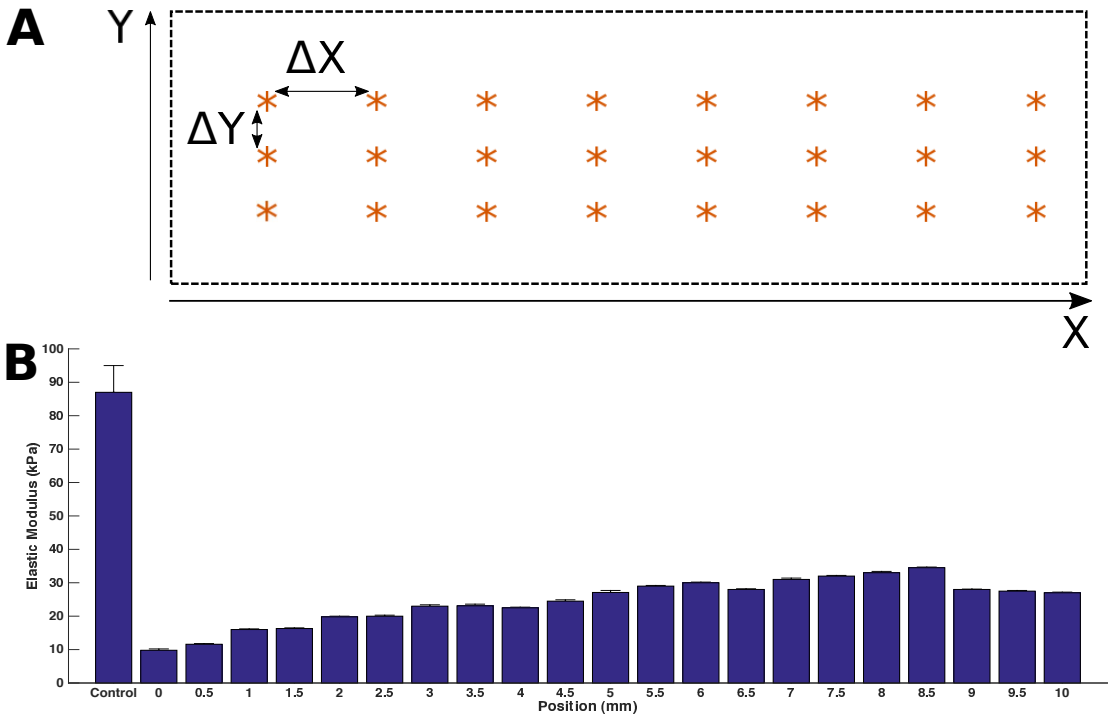

Figure E.5: AFM calibration of gradient stiffness PA gel. (A) Schematic of AFM measurement locations (asterisks) in gradient region of PA gel (dashed outline). (B) Results of the elastic modulus measurements on gradient stiffness PA gel.

APPENDIX F: Cytoplast Statistics on Stiffness and Force Response

In Section 3.4, AFM measurements were performed to measure the mechanical properties properties of cytoplasts in order to determine if aberrant mechanotransduction behaviors were the result of changes in intrinsic mechanical properties of the cell due to removal of the nucleus. To investigate this, stiffness and force response measurements were performed for the center of cytoplasts, intact fibroblasts nuclear region and intact fibroblasts cytosol region. Because these experiments were performed over the course of several days and sample preparations, comparisons were made to confirm the differences observed were characteristic of the cell types.

Section F.1: Elastic Modulus

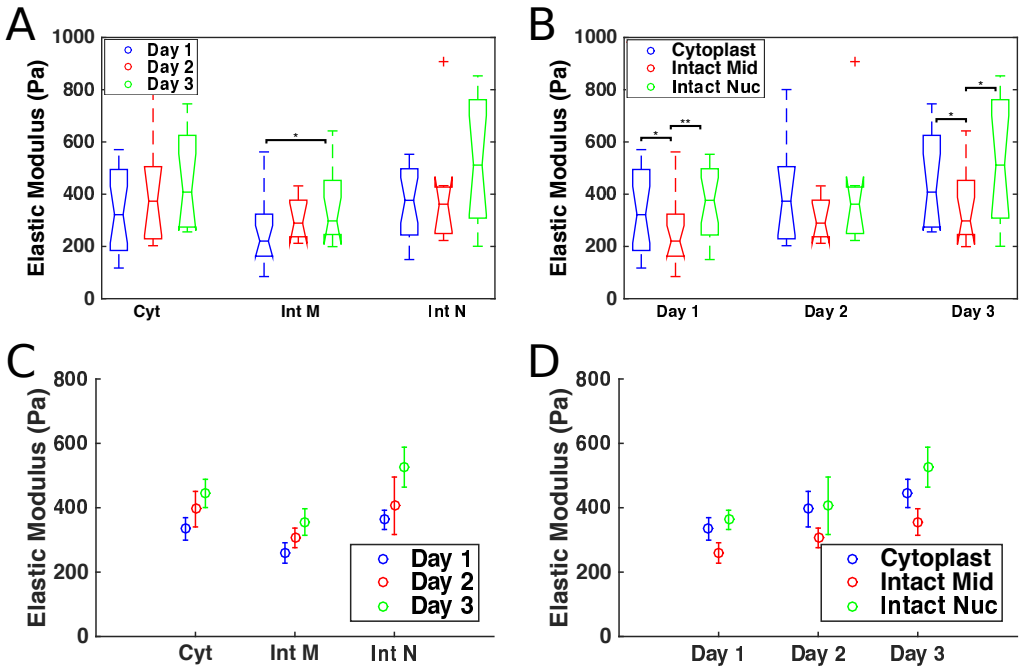

Figure F.1: Distributions of elastic modulus grouped by cell type and day, (A) showing significant difference between the same cell type/location on different days and (B) between different cell types/locations on the same day. Average elastic modulus and standard error mean grouped by cell type and day, illustrating trends in elastic modulus between different (C) days and (D) cell types/locations.

Comparisons were made to confirm the differences observed were characteristic of the cell types, and not due to variations between sample preparations on different experiment days, cloning rings or outlier cells. We compared data sets for different experiment days; these plots of distributions and averages are shown in Figure F.1. The results show the distribution of elastic modulus for each cell type are consistent over multiple days (i.e., no significant difference between days for the same cell type/location) with the

exception of the midzone of intact fibroblasts, which differs between Days 1 and 3 (Figure F.1A). However, on Days 1 and 3, when the midzone values differed significantly, the trend in elastic modulus between the cells was the same and significant (Figure F.1B). On both Days 1 and 3, the midzone was significantly softer than the cytoplasts and the nuclei of the fibroblasts, reflective of the trend observed in the entire data set. The trend of stiffer elastic modulus measured on each day was negligible to the point of agreement within standard deviations even for the measurement of the midzone region of intact fibroblasts (Figure F.1C). The difference in absolute stiffness for different days while maintaining the same trend in stiffness between cell types/location indicated a systematic error in the determination of the elastic modulus. This could likely be attributed to slight overmeasurement of the stiffness of the cantilever resulting in stiffer elastic modulus values than were actually true, or to defects in the AFM tip which could produce an error determination of the elastic modulus from Hertz fitting. Since the overall trend was unaffected, these issues are worth noting but do not effect the overall results of the experiment. On Day 2, no significant difference was measured in the distributions of elastic modulus(Figure F.1B); however, both the medians (observed as the center line at the waist of the box plots) and the average values of the cell types/location (Figure F.1D) follow the same trend of the midzone being softer, despite no significance measured. The lack of significance measured was likely the result of the fewer number of cells measured on Day 2 relative to Days 1 and 3, as evidenced by the plots of average elastic modulus for each cell in Figure F.2. Further analysis of individual cell behavior shows a large variability in elastic modulus from cell to cell (Figure F.2A, C, E). This is unsurprising, as heterogeneity among cells of the same type is expected, thus justifying the use of large combined data sets as in Figure 3.15. Less variation was observed when taking into account the bulk behavior of a cell type/location for many cells (Figure F.2B, D, F). For this reason, measurements of the elastic modulus of each cell type/location could be directly compared across days.

Section F.2: Force Response

To investigate the stiffening response of cytoplasts in response to an externally applied force, for each cell type/location, up to 10 force curves were acquired and analyzed to measure stiffness. In order to investigate the force response, I normalized the elastic modulus of each force curve in a series to the elastic modulus of the first force curve. An increase in stiffness is greater than one and a decrease in stiffness is less than one. The average of this analysis over all cells is shown in Figure F.3A. There was a slight increase in the average stiffness over the course of subsequent force curves for all cell types/locations; however, most subsequent force curves were within a standard deviation of a null stiffening response (i.e., 1). On Day 3, force parameters were adjusted to mimic magnetic bead pulling experiments with a force application

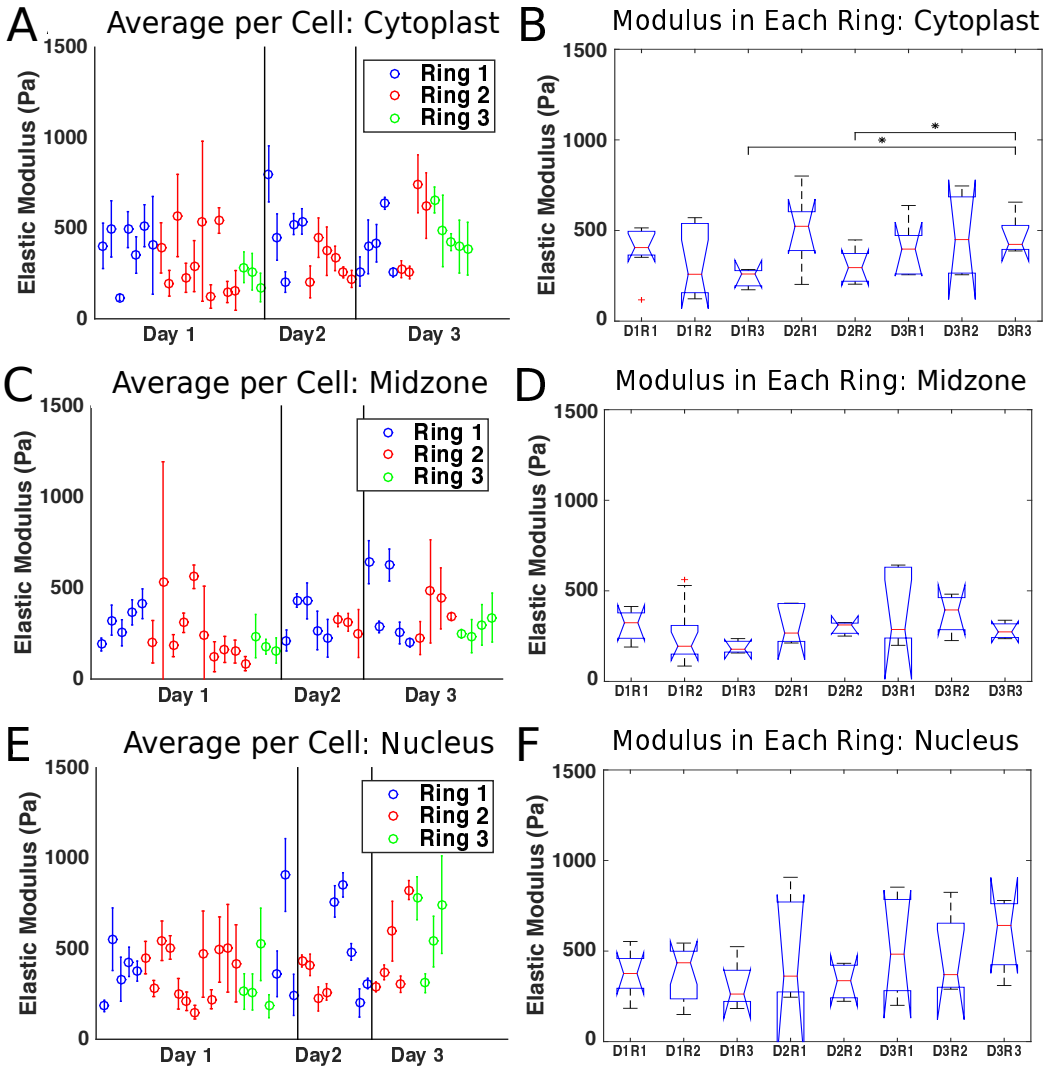

Figure F.2: Distributions in each cloning ring and on each cell. (Left column) Average elastic modulus for each cell, grouped by day and color-coded by cloning ring, for all the (A) cytoplasts, (C) intact midzones, and (E) intact nuclei. (Right column) Distribution of elastic modulus in each cloning ring for (B) cytoplasts, (D) intact midzones, and (F) intact nuclei. Box plot with Tukey whiskers and asterisks (*) represent a significance value of $P<0.05$ as determined by the Wilcoxon rank sum test. The cloning rings are given names such as DXRY, where X and Y refer to the day and ring number, respectively. (i.e. D1R2 is the second ring on the first Day).

dwell time of 4 seconds and a 6 second pause between subsequent force curves (similar to the on-time for the magnetic bead experiments). No force response is seen for cytoplasts or fibroblasts on-nucleus (Figure F.3B); however, the midzone fibroblast measurements show an increase in their stiffness with multiple force applications.

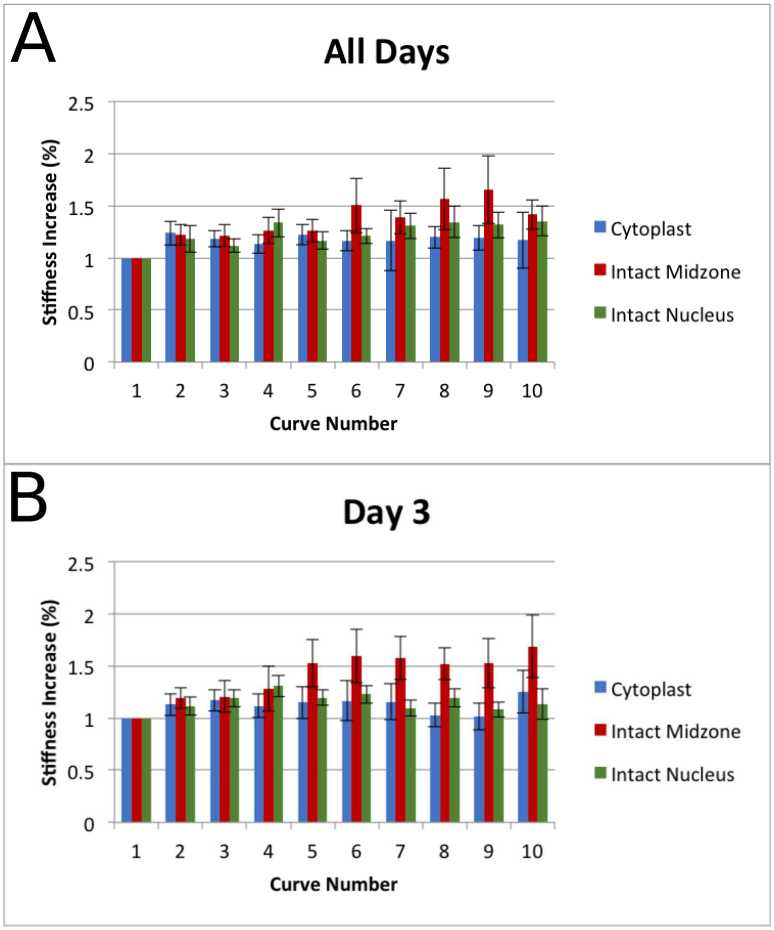

Figure F.3: Average stiffening of cells reported as values normalized to the first force curve for (A) all days of experiments and for (B) Day 3, in which dwell parameters were set to mimic magnetic bead pulling experiments (i.e., AFM cantilever held at constant force for a 4 second dwell in contact with the cell and 6 second dwell away from the cell).

APPENDIX G: Measuring the Gaussian Beam Width

Section G.1: Gaussian Beams

The output of most lasers, including the laser in our system, is a Gaussian beam to allow for focus to its most concentrated spot. When a laser beam passes through lenses in an optics system a different Gaussian beam is produced.

A Gaussian beam has transverse magnetic and electric field amplitude profiles given by the Gaussian function, which implies a Gaussian intensity profile. A Gaussian beam has no obvious boundaries to denote characteristic dimensions like radius, so the radius is defined as the distance from the axis where beam intensity is $1/e^2$ the maximum value. This means approximately 87% of the beams power is concentrated within the radius around the beam's center.

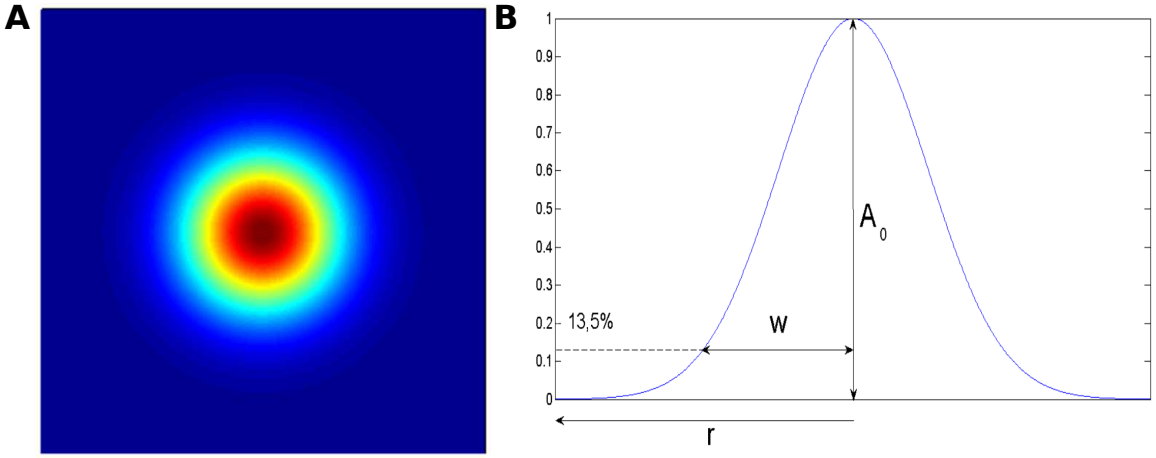

Figure G.1: (A) The model of Gaussian beam and (B) the intensity profile with basic parameters. Figure modified from `http://people.fjfi.cvut.cz/blazejos/public/ul7en.pdf`.(24)

Along the axis of beam propagation, the beam waist is variable coming to a position of smallest radius referred to as the beam waist and denoted w_0. The radius of the Gaussian beam a distance z from the beam waist is given by:

$$w(z) = w_0\sqrt{1+\left(\frac{z}{z_R}\right)^2}$$

where z_R is the Rayleigh range. The Rayleigh range is the distance from the beam waist where the beam area is twice the beam area at the beam waist, given by:

$$z_R = \frac{\pi w_0^2}{\lambda}$$

where λ is the wave length of the laser. Other parameters characteristic of the Gaussian beam depicted in Figure G.2 are the total angular spread of the beam (Θ) and the depth of focus (b). The total angular spread is inversely proportional to the spots size for a given wavelength ($\Theta \cong 2\lambda/(\pi w_0)$). The depth of focus is the distance between Rayleigh range positions.

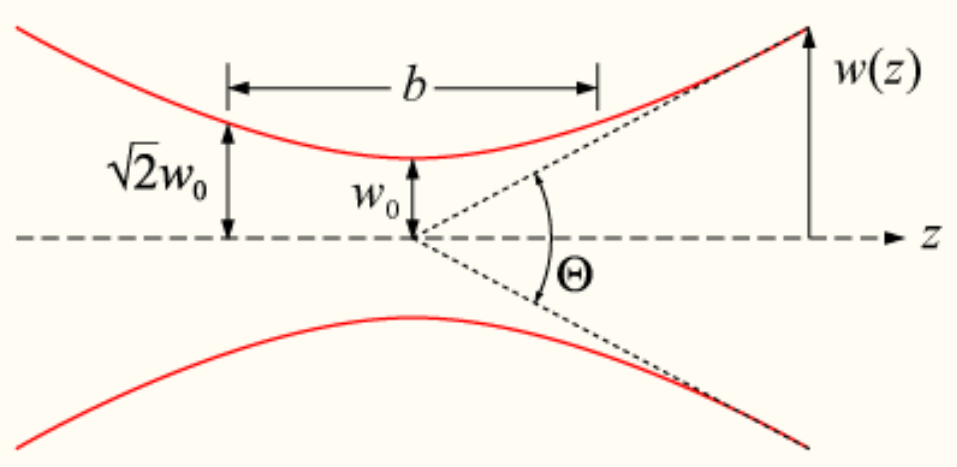

Figure G.2: Diagram of Gaussian beam waist parameters.(25)

Section G.2: Knife-Edge Method

The knife-edge method uses a sharp edge, i.e. the knife (or in our case a razor blade), translated perpendicular through the beam while recording the power of light not blocked by the knife (Figure G.3). The result is a power distribution dependent on the knife position, which corresponds to integrating the 2D Gaussian beam profile.

The estimation of the beam width can be done in several ways, one of which is the 90-10% clipping method. The idea is to determine the x-positions of the knife corresponding to power outputs of 10% and 90% of the total power. The beam width can be calculated from the absolute distance between these points with

$$|x_{90\%} - x_{10\%}| = 1.28 w_z$$

This can be measurement of beam waist can be performed for any percentage of total power output; however, 10%-90% clipping levels are snow to be robust against contamination of the higher order modes.(278)

This method was used for calculation of beam waist as it propagated through the optics and to the specimen. Once at the specimen, the light sheet width was calculated by moving a point source through

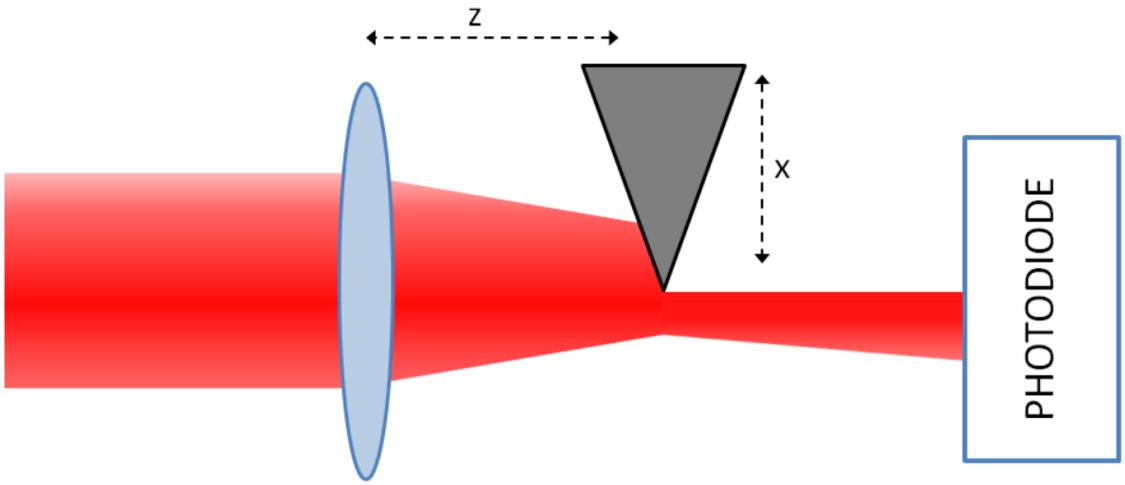

Figure G.3: The principle of the Knife-Edge Method. Figure modified from `http://people.fjfi.cvut.cz/blazejos/public/ul7en.pdf`.(24)

the excitation light using the AFM scan stage for a more precise measurement of the width. This method is discussed in greater detail in Section 4.3.

APPENDIX H: Determining the PRISM PSF

There are two common methods of measuring the resolution of a microscope system – measuring resolution form image reflected off a mirror slide and collecting the point spread function (PSF) of fluorescent microspheres. The mirror slide allows for analysis based on the excitation laser wavelength. Acquiring the PSF produced by microspheres allow for analysis based on the fluorescence emission wavelength.

The light originating from a sub-resolution fluorescent microsphere is diffracted as it travels through the optics of the microscope. The result is the Airy pattern of the point source, consisting of a central point surrounded by diffraction rings, which is much larger than the actual size of the object. For a point source, the pattern of diffracted light is more generally referred to as a PSF. The size of the PSF depends on several things including then wavelength of emitted light and the numerical aperture (NA) of the objective. High-NA objectives generate smaller PSFs and thus have a higher resolving power. Diffraction spreads the light out both along the lateral axis of the microscope and even more pronounced along the axial axis, in the direction of light propagation. The latter leads to an axial resolution that is three times worse than in the lateral direction. This is the driving motivation for our side-view microscopy technique, which makes the resolution in the axial direction comparable to the lateral resolution by rotating the light path with the use of a 45-degree reflecting surface.

Because I was interested in the specimen point of view resolution of the imaging system, I used a PSF analysis protocol similar to that laid out in the 2011 Nature Protocol paper.(279)

Samples consisting of 20 nm red fluorescent beads incubated with SKOV cells then rinsed and fixed using formaldehyde were prepared for characterization of the PSF for our imaging system. Two PSF were acquired for each bead analyzed on the system – a plan-view PSF and a side-view PSF. To acquire these PSF, a single bead is selected (preferably separated by large distances from other beads or the only bead in the field of view) and the 45-degree mirror is placed approximately 10 microns (this distance was chosen in order to avoid contact with the cell as in a standard cell experiment) from the mirror edge. Then two image stacks (one plan-view z-stack and one side-view x-stack) were acquired with a 50 nm image-stack interval between images. Both the plan- and side-view PSF could be captured in the same image-stack provided a large enough objective range and field of view; however, for ease of analysis it was easier to save them as separate stacks.

Next the each stack was analyzed with the ImageJ plugin MetroloJ, which measures among other things the optical resolution from the PSF of a 3D image.(280) More information on MetroloJ can be found at `http://imagejdocu.tudor.lu/doku.php?id=plugin:analysis:metroloj:start`. Briefly for plan-view, the plugin displays the 2D XY PSF and generates maximum intensity projections of the z-stack along the

axial direction. The X and Y profiles were collected along the line passing through the maximum intensity pixel in the XY image. The Z profile was collected on the XZ view, along the line passing through the maximum intensity pixel. All three profiles were fitted by a Gaussian function to determine the FWHM of the PSF. These values were then compared to the theoretical resolutions calculated from the following:

$$XY_{res} = \frac{0.61 \cdot \lambda_{emission}}{NA} \quad \text{and} \quad Z_{res} = \frac{2 \cdot \lambda_{emission}}{NA^2}$$

where $\lambda_{emission}$ is the wavelength of emitted fluorescence and NA is the numerical aperture of the objective, for our system $NA = 1.2$. The results for plan-view fits and calculations are in the chart in Figure H.1 A and B. The same calculations are made for the side-view x-stack with the axis labels changed accordingly (Figure H.1 C).

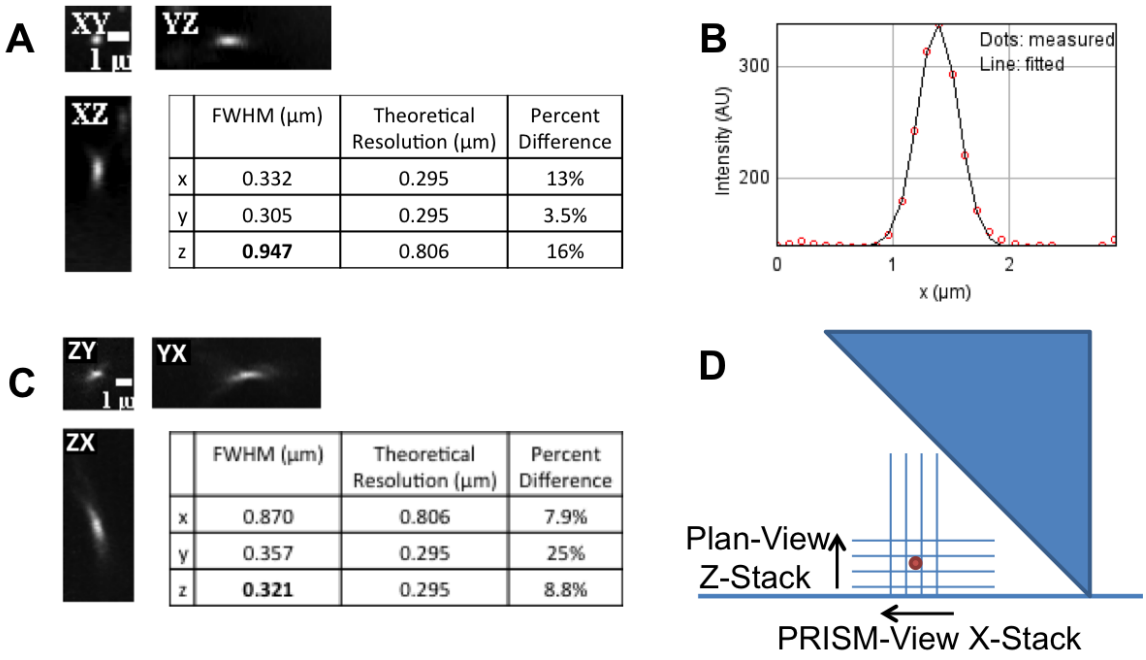

	FWHM (µm)	Theoretical Resolution (µm)	Percent Difference
x	0.332	0.295	13%
y	0.305	0.295	3.5%
z	**0.947**	0.806	16%

	FWHM (µm)	Theoretical Resolution (µm)	Percent Difference
x	0.870	0.806	7.9%
y	0.357	0.295	25%
z	**0.321**	0.295	8.8%

Figure H.1: PSF calculation for Plan- and PRISM-view. (A) MetroloJ output for plan-view PSF, includes a montage made from the three maximum intensity projections – XY, XZ, and YZ – and the resolution table holding FWHM determined from Gaussian fits, theoretical resolution and the percentage difference between the two. (B) Sample X-profile data and Gaussian fit for determination of FWHM. Similar data was used for Y- and Z- profile. (C) MetroloJ output for PRISM side-view PSF. (D) Cartoon illustration of the slices acquired on the PRISM system, for more details on imaging with the PRSIM system refer to SECTION XX.

The FWHM values for plan- and side-view stacks, demonstrate that our system provides a z-resolution in PRISM side-view images comparable to the XY-resolution in standard plan-view images. There are several factors that can affect the results of the PRISM side-view image including, tilt of the mirror. If the mirror is tilted to beyond 45-degrees then, the PSF will also be tilted, as can be seen in Figure 1 C. This is interesting

for two reasons: (1) the prism tilt results in an overestimation of the Z-FWHM and underestimation of the X-FWHM using the current plugin, and (2) the PSF tilt can be used to determine the tilt of the mirrored surface.

Using custom MATLAB code and mimicking MetroloJ, I calculated the maximum intensity pixel and used that location to create YZ, XZ and XY planes identical to those calculated by MetroloJ. A sample XZ plane produced by our MATLAB code can be seen in Figure H.2 A. We calculated the tilt in the PSF by fitting a line to the maximum intensity pixel in each column, when the X focal direction is always the x-axis, above a threshold value. This fit is shown as the blue line in Figure H.2 A. The grey-scale values of the pixels corresponding to this line are plotted as a function of position and fit with a Gaussian to determine the FWHM of the PSF in the x-direction defined by the x-direction defined in plan-view. A line normal to the tilt line (red line Figure H.2 A), is used in the same manner to determine the FWHM of the PSF (Figure H.2 B) in the true z-direction corresponding to the z-direction defined in plan-view. The results tilt-corrected FWHM for all three axis are reported in the table in Figure H.2 C. As expected, there was a reduction in the FWHM due to correcting for tilt in both the Y and Z direction, and an increase in the reported FWHM in the X-direction.

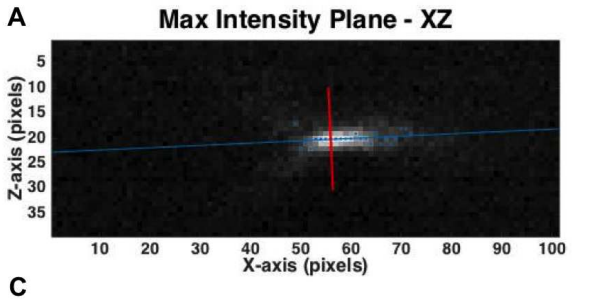

C

FWHM	Uncorrected (μm)	Tilt Corrected (μm)	Theoretical Resolution (μm)	Percent Difference
X	0.870	0.921	0.806	14.3 %
Y	0.357	0.308	0.295	4.4 %
Z	0.321	0.305	0.295	3.4 %

Figure H.2: Plot of pathway rotated image x-stack for z-axis through maximum intensity pixel used for calculation of PSF tilt. Linear fit for tilt of PSF (blue) and normal line (red) used for calculation of resolution in plan-view axes. (B) Gaussian fit to intensity profile in z-direction corrected for mirror tilt (red line). (C) FWHM results of Gaussian fits to intensity profiles along each axis in image stack.

When the pathway rotating mirror is at an angle other than 45°, the point source will appear to move in the image stack and appear as a tilted PSF in the axial stacks, such as Figure H.2A. From the line fit to the Z-tilted PSF, I also calculated the mirror's tilt from the slope to be 2.6° beyond 45°. So the mirror actually forms a 42.4° angle with the glass substrate. Like wise, from the Y-tilted PSF I determined that

the mirror was at an angle of 16.2° with the plan-view y-axis. Understanding these parameters allowed us refine placement of the pathway rotating mirror near the sample for optimum imaging quality.

These type of corrections could be applied to the PRISM side-view images captured during live cell experiments to produce z-resolution of ∼300 nm, an ∼7% improvement over the original estimation. However, even without these corrections the PRISM Z-resolution is comparable to the plan-view X and Y-resolution. This verifies the initial motivation for designing our side-view microscopy technique, to make the axial resolution comparable to the lateral resolution by rotating the light path.

APPENDIX I: AFM Bead Attachment Protocol

As referenced in Chapter 4, beaded AFM tips were made in-house by attaching 5 μm beads to long, commercially available tipless cantilevers. The following protocol was settled upon after several failed attempts at attaching beads to tipless cantilevers. The key was the incorporation of trichlorosilane ($HSiCl_3$) which forms self assembled monolayers containing fluorine to decrease surface energy and reduce sticking.

1. Treat clean glass slides with $HSiCl_3$.
    - Put $\sim$100μL of $HSiCl_3$ in small beaker into bell jar with clean glass slides.
    - Tun vacuum pump and allow 1 to 2 hours for vapor deposition to take place.
2. Dry beads onto $HSiCl_3$-treated glass slide.
    - Put a dilution of 1:100 5 μm yellow-green beads in ethanol onto the glass slide and allow to dry for $\sim$30 minutes.
    - Remember to mix solution throughly, possibly even consider sonicating, to break up clumps of beads.
3. Put adhesive onto the bead coated slide.
    - After the bead solution dries, put a small amount of Norland Optical Adhesive 81 onto slide. Only the tiniest amount of Norland is required because if the drop is too large, then the AFM cantilever can be crashed into it and break.
    - Then use a razor to spread the Norland into a long thin line.
4. Attach a bead to tipless cantilever.
    - Load the slide with beads and Norland onto the scan stage with the dot/line just to the right of center. The reason the dot should be to the right (or the side furthest from the AFM cantilever chip) is to avoid the possibility of accidentally running into Norland with the cantilever spring clip.
    - Load a tipless cantilever into the AFM holder and align the laser to maximize the SLD signal (Sum). There is no need to perform virtual deflection, deflection inverse optical lever sensitivity, or thermal calibrations to determine the spring constant. For the PRISM system with modifications described in Chapter 4, both Arrow TL1 and Arrow CONT cantilevers can be used.
    - Engage the AFM cantilever and bring the end of the cantilever into contact with the Norland using the thumbwheel. Then thumbwheel back up to remove the cantilever from Norland.

- There should only be a small amount of Norland on the end of the cantilever to make picking up a bead easiest and to avoid coating the entire bead in Norland (Figure I.1). To remove excess Norland, simply bring the cantilever back into contact with the glass in an area with no beads.
- Align the cantilever over the bead and bring it down on top of the bead using the thumbwheel, just until the cantilever engages to it's set point and triggers on the surface. Then retract from the surface, also using the thumbwheel.
- If the bead doesn't attach, repeat a few more times. Do not hesitate to move onto a new bead and add Norland as required. It is better to move onto a new bead which may have a weaker attachment to the glass and avoid permanently deforming your AFM cantilever during this step.

5. UV cure Norland.

   - Once a bead has been picked up, the Norland needs to be cured in order to ensure firm attachment of the bead to the cantilever.
   - Do not remove the cantilever from the cantilever holder. Place the entire cantilever holder under the UV lamp and cure with long wavelength for approximately 5 minutes.

6. Check bead attachment.

   - Some times there is not enough Norland or it does not cure properly in which case the bead will not remain attached to the AFM cantilever during cell experiments.
   - To avoid losing a bead during an experiment, bring the bead into contact with clean glass to see if it is firmly attached to the cantilever.

7. Attach more beads to cantilevers.

   - If the bead comes off after UV curing or making more AFM beaded tips, then continue to repeat this procedure starting at Step 4.
   - Remember, just keep trying this is a probability game.

This method has been successful for the bead attachment needs required for this thesis work; however, to save others time below is a list and description of other failed bead attachment variants:

- Super glue as an adhesive. A variety of super glues with different viscous properties and dry times were experimented with; however, they often resulted in broken tips or stingy super glue strands hanging from the cantilever.

- Untreated glass slide. Drying the beads on to an untreated glass coverslip resulted in a frustratingly low probability of picking up an 5 μm bead with Norland.
- HMDS treated glass slide. HMDS treating the glass coverslips in an attempt to promote detachment of the beads from the coverslip had the opposite effect.

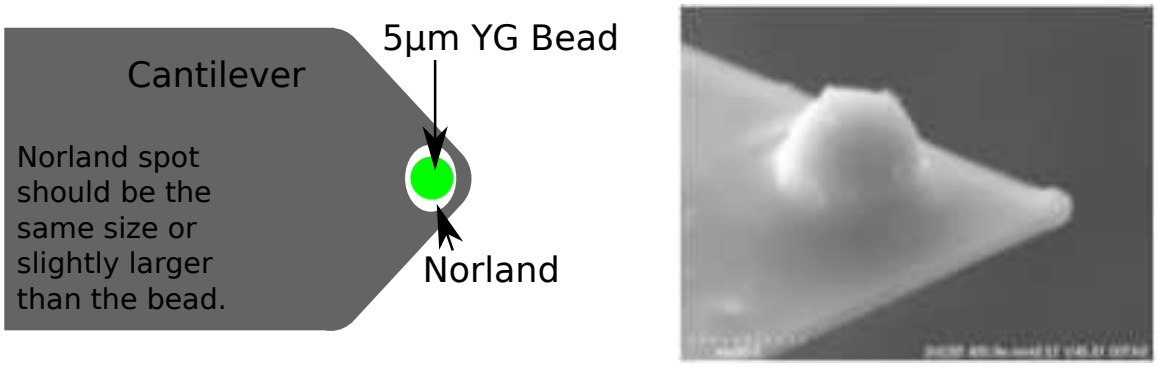

Figure I.1: (Left) Cartoon illustration to give scale to the size and location of Norland for bead attachment protocol. (Right) Scanning electron microscope (SEM) image of 5 μm bead attached to Arrow TL1 cantilever.

APPENDIX J: Temperature Control PRISM

As referenced in Chapter 4, future experiments with the PRISM system will likely require temperature control. The need for temperature control was made most apparent when attempting to observe mechanically induced calcium signaling in PRISM-view as a follow up to the work published by Lee, et al.(281) Mechanically induced calcium signaling in chondrocytes is known to be sensitive to the temperature at which experiments are performed.(282) Though I did not follow up on temperature controlled PRISM experiments, I did establish a means for performing PRISM experiments in controlled solution conditions.

There are two methods for controlling the temperature in AFM experiments: (1) use air temperature control to keep the air temperature inside the entire hood constant around the instrument, or (2) use a closed fluid cell to thermally control temperature of liquids involved in the experiment. There are draw backs to each of the temperature control methods. Controlling the temperature of the entire hood is accomplished by circulating heated air throughout the hood, which would introduce noise into our AFM system due to the fans and heater. Controlling the temperature of the liquid can be accomplished with the BioHeater^{TM} closed fluid cell, a standard accessory to the MFP-3D Bio AFM. The BioHeater consists of a closed fluid cell with an immersed heating element which symmetrically heats the surrounding fluid (Figure J.2 A). The BioHeater introduces no vibrational noise into AFM measurements, but does restrict physical parameters involved in placement of the prism due to the walls of the fluid cell.

Because I can over come the physical restraints of the BioHeater fluid cell more easily than the vibrations introduced by heating the entire acoustic hood, I chose to design an arm mount specifically for use in temperature control experiments. We designed and implemented a 3D printed plastic mount on to which the standard capillary tube mounted micro-prism could be attached. Figure J.1 shows SketchUp designs of the BioHeater-PRISM mount. The most notable features of the mont design are (1) a rectangular hole on the right side for flexibility when mounting the holder to the PRISM three-axis manipulation stage, (2) an angled region at the top left of the mount to avoid contact with the AFM cantilever holder and head, and (3) lips and walls on the capillary tube mounting region (Figure J.1 C) to create a small angle for avoiding the glass window and heating elements, and to allow for consistent position of the capillary tube. An angle of $\sim 8^{\circ}$ is needed to avoid the heating elements and inner lip of the BioHeater. Due to the limitations in scale of 3D printing, this angle was accomplished by placing a small lip on the end of the mount so that when adhered to the mount the capillary tube would have the desired incline. Figure J.2 shows images of the system implemented on our system.

Though this mounting apparatus was not used for prism imaging, I validated the use of this apparatus for temperature control experiments with in the physical constraints of the Asylum BioHeater. A SketchUp

model for 3D printing can be provided by request.

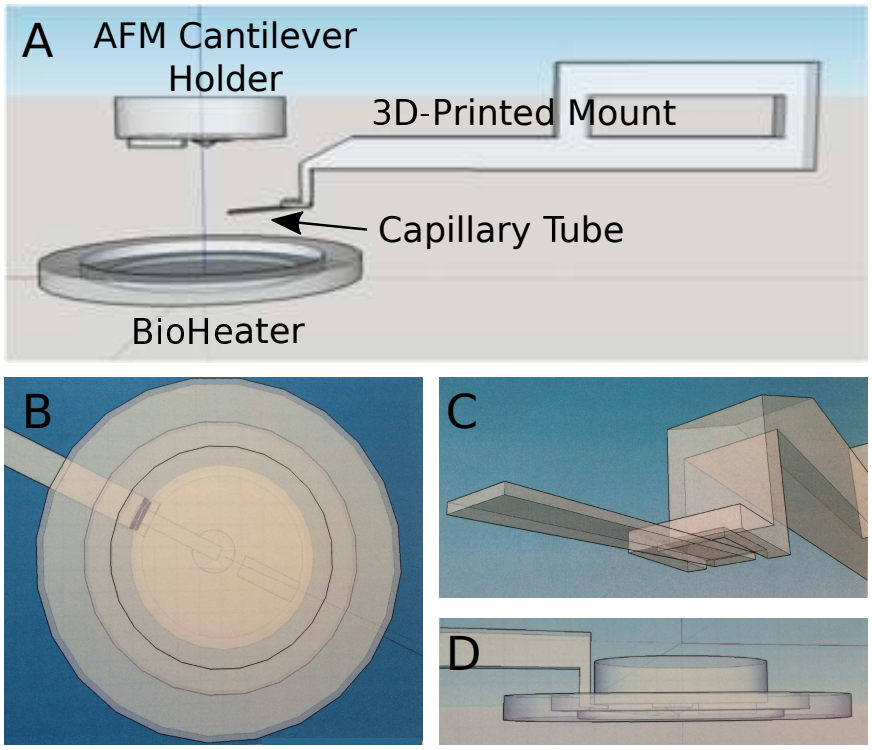

Figure J.1: SketchUp design for BioHeater-PRISM mount. (A) Side-view of all elements involved in mount design. (B) Bottom-view of system as seen through the microscope shows a limited range of motion in prism placement. (C) Close up on capillary tube attachment region, featuring lip to produce 8° angle and walls for alignment. (D) Simulating placements during experiment with AFM head lowered.

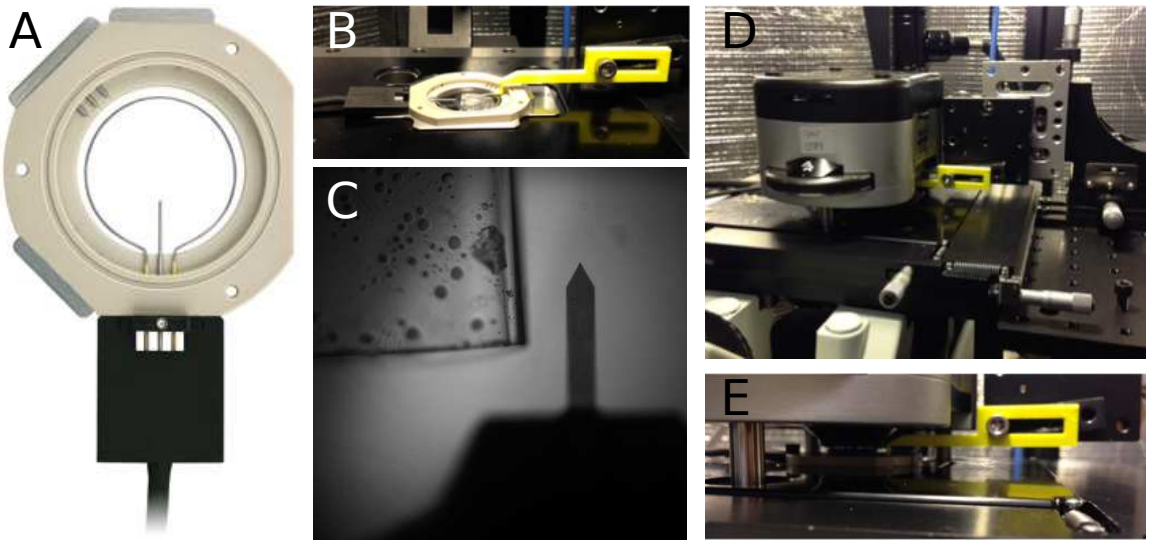

Figure J.2: Images of BioHeater PRISM mount. (A) Asylum BioHeater with heating elements for temperature control of fluid. (B) Side-view image similar to the SketchUp design in Figure J.1 A. (C) Microscope plan-view of AFM and capillary tube on BioHeater-PRISM mount in the BioHeater. (D) Setup with AFM head placed on BioHeater for experiment. (E) Magnification of region under the AFM head.

APPENDIX K: Supplemental PRISM Images

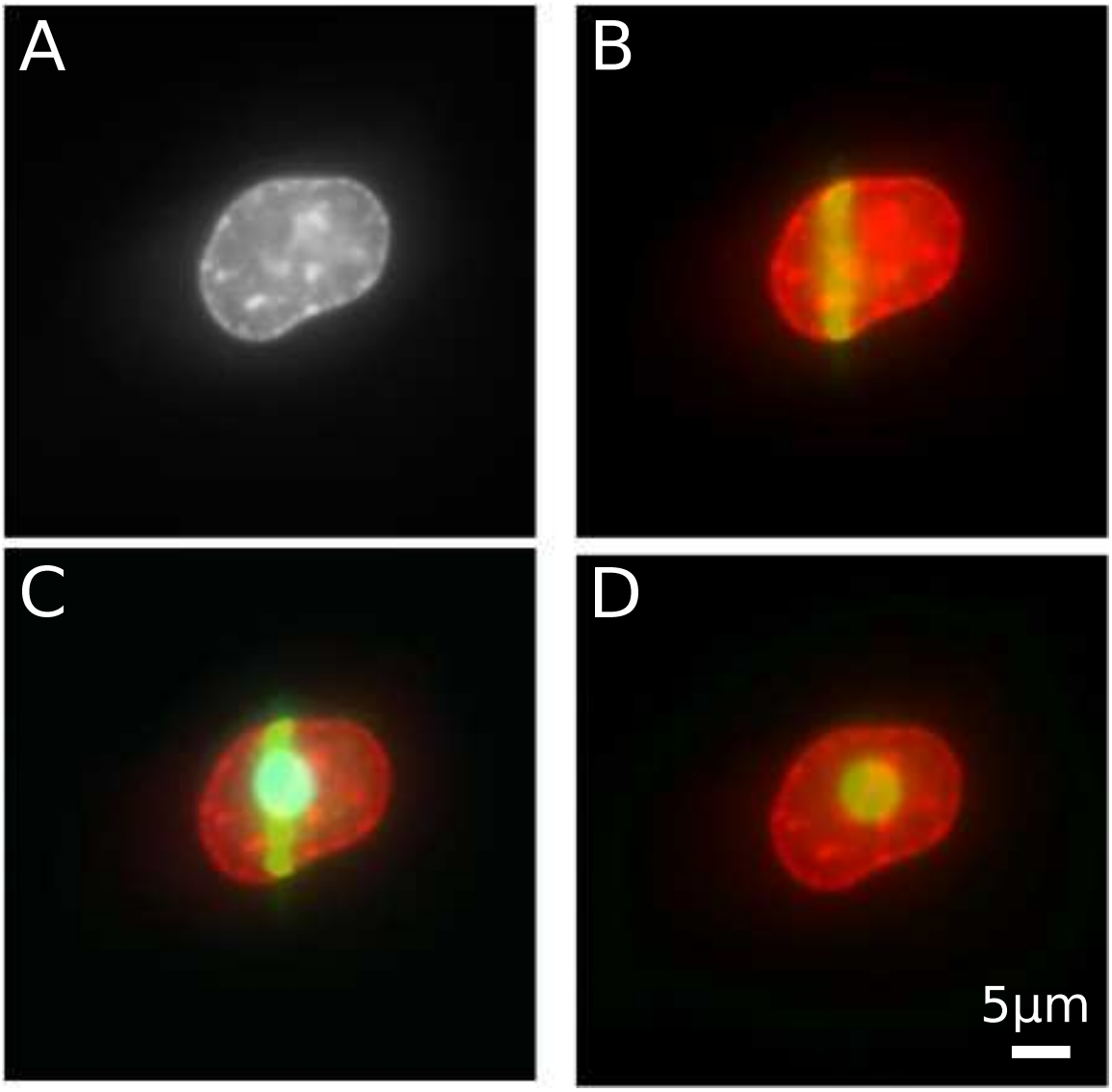

Figure K.1: Plan-view image of SYTO-labeled SKOV cell prior to synchronized AFM-PRISM-VLS experiment. (A) SYTO labeled SKOV cell in broad illumination. (B) Overlay of broad (red) and VLS (green) illumination. (C) Image (B) with additional inclusion of 5 μm yellow-green AFM bead (blue). (D) Overlay of broad illumination (red) and 5 μm yellow-green AFM bead (yellow). PRISM-view images of this cell to follow in Figure K.2

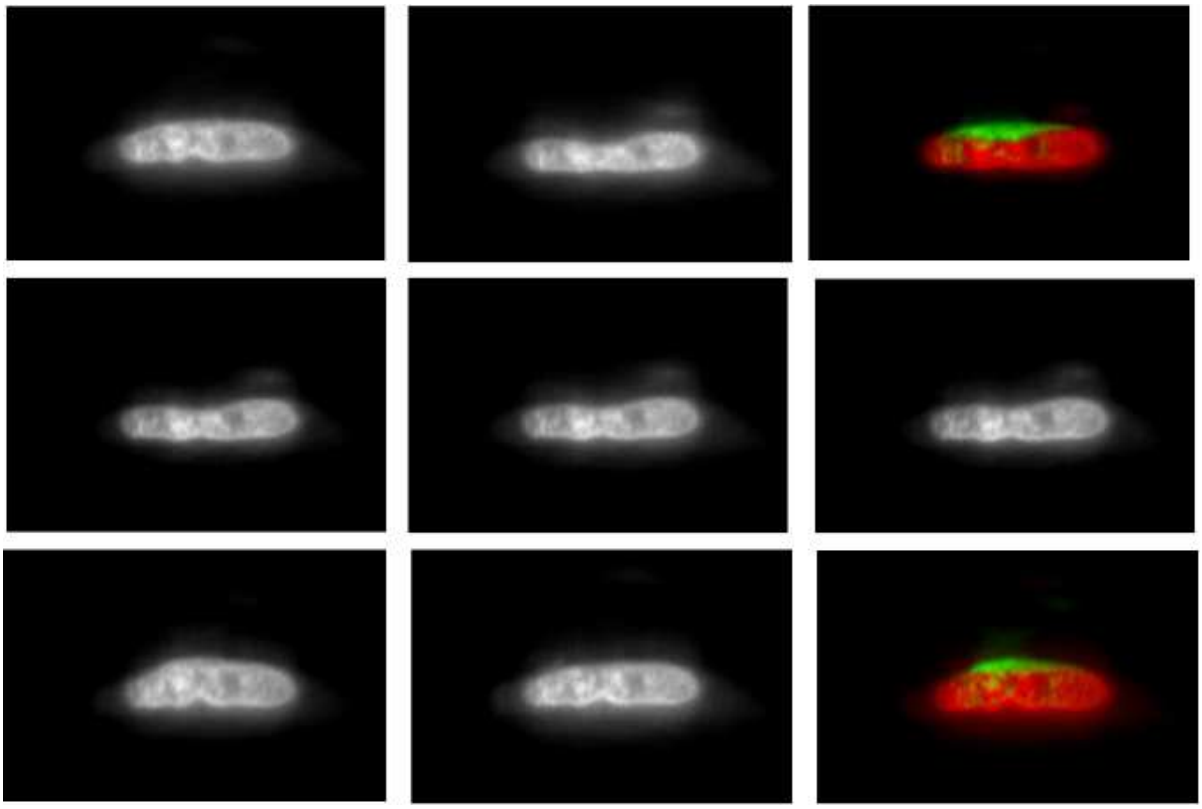

Figure K.2: Deformation and retraction images of SYTO-labeled SKOV cell from synchronized AFM-PRISM-VLS experiment. The nuclear structure is clearly visible due to PRISM-VLS imaging capabilities. Image of the cell (A) before indent, (B) at maximum indent, (D-F) during different, subsequent locations in the retraction curve, (G) just prior to final force rupture, and (H) following final force rupture and detachment of the cell from the AFM tip. (C) Overlaid images (A) in green and (B) in red to show the amount of deformation during indentation. (I) Overlaid images (G) in green and (H) in red to illustrate the degree to which the nucleus was lifted by forces applied to the cell surface.

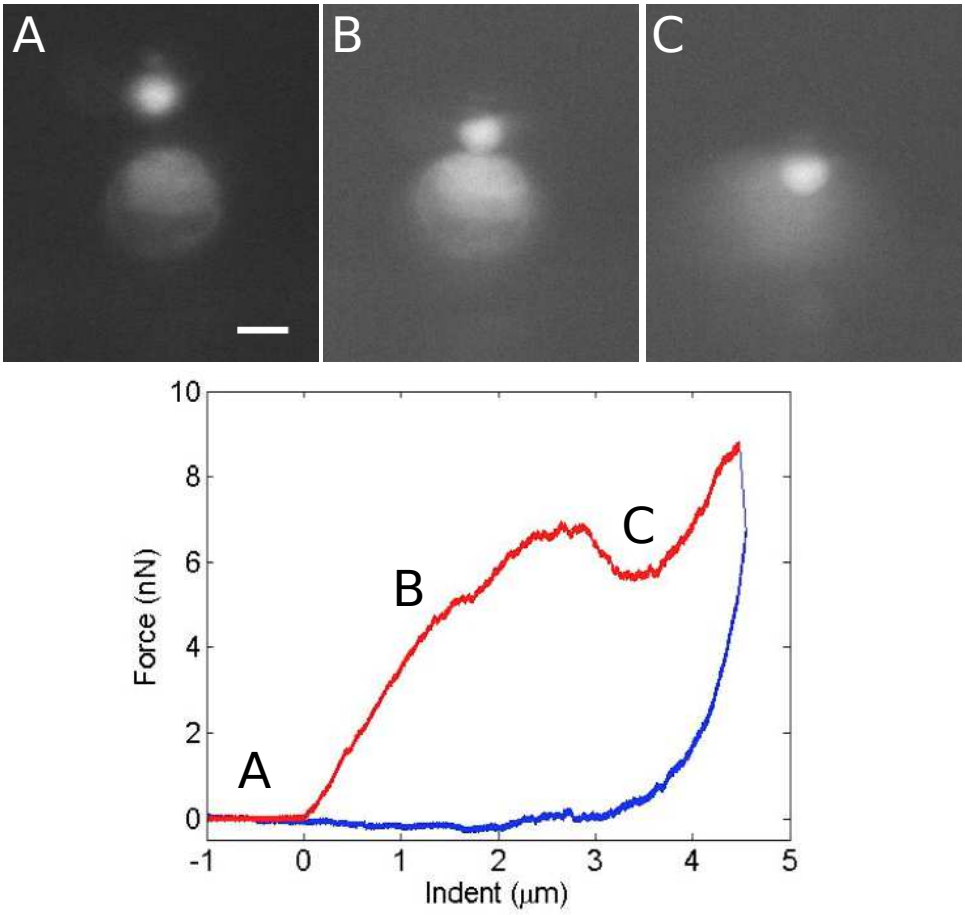

Figure K.3: Synchronized AFM-PRISM experiment on cell with anomalous 'rolling' behavior. These images were acquired prior to the installation of the VLS for improved image resolution and SNR. Image shown were stills acquired (A) before indent, (B) during the first portion of indent, and (C) following the abrupt drop in force associated with the cell moving out from under the AFM tip.

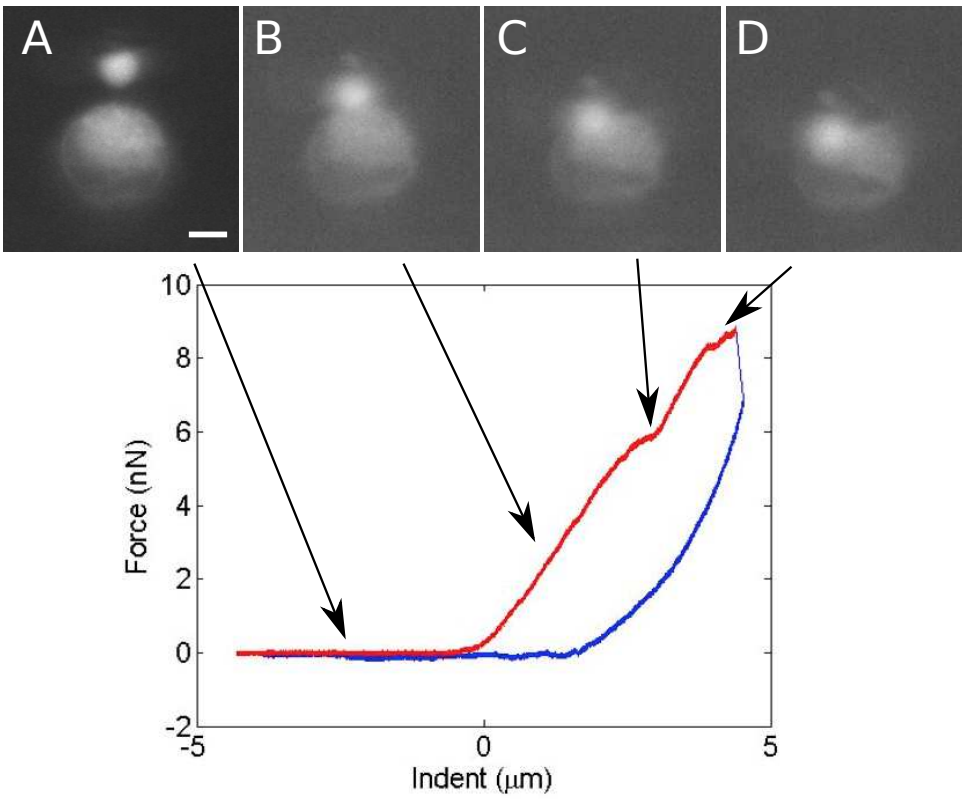

Figure K.4: Synchronized AFM-PRISM experiment on cell with anomalous 'rolling' behavior though slightly less pronounced than in Figure K.3. These images were acquired prior to the installation of the VLS for improved image resolution and SNR. Image shown were stills acquired (A) before indent, (B) during the first portion of indent, and (C) following the abrupt drop in force associated with the cell moving out from under the AFM tip toward the right.

REFERENCES

[1] Laurel E. Averett. *Single-molecule Force Spectroscopy Studies of Fibrin A-a Polymerization Interactions via the Atomic Force Microscope.* PhD thesis, University of North Carolina at Chapel Hill, 2010.

[2] Wendy E Thomas, Viola Vogel, and Evgeni Sokurenko. Biophysics of catch bonds. *Annu. Rev. Biophys.*, 37:399–416, 2008.

[3] Ning Wang, Jessica D Tytell, and Donald E Ingber. Mechanotransduction at a distance: mechanically coupling the extracellular matrix with the nucleus. *Nature reviews. Molecular cell biology*, 10(1):75–82, 2009.

[4] Benjamin L Ricca, Gautham Venugopalan, and Daniel A Fletcher. To pull or be pulled: parsing the multiple modes of mechanotransduction. *Current Opinion in Cell Biology*, 25(5):558–564, 2013.

[5] Subra Suresh. Biomechanics and biophysics of cancer cells. *Acta Materialia*, 55(12):3989–4014, 2007.

[6] O. Loh, A. Vaziri, and H. D. Espinosa. The potential of MEMS for advancing experiments and modeling in cell mechanics. *Experimental Mechanics*, 49(1):105–124, 2009.

[7] K a Dill and H S Chan. From Levinthal to pathways to funnels. *Nature structural biology*, 4(1):10–19, 1997.

[8] V. Swaminathan, K. Mythreye, E. T. O'Brien, A. Berchuck, G. C. Blobe, and R. Superfine. Mechanical Stiffness Grades Metastatic Potential in Patient Tumor Cells and in Cancer Cell Lines. *Cancer Research*, 71(15):5075–5080, 2011.

[9] C Guilluy, L D Osborne, Landeghem L Van, L Sharek, R Superfine, R Garcia-Mata, and K Burridge. Isolated nuclei adapt to force and reveal a mechanotransduction pathway in the nucleus. *Nat.Cell Biol.*, 16(1476-4679 (Electronic)):376–381, 2014.

[10] S Hirsch, A Manhart, and C Schmeiser. Bistability of Lamellipodial Fragments, 2015, 1511.08602.

[11] Michel Bornens. The Centrosome in Cells and Organisms. *Science*, 335(6067):422–426, 2012.

[12] Ryan J Petrie, Hyun Koo, and Kenneth M Yamada. Generation of compartmentalized pressure by a nuclear piston governs cell motility in a 3D matrix. *Science*, 345(6200):1062–1065, 2014.

[13] Guillaume T Charras and Mike a Horton. Single cell mechanotransduction and its modulation analyzed by atomic force microscope indentation. *Biophysical journal*, 82(6):2970–2981, 2002.

[14] H Liu, J Wen, Y Xiao, J Liu, S Hopyan, M Radisic, C A Simmons, and Y Sun. In Situ Mechanical Characterization of the Cell Nucleus by Atomic Force Microscopy. *ACS nano*, 8(4):3821–3828, 2014.

[15] Elisabetta Canetta, Alain Duperray, Anne Leyrat, and Claude Verdier. Measuring cell viscoelastic properties using a force-spectrometer: influence of protein-cytoplasm interactions. *Biorheology*, 42(5):321–33, 2005.

[16] Chawin Ounkomol, Hongtao Xie, Paul a. Dayton, and Volkmar Heinrich. Versatile horizontal force probe for mechanical tests on pipette-held cells, particles, and membrane capsules. *Biophysical Journal*, 96(3):1218–1231, 2009.

[17] Ovijit Chaudhuri, Sapun H Parekh, Wilbur a Lam, and Daniel a Fletcher. Combined atomic force microscopy and side-view optical imaging for mechanical studies of cells. *Nature methods*, 6(5):383–387, 2009, NIHMS150003.

[18] Ksenija Radotic, Charles Roduit, Jasna Simonovic, Patricia Hornitschek, Christian Fankhauser, Dragosav Mutavdzic, Gabor Steinbach, Giovanni Dietler, and Sandor Kasas. Atomic force microscopy stiffness tomography on living arabidopsis thaliana cells reveals the mechanical properties of surface and deep cell-wall layers during growth. *Biophysical Journal*, 103(3):386–394, 2012.

[19] Charles Roduit, Serguei Sekatski, Giovanni Dietler, Stefan Catsicas, Frank Lafont, and Sandor Kasas. Stiffness tomography by atomic force microscopy. *Biophysical Journal*, 97(2):674–677, 2009.

[20] Wikipedia. Chemotaxis — Wikipedia The Free Encyclopedia, 2016.

[21] Adam J. Engler, Ludovic Richert, Joyce Y. Wong, Catherine Picart, and Dennis E. Discher. Surface probe measurements of the elasticity of sectioned tissue, thin gels and polyelectrolyte multilayer films: Correlations between substrate stiffness and cell adhesion. *Surface Science*, 570(1-2):142–154, 2004.

[22] Raimon Sunyer, Albert J. Jin, Ralph Nossal, and Dan L. Sackett. Fabrication of Hydrogels with Steep Stiffness Gradients for Studying Cell Mechanical Response. *PLoS ONE*, 7(10):1–9, 2012.

[23] Asylum Research. Automating Your Asylum AFM with the MacroBuilder Interface, 2011.

[24] Josef Blazej. The measurement of a transverse profile of laser beam by Knife Edge method.

[25] Wikipedia. Gaussian Beam — Wikipedia{,} The Free Encyclopedia, 2004.

[26] Roy Yuen-Chi Lau and Xia Guo. A review on current osteoporosis research: with special focus on disuse bone loss. *Journal of osteoporosis*, 2011:293808, 2011.

[27] S. Derler and L. C. Gerhardt. Tribology of skin: Review and analysis of experimental results for the friction coefficient of human skin. *Tribology Letters*, 45(1):1–27, 2012.

[28] David N. Ku. Blood Flow in Arteries. *Annual Review of Fluid Mechanics*, 29(1):399–434, 1997.

[29] Donald E Ingber. Cellular mechanotransduction: putting all the pieces together again. *The FASEB*

journal, 20(7):27, 2006, 33744488545.

[30] Viola Vogel. MECHANOTRANSDUCTION INVOLVING MULTIMODULAR PROTEINS: Converting Force into Biochemical Signals. *Annual Review of Biophysics and Biomolecular Structure*, 35(1):459–488, 2006.

[31] Armando Rio, Raul Perez-jimenez, Ruchuan Liu, Pere Roca-cusachs, Julio M Fernandez, and Michael P Sheetz. Stretching Single Talin Rod. *Science*, 323(January):638–641, 2009.

[32] Patricia M. Davidson and Jan Lammerding. Broken nuclei âĂŞ lamins, nuclear mechanics, and disease. *Trends in Cell Biology*, 24(4):247–256, 2014.

[33] Dennis E Discher, Paul Janmey, and Yu-Li Wang. Tissue cells feel and respond to the stiffness of their substrate. *Science (New York, N.Y.)*, 310(5751):1139–43, 2005.

[34] C. S. Chen. Mechanotransduction - a field pulling together? *Journal of Cell Science*, 121(20):3285–3292, 2008.

[35] Patrick Delmas, Jizhe Hao, and Lise Rodat-Despoix. Molecular mechanisms of mechanotransduction in mammalian sensory neurons. *Nature reviews. Neuroscience*, 12(3):139–153, 2011.

[36] Cynthia A. Reinhart-King, Micah Dembo, and Daniel A. Hammer. Cell-Cell Mechanical Communication through Compliant Substrates. *Biophysical Journal*, 95(12):6044–6051, 2008.

[37] Jeffrey K. Moore and John A. Cooper. Coordinating mitosis with cell polarity: Molecular motors at the cell cortex. *Seminars in Cell and Developmental Biology*, 21(3):283–289, 2010.

[38] Revathi Ananthakrishnan and Allen Ehrlicher. The forces behind cell movement. *International Journal of Biological Sciences*, 3(5):303–317, 2007.

[39] Ovijit Chaudhuri and Daniel A Fletcher. Protrusive forces generated by dendritic actin networks during cell crawling. In *Actin-based Motility: Cellular, Molecular and Physical Aspects*, pages 359–379. Springer, 2010.

[40] Claudia Veigel and Christoph F Schmidt. Moving into the cell: single-molecule studies of molecular motors in complex environments. *Nature reviews. Molecular cell biology*, 12(3):163–76, 2011.

[41] Elizabeth A. Booth-Gauthier, Turi A. Alcoser, Ge Yang, and Kris N. Dahl. Force-induced changes in subnuclear movement and rheology. *Biophysical Journal*, 103(12):2423–2431, 2012.

[42] Hans-Jurgen Butt, Brunero Cappella, and Michael Kappl. Force measurements with the atomic force microscope: Technique, interpretation and applications. *Surface Science Reports*, 59(1-6):1–152, 2005.

[43] G. Binnig and C. F. Quate. Atomic Force Microscope. *Physical Review Letters*, 56(9):930–933, 1986.

[44] Pierre Henri Puech, Kate Poole, Detlef Knebel, and Daniel J. Muller. A new technical approach to quantify cell-cell adhesion forces by AFM. *Ultramicroscopy*, 106(8-9):637–644, 2006.

[45] Brenton D Hoffman, Carsten Grashoff, and Martin a Schwartz. Dynamic molecular processes mediate cellular mechanotransduction. *Nature*, 475(7356):316–323, 2011.

[46] M Benoit, D Gabriel, G Gerisch, and H E Gaub. Discrete interactions in cell adhesion measured by single-molecule force spectroscopy. *Nature cell biology*, 2(6):313–317, 2000.

[47] E.A. Evans and D.A. Calderwood. Forces and bond dynamics in cell adhesion. *Science*, 316(May):1148–1154, 2007.

[48] E L Florin, V T Moy, and H E Gaub. Adhesion forces between individual ligand-receptor pairs. *Science (New York, N.Y.)*, 264(5157):415–417, 1994.

[49] P Hinterdorfer, W Baumgartner, H J Gruber, K Schilcher, and H Schindler. Detection and localization of individual antibody-antigen recognition events by atomic force microscopy. *Proceedings of the National Academy of Sciences of the United States of America*, 93(8):3477–3481, 1996.

[50] Peter Hinterdorfer and Yves F Dufrêne. Detection and localization of single molecular recognition events using atomic force microscopy. *Nature methods*, 3(5):347–355, 2006.

[51] Matthias Rief, Mathias Gautel, Filipp Oesterhelt, Julio M Fernandez, and Hermann E Gaub. Reversible unfolding of individual titin immunoglobulin domains by AFM. *Science (New York, N.Y.)*, 276(5315):1109–1112, 1997.

[52] a F Oberhauser, P E Marszalek, H P Erickson, and J M Fernandez. The molecular elasticity of the extracellular matrix protein tenascin. *Nature*, 393(6681):181–185, 1998.

[53] M Rief, H Clausen-Schaumann, and H E Gaub. Sequence-dependent mechanics of single DNA molecules. *Nature structural biology*, 6(4):346–349, 1999.

[54] Jacob Notbohm, Ayelet Lesman, Phoebus Rosakis, David A Tirrell, and Guruswami Ravichandran. Microbuckling of fibrin provides a mechanism for cell mechanosensing. *Journal of the Royal Society, Interface / the Royal Society*, 12(108):20150320, 2015, 1407.3510.

[55] Eoin D. O'Cearbhaill, Mary Murphy, Frank Barry, Peter E. McHugh, and Valerie Barron. Behavior of human mesenchymal stem cells in fibrin-based vascular tissue engineering constructs. *Annals of Biomedical Engineering*, 38(3):649–657, 2010.

[56] Jihye Seong, Ning Wang, and Yingxiao Wang. Mechanotransduction at focal adhesions: From physiology to cancer development. *Journal of Cellular and Molecular Medicine*, 17(5):597–604, 2013.

[57] L E Averett, C B Geer, R R Fuierer, B B Akhremitchev, O V Gorkun, and M H Schoenfisch. Complexity of "A- a" Knob- Hole Fibrin Interaction Revealed by Atomic Force Spectroscopy. *Langmuir*,

24(D):4979–4988, 2008.

[58] John W. Weisel. Biophysics. Enigmas of blood clot elasticity. *Science (New York, N.Y.)*, 320(5875):456–457, 2008.

[59] Agnes Henschen and Jan Mcdonagh. Fibrinogen, fibrin and factor XIII. *New Comprehensive Biochemistry*, 13:171–241, 1986.

[60] John W Weisel. Fibrinogen and Fibrin. In *Fibrous Proteins: Coiled-Coils, Collagen and Elastomers*, volume 70 of *Advances in Protein Chemistry*, pages 247–299. Academic Press, 2005.

[61] Justin M Kollman, Leela Pandi, Michael R Sawaya, Marcia Riley, and Russell F Doolittle. Crystal structure of human fibrinogen. *Biochemistry*, 48(18):3877–86, 2009.

[62] Andrew P Laudano, Barbara A Cottrell, and Russell F Doolittle. Synthetic Peptides Modeled on Fibrin Polymerization Sites. *Annals of the New York Academy of Sciences*, 408(1 Molecular Bio):315–329, 1983.

[63] Andrei Z Budzynski and John R Shainoff. Fibrinogen and fibrin: biochemistry and pathophysiology. *Critical reviews in oncology/hematology*, 6(2):97–146, 1986.

[64] Z Yang, I Mochalkin, and R F Doolittle. A model of fibrin formation based on crystal structures of fibrinogen and fibrin fragments complexed with synthetic peptides. *Proceedings of the National Academy of Sciences of the United States of America*, 97(26):14156–61, 2000.

[65] André E.X. Brown, Rustem I. Litvinov, Dennis E. Discher, and John W. Weisel. Forced Unfolding of Coiled-Coils in Fibrinogen by Single-Molecule AFM. *Biophysical Journal*, 92(5):L39–L41, 2007.

[66] M. Matsuda, M. Baba, K. Morimoto, and C. Nakamikawa. 'Fibrinogen Tokyo II'. An abnormal fibrinogen with an impaired polmerization site on the aligned DD domain of fibrin molecules. *Journal of Clinical Investigation*, 72(3):1034–1041, 1983.

[67] O V Gorkun, Y I Veklich, L V Medved, A H Henschen, and J W Weisel. Role of the alpha-c domains of fibrin in clot formation. *Biochemistry*, 33(22):6986–6997, 1994.

[68] M D Bale, M F Müller, and J D Ferry. Effects of fibrinogen-binding tetrapeptides on mechanical properties of fine fibrin clots. *Proceedings of the National Academy of Sciences of the United States of America*, 82(5):1410–3, 1985.

[69] Bohdan Kudryk, Birger BIomböck, and Margareta Blombäck. Fibrinogen Detroit - an abnormal fibrinogen with non-functional NH2-terminal polymerization domain. *Thrombosis Research*, 9(1):25–36, 1976.

[70] John W. Weisel. The mechanical properties of fibrin for basic scientists and clinicians. *Biophysical Chemistry*, 112(2-3 SPEC. ISS.):267–276, 2004.

[71] Jean-Philippe Collet, Henry Shuman, Robert E Ledger, Seungtaek Lee, and John W Weisel. The elasticity of an individual fibrin fiber in a clot. *Proceedings of the National Academy of Sciences of the United States of America*, 102(26):9133–9137, 2005.

[72] Izabela K. Piechocka, Rommel G. Bacabac, Max Potters, Fred C. Mackintosh, and Gijsje H. Koenderink. Structural hierarchy governs fibrin gel mechanics. *Biophysical journal*, 98(10):2281–2289, 2010.

[73] W Liu, L M Jawerth, E A Sparks, M R Falvo, R R Hantgan, R Superfine, S T Lord, and M Guthold. Fibrin Fibers Have Extraordinary Extensibility and Elasticity. *Science*, 313(5787):634, 2006.

[74] W. Liu, C. R. Carlisle, E. A. Sparks, and M. Guthold. The mechanical properties of single fibrin fibers. *Journal of Thrombosis and Haemostasis*, 8(5):1030–1036, 2010.

[75] Michael R. Falvo, D. Millard, E. T. O'Brien, R. Superfine, and S. T. Lord. Length of tandem repeats in fibrin's γC region correlates with fiber extensibility. *Journal of Thrombosis and Haemostasis*, 6(11):1991–1993, 2008.

[76] Martin Guthold, Wenhua Liu, Eric a Sparks, L M Jawerth, L Peng, Michael Falvo, Richard Superfine, Roy R Hantgan, and Susan T Lord. A comparison of the mechanical and structural properties of fibrin fibers with other protein fibers. *Cell biochemistry and biophysics*, 49(3):165–81, 2007.

[77] Nathan E. Hudson, John R. Houser, E. Timothy O'Brien, Russell M. Taylor, Richard Superfine, Susan T. Lord, and Michael R. Falvo. Stiffening of individual fibrin fibers equitably distributes strain and strengthens networks. *Biophysical Journal*, 98(8):1632–1640, 2010.

[78] C. R. Carlisle, E. A. Sparks, C. Der loughian, and M. Guthold. Strength and failure of fibrin fiber branchpoints. *Journal of Thrombosis and Haemostasis*, 8(5):1135–1138, 2010.

[79] Laurel E. Averett, Mark H. Schoenfisch, Boris B. Akhremitchev, and Oleg V. Gorkun. Kinetics of the multistep rupture of fibrin 'A-a' polymerization interactions measured using atomic force microscopy. *Biophysical Journal*, 97(10):2820–2828, 2009.

[80] Bernard B C Lim, Eric H. Lee, Marcos Sotomayor, and Klaus Schulten. Molecular Basis of Fibrin Clot Elasticity. *Structure*, 16(3):449–459, 2008.

[81] Russell F. Doolittle and Justin M. Kollman. Natively unfolded regions of the vertebrate fibrinogen molecule. *Proteins: Structure, Function and Genetics*, 63(2):391–397, 2006.

[82] Galina Tsurupa, Roy R. Hantgan, Robert A. Burton, Igor Pechik, Nico Tjandra, and Leonid Medved. Structure, stability, and interaction of the fibrin(ogen) γC-domains. *Biochemistry*, 48(51):12191–12201, 2009.

[83] John R. Houser, Nathan E. Hudson, Lifang Ping, E. Timothy O'Brien, Richard Superfine, Susan T. Lord, and Michael R. Falvo. Evidence that αC Region Is Origin of Low Modulus, High Extensibility, and Strain Stiffening in Fibrin Fibers. *Biophysical Journal*, 99(9):3038–3047, 2010.

[84] André E X Brown, Rustem I Litvinov, Dennis E Discher, Prashant K Purohit, and John W Weisel. Multiscale mechanics of fibrin polymer: gel stretching with protein unfolding and loss of water. *Science (New York, N.Y.)*, 325(5941):741–744, 2009.

[85] Michael R. Falvo, Oleg V. Gorkun, and Susan T. Lord. The molecular origins of the mechanical properties of fibrin. *Biophysical Chemistry*, 152(1-3):15–20, 2010.

[86] Artem Zhmurov, AndreÂăE.X. Brown, RustemÂăI. Litvinov, RuxandraÂăI. Dima, JohnÂăW. Weisel, and Valeri Barsegov. Mechanism of Fibrin(ogen) Forced Unfolding. *Structure*, 19(11):1615–1624, 2011.

[87] Michael Schlierf, Hongbin Li, and Julio M Fernandez. The unfolding kinetics of ubiquitin captured with single-molecule force-clamp techniques. *Proceedings of the National Academy of Sciences of the United States of America*, 101(19):7299–7304, 2004.

[88] Nobuo Okumura, Oleg V. Gorkun, and Susan T. Lord. Severely impaired polymerization of recombinant fibrinogen γ-364 Asp âĘŠ His, the substitution discovered in a heterozygous individual. *Journal of Biological Chemistry*, 272(47):29596–29601, 1997.

[89] Oleg Y Gorkun and John W Weisel. Interactions Mediated by the N-Terminus of F ibrinogen's. *Biochemistry*, 8(6):14843–14852, 2006.

[90] Jeffrey L. Hutter and John Bechhoefer. Calibration of atomic-force microscope tips. *Review of Scientific Instruments*, 64(7):1868–1873, 1993.

[91] J. P. Cleveland, S. Manne, D. Bocek, and P. K. Hansma. A nondestructive method for determining the spring constant of cantilevers for scanning force microscopy. *Review of Scientific Instruments*, 64(2):403–405, 1993.

[92] R Proksch, T E Schäffer, J P Cleveland, R C Callahan, and M B Viani. Finite optical spot size and position corrections in thermal spring constant calibration. *Nanotechnology*, 15(9):1344–1350, 2004.

[93] John D. Ferry and Peter R. Morrison. Preparation and Properties of Serum and Plasma Proteins. VIII. The Conversion of Human Fibrinogen to Fibrin under Various Conditions1,2. *J. Am. Chem. Soc.*, 69(2):388–400, 1947.

[94] John T. Edsall and Walter F. Lever. Effects of ions and neutral molecules on fibrin clotting. *The Journal of biological chemistry*, 191(2):735–756, 1951.

[95] E Di Stasio, C Nagaswami, J W Weisel, and E Di Cera. Cl- regulates the structure of the fibrin clot. *Biophysical journal*, 75(4):1973–1979, 1998.

[96] Zbigniew S Latallo, Anthony P Fletcher, Norma Alkjaersig, and Sol Sherry. Influence of pH, ionic strength, neutral ions, and thrombin on fibrin polymerization. *American Journal of Physiology – Legacy Content*, 202(4):675–680, apr 1962.

[97] Sydney Shulman, Sidney Katz, and John D. Ferry. The Conversion of Fibrinogen to Fibrin. *The Journal of General Physiology*, pages 759–766, 1953.

[98] Edward F Casassa. The Conversion of Fibrinogen to Fibrin. XIX . The Structure of the Intermediate Polymer of Fibrinogen Formed in Alkaline Solutions. *Journal of the American Chemical Society*, 369:3980–3985, 1956.

[99] C. H. Nair, G.A. Shah, and D.P. Dhall. Effect of Temperature, pH and Ionic Strength and Composition of Fibrin Network Structure and its Development. *Thrombosis Research*, 42(6):809–816, 1986.

[100] M Okude, A Yamanaka, and S Akihama. The effects of pH on the generation of turbidity and elasticity associated with fibrinogen-fibrin conversion by thrombin are remarkably influenced by sialic acid in fibrinogen. *Biological & pharmaceutical bulletin*, 18(2):203–7, 1995.

[101] Giovanni Dietler, Werner Kanzig, Andre Haeberli, and P Werner Straub. Temperature Dependence of Fibrin Polymerization: A Light Scattering Study. *Biochemistry*, 24(23):6701–6706, 1985.

[102] M Kaminski, K R Siebenlist, and M W Mosesson. Evidence for thrombin enhancement of fibrin polymerization that is independent of its catalytic activity. *The Journal of laboratory and clinical medicine*, 117(3):218–225, mar 1991.

[103] Ernst E. and Resch K.L. Fibrinogen as a cardiovascular risk factor: A meta-analysis and review of the literature. *Annals of Internal Medicine*, 118(12):956–963, 1993.

[104] J W Weisel and Chandrasekaran Nagaswami. Computer modeling of fibrin polymerization kinetics correlated with electron microscope and turbidity observations: clot structure and assembly are kinetically controlled. *Biophysical journal*, 63(1):111–28, 1992.

[105] Laurel E. Averett, Boris B. Akhremitchev, Mark H. Schoenfisch, and Oleg V. Gorkun. Calcium dependence of fibrin nanomechanics: The γ1 calcium mediates the unfolding of fibrinogen induced by force applied to the "a-a" bond. *Langmuir*, 26(18):14716–14722, 2010.

[106] Michael S Kostelansky, Laurie Betts, Oleg V Gorkun, and Susan T Lord. 2.8 A crystal structures of recombinant fibrinogen fragment D with and without two peptide ligands: GHRP binding to the "b" site disrupts its nearby calcium-binding site. *Biochemistry*, 41(40):12124–32, 2002.

[107] Philip R Bevington. *Data Reduction and Error Analysis for the Physical Sciences*. McGraw Hill, first edition, 1969.

[108] David J Brockwell, Emanuele Paci, Rebecca C Zinober, Godfrey S Beddard, Peter D Olmsted, D Alastair Smith, Richard N Perham, and Sheena E Radford. Pulling geometry defines the mechanical resistance of a beta-sheet protein. *Nature structural biology*, 10(9):731–737, 2003.

[109] G Marguerie and H B Stuhrmann. Neutron small-angle scattering study of bovine fibrinogen. *Journal of molecular biology*, 102:143, 1976.

[110] P L Privalov. Stability of proteins. Proteins which do not present a single cooperative system. *Advances in protein chemistry*, 35:1, 1982.

[111] T Godal, B Myrvang, S S Froland, J Shao, and G Melaku. Evidence that the mechanism of immunological tolerance ('central failure') is operative in the lack of host resistance in lepromatous leprosy. *Scandinavian journal of immunology*, 1(4):311–321, 1972.

[112] T H Donnelly, M Laskowski, N Notley, and H A Scheraga. Equilibria in the Fibrinogen-Fibrin Conversion. II. Reversibility of the Polymerization Steps. *Archives of Biochemistry and Biophysics*, 56(2):369–387, 1954.

[113] K. Laki. The Clotting of Fibrinogen. *Blood*, 125(24):3702–3710, 1953.

[114] Harold A. Scheraga. The thrombin-fibrinogen interaction. *Biophysical Chemistry*, 112(2-3 SPEC. ISS.):117–130, 2004.

[115] Marcus E Carr and Jan Hermans. Size and density of fibrin fibers from turbidity. *Macromolecules*, 11(1):46–50, 1978.

[116] J W Weisel, C Nagaswami, and L Makowski. Twisting of fibrin fibers limits their radial growth. *Proceedings of the National Academy of Sciences of the United States of America*, 84(24):8991–8995, 1987.

[117] Russell F Doolittle. Fibrinogen and Fibrin. *Annual Reviews in Biochemistry*, 53:195–229, 1984.

[118] Toni Hoffmann and Lorna Dougan. Single molecule force spectroscopy using polyproteins. *Chemical Society Reviews*, 41(14):4781–4796, 2012.

[119] George I Bell. Models for the specific adhesion of cells to cells. *Science*, 200(4342):618–627, 1978.

[120] E. Evans and K. Ritchie. Dynamic strength of molecular adhesion bonds. *Biophysical Journal*, 72(4):1541–1555, 1997.

[121] Sergi Garcia-Manyes, Jasna Brujić, Carmen L Badilla, and Julio M Fernández. Force-clamp spectroscopy of single-protein monomers reveals the individual unfolding and folding pathways of I27 and ubiquitin. *Biophysical journal*, 93(7):2436–2446, 2007.

[122] Lewyn Li, Hector Han Li Huang, Carmen L. Badilla, and Julio M. Fernandez. Mechanical unfolding intermediates observed by single-molecule force spectroscopy in a fibronectin type III module. *Journal of Molecular Biology*, 345(4):817–826, 2005.

[123] A S R Koti, A P Wiita, L Dougan, E Uggerud, and J M Fernandez. Single-molecule force spectroscopy measurements of bond elongation during a bimolecular reaction. *Journal of the American Chemical Society*, 130(20):6479–6487, 2008.

[124] Christine Horejs, Robin Ristle, Rupert Tscheliessnig, Uwe B Sleytr, and Dietmar Pum. Single-molecule Force Spectroscopy Reveals the Individual Mechanical Unfolding Pathways of a Surface Layer Protein. *Journal of Biological Chemistry*, 286(31):27416–27414, 2011.

[125] P E Marszalek, H Lu, H Li, M Carrion-Vazquez, a F Oberhauser, K Schulten, and J M Fernandez. Mechanical unfolding intermediates in titin modules. *Nature*, 402(November):100–103, 1999.

[126] A F Oberhauser, P K Hansma, M Carrion-Vazquez, and J M Fernandez. Stepwise unfolding of titin under force-clamp atomic force microscopy. *Proceedings of the National Academy of Sciences of the United States of America*, 98(2):468–472, 2001.

[127] S. Unnikrishna Papoulis, Athanasios Papoulis and Pillai. *Probability, Random Variables, and Stochastic Processes*. McGraw-Hill, 1965.

[128] Evan Evans. Probing the relation between force–lifetime–and chemistry in single molecular bonds. *Annual Review of Biophysics and Biomolecular Structure*, 30:105–28, 2001.

[129] Jasna Brujić, Rodolfo I. Hermans Z., Kirstin a. Walther, and Julio M. Fernandez. Single-molecule force spectroscopy reveals signatures of glassy dynamics in the energy landscape of ubiquitin. *Nature Physics*, 2(4):282–286, 2006.

[130] Jasna Brujić, Rodolfo I.Z. Hermans, Sergi Garcia-Manyes, Kirstin A. Walther, and Julio M. Fernandez. Dwell-Time Distribution Analysis of Polyprotein Unfolding Using Force-Clamp Spectroscopy. *Biophysical Journal*, 92(8):2896–2903, 2007.

[131] Tzu-Ling Kuo, Sergi Garcia-Manyes, Jingyuan Li, Itay Barel, Hui Lu, Bruce J Berne, Michael Urbakh, Joseph Klafter, and Julio M Fernández. Probing static disorder in Arrhenius kinetics by single-molecule force spectroscopy. *Proceedings of the National Academy of Sciences of the United States of America*, 107(25):11336–11340, 2010.

[132] J W Donovan and E Mihalyi. Conformation of fibrinogen: calorimetric evidence for a three-nodular structure. *Proceedings of the National Academy of Sciences of the United States of America*, 71(10):4125–4128, 1974.

[133] V C Yee, K P Pratt, H C Côté, I L Trong, D W Chung, E W Davie, R E Stenkamp, and D C Teller. Crystal structure of a 30 kDa C-terminal fragment from the gamma chain of human fibrinogen. *Structure*, 5(1):125–138, 1997.

[134] Nathan E Hudson. *The Structural Hierarchy and Mechanical Properties of Fibrin Described with a Multi-scale Model*. PhD thesis, University of North Carolina at Chapel Hill, 2011, arXiv:1011.1669v3.

[135] Feng Ding, Douglas Tsao, Huifen Nie, and Nikolay V. Dokholyan. Ab Initio Folding of Proteins with All-Atom Discrete Molecular Dynamics. *Structure*, 16(7):1010–1018, 2008.

[136] S. L. Betts, B. K. Merenbloom, and S. T. Lord. The structure of fibrinogen fragment D with the 'A' knob peptide GPRVVE. *Journal of Thrombosis and Haemostasis*, 4(5):1139–1141, 2006.

[137] Leonid Medved, Tatiana Ugarova, Yuri Veklich, Nina Lukinova, and John Weisel. Electron microscope investigation of the early stages of fibrin assembly. Twisted protofibrils and fibers. *Journal of Molecular Biology*, 216(3):503–509, 1990.

[138] Changbong Hyeon, Greg Morrison, David L Pincus, and D Thirumalai. Refolding dynamics of stretched biopolymers upon force quench. *Proceedings of the National Academy of Sciences of the United States of America*, 106(48):20288–20293, 2009, 0911.3530.

[139] Mai Suan Li, Chin-Kun Hu, Dmitri K Klimov, and D Thirumalai. Multiple stepwise refolding of immunoglobulin domain I27 upon force quench depends on initial conditions. *Proceedings of the National Academy of Sciences of the United States of America*, 103(1):93–98, 2006.

[140] Changbong Hyeon and D Thirumalai. Forced-unfolding and force-quench refolding of RNA hairpins. *Biophysical journal*, 90(10):3410–3427, 2006, 0601043.

[141] Changbong Hyeon and D Thirumalai. Measuring the energy landscape roughness and the transition state location of biomolecules using single molecule mechanical unfolding experiments. *Journal of Physics: Condensed Matter*, 19(11):44, 2006, 0612433.

[142] S Iyer, R M Gaikwad, V Subba-Rao, C D Woodworth, and Igor Sokolov. Atomic force microscopy detects differences in the surface brush of normal and cancerous cells. *Nature nanotechnology*, 4(6):389–393, 2009.

[143] Sarah E Cross, Yu-Sheng Jin, Jianyu Rao, and James K Gimzewski. Nanomechanical analysis of cells from cancer patients. *Nature nanotechnology*, 2(12):780–3, 2007.

[144] Małgorzata Lekka, Dorota Gil, Katarzyna Pogoda, Joanna Dulińska-Litewka, Robert Jach, Justyna Gostek, Olesya Klymenko, Szymon Prauzner-Bechcicki, Zbigniew Stachura, Joanna Wiltowska-Zuber, Krzysztof Okoń, and Piotr Laidler. Cancer cell detection in tissue sections using AFM. *Archives of Biochemistry and Biophysics*, 518(2):151–156, 2012.

[145] S. Suresh, J. Spatz, J. P. Mills, a. Micoulet, M. Dao, C. T. Lim, M. Beil, and T. Seufferlein. Connections between single-cell biomechanics and human disease states: Gastrointestinal cancer and malaria. *Acta Biomaterialia*, 1(1):15–30, 2005.

[146] Wenwei Xu, Roman Mezencev, Byungkyu Kim, Lijuan Wang, John McDonald, and Todd Sulchek. Cell Stiffness Is a Biomarker of the Metastatic Potential of Ovarian Cancer Cells. *PLoS ONE*, 7(10), 2012.

[147] W. R. Trickey, G. M. Lee, and F. Guilak. Viscoelastic properties of chondrocytes from normal and osteoarthritic human cartilage. *Journal of Orthopaedic Research*, 18(6):891–898, 2000.

[148] J Patrick Shelby, John White, Karthikeyan Ganesan, Pradipsinh K Rathod, and Daniel T Chiu. A microfluidic model for single-cell capillary obstruction by Plasmodium falciparum-infected erythrocytes. *Proceedings of the National Academy of Sciences of the United States of America*, 100(25):14618–14622, 2003.

[149] Tamara K Berdyyeva, Craig D Woodworth, and Igor Sokolov. Human epithelial cells increase their rigidity with ageing in vitro: direct measurements. *Physics in medicine and biology*, 50(1):81–92, 2005.

[150] Martin Stolz, Riccardo Gottardi, Roberto Raiteri, Sylvie Miot, Ivan Martin, Raphaël Imer, Urs Staufer, Aurelia Raducanu, Marcel Düggelin, Werner Baschong, A. U. Daniels, Niklaus F. Friederich, Attila Aszodi, and Ueli Aebi. Early detection of aging cartilage and osteoarthritis in mice and patient samples using atomic force microscopy. *Nature Nanotechnology*, 4(3):186–192, 2009.

[151] Jasmin T. Zahn, Ilia Louban, Simon Jungbauer, Martin Bissinger, Dieter Kaufmann, Ralf Kemkemer, and Joachim P. Spatz. Age-dependent changes in microscale stiffness and mechanoresponses of cells. *Small*, 7(10):1480–1487, 2011.

[152] F Guilak, J R Tedrow, and R Burgkart. Viscoelastic properties of the cell nucleus. *Biochemical and biophysical research communications*, 269(3):781–786, 2000.

[153] Nathalie Caille, Olivier Thoumine, Yanik Tardy, and Jean Jacques Meister. Contribution of the nucleus to the mechanical properties of endothelial cells. *Journal of Biomechanics*, 35(2):177–187, 2002.

[154] Ashkan Vaziri and M. R K Mofrad. Mechanics and deformation of the nucleus in micropipette aspiration experiment. *Journal of Biomechanics*, 40(9):2053–2062, 2007.

[155] M.L. Rodriguez, P.J. McGarry, and N.J. Sniadecki. Review on cell mechanics: Experimental and modeling approaches. *Applied Mechanics Reviews*, 65(6):060801, 2013.

[156] Kristina Haase, Zeinab Al-Rekabi, Louise Guolla, Ryan Hickey, Dominique Tremblay, and Andrew E. Pelling. Simultaneous optical and mechanical probes to investigate complex cellular responses to physical cues. *SPIE*, 9327:11, 2015.

[157] Denis Wirtz, Konstantinos Konstantopoulos, and Peter C Searson. The physics of cancer: the role of physical interactions and mechanical forces in metastasis. *Nature reviews. Cancer*, 11(7):512–522, 2011.

[158] Carmela Pasternak, Scott Wong, and Elliot L. Elson. Mechanical function of dystrophin in muscle cells. *Journal of Cell Biology*, 128(3):355–361, 1995.

[159] Jochen Guck, Stefan Schinkinger, Bryan Lincoln, Falk Wottawah, Susanne Ebert, Maren Romeyke, Dominik Lenz, Harold M. Erickson, Revathi Ananthakrishnan, Daniel Mitchell, Josef Käs, Sydney Ulvick, and Curt Bilby. Optical Deformability as an Inherent Cell Marker for Testing Malignant Transformation and Metastatic Competence. *Biophysical Journal*, 88(5):3689–3698, 2005.

[160] Philipp Isermann and Jan Lammerding. Nuclear mechanics and mechanotransduction in health and disease. *Current Biology*, 23(24):R1113–R1121, 2013, NIHMS150003.

[161] Monika Zwerger, Chin Yee Ho, and Jan Lammerding. Nuclear Mechanics in Disease. *Annu Rev Biomed Eng*, 13(1):397–428, 2011.

[162] Kris Noel Dahl, Alexandre J.S. S Ribeiro, and Jan Lammerding. Nuclear Shape, Mechanics, and Mechanotransduction. *Circulation Research*, 102(11):1307–1318, 2008.

[163] Christophe Guilluy and Keith Burridge. Nuclear mechanotransduction: Forcing the nucleus to respond. *Nucleus*, 6(1):19–22, 2015.

[164] Katarina Wolf, Mariska te Lindert, Marina Krause, Stephanie Alexander, Joost te Riet, Amanda L. Willis, Robert M. Hoffman, Carl G. Figdor, Stephen J. Weiss, and Peter Friedl. Physical limits of cell migration: Control by ECM space and nuclear deformation and tuning by proteolysis and traction force. *Journal of Cell Biology*, 201(7):1069–1084, 2013.

[165] Peter Friedl, Katarina Wolf, and Jan Lammerding. Nuclear mechanics during cell migration. *Current Opinion in Cell Biology*, 23(1):55–64, 2011.

[166] Amy C. Rowat, Jan Lammerding, Harald Herrmann, and Ueli Aebi. Towards an integrated understanding of the structure and mechanics of the cell nucleus. *BioEssays*, 30(3):226–236, 2008.

[167] Kristina Haase, Andrew E Pelling, and Kristina Haase. Investigating cell mechanics with atomic force microscopy. *Journal of the Royal Society, Interface / the Royal Society*, 12(figure 1):20140970, 2015.

[168] Gawain Thomas, Nancy a Burnham, Terri Anne Camesano, and Qi Wen. Measuring the mechanical properties of living cells using atomic force microscopy. *Journal of visualized experiments : JoVE*, 76:1–8, 2013.

[169] D C Lin, E K Dimitriadis, and F Horkay. Robust strategies for automated AFM force curve analysis–I. Non-adhesive indentation of soft, inhomogeneous materials. *J Biomech Eng*, 129(3):430–440, 2007.

[170] J. K. Fisher, J. Cribb, K. V. Desai, L. Vicci, B. Wilde, K. Keller, R. M. Taylor, J. Haase, K. Bloom, E. Timothy O'Brien, and R. Superfine. Thin-foil magnetic force system for high-numerical-aperture microscopy. *Review of Scientific Instruments*, 77(2), 2006.

[171] Teru Kanda, Kevin F Sullivan, and Geoffrey M Wahl. Histone-GFP fusion protein enables sensitive analysis of chromosome dynamics in living mammalian cells. *Current biology : CB*, 8(7):377–385, 1998.

[172] M. Tartibi, Y. X. Liu, G. Y. Liu, and K. Komvopoulos. Single-cell mechanics - An experimental-computational method for quantifying the membrane-cytoskeleton elasticity of cells. *Acta Biomaterialia*, 27:224–235, 2015.

[173] Carina Gonnermann, Chaolie Huang, Sarah F. Becker, Dimitar R. Stamov, Doris Wedlich, Jubin Kashef, and Clemens M. Franz. Quantitating membrane bleb stiffness using AFM force spectroscopy and an optical sideview setup. *Integr. Biol.*, 7(3):356–363, 2015.

[174] Igor Sokolov, Swaminathan Iyer, Venkatesh Subba-Rao, Ravi M. Gaikwad, and Craig D. Woodworth. Detection of surface brush on biological cells in vitro with atomic force microscopy. *Applied Physics Letters*, 91(2), 2007.

[175] Marija Plodinec, Marko Loparic, Christophe A Monnier, Ellen C Obermann, Rosanna Zanetti-Dallenbach, Philipp Oertle, Janne T Hyotyla, Ueli Aebi, Mohamed Bentires-Alj, Roderick Y H Lim, and Cora-Ann Schoenenberger. The nanomechanical signature of breast cancer. *Nature nanotechnology*, 7(11):757–65, 2012.

[176] D. R. Gossett, H. T. K. Tse, S. a. Lee, Y. Ying, a. G. Lindgren, O. O. Yang, J. Rao, a. T. Clark, and D. Di Carlo. Hydrodynamic stretching of single cells for large population mechanical phenotyping. *Proceedings of the National Academy of Sciences*, 109(20):7630–7635, 2012.

[177] David B Agus, Jenolyn F Alexander, Wadih Arap, Shashanka Ashili, Joseph E Aslan, Robert H Austin, Vadim Backman, Kelly J Bethel, Richard Bonneau, Wei-Chiang Chen, Chira Chen-Tanyolac, Nathan C Choi, Steven a Curley, Matthew Dallas, Dhwanil Damania, Paul C W Davies, Paolo Decuzzi, Laura Dickinson, Luis Estevez-Salmeron, Veronica Estrella, Mauro Ferrari, Claudia Fischbach, Jasmine Foo, Stephanie I Fraley, Christian Frantz, Alexander Fuhrmann, Philippe Gascard, Robert a Gatenby, Yue Geng, Sharon Gerecht, Robert J Gillies, Biana Godin, William M Grady, Alex Greenfield, Courtney Hemphill, Barbara L Hempstead, Abigail Hielscher, W Daniel Hillis, Eric C Holland, Arig Ibrahim-Hashim, Tyler Jacks, Roger H Johnson, Ahyoung Joo, Jonathan E Katz, Laimonas Kelbauskas, Carl Kesselman, Michael R King, Konstantinos Konstantopoulos, Casey M Kraning-Rush, Peter Kuhn, Kevin Kung, Brian Kwee, Johnathon N Lakins, Guillaume Lambert, David Liao, Jonathan D Licht, Jan T Liphardt, Liyu Liu, Mark C Lloyd, Anna Lyubimova, Parag Mallick, John Marko, Owen J T McCarty, Deirdre R Meldrum, Franziska Michor, Shannon M Mumenthaler, Vivek Nandakumar, Thomas V O'Halloran, Steve Oh, Renata Pasqualini, Matthew J Paszek, Kevin G Philips, Christopher S Poultney, Kuldeepsinh Rana, Cynthia a Reinhart-King, Robert Ros, Gregg L Semenza, Patti Senechal, Michael L Shuler, Srimeenakshi Srinivasan, Jack R Staunton, Yolanda Stypula, Hariharan Subramanian, Thea D Tlsty, Garth W Tormoen, Yiider Tseng, Alexander van Oudenaarden, Scott S Verbridge, Jenny C Wan, Valerie M Weaver, Jonathan Widom, Christine Will, Denis Wirtz, Jonathan Wojtkowiak, and Pei-Hsun Wu. A physical sciences network characterization of non-tumorigenic and metastatic cells. *Scientific reports*, 3:1449, 2013.

[178] Michael Beil, Alexandre Micoulet, Götz von Wichert, Stephan Paschke, Paul Walther, M Bishr Omary, Paul P Van Veldhoven, Ulrike Gern, Elke Wolff-Hieber, Juliane Eggermann, Johannes Waltenberger, Guido Adler, Joachim Spatz, and Thomas Seufferlein. Sphingosylphosphorylcholine regulates keratin network architecture and visco-elastic properties of human cancer cells. *Nature cell biology*, 5(9):803–811, 2003.

[179] Jeremy A. Cribb, Lukas D. Osborne, Kellie Beicker, Matthew Psioda, Jian Chen, E. Timothy O'Brien, Russell M. Taylor II, Leandra Vicci, Joe Ping-Lin Hsiao, Chong Shao, Michael Falvo, Joseph G. Ibrahim, Kris C. Wood, Gerard C. Blobe, and Richard Superfine. An Automated High-throughput Array Microscope for Cancer Cell Mechanics. *Scientific Reports*, 6(January):27371, 2016.

[180] F Wong-Staal, R Dalla-Favera, Genoveffa Franchini, Edward P Gelmann, and Robert C Gallo. Three distinct genes in human DNA related to the transforming genes of mammalian sarcoma retroviruses. *Science (New York, N.Y.)*, 213(4504):226–8, 1981.

[181] Rosalyn M. Adam, Nishit K. Mukhopadhyay, Jayoung Kim, Dolores Di Vizio, Bekir Cinar, Kelly Boucher, Keith R. Solomon, and Michael R. Freeman. Cholesterol sensitivity of endogenous and myristoylated Akt. *Cancer Research*, 67(13):6238–6246, 2007.

[182] Dos D. Sarbassov, David A. Guertin, Siraj M. Ali, and David M. Sabatini. Phosphorylation and

Regulation of Akt / PKB by the Rictor-mTOR Complex. *Science*, 307:1098–1101, 2004.

[183] Regan M. Memmott and Phillip A. Dennis. Akt-dependent and -independent mechanisms of mTOR regulation in cancer. *Cellular Signalling*, 21(5):656–664, 2009.

[184] Michael L. Cleary, Stephen D. Smith, and Jeffrey Sklar. Cloning and structural analysis of cDNAs for bcl-2 and a hybrid bcl-2/immunoglobulin transcript resulting from the t(14;18) translocation. *Cell*, 47(1):19–28, 1986.

[185] Cheng-Yi Sun, Bai-Len Wang, Chao-Quan Hu, Rui-Yun Peng, Ya-Bing Gao, Qing-Yang Gu, and De-Wen Wang. Expression of bcl-2 gene and its significance in human pancreatic carcinoma. *Hepatobiliary & Pancreatic Diseases International*, 1(2):306–308, 2002.

[186] Joseph M. Galante, Melinda M. Mortenson, Tawnya L. Bowles, Subbulakshmi Virudachalam, and Richard J. Bold. ERK/BCL-2 Pathway in the Resistance of Pancreatic Cancer to Anoikis. *Journal of Surgical Research*, 152(1):18–25, 2009.

[187] C. Bassing, J. Yingling, D. Howe, T Wang, W. He, M. Gustafson, Paresh Shah, P. Donahoe, and Xiao-fan Wang. A transforming growth factor beta type I receptor that signals to activate gene expression. *Science*, 263(5143):87–89, 1994.

[188] Kelly J Gordon and Gerard C Blobe. Role of transforming growth factor-beta superfamily signaling pathways in human disease. *Biochimica et biophysica acta*, 1782(4):197–228, 2008.

[189] J Xu, Samy Lamouille, and R Derynck. TGF-beta-induced epithelial to mesenchymal transition. *Cell Res*, 19(2):156–172, 2009.

[190] Liqiang Song, Ping Wang, Yu Tian, De Chang, Kailong Li, Yongna Fan, Jing Shen, Hongzhen Du, Ruifang Mi, Xiaoxia Bian, and Xianchao Tang. Lung metastasis of pancreatic carcinoma is regulated by TGFβ signaling. *Tumor Biology*, 36(4):2271–2276, 2015.

[191] Colin A Martz, Kathleen A Ottina, Katerine R. Singleton, Jeff S Jasper, Suzzanne E Wardell Ashley Peraza-Penton, Grace R Anderson, Peter S Winter, Tim Wang, Holly M Alley, Lawrence N Kwong, Zachary A Cooper, Michael Tetzlaff, Pei-Ling Chen, Jeffrey C Rathmell, Keith T Flaherty, Jennifer A Wargo, Donald P McDonnell, David M. Sabatini, and Kris C Wood. Systematic identification of signaling pathways with potential to confer anticancer drug resistance. *Sci Signal*, 7(357), 2014.

[192] Nabeel Bardeesy and Ronald a DePinho. Pancreatic cancer biology and genetics. *Nature reviews. Cancer*, 2(12):897–909, 2002.

[193] H Ouyang, Lj Mou, C Luk, N Liu, J Karaskova, J Squire, and M S Tsao. Immortal human pancreatic duct epithelial cell lines with near normal genotype and phenotype. *The American journal of pathology*, 157(5):1623–1631, 2000.

[194] M Takeuchi, T Shichinohe, N Senmaru, M Miyamoto, H Fujita, M Takimoto, S Kondo, H Katoh, and N Kuzumaki. The dominant negative H-ras mutant, N116Y, suppresses growth of metastatic human

pancreatic cancer cells in the liver of nude mice. *Gene therapy*, 7(6):518–26, 2000.

[195] Sarah E Cross, Yu-Sheng Jin, Julianne Tondre, Roger Wong, JianYu Rao, and James K Gimzewski. AFM-based analysis of human metastatic cancer cells. *Nanotechnology*, 19(38):384003, 2008.

[196] Nadine Walter, Tobias Busch, Thomas Seufferlein, and Joachim P Spatz. Elastic moduli of living epithelial pancreatic cancer cells and their skeletonized keratin intermediate filament network. *Biointerphases*, 6(2):79–85, 2011.

[197] G Bao and S Suresh. Cell and molecular mechanics of biological materials. *Nature materials*, 2(11):715–725, 2003.

[198] Amnon Buxboim, Irena L Ivanovska, and Dennis E Discher. Matrix elasticity, cytoskeletal forces and physics of the nucleus: how deeply do cells 'feel' outside and in? *Journal of cell science*, 123(Pt 3):297–308, 2010, 76649104718.

[199] Paul a. Janmey and R. Tyler Miller. Mechanisms of mechanical signaling in development and disease. *Journal of cell science*, 124(Pt 1):9–18, 2011.

[200] L. Guolla, M. Bertrand, K. Haase, and a. E. Pelling. Force transduction and strain dynamics in actin stress fibres in response to nanonewton forces. *Journal of Cell Science*, 125(3):603–613, 2012.

[201] Kristina Haase and Andrew E. Pelling. Resiliency of the plasma membrane and actin cortex to large-scale deformation. *Cytoskeleton*, 70(9):494–514, 2013.

[202] Brian C DiPaolo, Guillaume Lenormand, Jeffrey J Fredberg, and Susan S Margulies. Stretch magnitude and frequency-dependent actin cytoskeleton remodeling in alveolar epithelia. *American journal of physiology. Cell physiology*, 299(2):C345–C353, 2010.

[203] a. Raman, S. Trigueros, a. Cartagena, a. P. Z. Stevenson, M. Susilo, E. Nauman, and S. Antoranz Contera. Mapping nanomechanical properties of live cells using multi-harmonic atomic force microscopy. *Nature Nanotechnology*, 6(12):809–814, 2011.

[204] E M Darling. Force scanning: a rapid, high-resolution approach for spatial mechanical property mapping. *Nanotechnology*, 22(17):175707, 2011, NIHMS150003.

[205] Jamie L. Maciaszek and George Lykotrafitis. Sickle cell trait human erythrocytes are significantly stiffer than normal. *Journal of Biomechanics*, 44(4):657–661, 2011.

[206] Valentin Lulevich, Christopher C Zimmer, Hyun-seok Hong, Lee-way Jin, and Gang-yu Liu. Single-cell mechanics provides a sensitive and quantitative means for probing amyloid-β peptide and neuronal cell interactions. *Proceedings of the National Academy of Sciences*, 107(31):13872–13877, 2010.

[207] Constantine Y. Khripin, C. Jeffrey Brinker, and Bryan Kaehr. Mechanically tunable multiphoton fabricated protein hydrogels investigated using atomic force microscopy. *Soft Matter*, 6:2842, 2010.

[208] Miriam V. Flores-Merino, Somyot Chirasatitsin, Caterina LoPresti, Gwendolen C. Reilly, Giuseppe Battaglia, and Adam J. Engler. Nanoscopic mechanical anisotropy in hydrogel surfaces. *Soft Matter*, 6(18):4466, 2010.

[209] Eric M. Darling, Stefan Zauscher, Joel A. Block, and Farshid Guilak. A Thin-Layer Model for Viscoelastic, Stress-Relaxation Testing of Cells Using Atomic Force Microscopy: Do Cell Properties Reflect Metastatic Potential? *Biophysical Journal*, 92(5):1784–1791, 2007.

[210] P Maguire, J I Kilpatrick, G Kelly, P J Prendergast, V A. Campbell, B C O'Connell, and S P Jarvis. Direct mechanical measurement of geodesic structures in rat mesenchymal stem cells. *HFSP Journal*, 1(3):181–91, 2007.

[211] Valentin Lulevich, Tiffany Zink, Huan-yuan Chen, Fu-tong Liu, and Gang-yu Liu. Cell mechanics using atomic force microscopy-based single-cell compression. *Langmuir*, 22(19):8151–8155, 2006.

[212] A. Engler, M. Sheehan, H. L. Sweeney, and D. E. Discher. Substrate compliance vs ligand density in cell on gel responses. *European Cells and Materials*, 6(SUPPL. 1):7–8, 2003.

[213] James Jonkman and Claire M Brown. Any Way You Slice It-A Comparison of Confocal Microscopy Techniques. *Journal of biomolecular techniques : JBT*, 26(2):54–65, 2015.

[214] S. Lindek, T. Stefany, and E. H. K. Stelzer. Single-lens theta microscopy âĂŤ a new implementation of confocal theta microscopy. *Journal of Microscopy*, 188(3):280–284, 1997.

[215] Steffen Lindek, Jim Swoger, and Ernst H. K. Stelzer. Single-lens theta microscopy: resolution, efficiency and working distance. *Journal of Modern Optics*, 46(5):843–858, 1999.

[216] C a Boocock, a F Brown, and G a Dunn. A simple chamber for observing microscopic specimens in both top and side views. *Journal of microscopy*, 137(Pt 1):29–34, 1985.

[217] J Cao, S Usami, and C Dong. Development of a side-view chamber for studying cell-surface adhesion under flow conditions. *Annals of biomedical engineering*, 25(3):573–580, 1997.

[218] Jin Yang, Robert J Melder, Rakesh K Jain, and Lance L Munn. Lateral View Flow System for Studies of Cell Adhesion and Deformation under Flow Conditions. *Biotechniques*, 30(2):388–394, 2001.

[219] Jordan Leyton-Mange, Sung Yang, Meghan H. Hoskins, Robert F. Kunz, Jeffrey D. Zahn, and Cheng Dong. Design of a side-view particle imaging velocimetry flow system for cell-substrate adhesion studies. *Journal of Biomechanical Engineering*, 128:271–278, 2006.

[220] K T Seale, R S Reiserer, D a Markov, I a Ges, C Wright, C Janetopoulos, and J P Wikswo. Mirrored pyramidal wells for simultaneous multiple vantage point microscopy. *Journal of microscopy*, 232(1):1–6, 2008.

[221] Kevin Seale, Chris Janetopoulos, and John Wikswo. Micro-Mirrors for Nanoscale Three- Dimensional

Microscopy. *ACS Nano*, 3(3):493–497, 2009.

[222] Houssam Hajjoul, Julien Mathon, Yannick Viero, and Aurélien Bancaud. Optimized micromirrors for three-dimensional single-particle tracking in living cells. *Applied Physics Letters*, 98(24):1–4, 2011.

[223] Nataliia Guz, Maxim Dokukin, Vivekanand Kalaparthi, and Igor Sokolov. If Cell Mechanics Can Be Described by Elastic Modulus: Study of Different Models and Probes Used in Indentation Experiments. *Biophysical Journal*, 107(3):564–575, 2014.

[224] Andrew R Harris and G T Charras. Experimental validation of atomic force microscopy-based cell elasticity measurements. *Nanotechnology*, 22(34):345102, 2011.

[225] P. A. Santi. Light Sheet Fluorescence Microscopy: A Review. *Journal of Histochemistry & Cytochemistry*, 59(2):129–138, 2011.

[226] Emmanuel G Reynaud, Uros Krzic, Klaus Greger, and Ernst H K Stelzer. Light sheet-based fluorescence microscopy: more dimensions, more photons, and less photodamage. *HFSP journal*, 2(5):266–75, 2008.

[227] J. Huisken and D. Y. R. Stainier. Selective plane illumination microscopy techniques in developmental biology. *Development*, 136(12):1963–1975, 2009.

[228] Jerome Mertz. Optical sectioning microscopy with planar or structured illumination. *Nature Methods*, 8(10):811–819, 2011.

[229] J Christof M Gebhardt, David M Suter, Rahul Roy, Ziqing W Zhao, Alec R Chapman, Srinjan Basu, Tom Maniatis, and X Sunney Xie. Single-molecule imaging of transcription factor binding to DNA in live mammalian cells. *Nature methods*, 10(5):421–6, 2013.

[230] R P Baker, M J Taormina, M Jemielita, and R Parthasarathy. A combined light sheet fluorescence and differential interference contrast microscope for live imaging of multicellular specimens. *Journal of microscopy*, 00(0):1–7, 2015.

[231] Raghav K Chhetri, Fernando Amat, Yinan Wan, Burkhard Höckendorf, William C Lemon, and Philipp J Keller. Whole-animal functional and developmental imaging with isotropic spatial resolution. *Nature Methods*, 12(12):1171–1178, 2015.

[232] Edward J Botcherby, Rimas Juskaitis, Martin J Booth, and Tony Wilson. Aberration-free optical refocusing in high numerical aperture microscopy. *Optics Letters*, 32(14):2007–2009, 2007.

[233] E.J. Botcherby, R. Juškaitis, M.J. Booth, and T. Wilson. An optical technique for remote focusing in microscopy. *Optics Communications*, 281(4):880–887, 2008.

[234] E. J. Botcherby, C. W. Smith, M. M. Kohl, D. Debarre, M. J. Booth, R. Juskaitis, O. Paulsen, and T. Wilson. Aberration-free three-dimensional multiphoton imaging of neuronal activity at kHz rates.

Proceedings of the National Academy of Sciences, 109(8):2919–2924, 2012.

[235] Remi Galland, Gianluca Grenci, Ajay Aravind, Virgile Viasnoff, Vincent Studer, and Jean-Baptiste Sibarita. 3D high- and super-resolution imaging using single-objective SPIM. *Nature methods*, 12(August 2014):641–4, 2015.

[236] Michael Smutny and Alpha S. Yap. Neighborly relations: cadherins and mechanotransduction. *Journal of Cell Biology*, 189(7):1107–1115, 2010.

[237] Quint Le Duc, Quanming Shi, Iris Blonk, Arnoud Sonnenberg, Ning Wang, Deborah Leckband, and Johan De Rooij. Vinculin potentiates E-cadherin mechanosensing and is recruited to actin-anchored sites within adherens junctions in a myosin II-dependent manner. *Journal of Cell Biology*, 189(7):1107–1115, 2010.

[238] Martial Hervy, Laura Hoffman, and Mary C. Beckerle. From the membrane to the nucleus and back again: bifunctional focal adhesion proteins. *Current Opinion in Cell Biology*, 18(5):524–532, 2006.

[239] Sirio Dupont, Leonardo Morsut, Mariaceleste Aragona, Elena Enzo, Stefano Giulitti, Michelangelo Cordenonsi, Francesca Zanconato, Jimmy Le Digabel, Mattia Forcato, Silvio Bicciato, Nicola Elvassore, and Stefano Piccolo. Role of YAP/TAZ in mechanotransduction. *Nature*, 474(7350):179–183, 2011.

[240] Melissa Crisp, Qian Liu, Kyle Roux, J. B. Rattner, Catherine Shanahan, Brian Burke, Phillip D. Stahl, and Didier Hodzic. Coupling of the nucleus and cytoplasm: Role of the LINC complex. *Journal of Cell Biology*, 172(1):41–53, 2006.

[241] Farhana Haque, David J Lloyd, Dawn T Smallwood, Carolyn L Dent, Catherine M Shanahan, Andrew M Fry, Richard C Trembath, and Sue Shackleton. SUN1 interacts with nuclear lamin A and cytoplasmic nesprins to provide a physical connection between the nuclear lamina and the cytoskeleton. *Molecular and cellular biology*, 26(10):3738–51, 2006.

[242] C M Waterman-Storer, A Desai, J C Bulinski, and E D Salmon. Fluorescent speckle microscopy, a method to visualize the dynamics of protein assemblies in living cells. *Current biology : CB*, 8(22):1227–1230, 1998.

[243] Kyoko Chiba, Yuki Shimada, Masataka Kinjo, Toshiharu Suzuki, and Seiich Uchida. Simple and Direct Assembly of Kymographs from Movies Using KYMOMAKER. *Traffic*, 15(1):1–11, 2014.

[244] Donald Ingber. Integrins, Tensigrity, and Mechanotransduction, 1997.

[245] Yu-li Wang and Dennis E Discher. *Cell mechanics*, volume 83. Academic Press, 2007.

[246] M Takahashi, T Ishida, O Traub, M A Corson, and B C Berk. Mechanotransduction in endothelial cells: temporal signaling events in response to shear stress. *Journal of vascular research*, 34(3):212–9, 1997.

[247] Junichi Sadoshima and Seigo Izumo. the Cellular and Molecular Response of Cardiac Myocytes To Mechanical Stress. *Annu. Rev. Physiol*, 59(56):551–71, 1997.

[248] Shirish Vichare, Shamik Sen, and Mandar M Inamdar. Cellular mechanoadaptation to substrate mechanical properties: contributions of substrate stiffness and thickness to cell stiffness measurements using AFM. *Soft matter*, 10(8):1174–81, 2014.

[249] Shaohua Hu, Jianxin Chen, Ben Fabry, Yasushi Numaguchi, Andrew Gouldstone, Donald E Ingber, Jeffrey J Fredberg, James P Butler, and Ning Wang. Intracellular stress tomography reveals stress focusing and structural anisotropy in cytoskeleton of living cells. *American journal of physiology. Cell physiology*, 285(5):C1082–C1090, 2003.

[250] A J Maniotis, C S Chen, and D E Ingber. Demonstration of mechanical connections between integrins, cytoskeletal filaments, and nucleoplasm that stabilize nuclear structure. *Proceedings of the National Academy of Sciences of the United States of America*, 94(3):849–54, 1997.

[251] Andrew E Pelling, Brian M Nicholls, Yaron R Silberberg, and Michael A Horton. Approaches for investigating mechanobiological dynamics in living cells with fluorescence and atomic force microscopies. *Modern Research and Educational Topics in Microscopy*, pages 26–28, 2007.

[252] Philippe Carl and Hermann Schillers. Elasticity measurement of living cells with an atomic force microscope: Data acquisition and processing. *Pflugers Archiv European Journal of Physiology*, 457(2):551–559, 2008.

[253] S. Kasas, X. Wang, H. Hirling, R. Marsault, B. Huni, A. Yersin, R. Regazzi, G. Grenningloh, B. Riederer, L. Forrò, G. Dietler, and S. Catsicas. Superficial and deep changes of cellular mechanical properties following cytoskeleton disassembly. *Cell Motility and the Cytoskeleton*, 62(2):124–132, 2005.

[254] M. M. Knight, Z. Bomzon, E. Kimmel, A. M. Sharma, D. A. Lee, and D. L. Bader. Chondrocyte deformation induces mitochondrial distortion and heterogeneous intracellular strain fields. *Biomechanics and Modeling in Mechanobiology*, 5(2-3):180–191, 2006.

[255] Yaron R. Silberberg, Andrew E. Pelling, Gleb E. Yakubov, William R. Crum, David J. Hawkes, and Mike A. Horton. Tracking displacements of intracellular organelles in response to nanomechanical forces. *2008 5th IEEE International Symposium on Biomedical Imaging: From Nano to Macro, Proceedings, ISBI*, 21:1335–1338, 2008.

[256] Rehana Afrin, Takafumi Yamada, and Atsushi Ikai. Analysis of force curves obtained on the live cell membrane using chemically modified AFM probes. *Ultramicroscopy*, 100(3-4):187–195, 2004.

[257] M. M. Lotz, C. A. Burdsal, H. P. Erickson, and D. R. McClay. Cell adhesion to fibronectin and tenascin: Quantitative measurements of initial binding and subsequent strengthening response. *Journal of Cell Biology*, 109(4 I):1795–1805, 1989.

[258] Gaurav Girdhar and Jin-Yu Shao. Simultaneous Tether Extraction from Endothelial Cells and Leukocytes: Observation, Mechanics, and Significance. *Biophysical Journal*, 93(11):4041–4052, 2007.

[259] Imre Derényi, Frank Jülicher, and Jacques Prost. Formation and Interaction of Membrane Tubes. *Physical Review Letters*, 88(23):238101, 2002, 0205630.

[260] H. P. Erikson, N. Carrell, and J. McDonagh. Fibronectin molecule visualized in electron microscopy: A long, thin, flexible strand. *Journal of Cell Biology*, 91(3 I):673–678, 1981.

[261] Sietze Reitsma, Dick W. Slaaf, Hans Vink, Marc A M J Van Zandvoort, and Mirjam G A Oude Egbrink. The endothelial glycocalyx: Composition, functions, and visualization. *Pflugers Archiv European Journal of Physiology*, 454(3):345–359, 2007.

[262] Eno E. Ebong, Frank P. MacAluso, David C. Spray, and John M. Tarbell. Imaging the endothelial glycocalyx in vitro by rapid freezing/freeze substitution transmission electron microscopy. *Arteriosclerosis, Thrombosis, and Vascular Biology*, 31(8):1908–1915, 2011, NIHMS150003.

[263] Claire M Brown, Benedict Hebert, David L Kolin, Jessica Zareno, Leanna Whitmore, Alan Rick Horwitz, and Paul W Wiseman. Probing the integrin-actin linkage using high-resolution protein velocity mapping. *Journal of cell science*, 119(Pt 24):5204–5214, 2006.

[264] Benedict Hebert, Santiago Costantino, and Paul W. Wiseman. Spatiotemporal Image Correlation Spectroscopy (STICS) Theory, Verification, and Application to Protein Velocity Mapping in Living CHO Cells. *Biophysical Journal*, 88(5):3601–3614, 2005.

[265] J. Swift and D. E. Discher. The nuclear lamina is mechano-responsive to ECM elasticity in mature tissue. *Journal of Cell Science*, 127(14):3005–3015, 2014.

[266] Valentin T. Jordanov, Glenn F. Knoll, Alan C. Huber, and John A. Pantazis. Digital techniques for real-time pulse shaping in radiation measurements. *Nuclear Inst. and Methods in Physics Research, A*, 353(1-3):261–264, 1994.

[267] William T. King, Meihong Su, and Guoliang Yang. Monte Carlo simulation of mechanical unfolding of proteins based on a simple two-state model. *International Journal of Biological Macromolecules*, 46(2):159–166, 2010.

[268] J. D. Bryngelson, J. N. Onuchic, N. D. Socci, and P. G. Wolynes. Funnels, pathways, and the energy landscape of protein folding: A synthesis. *Proteins: Structure, Function and Genetics*, 21(3):167–195, 1995, 9411008.

[269] T Lazaridis. "New View" of Protein Folding Reconciled with the Old Through Multiple Unfolding Simulations. *Science*, 278(5345):1928–1931, 1997.

[270] Changbong Hyeon and D Thirumalai. Can energy landscape roughness of proteins and RNA be measured by using mechanical unfolding experiments? *Proceedings of the National Academy of Sciences of the United States of America*, 100(18):10249–10253, 2003.

[271] Alan Fersht. *Structure and mechanism in protein science: a guide to enzyme catalysis and protein folding*, volume 13409. Macmillan, 1999.

[272] H Frauenfelder, S. Sligar, and P. Wolynes. The energy landscapes and motions of proteins. *Science*, 254(5038):1598–1603, 1991.

[273] Dennis E Discher, Paul Janmey, and Yu-Li Wang. Tissue cells feel and respond to the stiffness of their substrate. *Science (New York, N.Y.)*, 310(5751):1139–43, 2005.

[274] Theresa A. Ulrich, Elena M. De Juan Pardo, and Sanjay Kumar. The mechanical rigidity of the extracellular matrix regulates the structure, motility, and proliferation of glioma cells. *Cancer Research*, 69(10):4167–4174, 2009, NIHMS150003.

[275] Fitzroy J. Byfield, Qi Wen, Ilya Levental, Kerstin Nordstrom, Paulo E. Arratia, R. Tyler Miller, and Paul A. Janmey. Absence of filamin A prevents cells from responding to stiffness gradients on gels coated with collagen but not fibronectin. *Biophysical Journal*, 96(12):5095–5102, 2009.

[276] Adam J. Engler, Shamik Sen, H. Lee Sweeney, and Dennis E. Discher. Matrix Elasticity Directs Stem Cell Lineage Specification. *Cell*, 126(4):677–689, 2006.

[277] Robert R Kay, Paul Langridge, David Traynor, and Oliver Hoeller. Changing directions in the study of chemotaxis. *Nature reviews. Molecular cell biology*, 9(6):455–463, 2008.

[278] Anthony E. Siegman, M. W. Sasnett, and T. F. Johnston. Choice of clip levels for beam width measurements using knife-edge techniques. *IEEE Journal of Quantum Electronics*, 27(4):1098–1104, 1991.

[279] Richard W Cole, Tushare Jinadasa, and Claire M Brown. Measuring and interpreting point spread functions to determine confocal microscope resolution and ensure quality control. *Nature Protocols*, 6(12):1929–1941, 2011.

[280] Cédric Matthews and Fp Fabrice P. Cordelières. MetroloJ : an ImageJ plugin to help monitor microscopes' health. *ImageJ User & Developer Conference*, pages 2–7, 2010.

[281] Whasil Lee, Holly A Leddy, Yong Chen, Suk Hee Lee, Nicole A Zelenski, Amy L McNulty, Jason Wu, Kellie N Beicker, Jeffrey Coles, Stefan Zauscher, Jörg Grandl, Frederick Sachs, Farshid Guilak, and Wolfgang B Liedtke. Synergy between Piezo1 and Piezo2 channels confers high-strain mechanosensitivity to articular cartilage. *Proceedings of the National Academy of Sciences of the United States of America*, 111(47):E5114–22, 2014.

[282] Sang-Kuy Han, Wim Wouters, Andrea Clark, and Walter Herzog. Mechanically induced calcium signaling in chondrocytes in situ. *Journal of orthopaedic research : official publication of the Orthopaedic Research Society*, 30(3):475–81, 2012.